University of Canterbury

Masters of Engineering Thesis

Rapid Synchronization Control of Compressed Gas Energy Storage Generator During Power Grid Contingent and Extended Contingent Events

Author:
Yi-Yu (Patrick) Chen

Supervisors:
Dr. Alan Wood
Dr. Chris Bumby
Dr. Rod Badcock

A thesis submitted in fulfilment of the requirements
for the degree of

Masters of Enigneering

in

Department of Electrical and Computer Engineering

at the

University of Canterbury

September 2015

Declaration of Authorship

I, Yi-Yu (Patrick) Chen, declare that this thesis titled, 'Rapid Synchronization Control of Compressed Gas Energy Storage Generator During Power Grid Contingent and Extended Contingent Events' and the work presented in it are my own. I confirm that:

- This work was done wholly or mainly while in candidature for a research degree at this University.
- Where any part of this thesis has previously been submitted for a degree or any other qualification at this University or any other institution, this has been clearly stated.
- Where I have consulted the published work of others, this is always clearly attributed.
- Where I have quoted from the work of others, the source is always given. With the exception of such quotations, this thesis is entirely my own work.
- I have acknowledged all main sources of help.
- Where the thesis is based on work done by myself jointly with others, I have made clear exactly what was done by others and what I have contributed myself.

Signed: 陳奕宇

Date: 28 / 09 / 2015

Abstract

Electric power system (EPS) operates with economy, supply reliability, and renewability in mind. This means that the power generated must be cheap, clean, and can rapidly maintain the EPS frequency within the nominal range following the loss of an EPS asset to prevent causing damages to the connected equipments. To maintain frequency during contingent events, fast responding generation units called instantaneous reserves (IR) are offered, and these are typically provided by spinning hydro turbines in New Zealand.

The gradual increase in price, reduction in supply and the damage caused to the environment of using nonrenewable energy sources such as fossil fuel and nuclear energy are attracting the interests in the research and development of clean energy production technologies such as photovoltaics (PV), wind turbines, and tidal power to supply the electric grid. These nonrenewable energies are however restricted by environmental conditions such as the sun's illumination, wind direction, wind intensity and tidal flow velocities. For these reasons, a fast responding and steady output cannot be always be guaranteed, making these intermittent generation resources unsuitable to be used as instantaneous reserves.

Callaghan Innovation scientists and engineers have proposed a novel energy storage system which stores the excess energy in a form of compressed gas at a capacity capable of meeting the time required by the FIR specification without losing the energy that is typically observed in a tail-water depressed hydro reserve unit. The proposed system is able to offer torque via compressed air and hydraulics such that a generator able to reach synchronization speed within 0.4 seconds, and is cheaper to be offered as instantaneous reserve compared to a small scale hydro-turbines.

To fulfill the master thesis requirement, a rapid synchronization control scheme is developed to ensure that the generator is able to spin up to the power system frequency, synchronize with the distorted power system voltages, and begin delivering power within 1 second of receiving the FIR dispatch signal. This thesis describes the operation of the proposed compressed gas energy storage system, documents the instrumentation algorithm selection and implementation process, details the modeling and control strategy design techniques utilized to achieve successful simulated synchronization outcome, and provides a stability study of generator rotors following the synchronization breaker closure as a result of using the developed synchronization control scheme.

Acknowledgments

I would like to express my most sincere gratitude for the infinite patience, academic guidance and inspiring discussions my supervisor Dr. Alan Wood has provided me throughout my masters degree. I am thankful of the time and energy Alan had spent in finding me this opportunity when I was struggling with employment, and Alan's efforts have helped me define a clear career objective. His approach to my inquiries has been nothing but friendly and helpful, and the speed he arrive at a clear and feasible solution has never ceased to amaze me. This thesis cannot be completed without Alan's encouragement and support.

I would also like to show my profound appreciation for my industry sponsors and supervisors Dr. Chris Bumby, Dr. Rod Badcock and Dr. James Storey from Victoria University of Wellington (former Callaghan Innovation), as well as Derek Shotbolt from Energy Hydraulics Ltd (EHL). None of this would be possible without the professional guidance and the resources they have offered. I have immensely enjoyed working with industrial equipments, collaborating with experts from various fields of science and engineering, and the memorable time I spent in Wellington. I am thankful for how easy they have made the relocation and accommodation. The value of the work experience has been immeasurable to me.

Thanks to all the University of Canterbury technical staff for providing me with consulting and sharing with me the practical consideration in the equipment making process when I was building my test devices. Their knowledge has made the experience much more efficient and enjoyable. Also, big thanks to Edsel, Ken, Jack, Paul and Randy for making the tutorial sessions so enjoyable during my time as a TA.

Finally, I would like to thank my parents for their love and support, and all my postgraduate colleges for maintaining the office environment full of novel ideas and interesting discussions. I would also like to acknowledge the cleaning staff, who has been keeping my table so spotlessly clean that will put my room to shame.

Contents

List of Figures

List of Tables

Symbols

AUFLS	Automatic Under-Frequency Load Shedding
RMS	Root Mean Square
CE	Contingent Event
EIPC	Electricity Industry Participation Code
ECE	Extended Contingent Event
LV	Low Voltage
MV	Medium Voltage
DG	Distributed Generation
THD	Total Harmonic Distortion
THD	total harmonic distortion
PV	Photovoltaics
CGESS	Compressed Gas Energy Storage System
CAES	Compressed Air Energy Storage
GES	Grid Energy Storage
EPS	Electric Power Grid
PTV	Proportional Throttle Valve
p.u.	Per Unit
LTI	Linear Time Invariant
FCV	Flow Control Valve
FIR	Fast Instantaneous Reserves
RoCoF	Rate of Change of Frequency
AUFLS	Automatic Under-Frequency Load Shedding
LTI	Linear time invariant
PLL	Phase Locked Loop
VCO	Voltage Controlled Oscillator
VUF	Voltage Unbalance Factor
ppr	pulse per revolution
cpr	effective counts per revolution
SSLKF	Steady State Linear Kalman Filter
HVDC	High Voltage Direct Current
IR	Instantaneous Reserve
mmf	magnetic motive force
FIR	Fast Instantaneous Reserve

SIR	Sustained Instantaneous Reserve
(SISO)	single-input single-output
(MIMO)	multiple-input multiple-output

Chapter 1

Introduction

1.1 Background and Motivation

Sufficient operating reserves must be present in an electric power system (EPS) to prevent the frequency from falling too far from its nominal value following a disturbance event such as losing generation units, transmission lines outages, or an abrupt addition of load. Operating reserves are grid connected generators that are capable of supplying the power deficit in a very short amount of time after these interruptions, either by relying on partially loaded or unloaded hydro generators, or through various forms of energy storage devices.

Energy storage systems or reserves are vital to stabilize the electricity grid. There are two types of reserves in New Zealand: fast instantaneous reserves (FIR) and sustained instantaneous reserve (SIR) [1]. FIRs are required to respond within 6 seconds after an event and the output capacity must be sustained for 60 seconds; while SIRs are required to provide additional capacity within 60 seconds and must be sustained for 15 minutes. These reserves are expensive, and in some cases the unloaded generators consume large amounts of power to simply overcome the forces. Callaghan Innovation and EHL scientists and engineers have proposed a compressed air energy storage device capable of storing and generating the power to meet the duration and output capacity required by the FIR definition, operating more efficiently and economically compared with an unloaded spinning reserve, and causing less harm to the environment when manufactured and disposed of. The challenge, and the purpose of this thesis, is to develop an control algorithm which enables the generator to spin up to the nominal frequency, synchronize with the EPS, and begin delivering power as soon as the FIR demand is received. The proposed energy storage system generator will be fully functional within the 6 seconds specified by the FIR criteria.

1.2 Thesis Objectives

In a conventional synchronisation procedure, the phase and frequency is controlled in such a way that the frequency and phase difference between the EPS and the generator will be zero at the instant the generator is connected to the EPS. The purpose of reducing phase and frequency error is to mitigate the transient torque and current which are capable of damaging the generator and disrupting the quality of the EPS voltages. In a conventional synchronisation procedure which takes more than a minute, the phase error is reduced by spinning the generator at a frequency very closely matched to the EPS frequency and allowing the phase error to gradually decrease with the passage of time. Since the energy storage is time limited by the FIR requirements, the aim of the thesis is to develop a similar control algorithm that regulates the generator phase and frequency to match that of the EPS within 1 second of receiving the FIR command.

There are several challenges to be resolved:

1. Define the instrumentation measurement performance requirements (such as measurement resolution and delay), perform literature research on viable signal processing methods using the selected hardware and implement the designed measurement algorithm
2. Develop a control and sensor connection circuit diagram.
3. Validate the simulated characteristics and the dynamics of the energy storage system by experimental measurement
4. Develop and design a control strategy which accommodates the nonlinear control valve while the system is operating in all the expected conditions.
5. Verify the generator stability following the breaker closure using the proposed synchronisation algorithm

While the solution described will be optimized for the particular energy storage system, any energy storage system can be controlled in a similar way since the need for fast instantaneous reserves are universal and the cost of keeping a reserve generator running is high.

1.3 Thesis Structure

The goal of the thesis is to define system performance, develop instrumentation algorithms, and synthesize a control scheme which will result in stable synchronisation responses when the proposed system is subjected to all the expected operating conditions. The thesis chapters are structured as follows:

1. **Chapter 2 - Background**
   This chapter contains an overview of the compressed air energy storage devices, describes the kinematics and dynamics of the Callaghan proposed energy storage system, shows the characteristics of a disturbed EPS, and gives the technical background in the instrumentation techniques implemented for the energy storage system.

2. **Chapter 3 - Instrumentation and Signal Processing**
   The raw hardware output signals must be conditioned such that the measurement noise and delay is within specified limits. The sensor signal processing performance metrics, methodologies of the implemented instrumentation system and sensing hardware selection are given in this section.

3. **Chapter 4 - System Modeling and Identification**
   To validate the control algorithm, a low powered energy storage test-rig was constructed and a set of experiments were performed in order to obtain a more accurate model of the energy storage system. This section describes the methodologies used to collect information from the hydraulic system, outlines the characterization process, shows the characterization results and proposes modifications to the energy storage device based on these findings.

4. **Chapter 5 - Synchronization Controller Design**
   The development of a nonlinear controller structure, practical implementation considerations and the simulated outcomes are documented in this section. The reliability of the controller is validated through testing with all the known electric power grid conditions as well as with a poorly performing electro-hydraulic control valve.

5. **Chapter 6 - Synchronization Stability Analysis**
   Due to the novel nature of the project, the proposed control strategy is unlike a standard synchronisation procedure. This chapter considers the possible instability which may arise due to the abnormal generator conditions and shows the stability benchmarks using conventional stability analysis methods. The section

also demonstrates the need for tightening the synchronisation limitations on the compressed gas energy storage device compare with those recommended by standard procedures.

Chapter 2

Background

2.1 Chapter Structure

Due to the novel nature of this project, the scope of work performed for the energy storage system has grown and this has lead to the work performed encompassing most of the electrical and controls aspect of the energy storage device. This chapter begins with the *Compressed Gas Energy Storage* section, which provides a brief overview of current energy storage systems, describes the technical properties of individual drive components in the Callaghan Innovation proposed energy storage system, and states the distinguishing features of the proposed energy storage system. In order to design an effective controller, the definition, understanding and the criteria of current synchronisation procedure are shown in the *Electric Power System* section. In this section, a complete overview of the possible power grid distortions are also summarized to provide a better model of the EPS upon which the measurement algorithm is designed and tested. To facilitate control system design, the section *Theory of Classical Controls* section aims to discuss different control design methods available to accommodate for the nonlinear properties of the energy storage system control valve. Within the section, the final modeling, analysis and control design approach employed for the project is also detailed. Finally, the *Instrumentation and Signal Processing* section introduces the fundamental and the augmented algorithm used to detect the power grid and the generator voltages with accuracies comparable to a conventional auto-synchronisation controller.

2.2 Compressed Gas Energy Storage

2.2.1 Section Overview

To analyze, develop a process plant model and synthesis a controller design for the CGESS, an overview of modern compressed gas energy storage devices, understanding of the proposed CGESS operating principles, and mathematical descriptions of the CGESS components, are presented in this section.

2.2.2 Modern Grid Energy Storage

An Grid Energy Storage (GES) system implemented in a power system can serve several purposes [2] [3] [4]. Energy storage devices are used to:

1. Store the excess energy generated by intermittent generation sources
2. Shift the generation capacity to meet the increase in load demand
3. Increase financial gain by purchasing and store energy when the electricity price is low, and sell when price is high (market timing)
4. Be provided as an ancillary service to aid frequency management and other forms of EPS regulation control

GES systems stores the energy in many mediums, which include pumped hydro, electrochemical batteries, chemical fuel cells, capacitors, thermal reservoirs, flywheels, superconductive magnets, and compressed air. The energy storage system Callaghan Innovation proposed is a compressed air energy storage (CAES) type, which has an advantage over the popular electrochemical batteries due to their low material toxicity, abundance of storage medium (air), large output capacity (MW to GW scale), long self discharge (tens of hours) and low impact on the environment upon disposal [5]. CAES plants however require much larger land area and are geologically dependent due to the need for a natural cavern used for air storage.

2.2.3 Compressed Air Energy Storage

Conventional grid scale CAES air compression is achieved through a chain of electrically powered air compressors, and the energy is released through expansion turbines [2] [6]. To recover the heat energy lost during the compression cycle, the air prior to entering

the expansion turbine is combusted with a mixture of fuel. Large natural geological formations, empty mines or saline aquifers are preferred as air storage cavities as they greatly lower the plant cost. Currently, there are two large scale CAES plants operating in the world: Huntorf (Germany) [7] and McIntosh (USA) [8]. A third 90MW plant named ADELE is expected to be completed in 2016 in Stassfurt, Germany [9] [10] [11].

Improving the efficiency of air compression/decompression is one focus of CAES research. Since compression of gas increases the gas temperature and decompression leads to heat being absorbed from the environment, efficiency is not only reduced through heat loss, but the temperature variations inflict thermal stress on the system components. There are many companies actively participating in the development of CAES technology. Dresser-Rand [12][13], Energy Storage Power Corporation [14], General Compression [15], Hydrodynamics Group [16], Hydrostor [17], Western Energy Hub [18], Pacific Gas & Electric [19], Sustain X [20], and LightSail Energy [21] are all attempting various thermodynamic processes and heat recovery methods to compress/decompress the air efficiently. While the expected quoted efficiencies range from 50% to 70% [2], LightSail Energy propose a novel heat recovery system capable of driving their CAES at round trip efficiency of 90% [21].

The fast ramping capabilities of CAES plants make them effective as frequency management devices. The Huntorf plant takes 11 minutes from standstill to full 290MW output, and the synchronisation speed can be reached in 2 minutes [22]. The McIntosh CAES is able to deliver 110MW in 12 minutes from standstill[8].

2.2.4 Proposed Compressed Air Energy Storage Device Overview

Since the Callaghan innovation proposed CAES utilizes nitrogen gas instead of air, compressed gas energy storage system (CGESS) is used to describe the system. Figure 2.1 is the simplified Callaghan Innovation CGESS hydraulic power drive design, and the original supplied hydraulic drawing is shown in Appendix A.

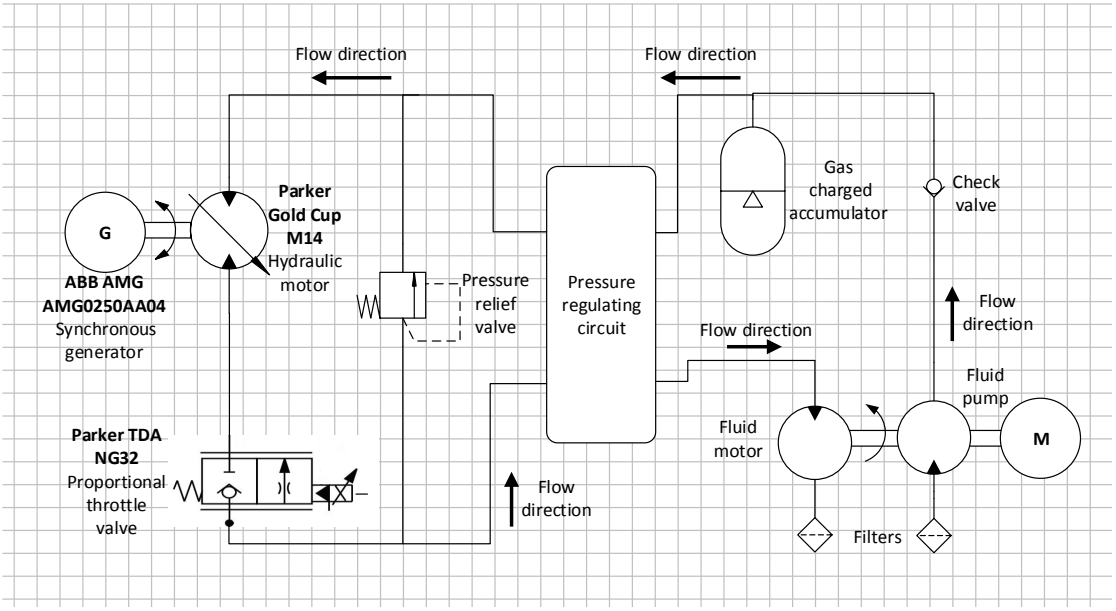

FIGURE 2.1: Simplified CGES hydraulic circuit diagram

The energy is stored economically by compressing the accumulator with an fluid pump when the electricity price is low; and released by operating the proportional valve and the hydraulic regulating circuit when FIR is required. The fluid power is converted to electrical power by a hydraulic motor and synchronous generator coupled at the shaft. The tracking and controlling of the generator electrical phase and frequency to that of the EPS quantities during the synchronisation process is achieved through a proportional throttle valve. By varying the valve spool position during fluid flow, a variable pressure loss across the hydraulic motor can be achieved and results in a variable generator drive torque. Once the synchronous generator is synchronized to the grid, the power output is then varied by adjusting the hydraulic motor displacement.

2.2.5 Synchronous Electrical Generator

2.2.5.1 Introduction

A synchronous generator is an electrical machine which converts mechanical rotational energy into electrical energy and it is an essential part of the CGESS. The relevant synchronous generator characteristics are outlined in this section.

2.2.5.2 Generator Properties

Inside the synchronous generator, field conductors are wound around the rotor pole bodies and armature conductors are wound in the stator slots. The generator terminal

voltages are created from the rotating magnetic fields that continuously penetrate the stator windings. The generator construction and field penetration of a typical single phase synchronous generator is shown in Figure 2.2.

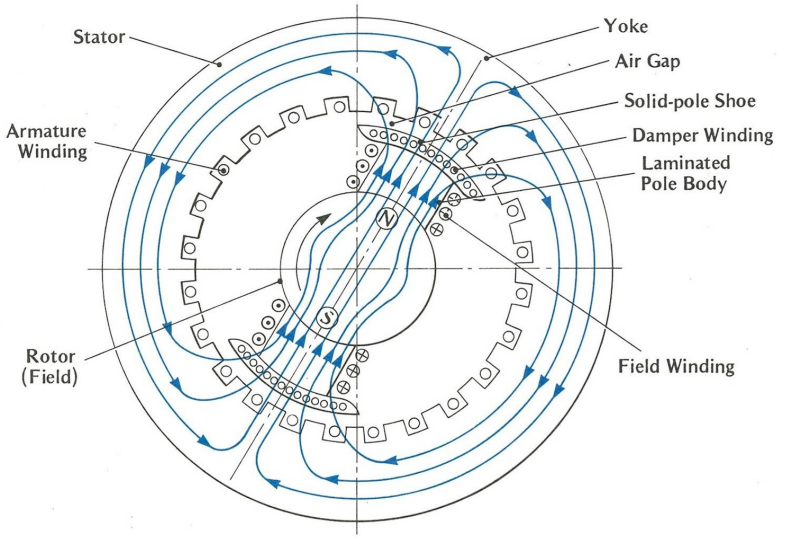

FIGURE 2.2: General single pole pair synchronous generator construction (source: [23])

When the generator is unloaded (i.e. not connected to the AC network), the phase angle of the terminal voltage is directly related to the mechanical angle of the generator shaft. This is due to the peaking of generator armature voltage induced in a line of stator conductors when a field pole face is 90^o behind the armature conductors if no interfering sources of magnetic flux are present [24] [25]. However, as soon as the generator is connected to the AC system, the stator currents modify the stator and rotor fields via armature reaction, and the machine rotor angle is no longer a direct indicator of the generator terminal voltage. For the pre-synchronized generator, the armature reaction is not important.

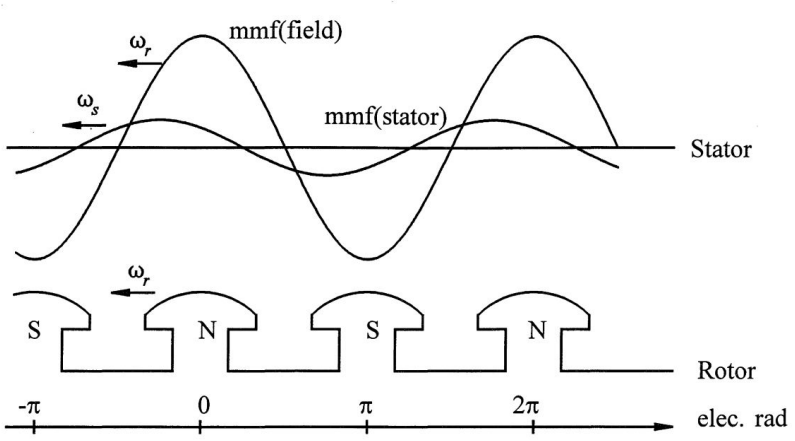

FIGURE 2.3: General single pole pair synchronous generator construction (source: [26])

2.2.5.3 Mechanical to Electrical Quantity Conversion

Often the rotor of a synchronous generator consists of more than 1 pole pair so the generator is allowed to spin at a slower speed than the nominal EPS frequency. The relationship between electrical frequency to mechanical revolutions per second in a synchronous generator is dependent on the number of pole pairs [24], and the frequency conversion equation is:

$$f_{elec} = n_{mech} \cdot N_{pp} \tag{2.1}$$

Where	f_{elec}	is electrical frequency	(Hz)
	n_{mech}	is the mechanical speed	(rev/s)
	N_{pp}	is the generator rotor pole pairs	(pole-pairs)

Similarly, the mechanical position to electrical phase is:

$$\theta_{elec} = \theta_{mech} \cdot N_{pp} \tag{2.2}$$

Where	θ_{elec}	is electrical phase	(rad)
	θ_{mech}	is the mechanical phase	(rad)

The conversion of mechanical power torque is:

$$P_{elec} = \tau \cdot \omega_{mech} \tag{2.3}$$

Where	P_{elec}	is electrical power	(W)
	τ	is the mechanical torque	(Nm)
	ω_{mech}	is the mechanical speed	(rad/s)

2.2.5.4 ABB-AMG Generator Specification

The CGESS generator is an ABB (Type: AMG0250AA04 DBSI) 4 pole shunt excited industrial synchronous generator. The relevant generator specification is illustrated in Table 2.1, and the full manual is included in Appendix C. The rating of the generator imposes a limitation on the permitted drive torque on drive-shaft.

TABLE 2.1: ABB AMG0250AA04 Industrial Synchronous Generator Performance Data

Parameter	Value
Main Standard	IEC 60034
Rated continuous output	100 kVA
Inertia	1.45 kgm^2
Voltage series star 3 phase	$400V_{l-l}/231V_{l-n}$
Frequency	50 Hz
Speed	1500 RPM
Stator winding resistance	0.0531 Ω per phase (with series star connection)
Rotor winding resistance	1.211 Ω
Excitor stator winding resistance	9.22 Ω
Excitor rotor winding resistance	0.200 Ω
Rated Excitation Current	5A continuous
Xd(u)	2.873 p.u.
Xd(s)	2.109 p.u.
Xq(u)	1.446 p.u.
X'd(u)	0.301 p.u.
X'd(s)	0.274 p.u.
X"d(u)	0.201 p.u.
X"d(s)	0.183 p.u.
X"q(u)	0.154 p.u.
X"q(s)	0.14 p.u.
X1(u)	0.076 p.u.
X2(u)	0.177 p.u.
X2(s)	0.161 p.u.
X0(u)	0.031 p.u.
Xp(s)	0.226 p.u.
Short circuit ratio (Ir0/Xd)	0.47
Td0'	1.645 s
Td'	0.076 s
Td"	0.0063 s
Ta	0.0135 s

*(u) = unsaturated, (s) = saturated; reactances in p.u. at rated voltage and power

Using Equations 2.3 and 2.1, the 100kVA 2 pole-pair synchronous machine has a rated torque of:

$$\begin{aligned} \tau_{rated} &= \frac{P_{elec}}{\omega_{mech}} = \frac{100 \times 10^3}{2\,\pi\,25} \\ &= 636.6\,Nm \end{aligned} \tag{2.4}$$

2.2.6 Hydraulic Accumulator

The hydraulic accumulator is an energy storage device which allows the system to store energy in the form of compressed gas, gravitational potential or compressed springs. Among the compressed gas accumulators, the separating elements can be a piston, bladder or a membrane [27]. The CGESS accumulator is a bladder type accumulator designed to be charged to 350 bar and supply the EPS with sufficient energy to fulfill the FIR requirement of 15 minutes. Although the pressure discharge characteristics is described by a standard nonlinear adiabatic process, the accumulator pressure is assumed to be a constant during the synchronisation period as it is a small fraction of the accumulator capability.

2.2.7 Proportional Throttle Valve

2.2.7.1 Introduction

In the past, hydraulic valves were simple on-off devices which enabled/obstructed fluid flow. Electro-hydraulic proportional control valves are modern hydraulic components capable of controlling fluid flow rate, regulating fluid pressure and reconfiguring flow direction by creating variable area orifices. The change in orifice area accomplishes the desired fluid flow and pressure drop through the orifice. Their capabilities allow them to control fluid acceleration, velocity and position [28] of hydraulic actuators and motors. Since the control valve is the main synchronisation control actuator in the CGESS, it is important to understand the control valve assembly, process dynamics and nonlinear behavior in order to successfully design a robust process controller.

The main control valve used in the CGESS is a *PARKER Hannifin TDA series 2/2 way proportional throttle valve*. Two valve sizes: NG-32 and NG-16, are modeled as the both valves were involved in the design process. The following sections provide the control valve modeling background and the NG-32/NG-16 datasheet models.

2.2.7.2 TDA Series Proportional Throttle Valve

The TDA series valve construction consisted of a DC piloted proportional (linear) solenoid, a spool, a spring and a poppet; all of which are encased in a valve body. A range of flowrates can be chosen, ranging from 220LPM at 10bar to 9600LPM when supplied with 10 bar of pressure. The construction of the Parker TDA series PTV is shown in Figure 2.4:

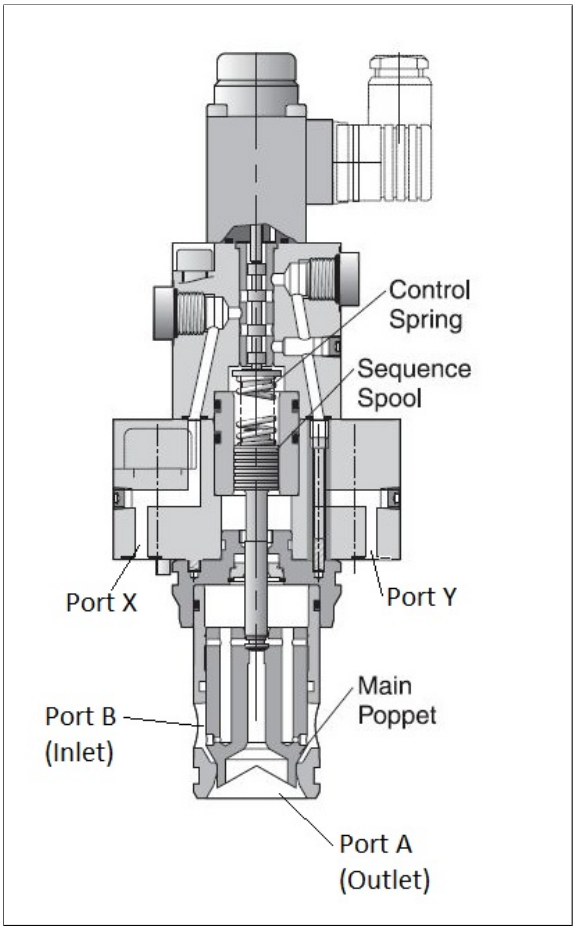

FIGURE 2.4: Parker TDA series proportional throttle valve construction

When no signal is applied to the to the pilot solenoid input, a poppet obstructs the openings between port B to port A. Once a current is applied, a magnetic field lifts a solenoid core. As the solenoid core is fixed to a spool, the spool is elevated to allow a fluid flow path from port X to port Y. This fluid travels through the spool in a way that the pressure imposed on the spool side is equal to the pressure on the poppet side, permitting the valve to lift the poppet by the same displacement (hence delivering equal performance) regardless of the differential pressure between ports A and B. The distance the spool/poppet travels is often referred to as **stroke** and are measured in % of full

poppet travel. For every unit of displacement the spool travels up towards the solenoid, a proportionally increasing orifice area opens to allow larger volume of fluid flow; which gives the term proportional valve.

2.2.7.3 Proportional Valve Model

An electro-hydraulic proportional valve dynamic is typically modeled by two blocks [29] [30]. The first block represents the transformation from the control input current or voltage to the percentage of full stroke, and the second block models the pressure and flow-rate as a result of the change in poppet displacement. The model topography is shown in Figure 2.5

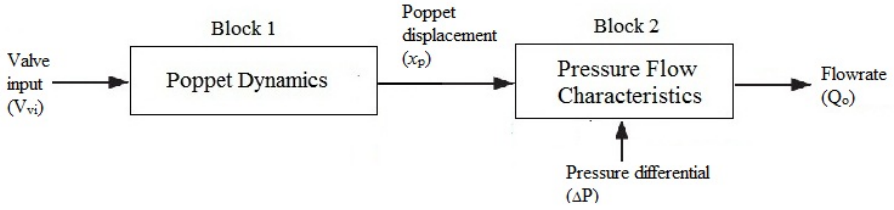

FIGURE 2.5: The two stage proportional valve behavior model

Poppet Dynamics Block

The first block models the dynamic behavior of the electro-hydraulic valve spool/poppet displacement in response to the changes in valve input, this includes the typical hydraulic valve components such as the flow obstruction body (i.e. poppet, ball, needle or disc), stems or shafts (i.e. spool), actuator and motion conversion mechanism (i.e. solenoid, torque motor and the amplifier), and other accessories [28]. The parameter identification of valve dynamics are standardized by ISO 10770-1 [31] and ISO 10770-2 [32]. The poppet stroke dynamics are described by a second order differential equation [29]:

$$K_{stk}\, v_{vi} = \frac{1}{\omega_n^2}\frac{d^2x_p}{dt^2} + \frac{2\zeta}{\omega_n}\frac{dx_p}{dt} + x_p \tag{2.5}$$

Where	v_{vi}	is the valve solenoid input voltage	(V)
	x_p	is the static poppet displacement	(m)
	K_{stk}	is the ratio of poppet displacement to the input voltage	$(\frac{m}{V})$
	ω_n	is the valve natural frequency	(rad/s)
	ζ	is the damping coefficient	

Taking the Laplace transform of Equation 2.5 and rearranging, the transfer function relating control input to poppet position is given by Equation 2.6, which is used in the poppet dynamic block.

$$\frac{X_p(s)}{V_{vi}(s)} = \frac{K_{stk} \cdot \omega_n^2}{s^2 + 2w_n\zeta s + \omega_n^2} \tag{2.6}$$

The characteristics of the step response of an electro-hydraulic valve are defined by its response time (t_r), peak time (t_p), and settling time (t_s). Figure 2.6 depicts the meaning of the parameters graphically. According to ISO 10770-1, the response time is specified by valve manufacturers is defined as the time taken for the output to reach 90% of its demanded value and the settling time is defined as the time required for the error between demand and the actual value to be less than 5% of the final value when a step command is applied to the valve control input. Although the step response is specified at 90% according to ISO, some manufacturers chose to evaluate the response time at 100% of commanded position.

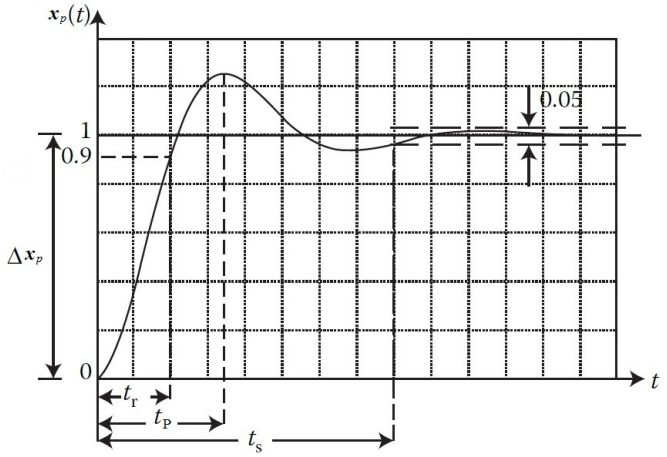

FIGURE 2.6: Step response of a standard second order system (Source: [29])

The algebraic relationship between the settling time, the damping coefficient and the natural frequency for the poppet displacement to reach 5% error of input value is:

$$t_s = \frac{3}{\zeta\omega_n} \tag{2.7}$$

Alternatively, the natural frequency can be calculated using Equation 2.8 when the rise time is known

$$t_r = \frac{1}{w_n\sqrt{1-\zeta^2}} \tan^{-1}\left(\frac{-\sqrt{1-\zeta^2}}{\zeta}\right) \tag{2.8}$$

The relationship between the damping coefficient η and a second order response described by Equation 2.6 is shown in Figure 2.7:

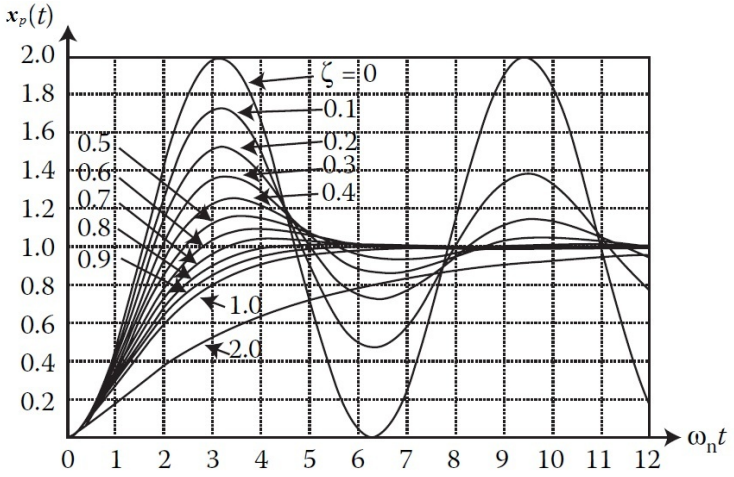

FIGURE 2.7: Influence of parameters on standard second order step response

Pressure Flow Characteristics Block

The second model block describes the flow through the valve as a result of the variable orifice area created from poppet displacement, given a known differential pressure across the valve. The pressure-flow relationship through a valve is described by the orifice equation [33] [34]:

$$Q_o = C_d A_o \sqrt{\frac{2\Delta P}{\rho}} \tag{2.9}$$

Where	Q_o	is the flow rate through the orifice	(m^3/s)
	C_d	is the coefficient of discharge	
	A_o	is the orifice cross sectional area	(m^2)
	ΔP	is the pressure drop through the orifice	(Pa)
	ρ	is the mass density of the fluid	(kg/m^3)

The discharge coefficient varies depends on the geometry of the orifice, downstream orifice size, and the fluid flow velocity. Since the orifice area is a function of the input, Equation 2.9 can be rewritten as a function of spool position

$$Q_v = C_d A_m \left(\frac{x_p}{x_{pm}} \right) \sqrt{\frac{2\Delta P_v}{\rho}} \tag{2.10}$$

Where A_m is the maximum valve orifice cross sectional area (m^2)
x_p is poppet position (m)
x_{pm} is the poppet displacement at full stroke (m)

2.2.7.4 TDA Series Valve Datasheet Characteristics

Pressure-flow Model

Depending on the valve construction and the electromechanical driver, the electrical control input to pressure/flowrate characteristics may be nonlinear [35][36]; and since the Parker TDA valve exact construction and orifice dimensions was not specified, the relationships between input to the coefficient of discharge and maximum orifice area are unknown. The relevant pressure to flowrate information given by the Parker TDA series valve technical information datasheet [37] is shown in Figure 2.8 and Equation 2.11:

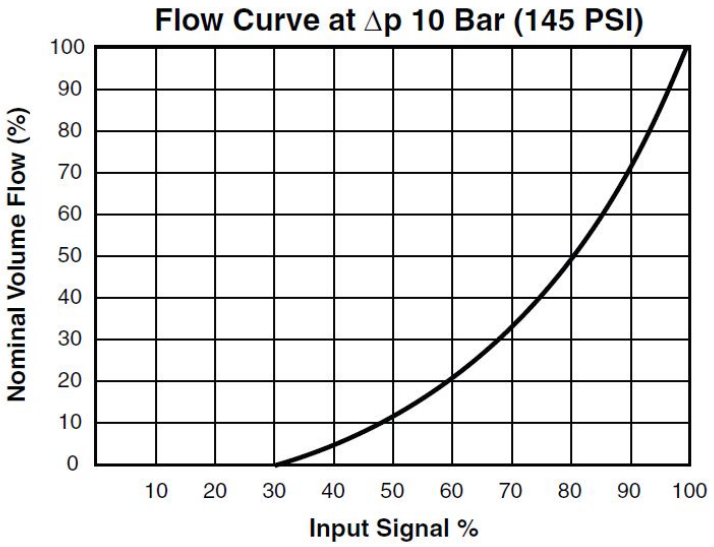

FIGURE 2.8: Parker TDA series nominal flowrate v.s. valve input characteristics (where $P_n = 10$ bar and nominal flowrate depends on the model)

$$\frac{Q_a}{Q_n} = \sqrt{\frac{\Delta P_a}{\Delta P_n}} \tag{2.11}$$

Where	ΔP_a	is the actual valve pressure differential	(bar)
	ΔP_n	is the rated (nominal) valve pressure differential	(bar)
	Q_a	is the actual flow rate	(LPM)
	Q_n	is the rated flow rate	(LPM)

C_d, A_o and ρ in Equation 2.9 can be obtained from rearranging Equation 2.11. Using Equation 2.9, Equation 2.13 and Equation 2.12 can be written to describe the rated flow and the actual flow profile using the same hydraulic fluid.

$$Q_a = C_{da} A_a \sqrt{\frac{2\Delta P_a}{\rho}} \tag{2.12}$$

$$Q_n = C_{dn} A_n \sqrt{\frac{2\Delta P_n}{\rho}} \tag{2.13}$$

Where	C_{da}	is the actual valve flow discharge coefficient	
	C_{dn}	is the rated valve flow discharge coefficient	
	ρ	is the fluid density	$(\mathrm{kg/m^3})$
	A_a	is the actual orifice area	$(\mathrm{m^2})$
	A_n	is the rated orifice area	$(\mathrm{m^2})$

Dividing Equation 2.12 by 2.13, we have:

$$\frac{Q_a}{Q_n} = \frac{C_{da} A_a}{C_{dn} A_n} \sqrt{\frac{\Delta P_a}{\Delta P_n}} \tag{2.14}$$

Comparing Equation 2.14 with the datasheet expression 2.11, $(C_{da}A_a)/(C_{dn}A_n) = 1$. As Figure 2.8 suggest that flowrate is constant at a selected valve input and nominal pressure, Expression 5.2.7 can be defined:

$$K_v = \frac{Q_n}{\sqrt{P_n}} \tag{2.15}$$

Equation 2.14 can be simplified to:

$$Q_a = K_v \sqrt{\Delta P_a} \tag{2.16}$$

Where	K_v	is the orifice flow coefficient	$(\mathrm{LPM}/\sqrt{\mathrm{bar}})$

Using Equation 2.15 with $P_n = 10$ and visually locating the individual flow-rates in Figure 2.8, the orifice flow coefficients at each valve input are calculated. The flow coefficient for a range of TDA valve selection is shown in Figure 2.9.

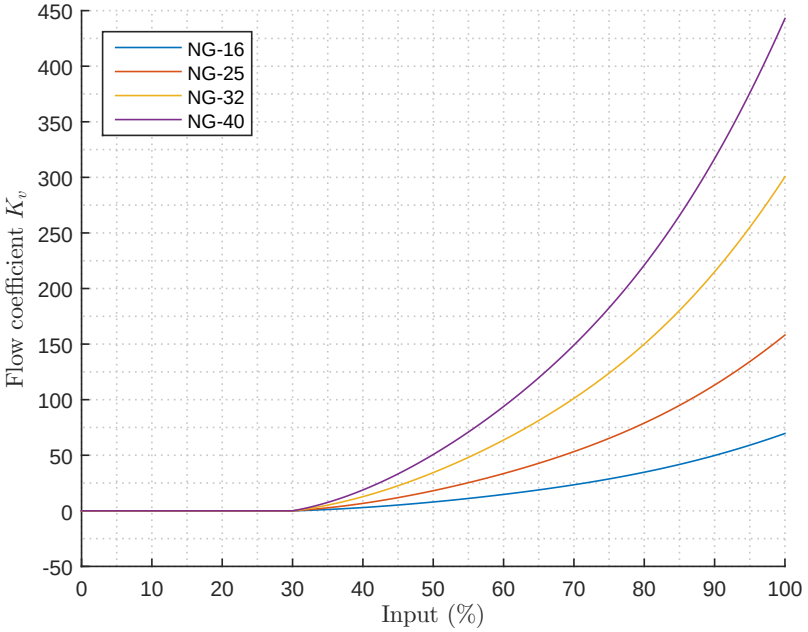

FIGURE 2.9: Parker TDA series PVT flow coefficients

Poppet Dynamics Model

Although the TDA series ideal poppet dynamic model can be derived from Equation 2.6, regarding the position output as the control input from which the flow coefficients are determined, the only specified poppet dynamic parameter is the response time (t_r) and the values do not agree with the step response transfer function models according to the literature reviews [29] [30], as the specified rise time includes the initial dead time. Furthermore, the poppet damping coefficient is unspecified. The poppet dynamic model is approached with an iterative least squared curve fitting method with various damping values to match the datasheet poppet response that is shown in Figure 2.10. The methodologies used and the responses are shown in Sections 4.2.2.3 and 4.2.2.7

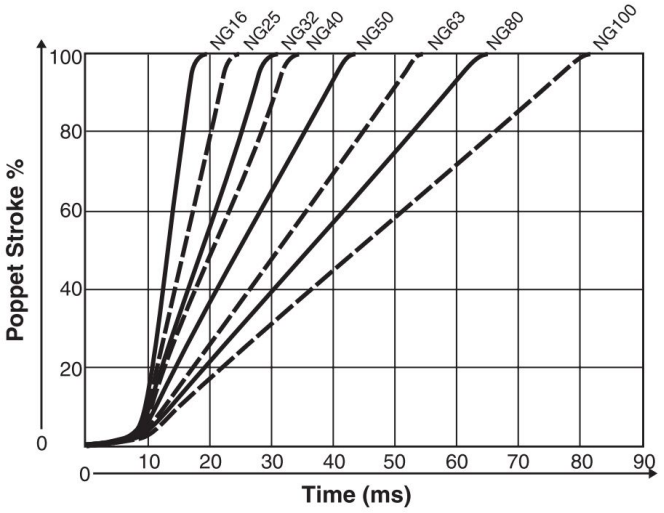

FIGURE 2.10: Parker TDA series PTV datasheet poppet response

2.2.7.5 Non-linear Properties of Control Valves

The flow rate to pressure relationship, hysteresis, repeatability and dead time are some of the nonlinear properties of a electro-hydraulic valve which complicate the controller design and reduce control performance [29] [38] [39] [40] [41] [42] [43] [44]. It is crucial to understand the properties of the nonlinearity in order to design robust controllers.

Dead time

When using a electro-hydraulic valve, it can often be observe that the flow-rate or pressure drop remains unchanged for a short period of time following a command input. This delay is called *dead time*, and it can be caused by electronic drive delays, backlash from the mechanical linkages to actuator shaft, mechanical friction, and the construction of the valve.

In terms of control valve construction, there is often an overlapping area between the spool/poppet and its housing manifold. Although this design is intended to reduce valve leakage when the valve is fully closed, additional time is required for the spool/poppet to clear the overlapping area before being able to create an orifice to allow fluid flow after the valve is commanded to open from a fully closed position. The valve start-up dead time is depicted in Figure 2.11:

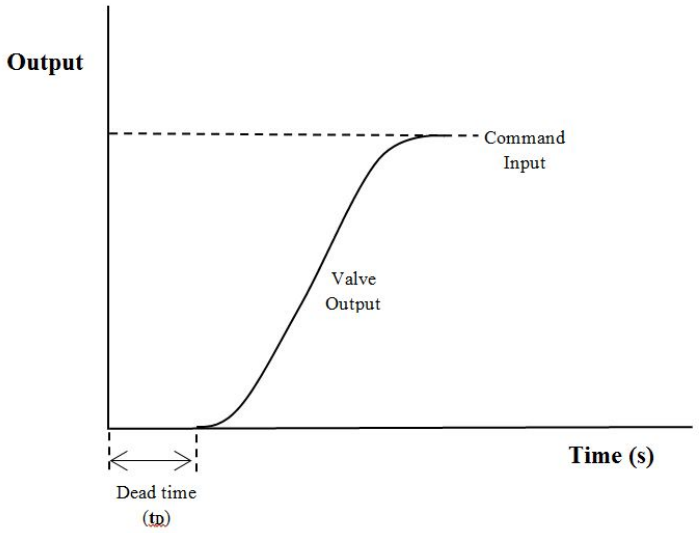

FIGURE 2.11: Control Valve dead time

Another major contribution to the valve dead time is static friction (or stiction), which is a frictional force that is required to be overcome before relative motion can be established between two surfaces. In a hydraulic valve, the stiction is created by the tight seals designed to reduce the fluid leakage, and it introduces a delay in spool movement from a command input. Once the spool breaks free, it is also likely that the spool may overshoot and again be stuck in a new undesirable position. This stick-slip motion causes an oscillation around the operating point.

Hysteresis

When the valve spool is suddenly commanded to move in the opposite direction to its original direction, a dead time region is often observed before the spool is able to move in the reverse direction. This causes a observable difference between the valve outputs from an increasing input and the valve outputs from a decreasing input. This inconsistency is called *hysteresis* and it is illustrated in Figure 2.12. Hysteresis is measured as a percentage of the total input evaluated at a given output [45]. Valve hysteresis is caused by static friction, solenoid core magnetic hysteresis, fluid dynamics, and it also be thought of as a secondary effect of mechanical friction [46][42].

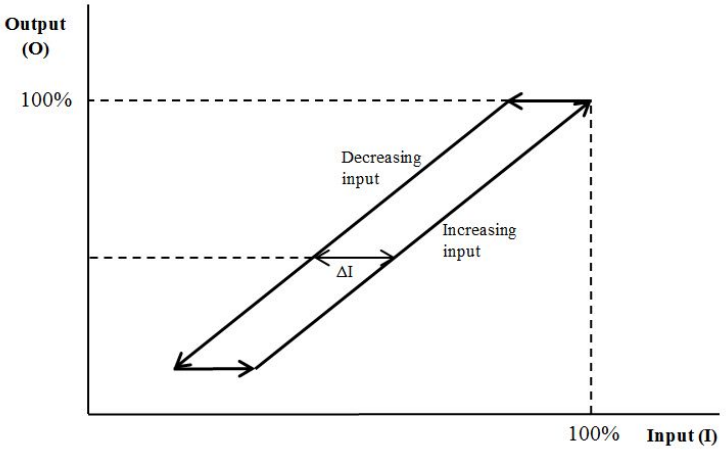

FIGURE 2.12: Effect of hysteresis in control valve outputs w

Common Solutions to Hysteresis and Stiction

To manage such hysteresis and stiction, dither or PWM is often generated in the valve control input by the electronic drivers. Dither or PWM is an oscillation added to the desired control input such that the valve spool moves in a back and forth motion, which can average the hysteresis and avoid valve stiction [47][45].

Repeatability

When the same input is applied to the valve repeatedly, the valve spool is unlikely to move to its exact demand location with every trial due to the variability of the driver electronic component and stiction [42]. Very often valve manufactures specify the valve repeatability, which is a measure of output variation when the same input is applied. The repeatability is a measure of valve accuracy and is expressed as the percentage of the maximum flow or pressure specified by the datasheet. Figure 2.13 shows an example of a valve with low repeatability

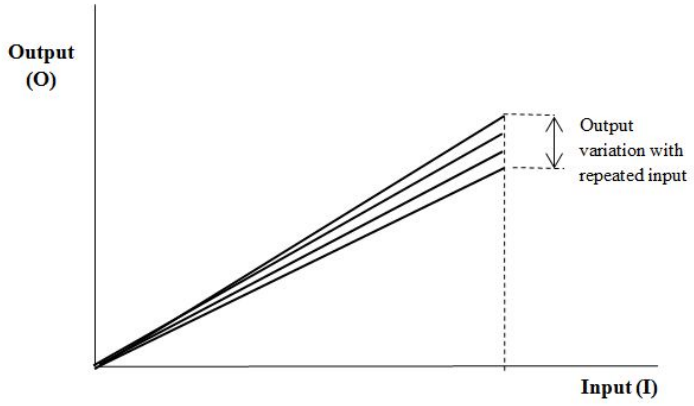

FIGURE 2.13: Repeatability measurement in control valves

Resolution

The resolution (or threshold) is defined by the smallest necessary change in input to create an measurable change in output. Two types of resolution exists, one is a specification provided by the controller/valve driver elements, and the other is the result of stiction in the valve [40] [48] [49] [50] [51].

The resolution of the controller/driver element cause the valve spool to move in small discrete step movements, and if the resolution is sufficiently low, the spool may stop its movement. As the spool stops, static friction takes place such that a dead time reappears at the beginning of each input cycle. Therefore, driver/controller elements with small output resolution negatively affect the dynamic performance of the process. From [50], [52] [53] and [54], a typical hydraulic valves have trouble resolving 0.5% of full span.

2.2.8 Hydraulic Motor

2.2.8.1 Introduction

Hydraulic motors are rotating machines which convert fluid power into rotational mechanical power. Three types of hydraulic motors: gear, vane, and piston motors are commonly used today [34] [55]. They are used for many applications such as cranes, conveyors, diggers, aircrafts.. etc. The motor used in the CGESS project is a Parker GOLD CUP M14V-3N1A axial piston variable displacement hydraulic motor, which is capable of adjusting its power output once the CGESS is synchronized to the EPS in order to meet the power demand.

2.2.8.2 General Motor Properties

The GOLD CUP M14V axial piston variable displacement hydraulic motor is capable of adjusting its torque (therefore power) output by controlling the displacement of its pistons. The cutaway view of the GOLD CUP series motor is shown in Figure 2.14, which shows that the piston displacement can be adjusted by changing the angle of the swash-plate relative to the drive shaft.

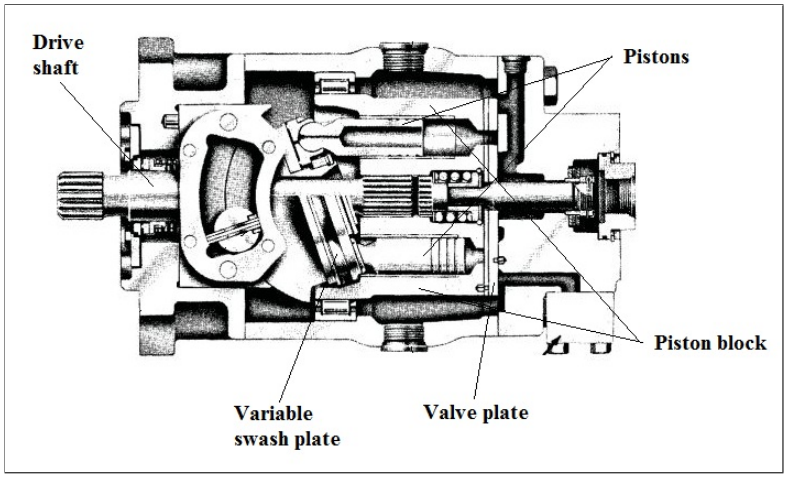

FIGURE 2.14: Parker GOLDCUP series technical performance specification (source: [56])

The relevant hydraulic motor mechanical performances and characteristics for the CGESS project are described by the following formulae [56] [57] [58]:

Flowrate:

$$Q_m = \frac{D\, n_s}{1000\, \eta_v} \tag{2.17}$$

Where Q_m is the flow-rate through the motor (LPM)
n_s is the hydraulic motor shaft speed (RPM)
D is hydraulic motor displacement (cm^3/rev)

Torque

$$T_m = \frac{\Delta P_m\, D\, \eta_m}{20\, \pi} \tag{2.18}$$

Where T_m is the motor developed torque (Nm)
ΔP_m is the motor inlet/outlet pressure differential (bar)

Power

$$P_m = \frac{Q_m \Delta P_m\, n_s\, \eta_o}{600} \tag{2.19}$$

Where P_m is the motor power (kW)

Acceleration

$$\alpha_m = \frac{T_m}{J_m} \tag{2.20}$$

Where α_m is the motor shaft acceleration (rad/s^2)
J_m is the motor shaft rotational inertia (kgm^2)

The datasheet motor parameters defined by Equations 2.17 to 2.20 for the Parker M14V hydraulic motor are given by Figure 2.15.

Series		Terms	P6	P7	P8	P11	P14
Displacement	*Max. displacement*	in³/rev.	6.00	7.25	8.00	11.00	14.00
		cm³/rev.	98,3	118,8	131,1	180,3	229,5
Pressure	*Continuous*	psi	5000	5000	3600	5000	5000
		bar	350	350	250	350	350
	Intermittent	psi	6000[7)]	6000[7)]	4500[7)]	6000[7)]	6000[7)]
		bar	420[7)]	420[7)]	310[7)]	420[7)]	420[7)]
Speed *(Pump)*	*max. @ full stroke*	rpm	3000	3000	2100	2400	2400
(Motor)	*max. @ full stroke*	rpm	3000	3000	NA	2400	2400
(Motor)	*max. @ 50% stroke*	rpm	3600	3600	NA	2800	2800
Mounting	*Flange -2 bolt*	SAE	127-2 (C)	127-2 (C)	127-2 (C)	-	-
Flange -4 bolt (opt. on 6,7 & 8)		SAE	152-4 (D)	152-4 (D)	152-4 (D)	165-4 (E)	165-4 (E)
	Shaft - keyed	SAE	32-1 (C)	32-1 (C)	32-1 (C)	44-1 (E)	44-1 (E)
	keyed	SAE	44-1 (D)	44-1 (D)	44-1 (D)	-	-
	Shaft - splined	SAE	32-4 (C)	32-4 (C)	32-4 (C)	44-4 (E)	44-4 (E)
	splined	SAE	44-4 (D)	44-4 (D)	44-4 (D)	-	-
Weight *(Pump) less controls*		lbs	175-300	175-300	175-300	325-530	325-530
	Mass	kg.	80-135	80-135	80-135	145-240	145-240
Weight *(Motor Fixed)*		lbs	110	110	N/A	250	250
	Mass	kg.	50	50	N/A	110	110
Weight *(Motor Variable) less controls*		lbs	110	110	N/A	300	300
	Mass	kg.	50	50	N/A	135	135
Rotating inertia		lbs-in²	92	92	92	290	290
		kg.m²	0,027	0,027	0,027	0,085	0,085
Torque *(Motor) theo. max.*	*per 100 psi*	lbs-in	95.5	115.4	NA	175	222
	per 100 bar	Nm	157	189	NA	287	362
	at 5000 psi	lbs-in	4774	5769	NA	8750	11100
	at 350 bar	Nm	539,5	651,9	NA	990	1250
Power *(Motor) theo. max.at 5000 psi, 350 bar*							
	per 100 rpm	hp	7.6	9.2	NA	13.8	17.6
		kW	5,7	6,8	NA	10,3	13,1
	at 2000 rpm	hp	151.5	183.1	NA	277.8	353.5
		kW	113,0	136,6	NA	207,0	263,7
Torque *(Motor) efficiency*	*- approx. stalled*	% theo.	81	81	NA	81	81
	running	% theo.	93	93	NA	93	93
Case pressure:	*max. allowable continuous*	psi	75	75	75	75	75
		bar	5,2	5,2	5,2	5,2	5,2
	intermittent	psi	125	125	125	125	125
		bar	8,6	8,6	8,6	8,6	8,6
(Not to exceed 25 psi,1,7 bar above inlet in open circuit units)							
Flow *(Pump) theo.at max.displ.@1500 rpm*		gpm	39	47	52	71	91
		lpm	148	178	197	269	344
	@1800 rpm	gpm	47	57	62	86	109
		lpm	178	216	235	326	413
Displacement	*(Internal aux. pump)*		**P6,7,8P,S,V**	**P11,14P,S**	**P11,14V**	**P24P**	**P24S[3)]**
		in³/rev.	1.07	(2) 1.07[4)]	1.07[5)]	2.81[6)]	2.81[6)]
		cm³/rev.	17,5	(2) 17,5	17,5	46,1	46,1
Flow *(Internal aux. pump)*	*@1500 rpm*	gpm	6.9	(2) 6.9	6.9	18.2	6.5
		lpm	26,1	(2) 26,1	26,1	68,9	24,6
	@1800 rpm	gpm	8.3	(2) 8.3	8.3	21.9	7.8
		lpm	31,4	(2) 31,4	31,4	82,9	29,5

FIGURE 2.15: Parker GOLD CUP series technical performance specification

Three types of efficiency are used to describe hydraulic motors: overall efficiency, volumetric efficiency and mechanical efficiency. The mechanical efficiency (or torque efficiency and torsional efficiency) is calculated by the theoretical torque required to drive it divided by the actual torque output by the motor. The mechanical efficiency is a function of motor rpm and differential pressure. Generally, the mechanical efficiency decreases as the rotational speed increases as friction is proportional to speed [59]. The volumetric efficiency is the ratio of the motor's theoretical flow to the actual flow. The difference in theoretical to actual flow-rates are due to the fluid leaking from the high pressure side back to the low pressure side. In the case of a piston pump, the volumetric losses are due to the leakage path between the piston wall and the piston, and the leakage between the inflow/return line and the motor casing [57]. Similar to mechanical efficiency, the volumetric efficiency is a function of motor differential pressure, rotational speed and viscosity. The overall efficiency is the ratio of total input power to output power, and it is the product of volumetric efficiency and mechanical efficiency.

These efficiencies are highly nonlinear and can contribute to the reduction of control system performance. The Parker GOLD CUP series efficiency values are shown in Figure 2.16:

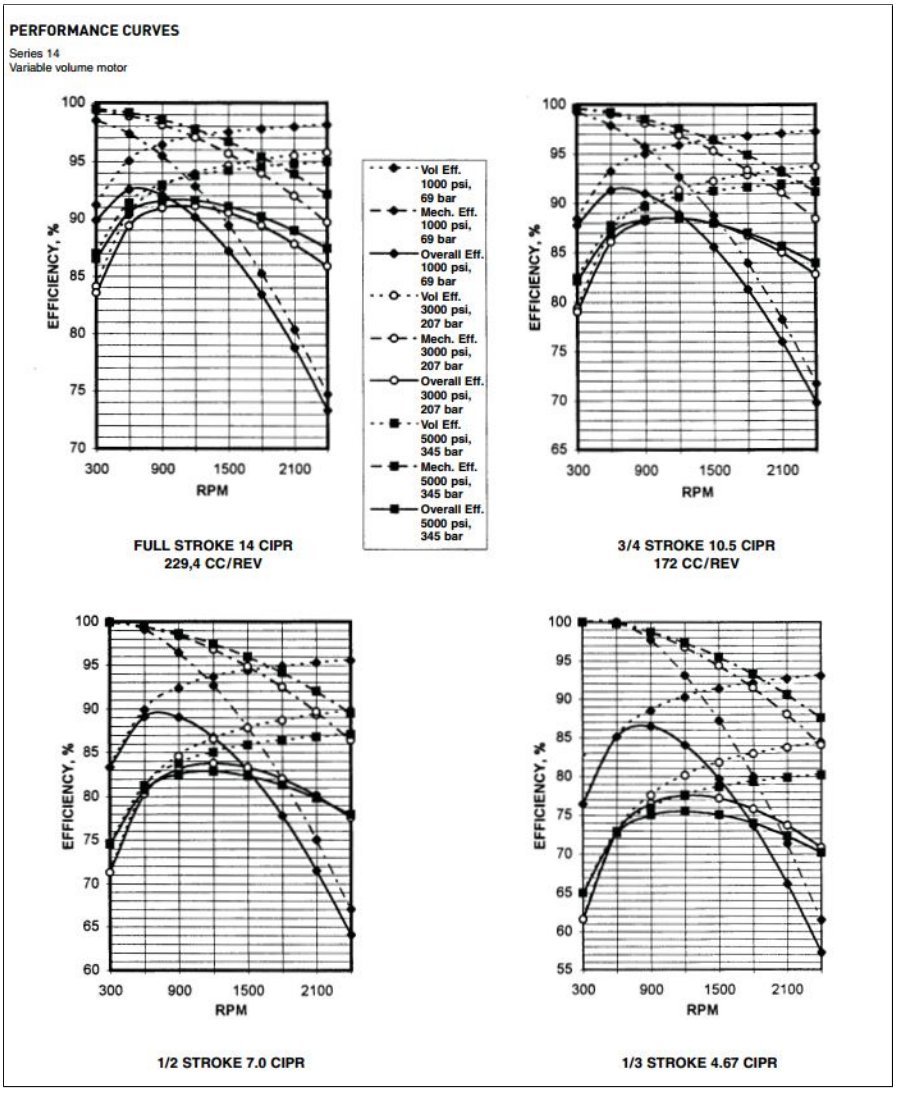

FIGURE 2.16: Parker series-14 hydraulic motor efficiency curve (source: [56])

The drive torque on the generator shaft should not exceed its rated torque at any point during synchronisation period. Figure 2.16 shows that the mechanical efficiency at stand-still is roughly 100%. Using the synchronous machine rated torque given by expression 2.4 with 100% mechanical efficiency and 350 bar accumulator charge in Equation 2.18, the maximum motor displacement setting is approximately 115cc/rev.

2.2.9 CGESS Peak Acceleration

The high motor/generator acceleration is the key to allowing rapid synchronisation. Substituting the motor output torque seen in expression 2.4 along with the combined generator/motor inertias seen in Table 2.1 and Figure 2.15 into Equation 2.20, the achievable acceleration is:

$$\alpha_{rated} = \frac{636.6}{1.45 + 0.085} = 414.7 \text{ rad/s}^2 \tag{2.21}$$

From expression 2.21, it can be shown that the fastest time taken to reach synchronisation speed is:

$$\begin{aligned} t_{msync} &= \frac{\omega_{sync}}{\alpha_{rated}} \\ &= \frac{2 \cdot \pi \ \cdot 25}{414.7} \\ &= 0.38\, s \end{aligned} \tag{2.22}$$

2.3 Electric Power System

2.3.1 Section Overview

Since the CGESS is designed to function only when the EPS is in an emergency condition, the EPS voltages in such environment will be distorted and provision of accurate measurement will be difficult. In order to provide reliable reference inputs for the CGESS synchronisation controller, EPS voltage disturbance types are described mathematically to benchmark instrumentation algorithm. This section will also provide an overview of synchronisation strategies, and common techniques used to study the generator stability post-synchronisation.

2.3.2 Under-Frequency Management

Generators and industrial machines are designed to operate within a certain range of service frequencies and large deviation from nominal frequency is known to damage most grid connected devices [60]. Service providers are obliged to maintain EPS frequency within the nominal range. In New Zealand, the frequency management standard is defined by **System Operator's Principal Performance Obligations** [61] outlined in Part 7 of the Electricity Industry Participation Code (EIPC) [1]. The New Zealand power system frequency bands are shown in Figure 2.17.

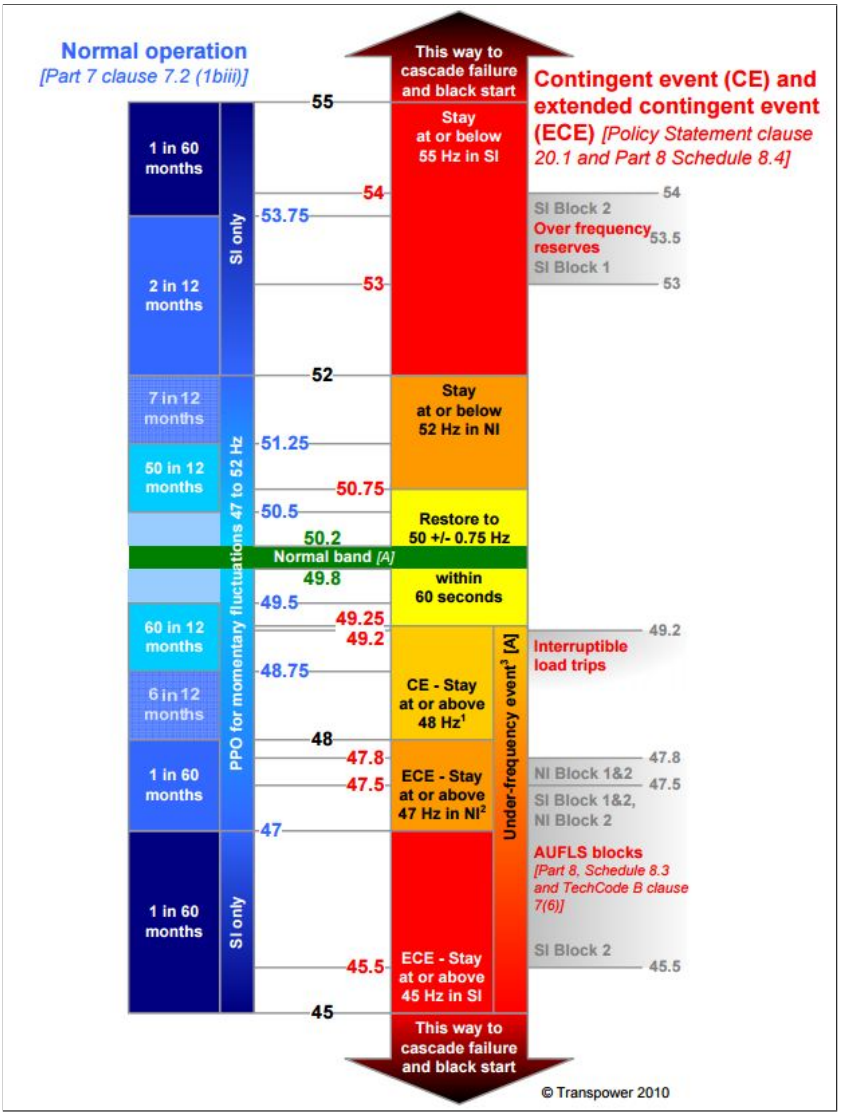

FIGURE 2.17: New Zealand frequency management barometer [62]

A sudden unbalance of load and generation causes the frequency to deviate from the nominal band. The restoration of frequency following an under-frequency excursion is provided by ancillary services, which is defined by Part 8 of the EIPC. The ancillary services that is capable of restoring power system frequency are called instantaneous reserves, which can be offered in the form of interruptible load, partially loaded spinning reserves and tail water depressed reserve. The instantaneous reserves can be offered as fast instantaneous reserve (FIR) and sustained instantaneous reserve (SIR). Part 1 of the EIPC defines these reserves as:

> **fast instantaneous reserve** means -
> (a) for providers of partly loaded spinning reserve and tail water depressed reserve, the additional capacity (in MW) provided 6 seconds after a Contingent Event (as defined in the policy statement) that is sustained for a period

of at least 60 seconds; and
(b) for providers of interruptible load, the drop in load (in MW) that occurs within 1 second of the grid system frequency falling to or below 49.2 Hertz that is sustained for a period of at least 60 seconds

sustained instantaneous reserve means -
(a) for providers of partly loaded spinning reserve and tail water depressed reserve, the average additional output (in MW) provided during the first 60 seconds after a Contingent Event (as defined in the policy statement) that is sustained for at least 15 minutes after the Contingent Event (unless a new dispatch instruction is given before the expiry of that 15 minute period); and
(b) for providers of interruptible load, the average drop in load (in MW) that occurs over the first 60 seconds after the grid system frequency falls to or below 49.2 Hz that is sustained until instructed by the system operator

The most common form of frequency response ancillary service in New Zealand is provided by of hydroelectric generators, which are synchronized to the grid while generating at less than maximum capacity. The CGESS performance requirement is set by the FIR definition, which states that the reserve must ramp up to the rated power within 6 seconds.

2.3.3 Frequency Characteristics during Disturbances

A sudden unbalance between generation capacity and load following an disturbance causes the EPS frequency to deviate from the nominal operating range. The relationship between the frequency deviation and the total generation units in service is [63] [64] :

$$\frac{df}{dt} = 50 \cdot \frac{\Delta P}{2\,J} \tag{2.23}$$

Where	df/dt	is the rate of change of frequency (RoCoF)	(Hz/s)
	ΔP	is the lost generation unit capacity	(MVA)
	J	is the summed inertia constant of post-event in-service synchronous machines	(MVA·s)

Equation [63] shows that the EPS rate of change of frequency (RoCoF) varies depending on the EPS operating condition. A power system disturbance involving the disconnection of generation and transmission assets in New Zealand can result in two types of event:

contingent event (CE) and extended contingent event (ECE). CE describes an event where the disconnection of load is unnecessary to restore the grid frequency, and an ECE describes a more severe case where the demand has to be shed to maintain EPS stability. Generally an CE is caused by the loss of the largest generation unit or a single HVDC pole and ECE is caused by the loss of both HVDC poles [65] [66], and both events are covered by IR.

In some instances, the frequency decay may be too steep for the FIRs to restore the EPS frequency to nominal band before cascading failure. The last ditch resort is to activate the Automatic Under-Frequency Load Shedding (AUFLS) scheme [67], which determines the most economical and safest loads to preemptively shed. The scheme is relevant to the CGESS design as it provides the range of expected rate of frequency decay during the reserve demand period. From the AUFLS design scheme technical summery, the expected RoCoF range was calculated from historical data and it is shown in Figure 2.18, which demonstrated that the RoCoF immediately after an event can be as severe as -2Hz/s:

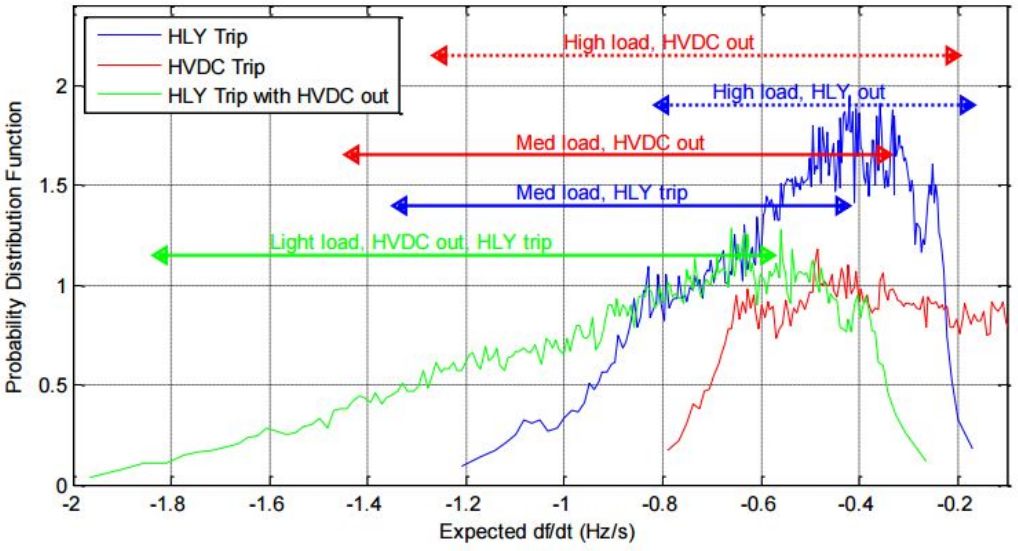

FIGURE 2.18: Expected RoCoF probability distribution (source: Transpower [63])

2.3.4 Per Unit System

Generally, the equipment electrical characteristics for transient stability and power flow studies are represented in per unit (p.u.) [68], which has the advantage of being constant valued regardless of which side of a transformer the quantity is referred to. This conversion is useful for analyzing the dynamics during synchronisation. The calculations for converting power (S), current (I) and impedance (Z) into their p.u. equivalent are

shown in Equations 2.24, 2.25, 2.26, and 2.27, and the conversion of p.u. impedance between machines with different base is given by Equation 5.2.7

$$I_{base} = \frac{S_{base}}{\sqrt{3} \cdot V_{LLbase}} \tag{2.24}$$

$$Z_{base} = \frac{V_{LLbase}^2}{S_{base}} \tag{2.25}$$

$$I_{p.u.} = \frac{I_{actual}}{I_{base}} \tag{2.26}$$

$$Z_{p.u.} = \frac{Z_{actual}}{Z_{base}} \tag{2.27}$$

$$Z_{p.u.(new)} = Z_{p.u.(old)} \cdot \left(\frac{V_{old}}{V_{new}}\right)^2 \cdot \frac{S_{new}}{S_{old}} \tag{2.28}$$

2.3.5 Voltage Quality During Disturbances

The three phase voltage waveforms are most likely going to be off-nominal immediately following an excursion and this makes CGESS tracking and synchronizing to the EPS difficult. The characteristics of the EPS voltages are described as **voltage quality**. This section shows the most likely voltage quality problems and their characteristics during an EPS disturbance to facilitate instrumentation algorithm and control system simulation.

2.3.5.1 Harmonic Distortion

The steady state EPS voltages are never purely sinusoidal and its voltages are often distorted by components oscillating at frequencies centered at integer multiples of the foundational frequency [69] [70]. These additional frequency components are called harmonic distortion, which is caused by:

1. non-ideal synchronous machine construction which generates non-sinusoidal voltages
2. nonlinear power transmission devices such as the HVDC link and the transformer core saturation.
3. power electronic converters and other forms of nonlinear loads that draw non-sinusoidal current

The level of harmonic distortion is more severe at the end of or near a heavily loaded feeder and severe distortion can cause heating and equipment malfunctioning [71] [72] [73] [74]. The level of harmonic distortion in an EPS is generally restricted by planning limits [75]. Table 2.2 shows the New Zealand planned harmonic limits for LV and MV systems where the CGESS are anticipated to be connected.

TABLE 2.2: New Zealand planned voltage harmonic distortion levels (percentage relative to the of the fundamental component calculated from their respective RMS values)

Order	LV system (<1kV) (%)	MV system (1kV< V_n <25kV) (%)
2	1.8	1.7
3	4.5	4.2
4	0.9	0.8
5	5.4	5.2
6	0.45	0.4
7	4.5	4.3
8	0.45	0.4
9	2.7	2.6
THD	7.2	6.8

In addition distortion to magnitude harmonic components have a direction of rotation. Positive sequence component rotate with the fundamental components, the negative sequence rotate in the reverse direction to the fundamental component, and the zero sequence is stationary and does not rotate. The typical directions of rotation are shown in Table 2.3.

TABLE 2.3: Harmonic order and sequences

Order	Value	Sequence
Fundamental	50Hz	+
2^{nd}	100Hz	-
3^{rd}	150Hz	0
4^{th}	200Hz	+
5^{th}	250Hz	-
6^{th}	300Hz	0
7^{th}	350Hz	+

2.3.5.2 Voltage Sags

Among the many types of power grid disturbances, voltage sags may have the most influence on the effectiveness of a conventional PLL grid measurement algorithm. Voltage sags refer to a sudden reduction in the grid voltage magnitude, and it generally occurs during faults, energization of transformers, and connection of induction machines [76] [77] [78] [79]. Voltage sag ride through capability for grid connected wind turbines and photo-voltaic devices has been an active area of research recently due to the incentive behind the implementation of renewable energy and the restrictions set by the grid codes [80] [81] [82] [83] [84]. Voltage sags have been the reason for improving the widely adapted synchronous reference frame phase locked loops.

Although the GES prototype was not expected to synchronize during a fault, it is necessary to design a power grid measurement algorithm capable of riding through the voltage sags. Furthermore, it is also necessary for the algorithm to also recover with sufficient performance after the disturbances has been partially or fully cleared. For this reason, the characteristics and the voltage vectors of different types of voltage sags are outlined in this section for simulation purposes.

Voltages sags are categorized into seven types by the ABC classification. These voltage phasors are shown in Figure 2.19,and their vectors are shown in Table 2.4. Figure 2.19 shows that while the voltages magnitude in type A,B and E are reduced, the phases remains symmetrically shifted by 120^o. Type C, D, F, and G however illustrates that both magnitude and phase can be affected, which may lead to measurement failure for a Parks Transform based algorithm designed for symmetrical three phase systems.

TABLE 2.4: Voltage sag vectors according to ABC classification

Type	Voltages	Type	Voltages
A	$\overline{V_a} = V$ $\overline{V_b} = -\frac{1}{2}V - \frac{1}{2}jV\sqrt{3}$ $\overline{V_c} = -\frac{1}{2}V + \frac{1}{2}jV\sqrt{3}$	B	$\overline{V_a} = V$ $\overline{V_b} = -\frac{1}{2}E - \frac{1}{2}jE\sqrt{3}$ $\overline{V_c} = -\frac{1}{2}E + \frac{1}{2}jE\sqrt{3}$
C	$\overline{V_a} = E$ $\overline{V_b} = -\frac{1}{2}E - \frac{1}{2}jV\sqrt{3}$ $\overline{V_c} = -\frac{1}{2}E + \frac{1}{2}jV\sqrt{3}$	D	$\overline{V_a} = V$ $\overline{V_b} = -\frac{1}{2}V - \frac{1}{2}jE\sqrt{3}$ $\overline{V_c} = -\frac{1}{2}V + \frac{1}{2}jE\sqrt{3}$
E	$\overline{V_a} = E$ $\overline{V_b} = -\frac{1}{2}V - \frac{1}{2}jV\sqrt{3}$ $\overline{V_c} = -\frac{1}{2}V + \frac{1}{2}jV\sqrt{3}$	F	$\overline{V_a} = V$ $\overline{V_b} = -\frac{1}{2}V - \left(\frac{1}{3}E + \frac{1}{6}V\right)j\sqrt{3}$ $\overline{V_c} = -\frac{1}{2}V + \left(\frac{1}{3}E + \frac{1}{6}V\right)j\sqrt{3}$
G	$\overline{V_a} = \frac{2}{3}E + \frac{1}{3}V$ $\overline{V_b} = -\left(\frac{1}{3}E + \frac{1}{6}V\right) - \frac{1}{2}jV\sqrt{3}$ $\overline{V_c} = -\left(\frac{1}{3}E + \frac{1}{6}V\right) + \frac{1}{2}jV\sqrt{3}$		

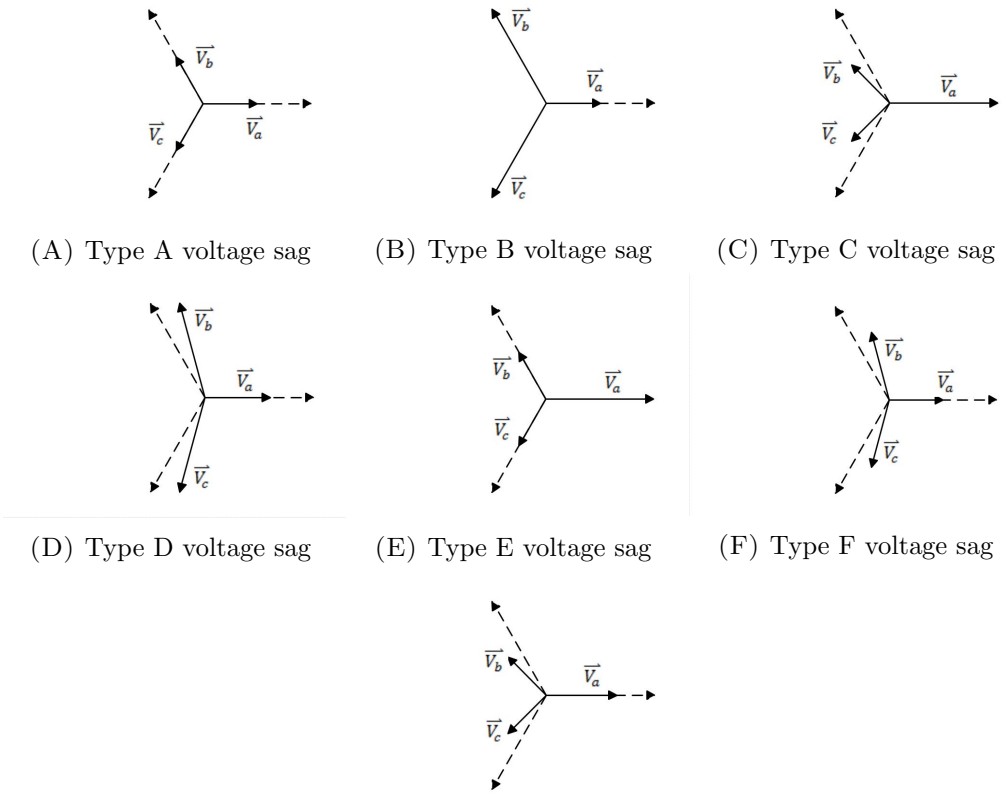

(A) Type A voltage sag (B) Type B voltage sag (C) Type C voltage sag

(D) Type D voltage sag (E) Type E voltage sag (F) Type F voltage sag

(G) Type G voltage sag

FIGURE 2.19: Voltage sags types due to different short circuits according to [77]. Dotted line indicates the voltage prior to short circuit, and solid lines indicates voltages during the disturbance

These voltage sags can last anywhere between 20ms to 3 seconds during fault and a balanced voltage sag can persist for an extended number of cycles after the fault has been extinguished. In addition, induction motors can further increase the voltage sag if the consumers decided to restart their motor after the fault has been cleared due to their large start-up current. In sever cases, the voltage magnitudes has been shown to decrease to as low as 85% [69].

2.3.5.3 Voltage Unbalance

The EPS voltages are described as unbalanced when the three phase RMS values are not equal and they phases angles are not exactly 120^o apart. The voltage unbalance can arise from the unbalance in load, single phase distributed generation, system impedance, and background voltages from the upstream system. Unbalanced supply voltages causes machine heating, and it is also limited according to local electricity regulation code. In

New Zealand, the unbalance limitation is adopted from IEC 6100-2-2 and IEC 61000-2-12 [70], which quantify the voltage unbalance using the voltage unbalance factor (VUF) and its calculation is given as follows:

$$VUF = \sqrt{\frac{1 - \sqrt{3 - 6\,\beta}}{1 + \sqrt{3 - 6\,\beta}}} \tag{2.29}$$

$$\beta = \frac{V_{ab}^4 + V_{bc}^4 + V_{ca}^4}{(V_{ab}^2 + V_{bc}^2 + V_{ca}^2)^2} \tag{2.30}$$

where V_{ab}, V_{bc}, and V_{ca} are phase to phase voltage measurements. The VUF is also known as the negative sequence voltage unbalance factor (NSVUF), which is be calculated by:

$$NSVUF = V_{neg}/Vpos \tag{2.31}$$

It is stated in to clause 7.2(1)(c)(iii) in the New Zealand Electricity Participation Code [1] that participants must meet:

> " *The requirement to use reasonable endeavours to maintain negative sequence voltage at less than 1% and to ensure that negative sequence voltage will be no more than 2% in any part of the grid.*"

Clause 7.2(1)(c)(iii) shows the voltage unbalance is limited by restricting the negative sequence voltage injection. However, as it is stated in also IEC standards that unbalanced levels up to 3% may occur, the simulation has to account for the worse case unbalance. Considering a likely scenario where the EPS voltage magnitudes are reduced to $V_{ab} = 0.95$ p.u. and $V_{ca} = 0.92$ p.u. after a fault and the VHF is at its worst of 0.03, the voltage magnitude of V_{bc} calculated with Equations 2.30 and 2.29 is 0.9 p.u.. These voltage magnitudes will be the unbalance levels considered in this thesis.

2.3.5.4 DC Injection

Renewable distributed generation (DG) installations such as the photovoltaic system are rapidly growing in the medium to low voltage distributed systems. The power electronic inverters in a typical PV system can pollute the EPS by injecting harmonics and DC current, which causes transformer saturation and an increases metering error [85] [86]. According to IEC 61727:2004 [87], IEEE 1547 [88] and IEEE 929-2000 [89] standards, the design qualification for grid connected PV systems species that the DC current injection

must not exceed the limitation measured at the connection point when the DG system is operating at its rated output. Their respective limitations are summarized by Table 2.5.

TABLE 2.5: DC Injection Limitation Guideline

Standard	Maximum DC injection perncentage
IEC 61727:2004	1%
IEEE 1547	0.5%
IEEE 929-2000	0.5%

During an EPS disturbance, nearby generators and synchronous condensers can also cause different magnitudes of dc currents being injected into all three phases [90][91]. The DC component decays at a rated determined by the generator's *aperiodic time constant (T_a)*, which can last from 0.01s up to 0.5s [92] depending on the size of the synchronous machine. The aperiodic time constant also decreases with increasing distance between the synchronous machine and the fault. As the CGESS is intended to be installed to a local distribution gird that is far from large turbo generators and synchronous condensers, it is assumed that the post-fault DC voltages has decayed to an relatively low percentage (1-2%) prior to the FIR command signal for simulation.

2.3.6 Synchronization Standards and Recommendations

Synchronisation of a generator to an EPS is achieved by closely matching the instantaneous frequency and phase angle of the EPS prior to closing the breaker [93] [94]. If the frequency and phase angle deviating too far from one another, the result can:

1. damage generator prime mover/ rotor shaft due to the large torque which attempts to bring the generator rotor into synchronism with the power grid
2. damage the step up transformer and/or causes the protective relay to trip from the large spike in current

Since neither the EIPC nor the Wellington network DG technical connection requirement [95] specified the synchronisation frequency and phase angle criteria for ancillary

services, the design limitations for this project is adopted from the IEEE 1547 [88]. Table 2.6 shows the IEEE-1547 recommended synchronisation limitation for a generator less than 500kVA, which encompasses the CGESS generator capacity.

TABLE 2.6: IEEE1547 Recommended Synchronization Criteria for 0-500kVA Rated Distributed Units Connecting to Electric Power Grid

Parameter	Recommended	Absolute
Voltage	10%	40V
Frequency	0.3Hz	0.3Hz
Phase angle	20^o	20^o

Similarly, the CGESS ABB-AMG generator manual also provides a recommendation synchronisation limitation to avoid damaging the generator construction [96]. The manual specification is shown in Table 2.7:

TABLE 2.7: User Manual Defined Synchronization Relative Parameter Error Values for ABB AMG-0250 Synchronous Generator

Parameter	Recommended	Absolute	Maximum	Absolute
Voltage	2%	8V	4.5 %	18V
Frequency	0.7%	0.35Hz	4%	2Hz
Phase angle	$< 15^o$	$< 15^o$	Unspecified	Unspecified

Conventionally, the synchronisation process is carried out by an automatic synchronizer or a synchronizing supervisory schemes. If manual synchronisation is required, the IEEE 672005 [97] recommended procedure are:

> a) At the moment of closing of the synchronizing breaker contacts, the phase angle between the generator and the bus is as close to zero degrees as possible with plus or minus ten electrical degrees being the maximum allowable deviation.
> b) The speed of the unit should be matched to the system speed such that the synchroscope is revolving, preferably clockwise, at a speed not greater than one revolution every 15 s (0.067 Hz).
> c) The voltage of the incoming generator should not differ from the system voltage by more than 0% to +5% immediately prior to synchronizing. The

> use of automatic synchronizing or synchronizing supervisory equipment is able to incorporate the closing time of the breaker results, usually within approximately five electrical degrees.

The synchronisation procedure is also offered by the ABB AMG generator manual [96], which states that:

> **Start-up of the machine**
> The starting of the machine depends on the application, but main guidelines are:
> 1. Switch the anti-condensation heaters off if not operated by switchgear.
> 2. Start to rotate the machine.
> 3. Maintain rated speed.
> 4. Switch the machine excitation on (unless self excited automatically).
> 5. Maintain rated voltage.
> 6. Check synchronizing parameters (if necessary).
> 7. Synchronize the machine to the grid (if necessary).

Both recommended procedures convey that the typical time to synchronisation is variable and can take longer than the 6 second FIR provision requirement.

2.3.7 Synchronization Stability

2.3.7.1 Introduction

The difference between the CGESS and the traditional synchronisation procedures is the generator's drive input torque, and the condition of the EPS voltages. A traditional synchronisation system utilizes speed control such that the phase errors can be reduced with the small frequency slip over the passage of time. Under such conditions, the net drive torque on the generator shaft only exists to overcome the frictional losses. Unlike the conventional synchronisation procedure, the proposed CGESS generator drive torque will be continuous to achieve rapid start up, and this torque must be met with equal and opposite forces such that the generator can spin in synchronism with the EPS after the breaker has closed. This section outlines the mathematical models used to investigate the generator synchronisation stability.

2.3.7.2 The Swing Equation

An unbalance between the mechanical input and the electrical output of a generator causes the rotor to accelerate. This relationship is described by Newton's second law:

$$J_{mac}\frac{d^2\delta_m}{dt^2} = T_M(t) - T_E(t) \tag{2.32}$$

Where	J_{mac}	is the total machine inertia	(kgm^2)
	δ_m	is the generator shaft angular position relative to the rotating axis given by the power grid	(rad)
	T_M	is the generator shaft mechanical input torque	(Nm)
	T_E	is the opposing generator shaft torque equivalent to the electrical output power and losses	(Nm)

Multiply Equation 2.32 by the mechanical speed, we have:

$$J_{mac}\cdot\omega_m\frac{d^2\delta_m}{dt^2} = P_M(t) - P_E(t) \tag{2.33}$$

Where	ω_m	is the mechanic rotor speed	(rad/s^2)
	P_M	is the generator mechanical input power	(MVA)
	P_E	is the generator electrical output power	(MVA)

Often in power system transient stability modeling, a generator a machine inertia constant H is defined as [68]:

$$\begin{aligned} H &= \frac{\text{Kinetic energy at rated speed}}{\text{Rated MVA}} \\ &= \frac{J_{mac}\cdot\omega_{msyn}^2}{2\cdot S_{rated}} \end{aligned} \tag{2.34}$$

Where	ω_{msyn}	is the rated mechanic rotor speed	(rad/s)
	S_{rated}	is the generator rated output power	(MVA)

Substitute Equation 2.34 into 2.33 we have:

$$2H\frac{S_{rated}\cdot\omega_m}{\omega_{msyn}^2}\cdot\frac{d^2\delta_m}{dt^2} = P_M(t) - P_E(t) \tag{2.35}$$

In practice, the rotor speed does not differ significantly from the synchronous speed, hence $\omega_m = \omega_{msyn}$, which can also be used to describe the CGESS generator if the speed deviation is small at the instance of breaker closure. Normalizing Equation 2.35 by the

machine rated power S_{rated} and converting the mechanical speed and phase parameters to electrical parameters with Equations 2.2 and 2.1, the per unit Swing Equation can be derived:

$$\frac{2H}{\omega_{syn}} \cdot \frac{d^2\delta_e}{dt^2} = P_{M(p.u.)}(t) - P_{E(p.u.)}(t) \tag{2.36}$$

Where	ω_{syn}	is the nominal electrical synchronous speed	(rad/s)
	δ_e	is the generator internal emf electrical angle relative to the EPS voltage angle (power angle)	(rad)
	P_M	is the mechanical power input	(p.u.)
	P_E	is the electrical power output	(p.u.)

2.3.7.3 Generator Power-Angle Equation

The generator rotor deceleration torque is developed by the transfer of electrical power from the generator to the EPS. For a salient rotor synchronous generator connected to the power grid, the steady state power angle relationship is approximated by: [91] [90]

$$P_E = \frac{V_g V_s}{x_d} \sin(\delta) - V_s^2 \frac{x_q - x_d}{2x_d x_q} \sin(2\delta) \tag{2.37}$$

Where	P_E	is the generator electric power output	(p.u.)
	V_g	is the generator internal air-gap voltage	(p.u.)
	V_s	is the electric power system voltage	(p.u.)
	δ	is the angle between V_g and V_s (power angle)	(Degree)
	x_d	is the direct axis reactance	(p.u.)
	x_q	is the quadrature axis synchronous reactance	(p.u.)

2.3.7.4 Equal Area Criterion

The generator power input and output characteristics is depicted by Figure 2.20. During steady state, the generator mechanical input is generally constant where as the electrical power output is dependent on the power angle as described by Equation 2.37. Figure 2.20 describes a scenario where the mechanical input power suddenly increased from P_{M0} to P_{M1}.

Usually the rotor angle stability can often be determined within the first 'swing', where the internal voltage and the generator power is assumed constant. The sudden step in input mechanical power causes the electrical power output to increase from δ_0 to δ_1 such

that input/output power are equal $P_{E1} = P_{M1}$, establishing a new steady state power angle δ_1.

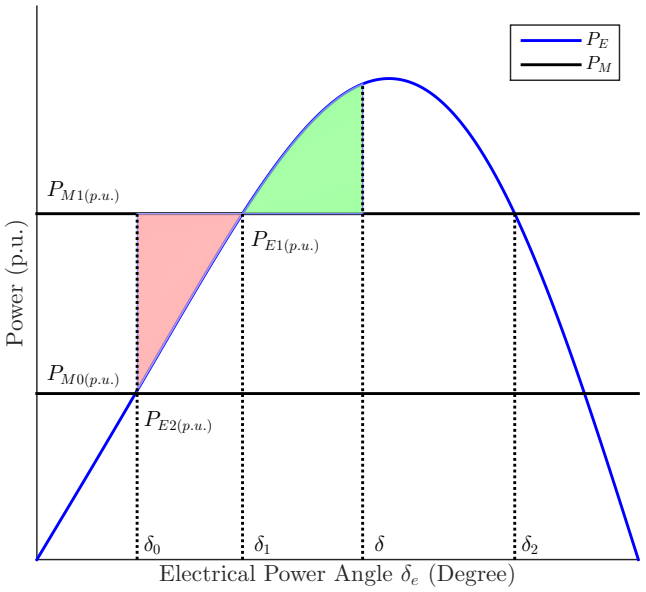

FIGURE 2.20: Generator input and output power relationship with power angle

The equal area criterion is a technique employed to determine the stability of a synchronous machine connected to an infinite system following an disturbance without solving the swing equation. It has been proven in [68] that by multiplying both side of Equation 2.36 by $d\delta_e/dt$, utilized the chain rule and rearranging the equation, the result can be integrated from δ_0 to δ to give:

$$\frac{\omega_{syn}}{H}\left(\frac{d\delta_e}{dt}\right)^2\Bigg|_{\delta_0}^{\delta} = \int_{\delta_0}^{\delta}\left(P_{M(p.u.)} - P_{E(p.u.)}\right)d\delta_e \tag{2.38}$$

Where δ_0 is the angle from which the power angle begins to accelerate (Degree)

δ is a the angle at which the power angle ceases to accelerate (Degree)

Prior to an disturbance, the generator rotor is generally operating in steady state such that the $d\delta_e/dt$ at δ_0 is zero. If stability can be achieved following a disturbance, the rotor will stop accelerating and begin to decelerate at arbitrary power angle δ, therefore, $d\delta_e/dt$ will also be zero at δ. As the left hand side of Equation 2.38 equates to zero, the

right hand side can be rewritten into the accelerating an decelerating components:

$$\int_{\delta_0}^{\delta_1} \left(P_{M(p.u.)} - P_{E(p.u.)}(t)\right) d\delta_e + \int_{\delta_1}^{\delta} \left(P_{M(p.u.)}(t) - P_{E(p.u.)}(t)\right) d\delta_e = 0 \tag{2.39}$$

Rearrange 2.39, we have:

$$\int_{\delta_0}^{\delta_1} \left(P_{M(p.u.)}(t) - P_{E(p.u.)}(t)\right) d\delta_e = \int_{\delta_1}^{\delta} \left(P_{E(p.u.)}(t) - P_{M(p.u.)}(t)\right) d\delta_e \tag{2.40}$$

Observing Figure 2.20, Equation 2.40 describes the red area with its left hand side and the green area with the right hand side. If Equation 2.40 can be satisfied, a power angle exists such that machine can attain stability. On the other hand, if the power angle swings past δ_2 (critical angle) at some point following the disturbance due to the accelerating area, the electromagnetic force falls below the applied mechanical force such that additional acceleration ensues, causing instability.

Using the concept, the stability of the CGESS generator after synchronisation can be determined. The power angle relationship describing the sudden appearance of the electrical connection while the generator is driven by a constant power is depicted by Figure 2.21

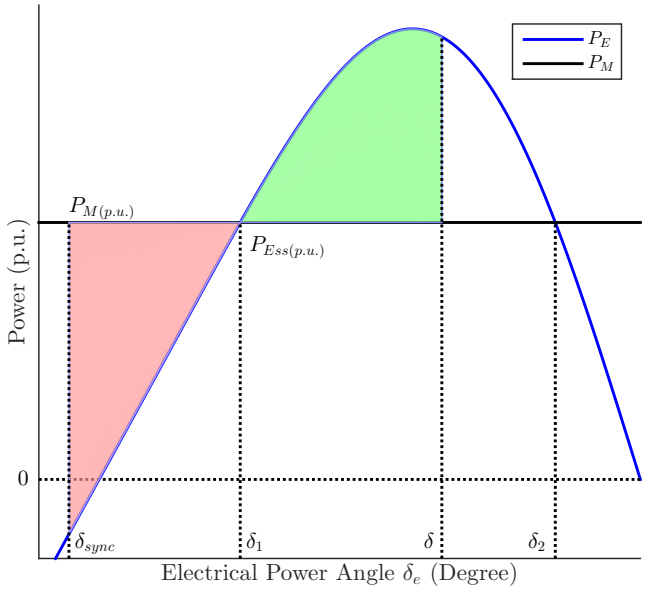

FIGURE 2.21: CGES generator input and output power relationship varying synchronisation angle error

The power angle at which the generator rotor starts to accelerate is equivalent to the initial synchronisation angle error δ_{sync}.

2.3.7.5 Subtransient Torque

Ideal synchronisation occurs when the speed, frequency and voltage are equal such that no circulating current can be observed. It has been derived in [90] that the synchronisation torque varies with time, voltage magnitudes and the initial angle difference at breaker closure. The expression describing the torque dynamics following an synchronisation procedure a is given by:

$$T_{p.u.}(t, \Delta\delta) = \frac{V_g V_s}{X_D} \sin(\Delta\delta)\left(1 - \cos(\omega t) + \tan(\frac{\Delta\delta}{2}) \sin(\omega t)\right) + \frac{V_g(V_g - V_s)}{X_D} \sin(\omega t) \tag{2.41}$$

Where	T	is the rotor torque	(p.u.)
	X_D	is the sum of reactances between the generator open circuit and the power grid voltage	(p.u.)
	$\Delta\delta$	is the angle difference at the breaker closure instance	(Degree)

As suggested by [90], the generator equivalent impedance should be approximated by the subtransient reactance if the generator is un-loaded prior to synchronisation. Although the torque does not decay with time due to the lack of resistance, Equation 2.41 is suitable for the CGESS torque simulation as it will be used to determine the maximum electromagnetic torque imposed on the generator shaft a short time after synchronisation.

2.4 Theory of Classical Controls

2.4.1 Section Overview

The control design process is complex due to the highly nonlinear property of the proportional throttle valve. In this section, the definition of nonlinearity, methods of nonlinear control, and the properties of the nonlinearity seen in the PTV is outlined.

2.4.2 Nonlinear Control

A linear system must satisfy **property of homogeneity** and the **principle of superposition** [98] [99]. Define a system which has an input outputs relationship:

$$y(t) = f(x(t)) \tag{2.42}$$

Where yt is the output
$f()$ is the dynamics of the system
$x(t)$ is the input

To satisfy the **property of homogeneity**, a constant-scaled input must also produce an equally scaled output (i.e. $x(t) = \alpha x_1(t)$ produces $y(t) = \alpha y_1(t)$, where α is a constant). To satisfy the **principle of superposition**, the inputs $x(t) = x_1(t) + x_2(t)$ must produce the outputs $y(t) = y_1(t) + y_2(t)$ if the input $x_1(t)$ results in output $y_1(t)$ and $x_2(t)$ results in $y_2(t)$. Many electromechanical, hydraulic and pneumatic systems are described by nonlinear differential equations . In pressure-flowrate characteristics shown in Equation 2.16, the input to pressure relationship is not only nonlinear, the pressure drop also depends on the flowrate.

There are numerous ways of designing controllers for nonlinear systems, such as sliding mode, back-stepping, Lyapunov redesign, model predictive, model reference adaptive, dynamic inversion, model based fault tolerant, flatness, and finally receding horizon control [100] [101] [102] [103] [104] [105]. Many of these nonlinear control design methods are complex and application specific.

Approximating the dynamic of nonlinear systems with equivalent linear systems and applying classical control design concepts is a common practice carried out by control engineers [106] [98] [99]. Traditionally in industrial hydraulics, the controller is designed based on the linearized valve dynamic [107] [108]. The most simplistic tangent method will be used to linearize the control valve behavior in this thesis.

2.4.3 Graphical Linear Approximation of Nonlinear Dynamics

Often the linearization is performed around an operation point. Taking the Taylor Series expansion of Equation 2.42 about an operating point x_o, we have:

$$y = f(x_o) + \frac{f'(x_0)}{1!}(x - x_o) + \frac{f''(x_0)}{2!}(x - x_o)^2 + \frac{f'''(x_0)}{3!}(x - x_o)^3 + ... \tag{2.43}$$

The second term in the Taylor series expansion is the slope of function y evaluated at operating point x_o. The first two terms of the Taylor series expansion alone are adequate

approximation to behavior of y given the input x does not deviated largely from x_o [109]. The small signal approximation of y becomes

$$y = f(x_o) + \frac{f'(x_0)}{1!}(x - x_o) = y_o + f'(x_0)(x - x_o) \tag{2.44}$$

Rewriting Equation 2.44, we have

$$y - y_o = f'(x_0)(x - x_o) \tag{2.45}$$

where $(y - y_o)$ and $(x - x_o)$ are small changes of x and y around the equilibrium points x_o and y_o.

Graphically, approximating the nonlinear equation by truncating the Taylor Series expansion is analogous to the tangent method, where the gradient is computed by using data points a small deviation from than the operating points. The graphical linearization is shown in Figure 2.22.

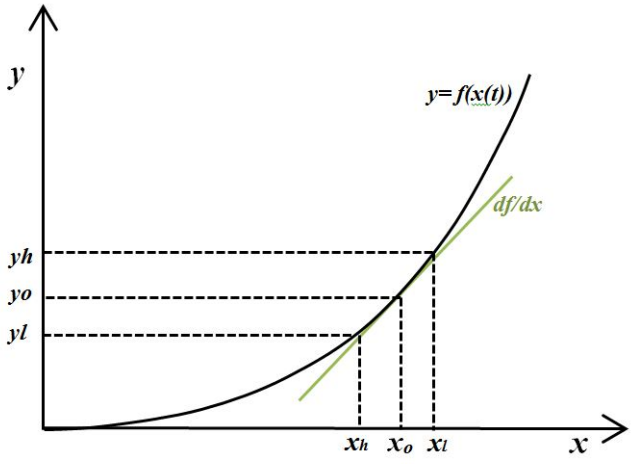

FIGURE 2.22: Graphical Linearizion Technique

2.4.4 Time delay and Padé Approximation

Referring to the valve poppet dynamic in Figure 2.10, the Parker TDA series valve outputs have delays of roughly 10ms, which takes up large fraction of the NG-16 and NG-25 valves total response time. This delay has to be incorporated into the plant model. A signal $y(t)$ that is determined by an output $f(t)$ with has time delay of T is described by Expression 2.46.

$$y(t) = f(t - T) \tag{2.46}$$

The transfer function of y(t) is [110]:

$$Y(s) = e^{-sT} F(s) \tag{2.47}$$

Therefore, the standard valve poppet transfer function shown in Equation 2.5 becomes:

$$\frac{X_p(s)}{V_{vi}(s)} = \frac{e^{-t_d s} \cdot K_{stk} \cdot w_n^2}{s^2 + 2\omega_n \zeta s + \omega_n^2} \tag{2.48}$$

Where t_d is the delay time (s)

Since Matlab design control algorithms cannot operate with ideal time delays, a common approximating technique for low frequency systems called the Padé approximation [111]is used. Padé approximation is a method of converting the irrational time delay into an approximation in the form of rational transfer functions. The Padé approximation of the ideal delay $e^{-t_d s}$ is [112]:

$$e^{-t_d s} \approx \frac{120 - 60\, s\, t_d + 12\, (s\, t_d)^2 - (s\, t_d)^3}{120 - 60\, s\, t_d + 12\, (s\, t_d)^2 + (s\, t_d)^3} \tag{2.49}$$

Approximation 2.49 will be used to approximate the valve delay.

2.4.5 Linear Controller Design and Root Locus Method

Feedback linearization and gain scheduling are two common ways of controlling two nonlinear systems by manipulating the controller/feedback variables such that the overall process dynamic appears linear [106] [99] [98]. Similarly, there are numerous control design methods for linear time invariant (LTI) systems and they are generally classified into two categories: classical and modern.

Classical design methods are limited to single-input single-output (SISO) problems, and the design methods include frequency response, root locus, PID and lead lag compensator. State space (modern) control methods are capable of handling multiple-input multiple-output (MIMO) systems that are often presented in aerospace engineering problems. State space design methods include: pole placement, pole placement using observers, state feedback, linear quadratic regulator(LQR), linear quadratic Gaussian (LQG) and H Infinity. Furthermore, a heuristic based PID control tuning procedure

called the Ziegler–Nichols method is also commonly used for on site adjustment of industrial controllers [98].

The control method implemented in this thesis is a gain scheduled controller, which is designed with a classical root locus method. The root locus method is a control system design tool which sketches the root progression of a control system that is subjected to a varying constant gain [99] [98]. The design process is carried out in Matlab SISO tool, which assists the design process by offering interactive pole-zero placement, real-time response plots, automatic tuning as well as being able to specifying performance criteria such as damping ratio and settling time.

To ensure stability, the classical phase margin (PM) and gain margin (GM) observation of the open loop transfer function bode plot are used in this thesis. Typically, a phase margin of 30 to 60 degrees is commonly chosen to ensure a relatively fast dynamic response and robustness [113].

2.4.6 Steady State Error

Given a simple negative feedback control system depicted by Figure 2.23 and its open loop transfer function shown in expression 2.50, the *type* of the system $P(s)$ is defined by the number of open loop poles located at zero [114].

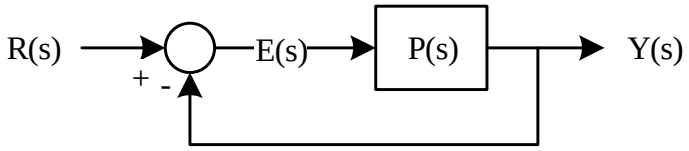

FIGURE 2.23: Simple negative feedback control structure (open loop transfer function: $P(s)$, input transfer function: $R(s)$, output transfer function :$Y(s)$)

$$P(s) = \frac{K_{dc} \prod_i (s - z_i)}{s^T \prod_j (s - p_j)} \tag{2.50}$$

Where K_{dc} is the open loop DC gain
T is the system type
z_i is the value of the i^{th} zero
p_i is the value of the j^{th} pole

The importance of system type is its effect on closed loop phase tracking error $E(s)$. In the CGESS application, the tracking error of the phase and frequency values cannot exceed a specified value. Given generic PLL phase angle signal input, a step input in phase ($\Delta\theta$), frequency ($\Delta\omega$) and acceleration ($\Delta\alpha$) are all likely to be the characteristics of the signal, which will affect the closed loop tracking capacities. These inputs are characterized in the s-domain as follows:

Step phase input:

$$R(s) = \frac{\Delta\theta}{s} \tag{2.51}$$

Step frequency input:

$$R(s) = \frac{\Delta\omega}{s^2} \tag{2.52}$$

Step acceleration input:

$$R(s) = \frac{\Delta\alpha}{s^3} \tag{2.53}$$

Using final value theorem

$$\lim_{t\to\infty} e(t) = \lim_{s\to 0} sE(t) \tag{2.54}$$

with the closed loop system error $E(s)$

$$E(s) = \frac{R(s)}{1 + P(s)} \tag{2.55}$$

gives:

$$\lim_{t\to\infty} e(t) = \lim_{s\to 0} \frac{sR(s)}{1 + P(s)} \tag{2.56}$$

Substituting input expressions 2.51, 2.52, 2.53 and various $P(s)$ system types into equation 2.56 and evaluated individually, the steady state error of type 1, type 2 and type 3 systems under different input conditions is given by Table 2.8.

TABLE 2.8: Relationship between steady state phase tracking error (E_{ss}), system types, and inputs

Input \ System type	Type 1	Type 2	Type 3
Phase step	E_{ss}=0	E_{ss}=0	E_{ss}=0
Frequency step	$E_{ss}=\frac{\Delta\omega}{K_{dc}}$	E_{ss}=0	E_{ss}=0
Acceleration step	$E_{ss}=\infty$	$E_{ss}=\frac{\Delta\alpha}{K_{dc}}$	E_{ss}=0

2.5 Instrumentation and Signal Processing

2.5.1 Section Overview

Accurate frequency and phase angle measurements of the EPS and the generator are crucial in ensuring the robustness of the control loop and the appropriate activation of the synchronisation relay. For the GES instrumentation, an incremental encoder and suitable filtering algorithm was intended to be implemented to measure the generator-side quantities; where a phase locked loop was designed to extract the EPS quantities from the measured voltages. This section details the relevant literature research, applicable methodologies, technical foundation and design background of the intended measurement algorithm.

2.5.2 Electric Power Grid Parameter Sensing

2.5.2.1 Introduction

Many power grid parameter estimation techniques exits. Among them, the most simplest method is the zero crossing detection technique [115],[116],[117], which is the methodology implemented by Transpower to measure the RoCoF [118]. Because only a single measurement can be made per half cycle and the presences of DC in the EPS during disturbances can cause measurement error. The zero crossing method is not considered for our application.

Many EPS frequency and phase measuring methods exists, the techniques ranged from wavelet theory [119], [120], [121], [122], digital FIR method [123] [124], numerical methods [125] [126], [127], Fourier transform [128], [129], [130], [131], [132], to Kalman filter [133], [134], [135], [136]. Amid the vast amount of estimation techniques, the phase

locked loop (PLL) method is the most prevalent method used to track EPS phase and frequency quantities [137], and it is chosen to be the CGESS parameter tracking algorithm. Many variations of the phase locked loop exists and their structure and designed process differ according to the application. Numerous papers have been published to analyze, review, and compare PLL topologies [138], [139] [140] [137], [141] [142] [143].

A common element in a three phase PLL is the utilization of the Clarke/Park's transform to convert the three phase rotating frame to a stationary synchronous frame. In this project, the PLL was designed using the PQ theory based qPLL [144] [145]. This section introduces a conventional PLL, provides the background and topology of a qPLL, and outlines the effect of distorted EPS voltages on the qPLL tracking capabilities.

2.5.2.2 Conventional PLL structure

A PLL is a negative feedback control system designed to generate an output signal which has the same phase as the input signal. The PLL is typically designed in the Laplace domain and its structure is depicted by Figure 2.24. A conventional PLL consists of a phase detector (PD), a loop filter $G(s)$ and an oscillator $O(s)$ [146] [147].

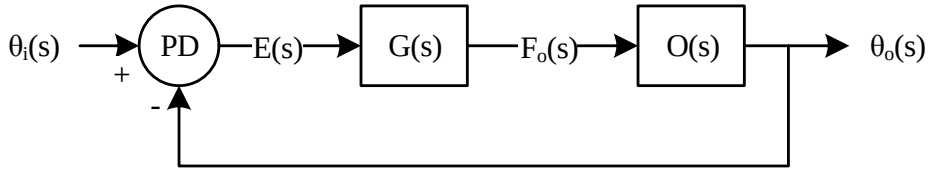

FIGURE 2.24: Generic PLL structure

The O(s) transfer function in Figure 2.24 typically represents an voltage controlled oscillator (VCO) because in an traditional electronic implementation of the PLL, the output at $F_o(s)$ is a voltage signal and the reconstruction of the input voltage waveform is generated by a VCO circuit. In digital implementation, the signal value at $F_o(s)$ is the signal frequency and the oscillator is represented by integrator that sums the frequency over time to derive the phase output. The oscillator transfer function is:

$$O(s) = \frac{1}{s} \tag{2.57}$$

Similar to all appropriately designed negative feedback control loops, the PLL attempts to minimize the phase difference between the input and output by generating a signal which is proportional to the input frequency. With the PLL control loop structure

established and given the performance criteria, the PLL dynamics and stability can be designed according to conventional control system design approaches.

2.5.2.3 Conventional qPLL Structure

In this thesis, the frequency and phase measurement algorithm designed for the CAESS is a PQ-PLL, which is predominantly based on the topologies proposed by [144] [145].

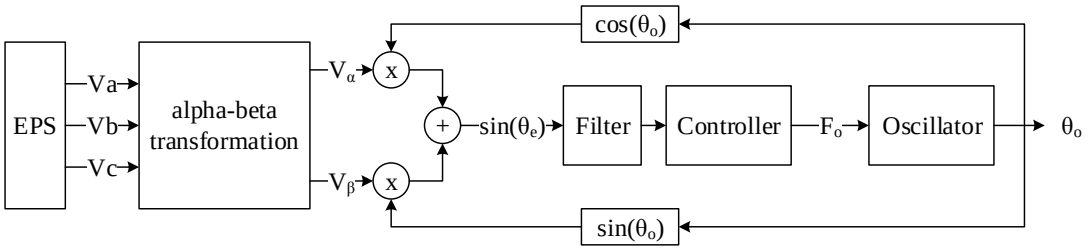

FIGURE 2.25: Basic q-PLL structure

The qPLL shown in Figure 2.25 is similar in structure to a single phase PLL. Clarke's transformation (or ABC to $\alpha\beta$ transformation) is used to convert the rotating three phase (ABC) quantities into a two quadrature vectors α andβ, which carries the information of the phase A voltage directly. Given a symmetrical three-phase system whose voltages are described by:

$$\begin{bmatrix} V_a \\ V_b \\ V_c \end{bmatrix} = \begin{bmatrix} \sin(\theta_s) \\ \sin(\theta_s - 120^o) \\ \sin(\theta_s + 120^o) \end{bmatrix} \tag{2.58}$$

The Clarke Transformation [148] of the three phase system is:

$$\begin{bmatrix} V_\alpha \\ V_\beta \\ V_\gamma \end{bmatrix} = \frac{2}{3} \begin{bmatrix} 1 & -\frac{1}{2} & -\frac{1}{2} \\ 0 & \frac{\sqrt{3}}{2} & -\frac{\sqrt{3}}{2} \\ \frac{1}{2} & \frac{1}{2} & \frac{1}{2} \end{bmatrix} \begin{bmatrix} V_a \\ V_b \\ V_c \end{bmatrix} \tag{2.59}$$

Evaluating Equations 2.58 and 2.59, the $\alpha\beta$ components are:

$$\begin{bmatrix} V_\alpha \\ V_\beta \end{bmatrix} = \begin{bmatrix} \sin(\theta_s) \\ -\cos(\theta_s) \end{bmatrix} \tag{2.60}$$

Using the trigonometric feedbacks shown in Figure 2.25 and applying the trigonometric identities, the reference error is therefore:

$$\begin{aligned} \sin(\theta_s)\cos(\theta_e) - \cos(\theta_s)\sin(\theta_e) &= \sin(\theta_s - \theta_o) \\ &= \sin(\theta_e) \end{aligned} \tag{2.61}$$

Expression 2.61 conveys that if the qPLL output is slightly below the EPS phase angle, $\sin(\theta_e)$ is positive and forces the controller output to increases to match the EPS phase angle. Conversely, the algorithm reduces the controller output when the EPS phase is below the qPLL output phase angle. A satisfactory qPLL controller regulates the phase detector output to be zero. Once equilibrium has been reached, the phase error is zero and making F_o in Figure 2.25 equal to the EPS frequency.

As the error $\sin(\theta_e)$ is a nonlinear function, the qPLL structure has to be linearized to facilitate LTI control system design and stability studies. If the angle difference is small (i.e. $\theta_s - \theta_o \approx 0$), $\sin(\theta) \approx \theta$ which makes the error gain of 1. The linearized s-domain model of the qPLL is depicted by Figure 2.26.

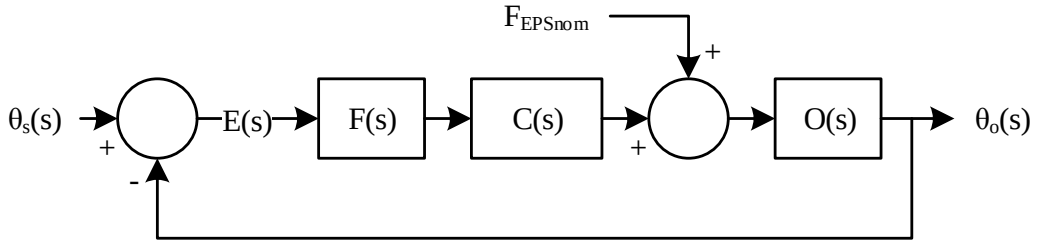

FIGURE 2.26: Small signal qPLL control model

Where $\theta_s(s)$ is the EPS phase
$\theta_o(s)$ is the qPLL output phase
$E(s)$ is PLL phase error
$F(s)$ is filter transfer function
$C(s)$ is controller transfer function
F_{EPSnom} is the constant centered at EPS nominal frequency
$O(s)$ is the oscillator (integrator) transfer function

2.5.2.4 Effect of EPS nonidealities and filters

Although the 50 Hz fundamental frequency results in an ideal DC value in the error output which the controller utilizes to regulate the phase output, the presence of harmonics, magnitude unbalance and DC create oscillating components in F(s) and $\theta_o(s)$.

The frequency oscillation and its causes are summarized by Table 2.9

TABLE 2.9: Effect of EPS nonidealities on Q-PLL frequency output [149]

Cause	Error output oscillation frequency
DC offset	50Hz
Voltage unbalance	100Hz
2^{nd} and 4^{th} harmonics	150Hz
5^{th} and 7^{th} harmonics	300Hz

Because the frequency oscillation caused by EPS disturbances are centered at integer multiples of the fundamental frequency, notch filters can be introduced to reject these selected frequencies. The general transfer function of a notch filter is given by [150]:

$$H_{notch}(s) = \frac{s^2 + \omega_n^2}{s^2 + Q\omega_n s + \omega_n^2} \tag{2.62}$$

Where ω_n is the filter center frequency
Q is the notch filter quality factor

2.5.3 Generator Parameter Sensing

2.5.3.1 Introduction

As the RoCoF of the CGESS generator is high compared with the EPS, the response of generator phase and frequency measurements using conventional PLL based methods may be insufficient. In section 2.2.5.2, the generator peak voltage has been shown to be directly below rotor pole faces and this allows the electrical phase to be measured mechanically by the rotor position. To remove the intermediate step in measuring phase and frequency from generator terminal voltages, a rotary encoder connected to the rotor shaft will be used to measure electrical phase and frequency. The adaptation of using optical rotary encoders on measuring the electrical quantities is not novel; in [151], a rotary encoder is used as generator load angle estimation.

In this section, different types of rotary encoders and the suitability of using these types of encoders in the CGESS are first introduced in Section 2.5.3.2, the encoder

specifications, signal properties and the appropriate filtering method are then defined in Sections 2.5.3.3, 2.5.3.4 and 2.5.3.5.

2.5.3.2 Optical Rotary Encoders Types

A optical rotatory encoder is a rotational motion sensor which converts position into digital pulses. Inside an encoder, a disk is placed between a pair of photo-emitters and photo-detectors [152][153][154]. A series of transparent and opaque regions are etched radially onto the disk, such that the beam produced by the photo-emitter could be interrupted based on the angular position of the disk. Because the encoder output represents the measured state of the photo-detector, relative or absolute position information can be transferred. Figure 2.27 illustrates the construction and the operation of an optical rotary encoder with two channels:

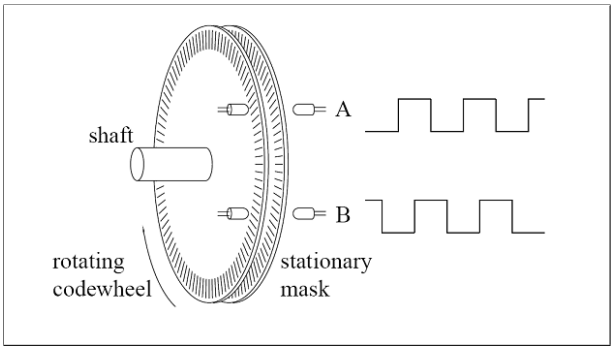

FIGURE 2.27: (Construction of an optical encoder (Illustration by [153]))

Rotary encoders are available in two types: absolute and incremental encoders. Both types are constructed similarly as depicted in Figure 2.27, however the rendition of movement information is different. Absolute encoder encoding disks are constructed with multiple layers of slits, whereas incremental encoder disks were made with only two, sometimes three, layers of slits (see Figure 2.28).

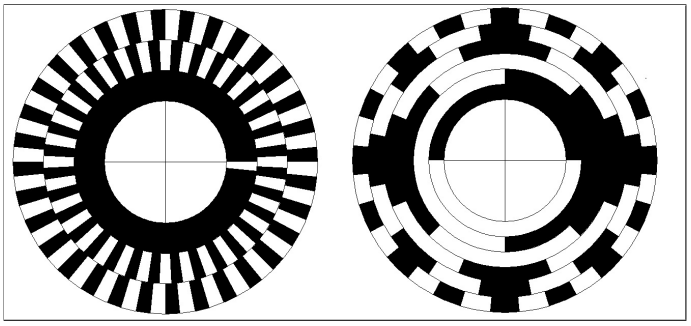

FIGURE 2.28: Comparison between incremental (left) and absolute (right) encoder encoding disk

Incremental encoders produces pulse trains, which by themselves cannot convey useful information. The encoder earns its incremental designation by deriving the actual position from accumulating the pulses over time. Some incremental encoders offer two output channels (often called channel A and B) to differentiate the rotation direction by offsetting the encoding wheel slits by 90 degrees. These quadrature outputs are illustrated in Figure 2.29. Very often a reference line (called channel Z), delivering one pulse per revolution, is also implemented to indicate the starting position of the encoder.

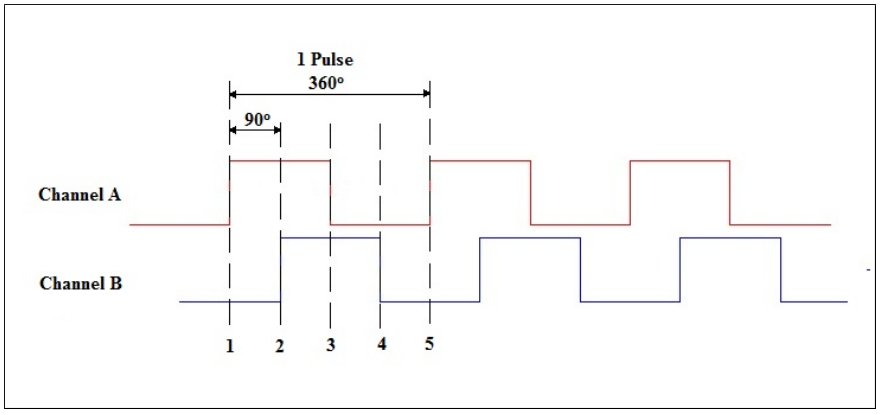

FIGURE 2.29: Incremental encoder quadrature output

Unlike incremental encoders, absolute encoders are capable of distinguishing the rotor position without accumulating the pulses. Because each layer of the encoding wheel on an absolute encoder presents one bit of information (as illustrated in Figure 2.30), each encoder position produces an unique binary combination. Without having to accumulate the pulses, the rotor position is available as soon as the device is powered on.

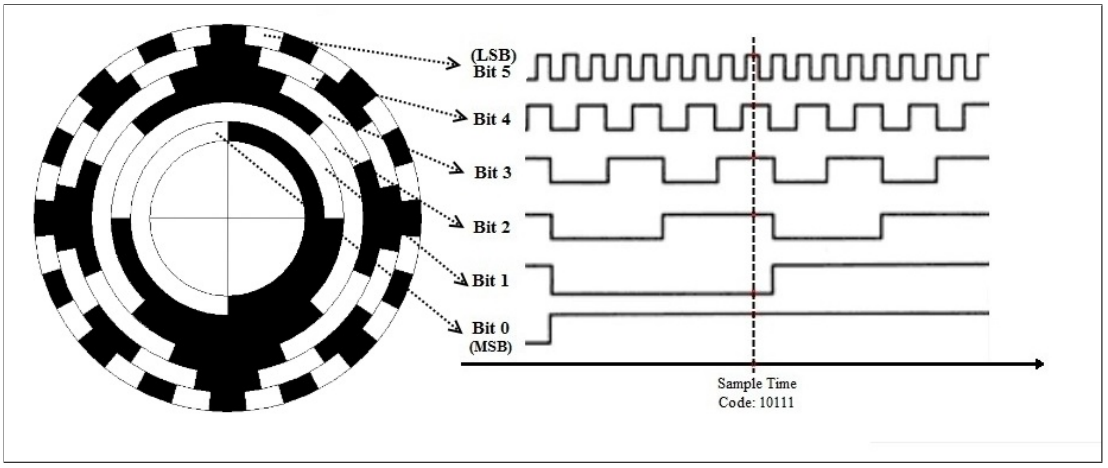

FIGURE 2.30: Absolute encoder binary output

The information extracted and the number of data lines from an absolute encoder is different from the incremental encoder, thus the hardware interface method must also be chosen appropriately. There exists many types of interfaces including parallel, SSI, CAN, PROFIBUS and Ethernet [155].

Although both types of rotary encoders are suitable for the CGESS system during synchronisation control, the functional requirement outside of the synchronisation control period must also be considered. Firstly, as the encoder will be mounted to the generator shaft and the measured rotor position has to be first adjusted to represent the voltage phase angle, the calibrated position value must be stored; secondly, the CGESS supply power may be temporarily lost due to a power cut; and thirdly, the generator rotor position may move during mechanical maintenance. An absolute encoder is able to store its calibrated position and provide a value regardless of these events, but an incremental encoder position memory requires the supply power. Although an incremental encoder can offer the same functionality by continuously storing its current position in non-volatile memory to mitigate the effect of a power failure, any rotor movement during a maintenance session on a powered-off CGESS system can cause the loss of calibration. This makes an absolute encoder a better suited device for the CGESS system.

Despite the advantage of absolute encoder, an incremental encoder was used to measure the generator quantities as only incremental encoders was readily available in the inventory at the time. The following sections detail the technical background tailored to the incremental encoders.

2.5.3.3 Incremental Encoder Specification

A highest angular resolution exists due to the limit in the number of slits that can be cut onto the encoding wheel, and is specified by manufacturers in pulse per revolution (ppr). For incremental encoders, a commonly practiced decoding technique depicted by Figure 2.29 is used to count both the rising and falling edges of the quadrature outputs to increase the usable position resolution by a factor of 4. To distinguish this difference for the remaining part of the thesis, N_{ppr} denotes the manufacturer specified pulse per revolution, and N_{cpr} describes the effective counts per revolution provided by the decoding technique. The conversion is simply:

$$N_{cpr} = 4 \cdot N_{ppr} \tag{2.63}$$

Where	N_{ppr}	is the specified pulse per revolution	(pulses/rev)
	N_{cpr}	is the effective count per revolution	(count/rev)

The encoder manufacturers also specify the maximum frequency which can be transmitted by the encoder due to the limitations of the internal electronics [156] [157]. Often manufacturers specify the maximum output frequency that is separate to the permissible mechanical speed and the conversion is given by:

$$n_{max} = \frac{F_{max}}{N_{ppr}} \tag{2.64}$$

Where	n_{max}	is the maximum functional mechanical speed	(rev/s)
	F_{max}	is the maximum encoder output frequency	(Hz)

While the internal electronics limits the maximum output frequency (equivalently the measurable shaft speed) of the encoder, the hardware must be also able to sample the output without missing the pulses. The minimum sample frequency of the hardware is given by the Nyquist frequency:

$$F_{s(min)} > 2 \cdot F_{max} \tag{2.65}$$

Where	$F_{s(min)}$	is the minimum hardware sample frequency	(Hz)

2.5.3.4 Incremental Encoder Sensing and Measurement Error

Because the quadrature PWM signals are generated when the optical sensor receiver is interrupted by the rotating disc, only the position information is directly conveyed. Conventionally, the measured speed is derived from counting the number of pulses over a fixed period, and the acceleration is computed by dividing the change in speed over the same interval. This backwards numerical differentiation method used to obtain speed and acceleration is expressed by Equation 2.66, 2.67 and 2.68.

$$\theta_{meas}(t_N) = N_{cnt}(t_N) \cdot \frac{2\pi}{N_{cpr}} \tag{2.66}$$

$$\omega_{meas}(t_N) = \frac{N_{cnt}(t_N) - N_{cnt}(t_{N-1})}{T_s} \cdot \frac{2\pi}{N_{cpr}} \tag{2.67}$$

$$\alpha_{meas}(t_N) = \frac{N_{cnt}(t_N) - 2N_{cnt}(t_{N-1}) + N_{cnt}(t_{N-2})}{T_s^2} \cdot \frac{2\pi}{N_{cpr}} \tag{2.68}$$

Where	N_{cnt}	is the measured encoder count	(counts)
	t_N	is the value at sample time N	(s)
	T_s	is the process sample period	(s)
	ω_{meas}	is the measured shaft speed	(rad/s)
	θ_{meas}	is the measured encoder shaft position	(rad)
	α_{meas}	is the measured shaft acceleration	(rad/s^2)

To clarify the terminology used in this thesis, the process sample period is the interval at which the measuring algorithm updates a new measurement value for the controller, whereas the encoder hardware sample period is the interval at which the hardware samples each channel output of the encoder output.

With numerical differentiation, the quantization errors in speed and acceleration depend the encoder ppr and process sample rate. The minimum resolution in position, speed and acceleration is calculated by:

$$\theta_{qerror} = \frac{1}{N_{cpr}} \cdot 2\pi \tag{2.69}$$

$$\omega_{qerror} = \frac{1}{N_{cpr} T_s} \cdot 2\pi \tag{2.70}$$

$$\alpha_{qerror} = \frac{1}{N_{cpr} T_s^2} \cdot 2\pi \tag{2.71}$$

Where	θ_{qerror}	is the position quantization error	(rad)
	ω_{qerror}	is the speed quantization error	(rad/s)
	α_{qerror}	is the acceleration quantization error	(rad/s^2)

On top of quantization errors, long signal cables, environmental electrical interference, improper cable termination, loose mechanical coupling, slippage and poor power supply quality also contributes to measurement inaccuracies by adding extra/canceling encoder pulses [158] [159]. Hence, it is reasonable to design the signal filter to also account for the additional noise sources.

2.5.3.5 Foundations of Kalman Filter

Considering the CGESS auto-synchronisation signal algorithm generates the breaker closure command based on the frequency and phase angle measurements, excessive instrumentation delays which will result in the CGESS missing its synchronisation window cannot be tolerated. It will be demonstrated in section 3.3.6.1 that since classical linear filters cannot meet the CGESS delay limit, the Steady State Linear Kalman Filter (SSLKF) [160] algorithm will be used.

Prior to outlining the SSLKF, we first introduce the Kalman filter [161], which is where the which the SSLKF was derived from. A Kalman filter, named after Rudolf E. Kalman, is an optimal recursive data processing algorithm [162] which has been employed in the field of marine, defense, aerospace, and GPS engineering. The Kalman filter is a minimum mean squared estimation filtering approach [163] [164] capable of estimating the states by placing a weighted average on the estimated states and the measured states using: (1) predicted system dynamics, (2) measurement noise distribution and predicted system dynamic error, and (3) initial conditions.

For a discrete dynamic model given in the form of

$$\begin{aligned} \mathbf{x}_k &= \mathbf{A}\mathbf{x}_{k-1} + \mathbf{w}_k \\ \mathbf{y}_k &= \mathbf{C}\mathbf{x}_k + \mathbf{v}_k \end{aligned} \tag{2.72}$$

Where	$\mathbf{x}$	is the state vector
	$\mathbf{y}$	is the measurement vector

A	is the state transition matrix
w	is the noise in the state vector
v	is the measurement noise
k	is the time index

the discrete Kalman filter consists of the recursive equations given by Equation 2.73 to 2.76 .

(1) *Prediction of States*

$$\hat{x}_k = A\bar{x}_{k-1} \tag{2.73}$$

(2) *Predicted State Error Covariance Matrix*

$$\hat{P}_k = A\bar{P}_{k-1}A^T + Q_k \tag{2.74}$$

(3) *Compute for Kalman Gain*

$$K_k = \hat{P}_k C^T (C\hat{P}_k C^T + R_k)^{-1} \tag{2.75}$$

(4) *Update State Estimation with Measurement*

$$\bar{x}_k = \hat{x}_k + K_k(Cx - C\hat{x}_k) \tag{2.76}$$

(5) *Update Error Covariance Matrix*

$$\bar{P}_k = (I - K_k C)\hat{P}_k \tag{2.77}$$

Where

$\hat{x}$	is the predicted state
x	is the sensor measured state
$\bar{x}$	is the estimated state (i.e. filter output)
A	is the state transition matrix
$\hat{P}$	is the predicted state error covariance matrix
$\bar{P}$	is the updated state error covariance matrix
R	is the measurement error covariance matrix
Q	is the process state error covariance matrix
K	is the Kalman gain
k	is the is the time at $t = k$

In layman's terms, the Kalman algorithm begins with predicting state using the dynamic model of the system evaluated at the previous time t_{k-1} using Equation 2.73, calculates the predicted state error variance $\hat{P}$ using the previous state error covariance matrix and the expected state estimation noise with Equation 2.74, computes the Kalman gain based on how noisy the expected measurement noise is by Equation 2.75, places a weighting factor on the reliability the sensor measurement, and finally updates the estimated error covariance matrix. Intuitively, the higher the Kalman gain, the more reliable the sensor measurements are as the noise in measurement R is inversely proportional to K.

2.5.3.6 Steady State Linear Kalman Filter

When applying the Kalman filter on an encoder signal output, the measurement errors Q and R can be regarded as constant if the sampling period and the ppr are fixed [165]. Since the computation of the Kalman gain relies on the error covariances Q and R, the Kalman gain can also be regarded as constant. Therefore, the Kalman filter algorithm can be simplified by omitting Equation 2.74, 2.75 and 2.77 from the classical Kalman. The resulting recursive equations are called the Steady State Linear Kalman filter (SSLKF).

The encoder measurement SSLKF used for this thesis was designed based on the research paper reference in [160], which expresses the SSLKF as a two step process:

$$x_{pred}(t) = A\, x_{est}(t-1) + B\, a_i \tag{2.78}$$

$$x_{est}(t) = x_{pred}(t) + g \cdot (\, \theta_{enc}(t) - C x_{pred}(t)\,) \tag{2.79}$$

Where
- x_{pred} is the predicted mechanical states vector
- t is the sample time
- A is the matrix modeling the dynamics of the states (system matrix)
- x_{est} is the state estimate vector (SSLKF output)
- B is the dynamic system input vector
- a_i is the initial guess of the dynamic input acceleration
- C is the state feedback input vector
- g is the Kalman gain vector
- θ_{enc} is a single encoder measured position value (SSLKF input)

Expressing in matrix form:

$$x_{pred} = \begin{bmatrix} \theta \\ \omega \\ \alpha_{error} \end{bmatrix} \qquad x_{est} = \begin{bmatrix} \theta \\ \omega \\ \alpha_{error} \end{bmatrix}$$

$$A = \begin{bmatrix} 1 & T_s & \frac{T_s^2}{2} \\ 0 & 1 & T_s \\ 0 & 0 & 1 \end{bmatrix} \qquad B = \begin{bmatrix} \frac{T_s^2}{2} \\ T_s \\ 0 \end{bmatrix} \qquad C = \begin{bmatrix} 1 \\ 0 \\ 0 \end{bmatrix} \qquad g = \begin{bmatrix} g_1 \\ g_2 \\ g_3 \end{bmatrix}$$

Equation 2.78 is the discrete representation of the rotational kinematic equation and the vector C provides the position input feedback. The SSLKF acceleration estimation is:

$$\alpha_{est} = \alpha_{error} + a_i \tag{2.80}$$

The Kalman gain vector g is computed by the sequence of steps expressed by Equations 2.81 to 2.92:

$$\rho_0 = exp(-p_0\, T_s) \tag{2.81}$$

$$\rho_1 = exp(-\mathrm{w}\, Ts\, cos(\phi)) \tag{2.82}$$

$$\varphi = \mathrm{w}\, T_s\, sin(\phi) \tag{2.83}$$

$$c_0 = -\rho_0\, \rho_1^2 \tag{2.84}$$

$$c_1 = \rho_1\, (2\rho_0\, cos(\varphi) + \rho_1) \tag{2.85}$$

$$c_2 = -2\, \rho_1\, cos(\varphi) - \rho_0 \tag{2.86}$$

$$l_1 = c_2 + 3 \tag{2.87}$$

$$l_2 = \frac{c_1 - c_0 - 4 + 3l_1}{2T_s} \tag{2.88}$$

$$l_3 = \frac{c_1 + c_0 - 2 + l_1}{T_s^2} \tag{2.89}$$

$$g_3 = l_3 \tag{2.90}$$

$$g_2 = l_2 - T_s\, g_3 \tag{2.91}$$

$$g_1 = l_1 - T_s\, g_2 - g_3\, \frac{T_s^2}{2} \tag{2.92}$$

The parameters p_0 is the negative real pole, w is the magnitude of the complex poles, and ϕ is the angle (in radians) of complex poles in the continuous time SSLFKF algorithm;

while T_s is the sampling period of the encoder signal.

2.5.3.7 Signal to Noise Ratio

Acceleration measurement is a process variable which is prone to noise pollution, as numerical differentiation is commonly employed when acceleration cannot be measured directly by an accelerometer. It is well known that the rapid magnitude change from noisy feedback measurements degrades process performance, particularly when the derivative control is employed. The method of assessing the filter performance, on top of the standard frequency response and phase shift, has been chosen to be the signal to noise ratio (SNR) given by the following expression [166]:

$$SNR = 10 \log_{10} \left(\frac{\mathrm{E}[(Y_i^2)]}{\mathrm{E}[(Y_i - X_i)^2]} \right) \tag{2.93}$$

Where	SNR	signal to noise ratio	(dB)
	E	is the expected value	
	Y	is the array of fundamental signal	
	X	is the array of noisy signals	
	i	denotes the sample time at i	

2.5.3.8 Voltage Magnitude Measurement

Prior to commanding the closure of circuit breaker, the controller must be able to ensure the generator RMS voltage matches the RMS EPS voltage. The RMS calculation is commonly performed digitally using the following equation:

$$V_{rms} = \sqrt{\frac{1}{N} \sum_{i=1}^{N} V_i^2} \tag{2.94}$$

Where	N	is the number of samples in the window	(dB)
	v_i	is the voltage taken at the sample i	

The measurement accuracy using Equation 2.94 depends on the sample frequency, the number of samples (window size), and the input signal frequency. A common window size for power system RMS measurements is at least one cycle of the EPS fundamental frequency [167] [168]. A sample window which is not an integer multiple of half of the

fundamental period is called incoherent sampling, which leads to measurement error due to spectral leakage [169] [170].

Because the measurement accuracy is strongly dependent on the fundamental frequency of the input signal, using the conventional algorithm with a fixed window width to measure the CGESS generator RMS voltage during the synchronization control period will result in measurement error due to the increasing generator frequency. Fortunately, solving the RMS measurement accuracy problem with signals containing frequency and voltage variations is not novel [171]. The most common and simple way of improving the RMS measurement accuracy of a frequency varying signal are using window function [170] [172] [173] [174]. The popular window functions are Hann, Hammming and Blackman windows. Furthermore, Kalman Filtering [175], quadrature sampling [176], double subset sampling [177], varying sample window [178] and non-coherent windowing [179] are novel methods designed to measure the RMS of frequency varying EPS voltages. In this thesis, the RMS measurement accuracies are investigated using various conventional windowing methods.

Chapter 3

Instrumentation and Signal Processing

3.1 Chapter Structure

The proposed CGESS controller achieves its synchronisation control strategy by taking the EPS frequency/phase measurements and attempts to match the equivalent generator quantities through regulating the drive acceleration. To meet the control objective, the measurement accuracy must be maximized and the delay must be minimized. This chapter documents the definition of measurement performance, the methodologies used to process the signals produced from their respective measurement devices, and details the hardware selection validation process.

3.2 EPS Instrumentation Model and Design

3.2.1 Introduction

As mentioned in the Section 2.5.2.3, a three phase qPLL depicted in Figure 2.25 is used to measure the frequency and phase of the distorted EPS voltage during the FIR demand period. As synchronous frame based PLLs are susceptible to EPS nonidealities, this section defines the performance requirements, outlines the design process, and specifies the sampling hardware required to facilitate robust synchronisation control.

3.2.2 Performance Criteria

The PLL design accuracy requirements are referenced from the off-the-shelf Alstom [180], Basler [181] and ABB [182] sync. check relays. Their specified phase, frequency and voltage accuracies are tabulated in Table 3.1.

TABLE 3.1: Comparing Recommended Synchronization Criteria with Desired EPS Measurement Accuracy

Parameters	IEEE and Datasheet Synchronisation Recommendation	Sync.Check Relay Accuracies	PLL Measurement Accuracy Requirement
Phase angle	15^o	$0.5^o - 2^o$	1^o
Frequency	0.3Hz	0.01Hz	0.01Hz
Voltage	8V	4V - 40V	0.4V

It is necessary to design a fast and accurate PLL that is capable of measuring the phase and frequency quantities with the accuracy specified in Table 3.1 while operating with the EPS voltage that has the characteristics typically observed in under-frequency events outlined in Section 2.3. In addition, the PLL must be able to ride through faults without losing synchronism.

3.2.3 PLL Design

The conventional PLL input is a ramped phase quantity that is increasing at rate of signal frequency. According to Section 2.4.6, an uncontrolled PLL shown in Figure 2.24 has a constant steady state error when the input signal frequency is fixed due to its integrator (type 1 system). Since a constant EPS frequency ramp is a step deceleration to the PLL input, a minimum of 2 integrators must be presented in the PLL open loop transfer function to establish a constant steady state error during the EPS frequency ramp. Although a type 3 PLL can eliminate the ramp error completely, the stability margins of a type 3 PLL are often compromised such that the PLL may become unstable if the EPS voltage magnitudes are sagging severely [183] [147]. Hence, only one integrator was introduced to the PLL controller structure as a type 2 system is immune to input magnitude dip.

Using Table 2.8, the error expression for a type 2 system experiencing steady acceleration α is:

$$E_{ss} = \frac{\Delta\alpha}{K_{dc}} \tag{3.1}$$

The open loop DC gain K_{dc} can be derived to ensure a constant phase tracking error given a step acceleration input. By substitute the phase angle measurement accuracy requirement of 0.01745 rad (1^o) and a typical EPS frequency ramp of -1.4 Hz/s into 3.1, the minimum PLL open loop DC gain is:

$$K_{dc} = \frac{2\pi \cdot (1.4)}{0.01745} = 504.1 \tag{3.2}$$

From Table 2.9, the qPLL frequency and phase output suffer from oscillations centered at distinct frequencies during disturbances. Using the standard notch transfer function given by Equation 2.62 with a Q factor of 2, a chain of notch filters was designed to reduce the effect of the EPS nonidealities. These notch filters are expressed by Equation 3.3 to 3.6:

$$H_{n50Hz}(s) = \frac{s^2 + 9.87 \times 10^4}{s^2 + 628.3s + 9.87 \times 10^4} \tag{3.3}$$

$$H_{n100Hz}(s) = \frac{s^2 + 3.948 \times 10^5}{s^2 + 1257s + 3.948 \times 10^5} \tag{3.4}$$

$$H_{n150Hz}(s) = \frac{s^2 + 8.883 \times 10^5}{s^2 + 1885s + 8.883 \times 10^5} \tag{3.5}$$

$$H_{n300Hz}(s) = \frac{s^2 + 3.553 \times 10^6}{s^2 + 3770s + 3.553 \times 10^6} \tag{3.6}$$

Thus, the filtering element seen in Figure 2.26 is defined by:

$$F(s) = H_{n50Hz}(s) \cdot H_{n100Hz}(s) \cdot H_{n150Hz}(s) \cdot H_{n300Hz}(s) \tag{3.7}$$

Combining the notch filter chain, DC gain, controller integrator and oscillator integrator, the PLL open loop transfer function is:

$$\begin{aligned} H_{op}(s) &= \frac{K_{dc}}{s} \cdot F(s) \cdot \frac{1}{s} \\ &= \frac{a_1\, s^8 + a_2\, s^6 + a_3\, s^4 + a_4\, s^2 + a_5}{s^{10} + b_1\, s^9 + b_2\, s^8 + b_3\, s^7 + b_4\, s^6 + b_5\, s^5 + b_6\, s^4 + b_7\, s^3 + b_8\, s^2} \end{aligned} \tag{3.8}$$

where

$$\begin{bmatrix} a_1 \\ a_2 \\ a_3 \\ a_4 \\ a_5 \end{bmatrix} = \begin{bmatrix} 505 \\ 2.492 \times 10^9 \\ 2.72 \times 10^{15} \\ 8.739 \times 10^{20} \\ 6.21 \times 10^{25} \end{bmatrix} \qquad \begin{bmatrix} b_1 \\ b_2 \\ b_3 \\ b_4 \\ b_5 \\ b_6 \\ b_7 \\ b_8 \end{bmatrix} = \begin{bmatrix} 7540 \\ 2.349 \times 10^7 \\ 3.944 \times 10^{10} \\ 3.905 \times 10^{13} \\ 2.336 \times 10^{16} \\ 8.237 \times 10^{18} \\ 1.566 \times 10^{21} \\ 1.23 \times 10^{23} \end{bmatrix}$$

Having defined the open loop transfer function, the controller can be designed using MATLAB's SISO Design Tool. The specified performance criteria for the PLL are:

1. The PLL must settle within 200ms, which is half of the time taken for the CGESS to reach synchronisation speed at maximum acceleration
2. When tested with the most severe frequency decay and voltage disturbances, the PLL must reach steady state tracking errors that has a maximum oscillation value below the specified measurement accuracies
3. The PLL phase margin must be in the range of $30^o - 60^o$ according to industrial control design standards

The uncompensated open loop root locus and Bode plots are shown in Figure 3.1, which indicate that the system is unstable. For the closed loop PLL to reach steady state within the specified 0.2s settling time, the open loop roots (denote by the pink markers in Figure 3.1) has to be to the left of the yellow shaded area. As root locus DC gain cannot be less than 1, it is not possible to bring one of the largest roots further to the left by scaling the DC gain alone.

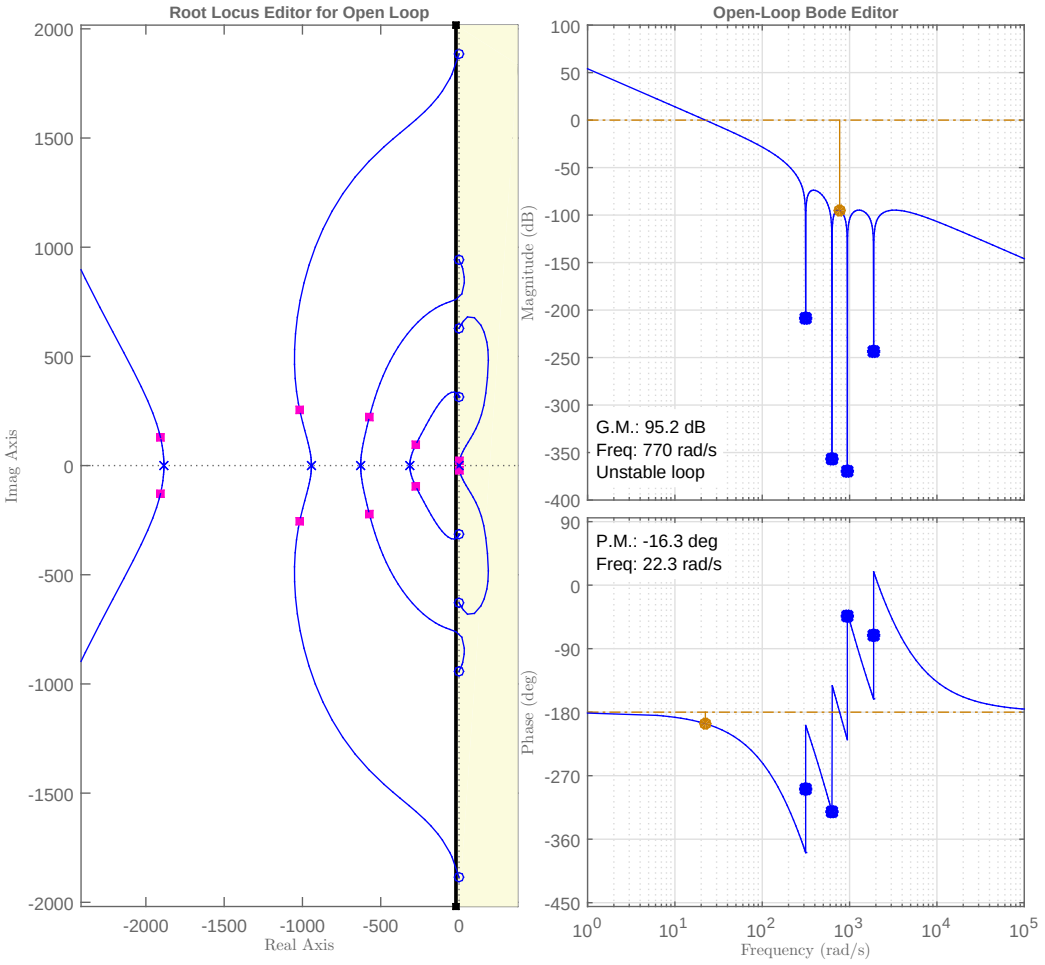

FIGURE 3.1: Uncompensated PLL open loop root locus and bode plot

The closed loop step response performance was improved by adding a zero at -15.5 and doubling the DC gain. Combining the controller integrator with a zero, C(s) in Figure 2.26 is:

$$C(s) = 504.1 \cdot 2 \cdot (0.06 + \frac{1}{s}) \tag{3.9}$$

Figure 3.2 shows that the controller meets the phase margin criteria, and Figure 3.3 shows the PLL is able to respond to a step input and settling within 200ms.

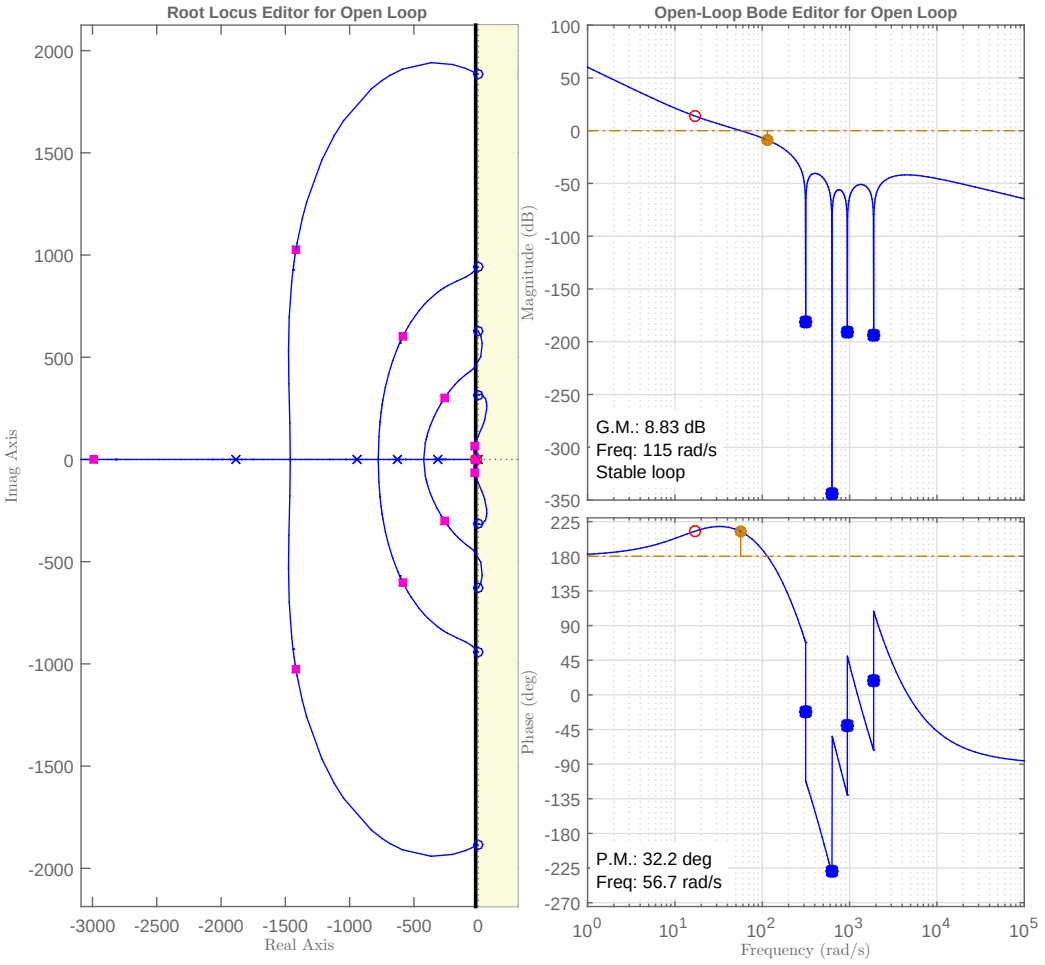

FIGURE 3.2: Controlled PLL system root locus and bode plot

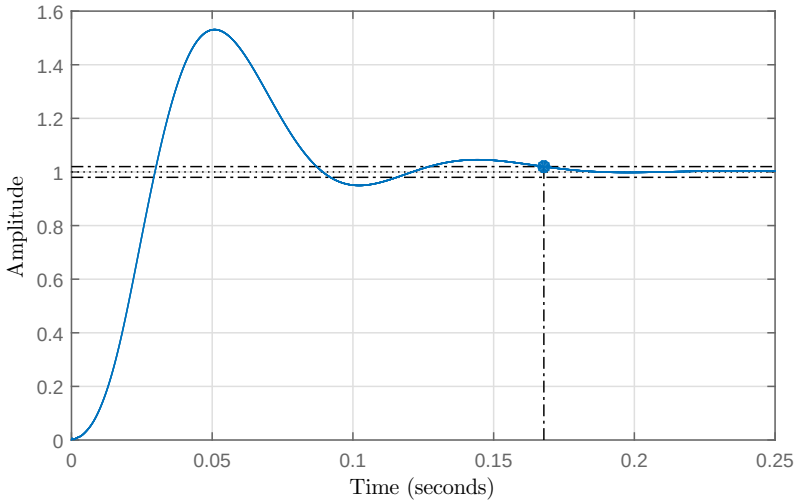

FIGURE 3.3: Closed loop PLL step response (overshoot = 53% at 0.05s) from a step phase input

To test tracking errors of the linearized PLL with the frequency steadily decreasing, the transfer functions was arranged according to Figure 3.4 and an acceleration input of 1Hz/s ($\Delta\alpha = 2\pi rad/s^2$) was applied. The time domain plots of the phase tracking error $\theta_e(s)$ and the frequency tracking error $\omega_e(s)$ are shown in Figures 3.5 and 3.6.

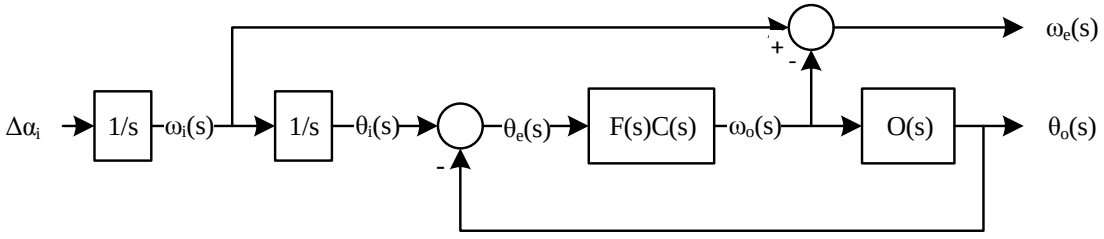

FIGURE 3.4: PLL structure used to test measurement errors from an acceleration step input

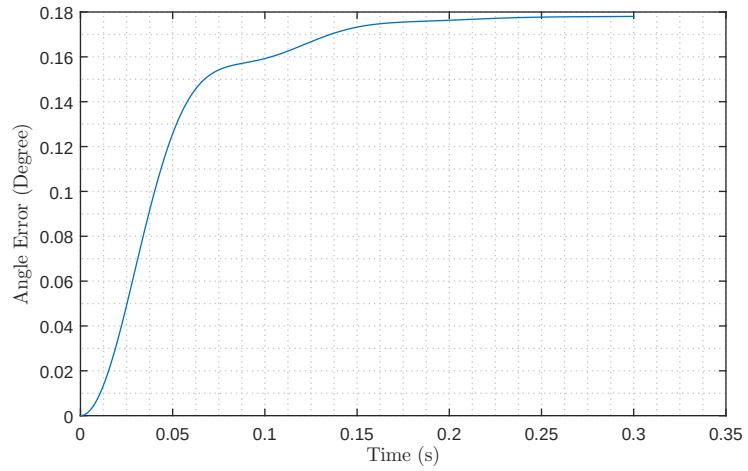

FIGURE 3.5: Phase tracking error due to acceleration step of 1Hz/s

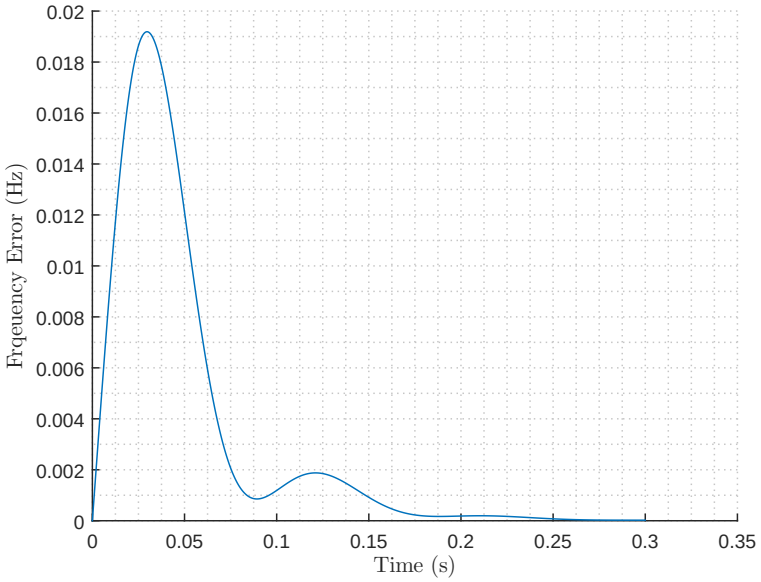

FIGURE 3.6: Frequency tracking error due to acceleration step of 1Hz/s

Figures 3.5 and 3.6 show the phase tracking error is always within 1^o and the frequency tracking error is within 0.01Hz after 70ms. Both steady state values are within the performance criteria specified by Table 3.1.

3.2.4 PLL Simulink Model

Figure 3.7 is the MATLAB Simulink model used to evaluated the performances qPLL under disturbed three phase EPS voltages. The upper and lower frequency saturation limits were set to 65Hz and 35Hz to avoid locking onto higher order harmonic frequencies,

which is a common problem to PLLs [184]. The implemented ABC to $\alpha\beta$ transformation, EPS distortion, and notch filter chain blocks are depicted by Figures 3.8, 3.9 and 3.10.

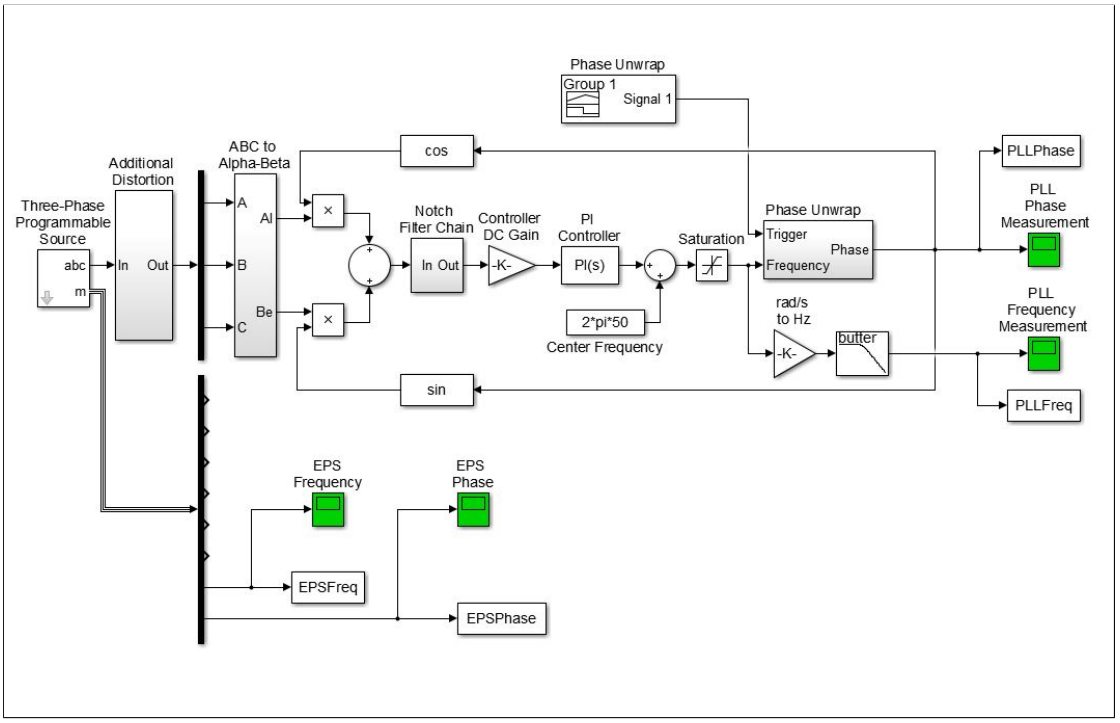

FIGURE 3.7: PLL Simulink model

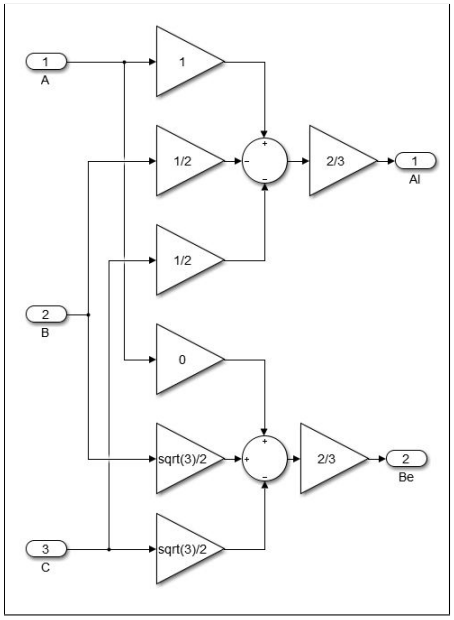

FIGURE 3.8: ABC to $\alpha\beta$ transformation block

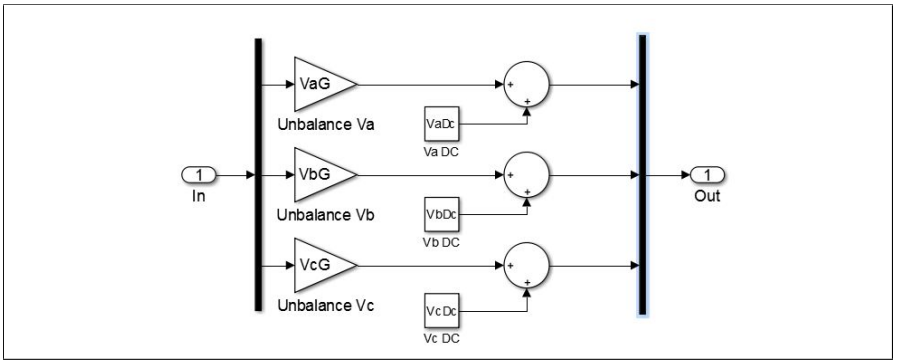

FIGURE 3.9: EPS voltage distortion block

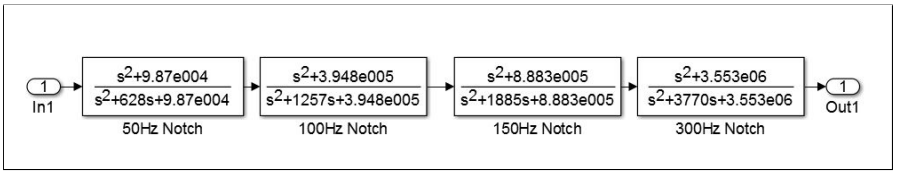

FIGURE 3.10: PLL notch filter chain block

As the initial expected operating EPS phase angles range between 0 to 2π, the PLL output is regulated by a phase reset mechanism which wraps the integrator to zero when the output exceeds 2π. Only when the FIR demand begins will the integrator be allowed to produces a continuous EPS trajectory for generator phase to target. Figure 3.11 depicts the phase unwrap mechanism.

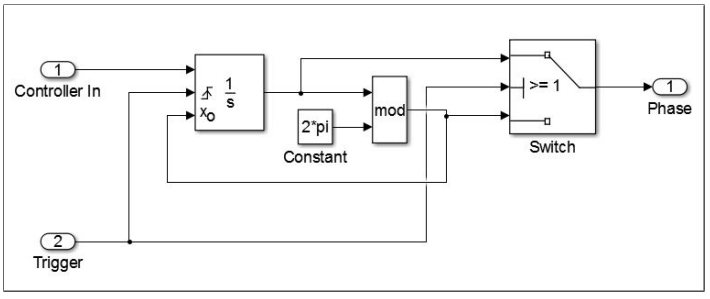

FIGURE 3.11: PLL phase unwrap mechanism block

3.2.5 Ideal EPS Voltages

The phase locked loop was designed to synchronize to the steady state EPS voltages indefinitely and is independent of the FIR demand signal. The PLL frequency and phase measurements compared with the actual generated values are shown in Figure 3.12 and 3.13, which show a synchronisation time of 120ms.

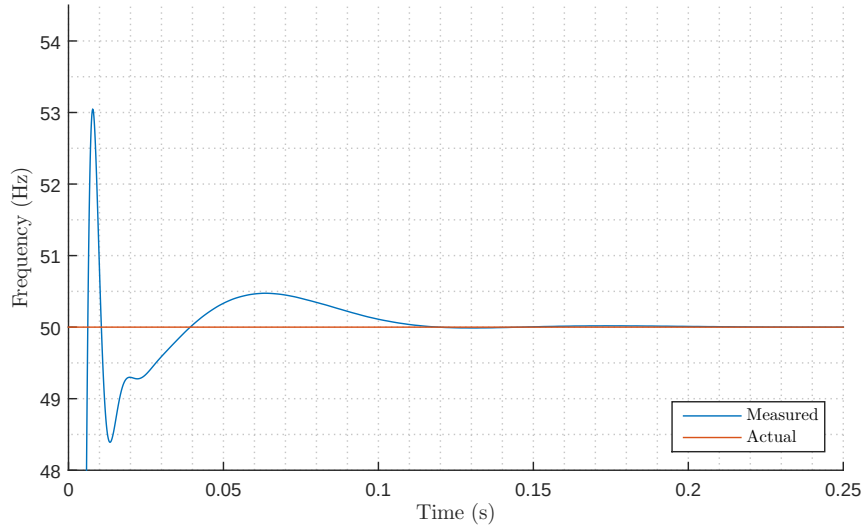

FIGURE 3.12: PLL frequency measurement during start up

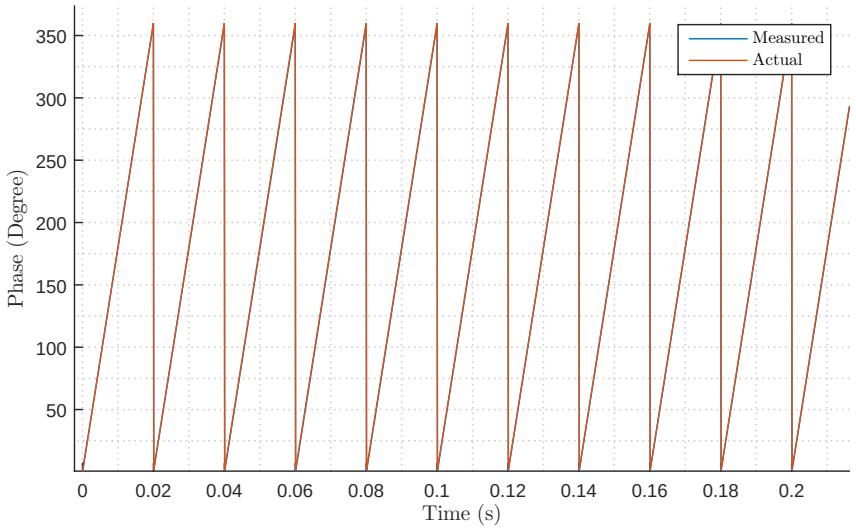

FIGURE 3.13: PLL phase measurement during start up

The time taken to synchronize the PLL to the EPS depends on the difference between the PLL output phase and the EPS phase at the instant the PLL is switched on. Due to the nonlinear PLL $\sin(\theta_e)$ error term, the control loop may become unstable for some start-up phase error values. It is necessary to ensure successful PLL to EPS synchronisation at all the possible given initial grid phase angles.

Figure 3.14 and Figure 3.15 are phase and frequency error plots obtained from varying the initial EPS phase angles while the PLL start-up oscillator output was set to 0. The results show that the PLL is able to synchronize with adequate stability. The settling times is shown to be varying between 0ms to 0.2ms.

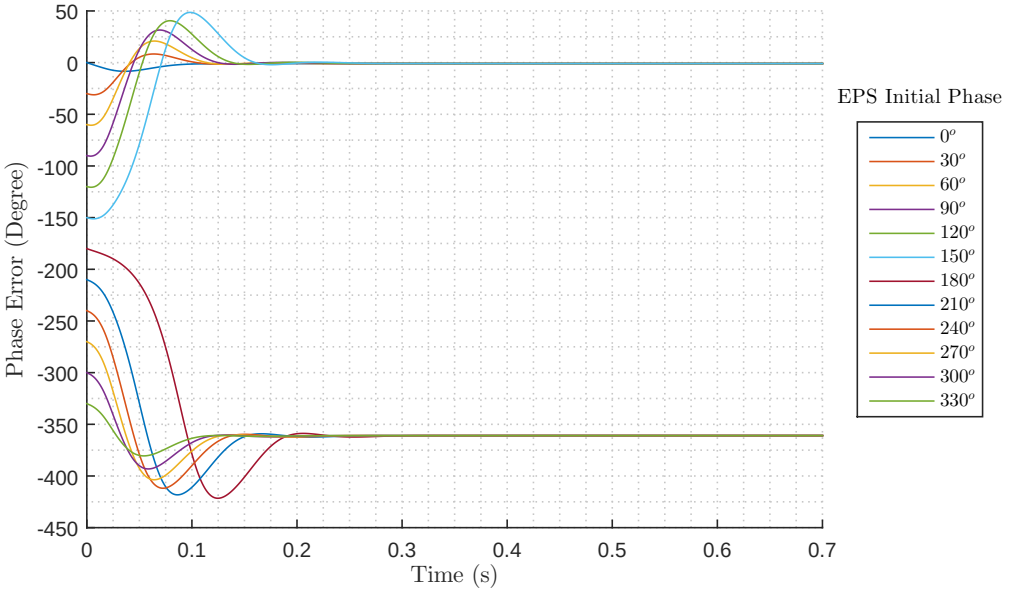

FIGURE 3.14: PLL start up phase measurement error with varying initial phases

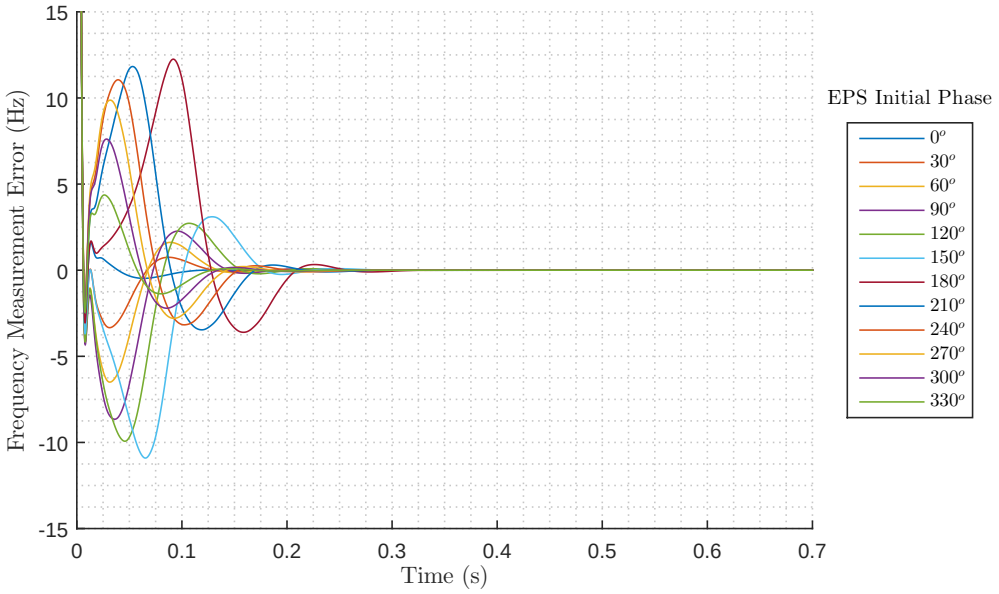

FIGURE 3.15: PLL start up frequency measurement error with varying initial phases

3.2.6 Ideal EPS Voltages with Frequency Ramp

As the PLL will only be operating at steady state, the speed at which the PLL locks onto the EPS during start up is not an appropriate benchmark of performance. Once the PLL has reached steady state, a decrease at a rate of -1.2Hz/s was applied. The

PLL frequency and phase angle measurements v.s. the generated parameters are shown in Figure 3.16 and Figure 3.17.

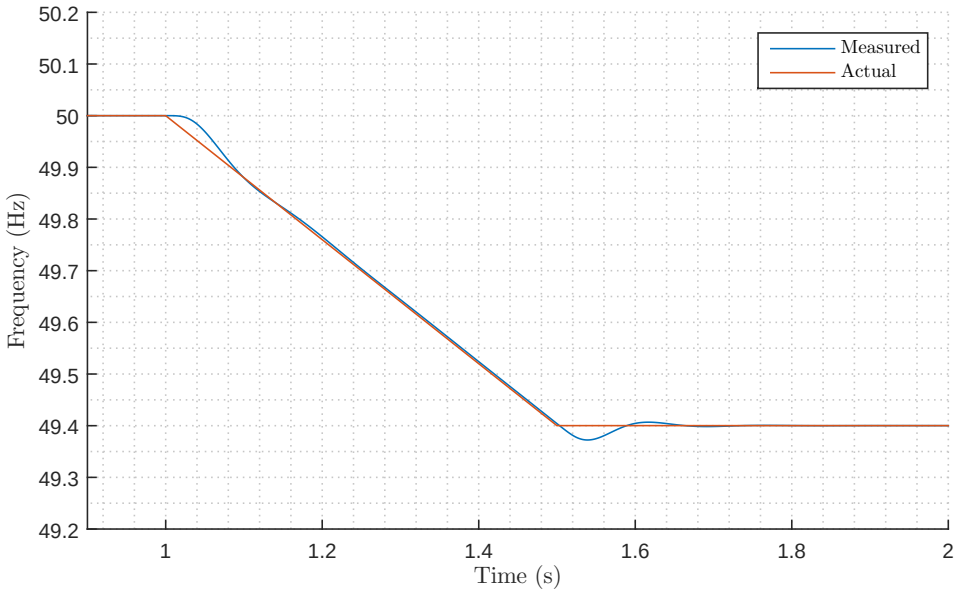

FIGURE 3.16: PLL measured frequency v.s. actual frequency during EPS frequency ramp of -1.2Hz/s

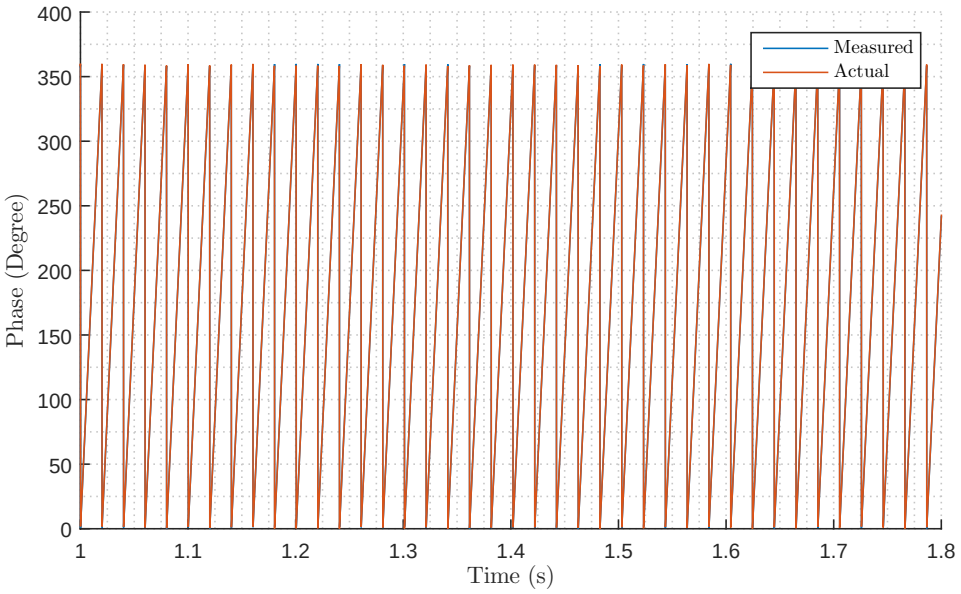

FIGURE 3.17: PLL measured phase angle v.s. actual phase angle during EPS frequency ramp of -1.2Hz/s

Frequency ramps with varying severity were used to test the PLL frequency measurement performance during under frequency events. The RoCoF values ranged between 0 and -2Hz/s, which is the worst predicted RoCoF value according to the Transpower

AUFLS scheme design technical summary [63]. The errors between measured and actual quantities can be seen in Figures 3.18 and 3.19.

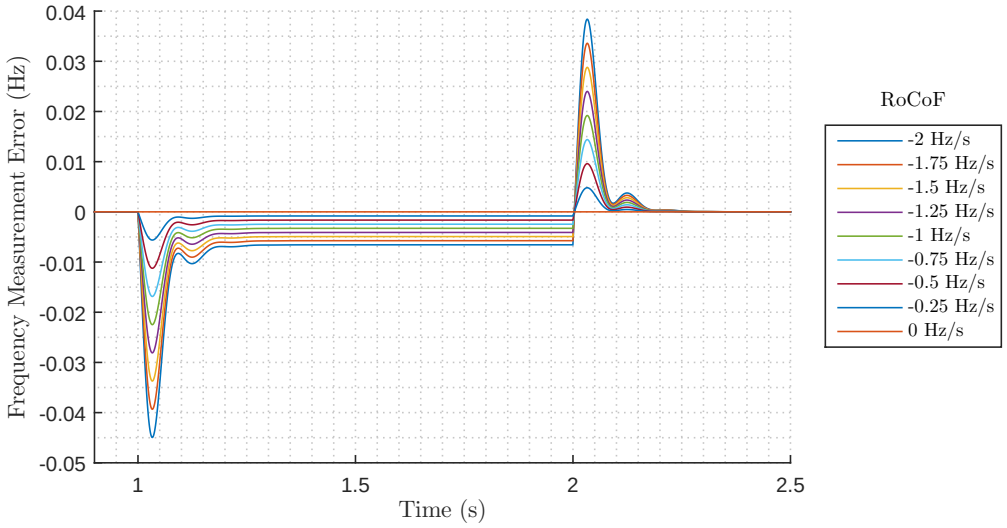

FIGURE 3.18: PLL Frequency measurement error during frequency decay with no distortion

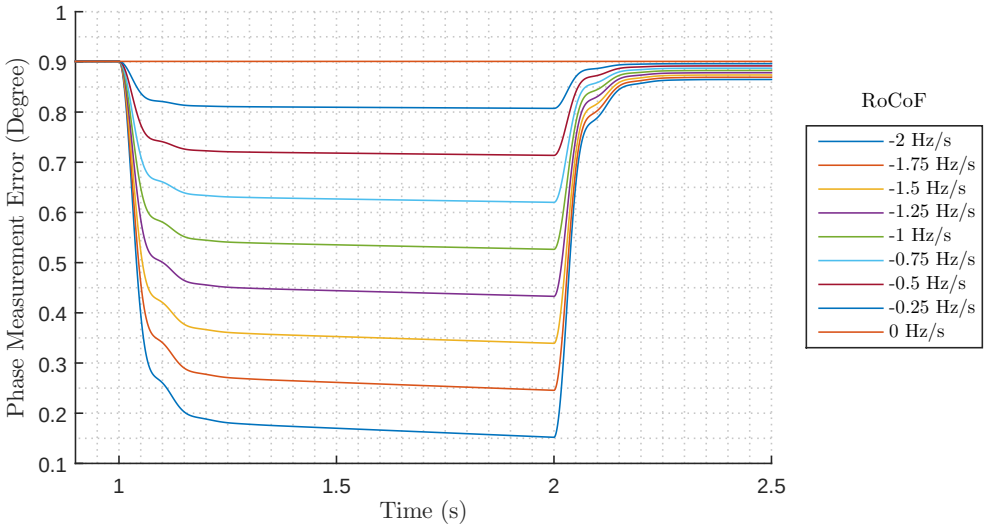

FIGURE 3.19: PLL phase measurement error during frequency decay with no distortion

Figure 3.18 shows that the steady state frequency tracking error obtained from even the most severe RoCoF ramp will be within the 0.01Hz measurement accuracy specified by Table 3.1 after 70ms. The phase angle measurement accuracy in Figure 3.19 also demonstrated that the phase angle measurement error is within the $\pm 1^o$ given by Table 3.1.

3.2.7 Distorted EPS Voltages with Frequency Ramp

In this section, the PLL phase and frequency tracking abilities are tested with severely distorted EPS voltages. The distortion includes harmonics, voltage unbalances and DC offsets as outlined in Sections 2.3.5. The disturbance types and their characteristics are illustrated by Table 3.2, and the consequent EPS voltages are depicted by Figure 3.20. Figures 3.21 and 3.22 shows the PLL measurement errors when given various EPS RoCoF for an duration of 1 second.

TABLE 3.2: EPS voltage non ideal characteristics parameters and values

Phase	Harmonics	Voltage magnitude scale	DC (p.u.)
A	5% 5^{th}, 5% 7^{th}	0.95	-0.03
B	5% 5^{th}, 5% 7^{th}	0.9	0
C	5% 5^{th}, 5% 7^{th}	0.92	0.03

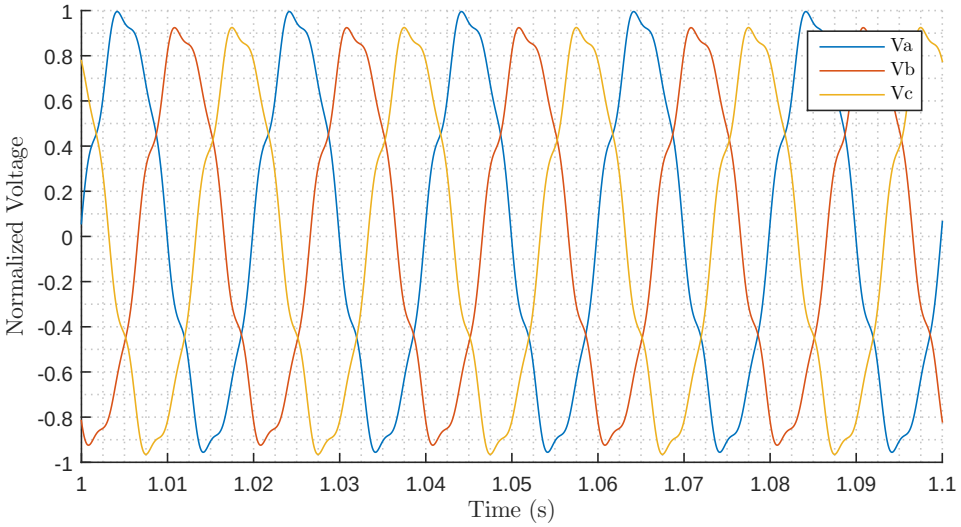

FIGURE 3.20: Distorted EPS voltages (normalized to 1 with $V_n = sqrt(2)400$)

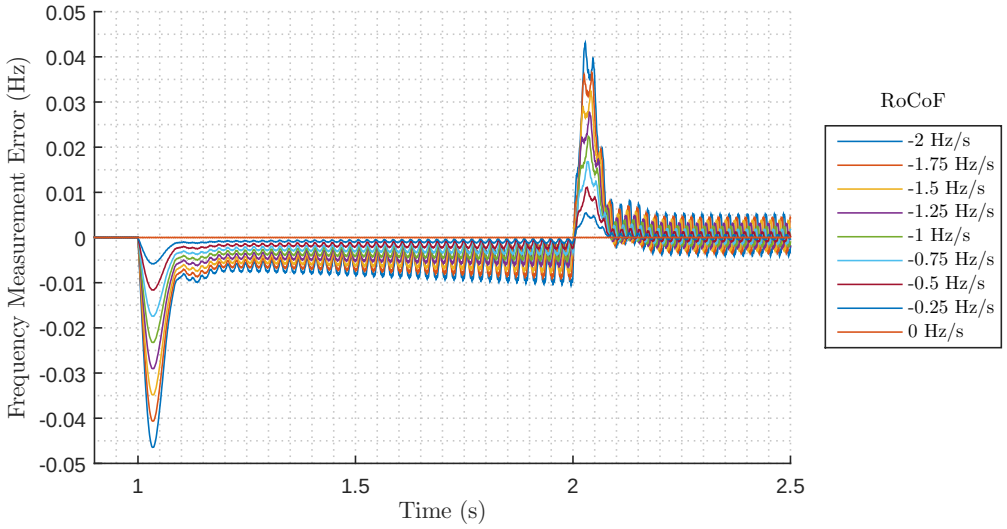

FIGURE 3.21: Frequency measurement error obtained with distorted EPS voltages

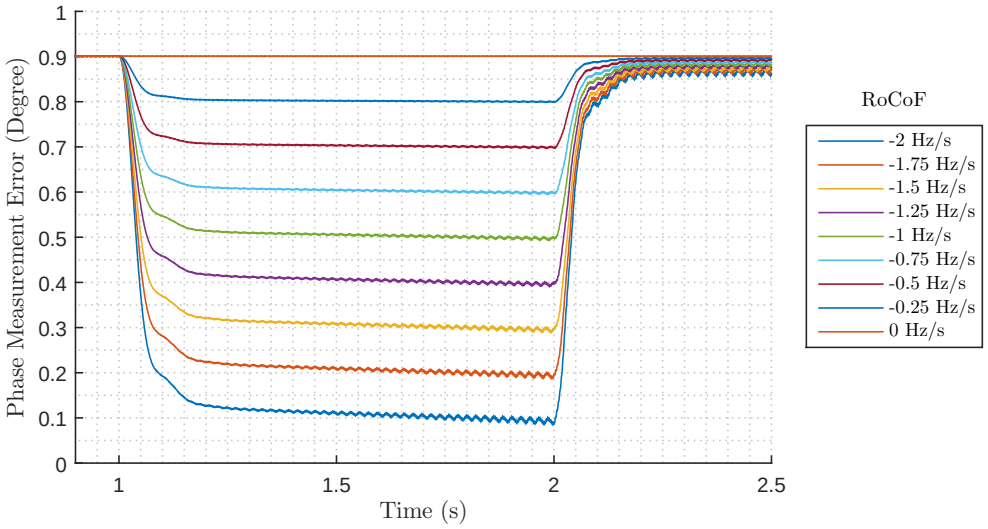

FIGURE 3.22: Phase measurement error obtained with distorted EPS voltages

Figure 3.21 revealed that the frequency tracking oscillation magnitude is more prominent at lower EPS frequencies, which is due to the oscillations moving further away from the notch filter stop band frequencies. Regardless, Figures 3.22 and 3.21 demonstrate that the PLL is able to track the phase angle and frequency with a satisfactory accuracy even if the EPS is severely distorted.

3.2.8 Fault Ride Through Capability

Park transformation based PLL algorithms are susceptible to asymmetrical EPS voltages. While the CGESS is not required to synchronize to the EPS during faulted conditions, the PLL must be able to recover from the voltage sags. Figure 3.23 depicts the three phase EPS voltages which is suffering from a type C voltage sag, whose characteristics is shown in Table 3.3.

TABLE 3.3: EPS type C voltage dip characteristics

Phase	Voltage magnitude (p.u.)	Phase shift (degree)
A	0.5	-35
B	0.5	35
C	1	0

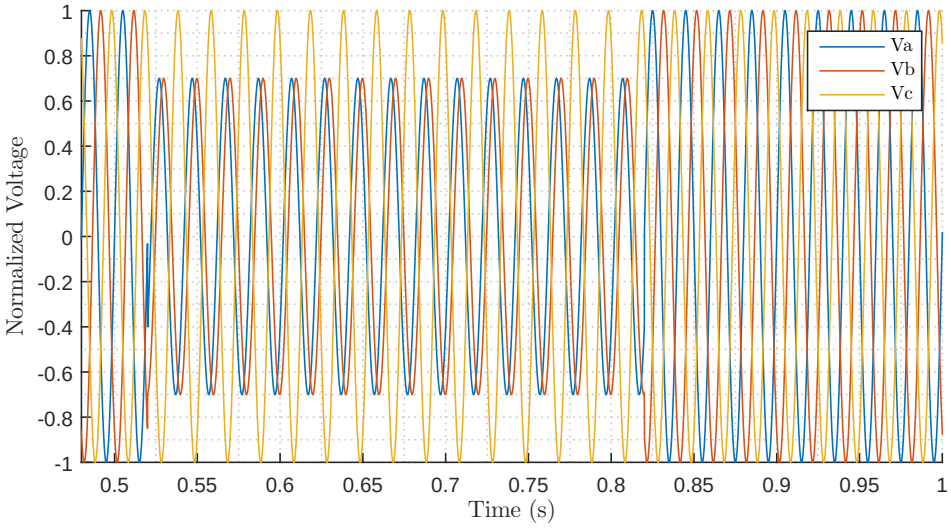

FIGURE 3.23: Type C voltage dip on EPS voltages (normalized to 1 with $V_n = sqrt(2)400$)

As the rate at which the PLL recovers from the fault depends on the initial EPS phase angle at the instant when the fault occurs and clears, the frequency and phase measurement errors can be plotted with various initial phase angles to investigate the post-fault PLL stability. The measurement errors are shown in Figures 3.24 and 3.25.

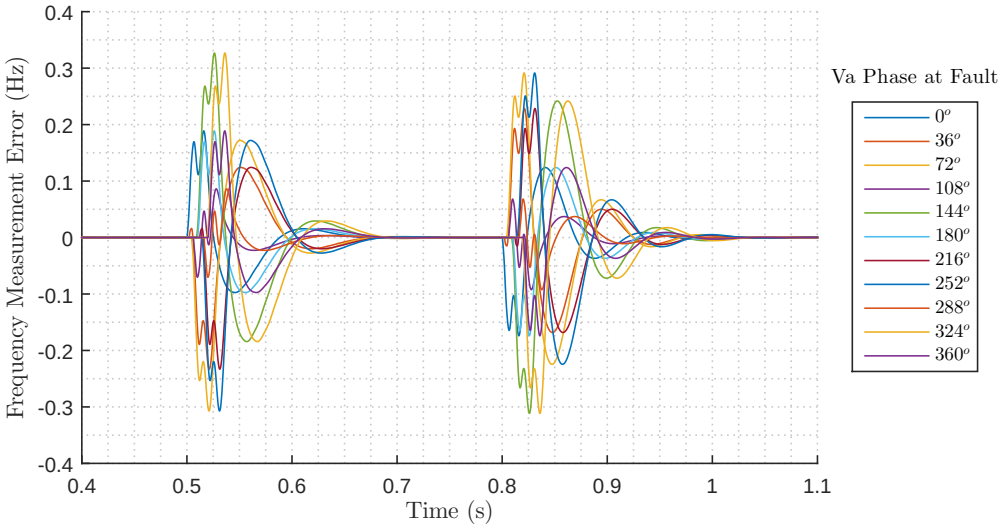

FIGURE 3.24: Frequency measurement transient error obtained from EPS temporary phase to phase fault

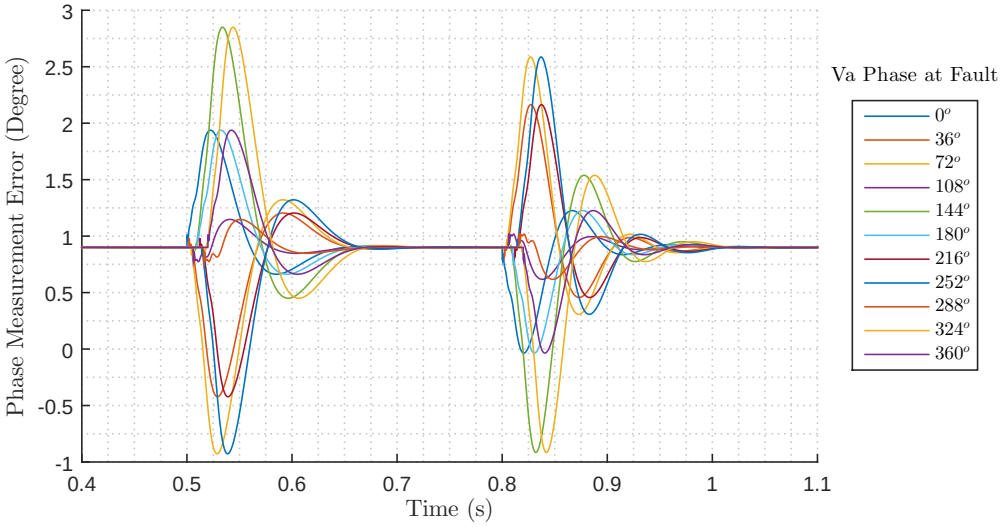

FIGURE 3.25: Phase measurement transient error obtained from EPS temporary phase to phase fault

Figures 3.25 and 3.25 indicated that the PLL is capable of recovering from the voltage sags and measure the EPS quantities with acceptable accuracies after 190ms. Figures 3.25 also demonstrated that although phase A has been phase shifted, the PLL is capable of tracking pre-fault phase angle.

3.2.9 Sample Rate Specification

The sample rate of the PLL hardware is set to 20kHz, which is the same value as the generator instrumentation sample rate, which is justified in Section 3.3.2.

3.2.10 Hardware Specification

The voltage amplitude measurement accuracy is set by the hardware DAC resolution. Considering the peak value of the rated 400Vrms generator terminal voltage, positive and negative swing of AC cycle and a reasonably selected 20% margin, the instantaneous generator voltage range could span up to 1358V. In order to provide the voltage measurements with 0.4V accuracy as seen in Table 3.1, the hardware resolution must have at least:

$$\frac{1358}{0.4} = 3395 \quad \text{discrete levels}$$

which corresponds to a minimum requirement of 12 bits. The NI-9215 analog input module is chosen based on the resolution, capability of measuring negative voltages, simultaneous sampling type and adequate sample rate. The module also offers differential sampling if generator step up transformer neutral cannot be accessed due to the delta configuration. The relevant module specification is shown in table 3.4

TABLE 3.4: NI-9215 analog input module specification

Field	Value
Channels	4
Channel type	Differential
Resolution	16 bit
Measurement range	$\pm 10V$
Sample rate	100kS/s
Sample type	Simultaneous

The EPS voltages were to be stepped down by resistive network instead of a conventional voltage transformer (VT). Although resister dividers lack the over-voltage protection VTs offer during core saturation, zero phase delay can be guaranteed with resistive dividers.

3.3 Generator Instrumentation Model and Design

3.3.1 Introduction

Fast and accurate generator parameter measurement is necessary to ensure the robustness of the feedback control system and the appropriate triggering of the breaker closure signal. This section justifies the need for building a custom automatic synchronisation algorithm, outlines the MATLAB simulated instrumentation signal outputs, and the signal processing methodologies employed to meet the specified measurement performance criteria.

As the exact rotor pole face position is difficult to measure, the rotor position relationship with the generator phase A voltage is intended to be calibrated with software. The generator is firstly be spun up to synchronous speed and the steady state terminal voltage phase is measured by an conventional phase locked loop; then the error between the rotor position and voltage phase can be zeroed.

3.3.2 Generator Measurement Sample Rate Determination

As established in the background section, a faster sample rate grants a better reconstruction of a signal but results in an increase in quantization error. To meet the measurement signal to noise ratio criteria using the highly quantized measurements, additional filtering may further degrade the measurement dynamics through the time delays. Hence, determining the appropriate sampling rate is necessary to avoid excessive cost on the hardware.

For control system requirement, the sample rate has be at minimum 10 times the control system bandwidth [99], which is 10Hz in Chapter 5. This control bandwidth suggests that the minimum sample rate must exceed 100Hz.

From a synchronization signal generation point of view, the proposed acceleration control scheme is unlike a typical synchronization strategy, where the generator is first controlled exhibit a constant low slip frequency and subsequently synchronized to the grid with either an automatic synchronizing system or synchronism check relay [93]. Considering that at maximum acceleration of 400 rad/s^2, the CGESS generator rotor frequency traverses the acceptable synchronisation frequency difference range of $\pm$0.3Hz in 4.7ms, the filtering applied to the frequency measurements in an typical off-the-shelf automatic synchronization device will not meet our performance standard. Sync-check relays from Alstom [180], Basler [181] and ABB [182] datasheet have demonstrated frequency delays exceeding 10ms, which is above our minimum measurement delay. These reasons

provides an incentive to develop an auto-synchronization algorithm, which demands an accurate measurement of the generator frequency and phase parameters.

Borrowing from [180], [181] and [182], where the phase, frequency and voltage resolutions ranged between $0.5^o - 2^o$, 0.01Hz and $0.1\% - 1\%$ of nominal voltage, the CGESS generator measurement algorithm accuracy requirement can be defined by Table 3.5.

TABLE 3.5: Comparing Synchronization Recommendation with Desired Generator Measurement Resolution

Parameter	IEEE and Datasheet Requirement	Electrical Measurement Accuracy Requirement	Mechanical Measurement Accuracy Requirement
Phase angle	15^o	1^o	0.5^o
Frequency	0.3Hz	0.01Hz	0.005 rev/s
Voltage	8V	0.4V	0.4 V

As specified by Table 3.5, the sample rate must be sufficiently high such that a 0.5^o change in mechanical phase angle can be detected. Using the sample rate calculation expressed by:

$$F_s = \frac{\text{Degree travelled per second}}{\text{Required degree resolution}} \tag{3.10}$$

the minimum sample rate is:

$$F_s > \frac{25\,\text{revolution}}{\text{second}} \cdot \frac{360^o}{\text{revolution}} \Big/ \frac{0.5^o}{\text{sample}} = 18,000\,\frac{\text{sample}}{\text{second}} \tag{3.11}$$

Similarly, the speed resolution also dictates the minimum the sample rate, and Equation 5.2.7 was developed:

$$F_s = \frac{\text{Revolutions travelled per second}}{\text{Required speed resolution}} \tag{3.12}$$

Using the maximum generator acceleration of 400rad/s^2, the sample rate required to meet the measured speed resolution is:

$$F_s > \frac{400}{2\pi} \frac{\text{revolution}}{\text{second} \cdot \text{second}} \Big/ \frac{0.005\,\text{revolution}}{\text{second} \cdot \text{sample}} = 12,732\,\frac{\text{sample}}{\text{second}} \tag{3.13}$$

From Equations 3.11 and 3.13, the generator encoder sample rate was chosen to be 20kHz.

3.3.3 Voltage Measurement Hardware Specification

Since the generator three phase voltages are similar in magnitude as the EPS and the accuracy specifications were derived from the same commercial sync.check modules, the same NI-9215 module used to measure the EPS voltages is capable of meeting the instrumentation requirements. The hardware selection is justified in Section 3.2.10.

3.3.4 Encoder and Sensing Hardware Specification

An spare Eltra-EL53A incremental encoder was provided by Callghan Innovation and its specifications are shown in Table 3.6:

TABLE 3.6: Eltra EL53A Incremental Encoder Specifications

Field	Value
Encoder resolution	4096ppr
Angular resolution	0.022^o
Output Type	Line Driver
Supply voltage	5V
Output voltage	5V
Output channels	6
Max no load current	100mA
Max load current per channel	20mA
Max output frequency	300kHz
Max mechanical speed	3000rpm
Shaft Inertia	Not Specified

Before selecting the hardware, the performance of the encoder had to be validated. While the encoder maximum operational mechanical speed is within the steady state speed of the generator, the maximum representable outputs speed was investigated with Equation 2.64. The the maximum output speed is:

$$n_{max} = \frac{300 \cdot 10^3}{4096} = 73.2 \text{ rev/s}$$

which is higher than both the mechanical speed tolerance and the CGESS generator steady state speed. It is advantageous to measure the generator shaft speed exceeding the steady state speed to account for the frequency swing while in power generation mode. Using Equation 2.65, the minimum sample rate to accommodate for the output frequency must exceed 600kHz (=1.6μs period).

With these specifications, the NI-9411 device was selected. The module not only provides the 5V regulator with the power without external supply, the module also offers a sinking option which is necessary to sink the current from the internal encoder line driver configuration [185] without additional pull down resistors. The NI-9411 electrical characteristics is shown in Table 3.7,

TABLE 3.7: NI9411 6 Channel Differential Digital Input Module

Field	Value
Input Type	Differential/Single-Ended
Input channels	6
Input delay time	500ns
Signal level	±5V, 24V
External supply input voltage	5 to 30V
External supply output current	200mA
External supply output voltage	5V

An additional SICK-DFS60B encoder was selected to be the back-up device when the Eltra encoder was transported to the CGESS for installation. The SICK-DFS60B incremental encoder specifications is shown in Table 3.8. The characteristics shows that the SICK encoder output capabilities are within our specifications, and are suitable to be driven by the NI-9411 hardware.

TABLE 3.8: SICK DFS60B Incremental Encoder Specifications

Field	Value
Encoder Resolution	4096ppr
Angular Resolution	0.022^o
Supply voltage	5V
Output voltage	5V
Max no load current	40mA
Max load current per channel	30mA
Max output frequency	820kHz
Output type	Push-Pull
Max mechanical speed	9000rpm
Shaft inertia	6.2gcm^2
Max angular acceleration	5×10^5 rad/s^2

3.3.5 Direct Encoder Signal Output Model

As conventional speed and acceleration measurements are performed with numerical differentiation, the resulting quantization error from using an incremental encoder had to be simulated in order to design an appropriate filter. Firstly, the discrete time equation of motion describing the progression of position under a constant acceleration is expressed as:

$$\theta_{syn} = \theta_0 + \omega_0 \cdot T_N + \frac{1}{2} \cdot \alpha_{syn} \cdot T_N \tag{3.14}$$

Where	θ_{syn}	is the synthesized shaft position	(rad)
	ω_{syn}	is the synthesized shaft speed	(rad/s)
	T_N	is the time stamp	(s)
	ω_0	is the initial shaft speed	(rad/s)
	θ_0	is the initial shaft position	(rad)

and the quantized position value is given by:

$$\theta_{quan} = \frac{2\pi}{N_{eppr}} \cdot int\left(\frac{\theta_{syn}}{2\pi} \cdot N_{eppr}\right) \tag{3.15}$$

Where	int	is the integer part of the position count	
	θ_{quan}	is the quantized position	(rad)

Equation 3.15 converts the position in radians to a fraction of a revolution, maps the result to the equivalent encoder representation in counts, floors the counts to the nearest integer, and reverts this discretized position back to radians.

To simulate the position measurements of the CGESS generator under maximum acceleration and with an previously established sample rate of 20 kHz, the rotor positions were synthesized using Equation 3.14 with α_{syn}=400 rad/s^2, ω_0 = 0 rad/s, θ =0 rad and $T_{int} = 50us$, Figure 3.26 shows the comparison between synthesized and quantized position

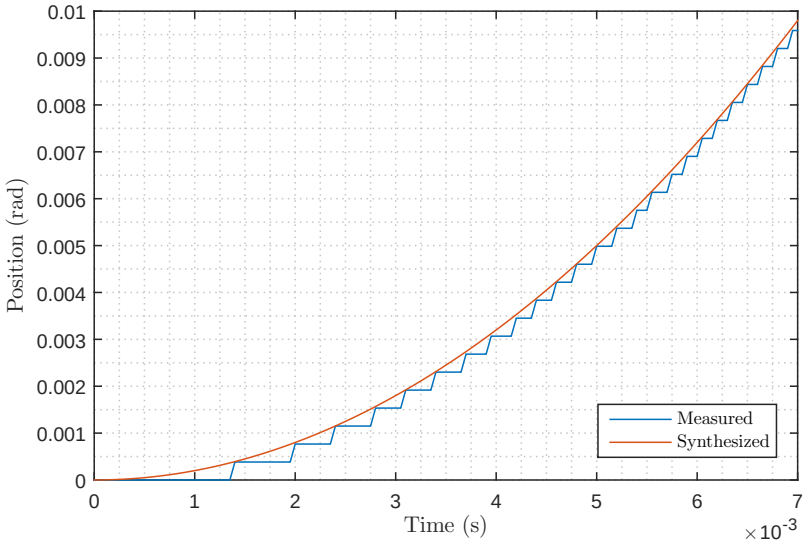

FIGURE 3.26: Comparison of actual position and quantized position

At every position sample instant, the position counts are always rounded down to the nearest integer due to the backwards looking property of the encoder wheel. Numerically differentiating the quantized position, the rotor speed is shown in Figure 3.27. Using Equation 2.70, the absolute speed error with a sample frequency of 20kHz and an encoder cpr of 2^{14} is approximately 7.67rad/s (=1.22rev/s), which cannot meet the 0.005rev/s defined by Table 3.5.

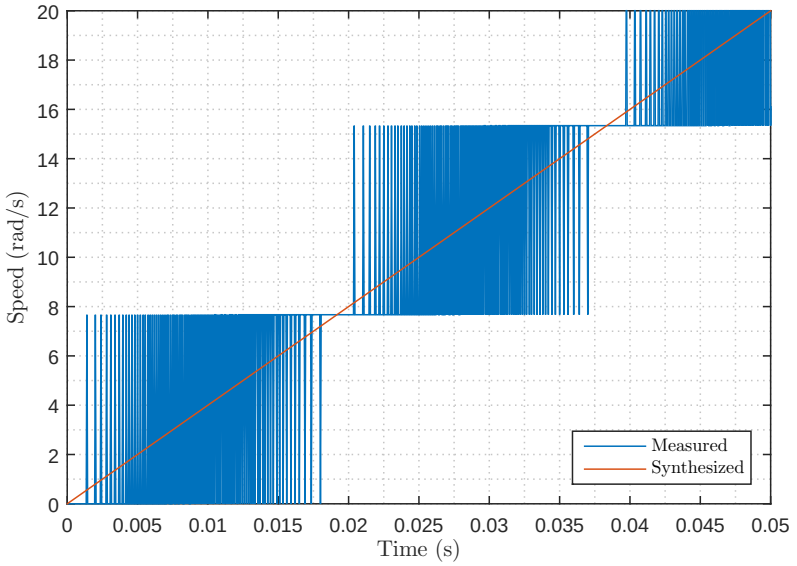

FIGURE 3.27: Comparison of actual speed and measured speed from numerical differentiation

Similarly, numerically differentiating the discretized speed over the time interval results in the measured acceleration, which is shown in Figure 3.28.

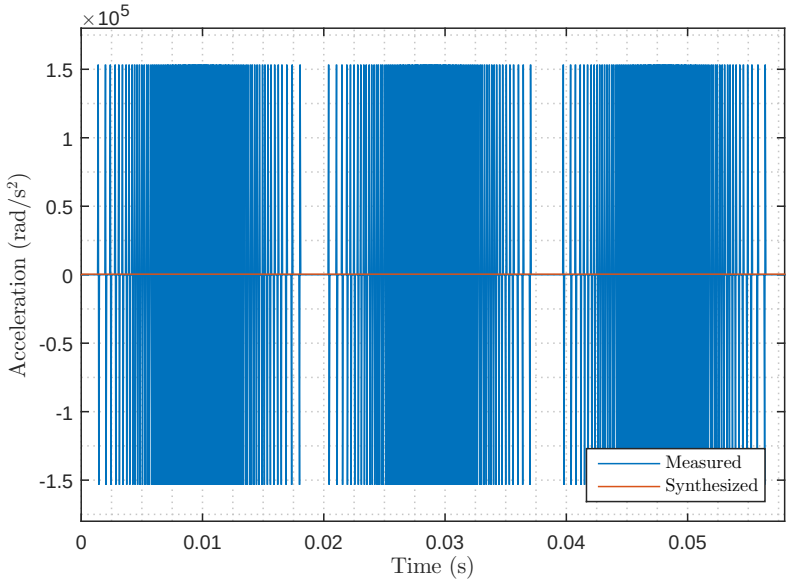

FIGURE 3.28: Comparison of actual acceleration and measured acceleration from numerical differentiation

The acceleration quantization error using Equation 2.71 is 3.8 $\times 10^4 \text{rad/s}^2$, which justify the necessity for signal conditioning.

3.3.6 Filter Design

The aim of the signal filter is to balance the SNR and a phase lag. In this section, Butterworth and Chebyshev type 2 filters were first designed and their performance was benchmarked with simulated encoder signals as inputs. These classical linear filters were discovered to be inadequate for meeting acceptable SNR and phase lag criteria such that an alternative approach is required. The Steady State Linear Kalman Filter was accordingly selected and implemented. The results demonstrate that the SSLKF is a competitive candidate for acceleration and speed filtering in the CGESS prototype.

3.3.6.1 Linear Filter Design

As the synchronization criteria demand accurate position and speed information, the tolerable time delay of the measurements from introducing signal conditioning methods is the restricting factor in designing a digital filter. A class of popular modern linear discrete time low pass filters such as the Chebyshev, the Butterworth, and the Elliptic filter were designed and their effectiveness as a speed filter were simulated in MATLAB. To begin the filter design, the frequency spectrum of the speed measurement error shown in Figure 3.29 is analyzed with FFT, and the result is shown in Figure 3.30.

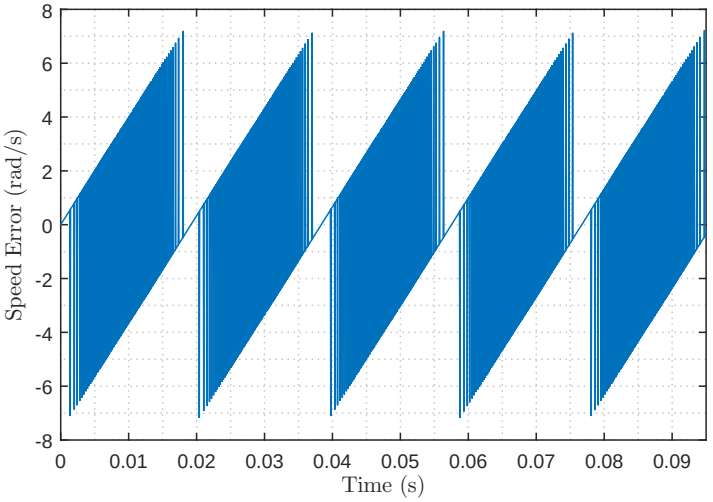

FIGURE 3.29: Speed measurement error due to quantization

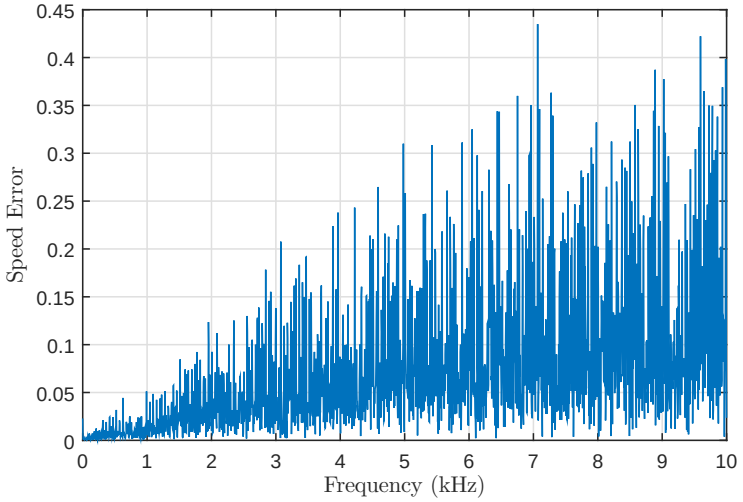

FIGURE 3.30: Frequency spectrum of speed measurement error using FFT with 4000 samples

Figure 3.30 reveals that the frequency of the quantization error has no distinct edge and spans up to the Nyquist frequency. A Butterworth and a type 2 Chebyshev filter were tired with varying orders and cutoff frequencies in attempt to filter the quantization noise. Their respective outputs are shown in Figure 3.31 and Figure 3.32.

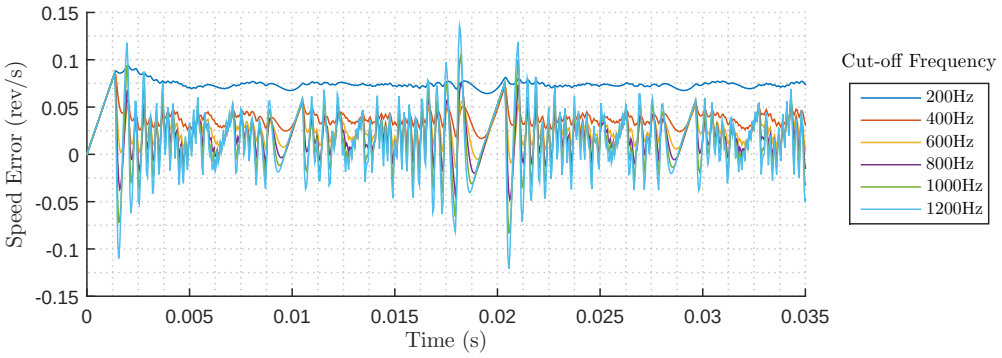

(A) 2^{nd} order Butterworth filter

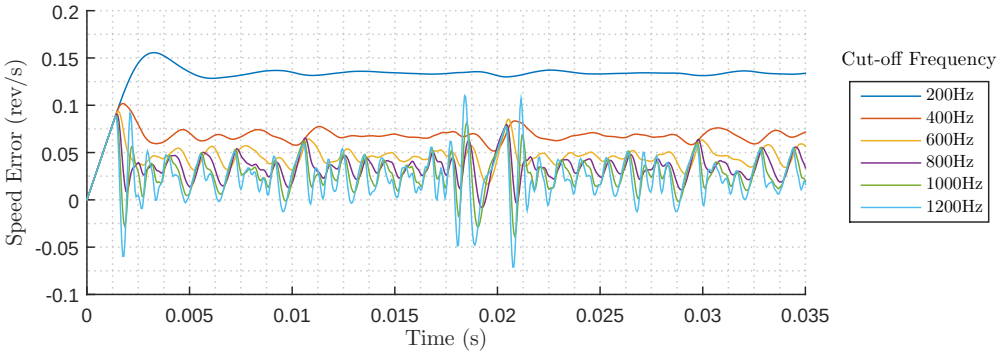

(B) 4^{th} order Butterworth filter

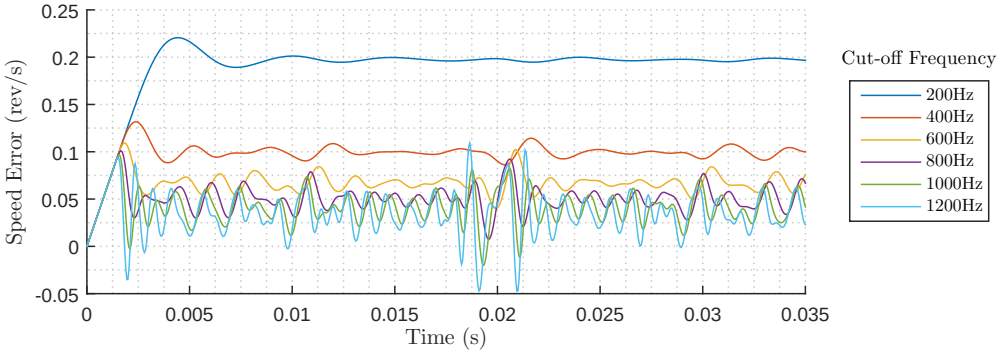

(C) 6^{th} order Butterworth filter

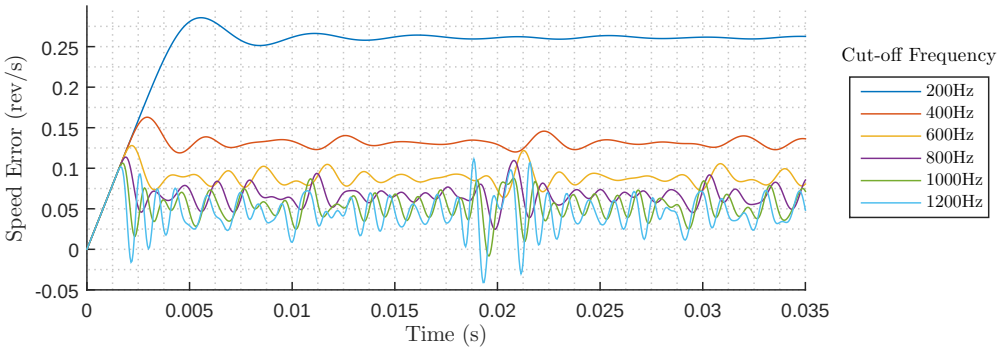

(D) 8^{th} order Butterworth filter

FIGURE 3.31: Filtered speed measurements using Butterworth filter with varying parameters

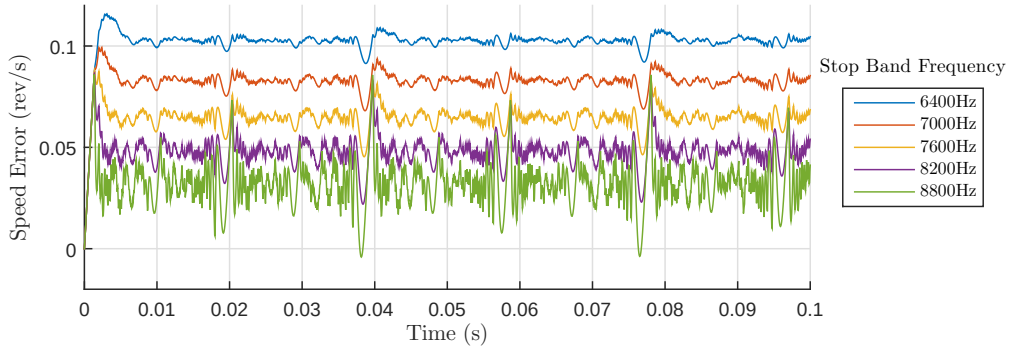

(A) 2^{nd} order 80dB stop-band attenuation Chebyshev type 2 filter

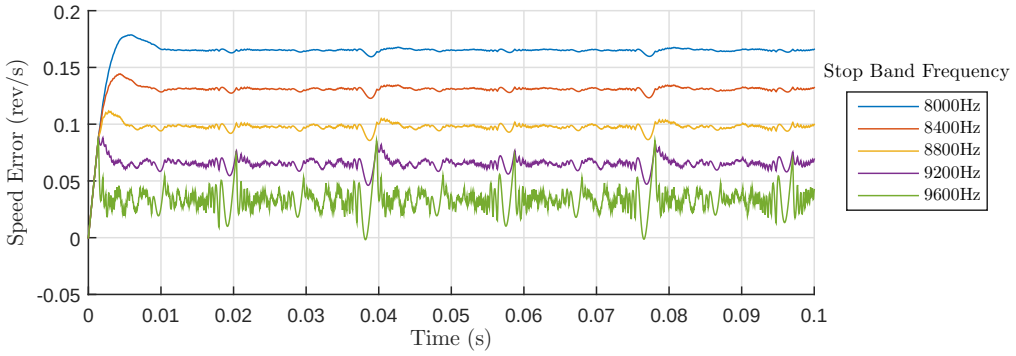

(B) 2^{nd} order 100dB stop-band attenuation Chebyshev type 2 filter

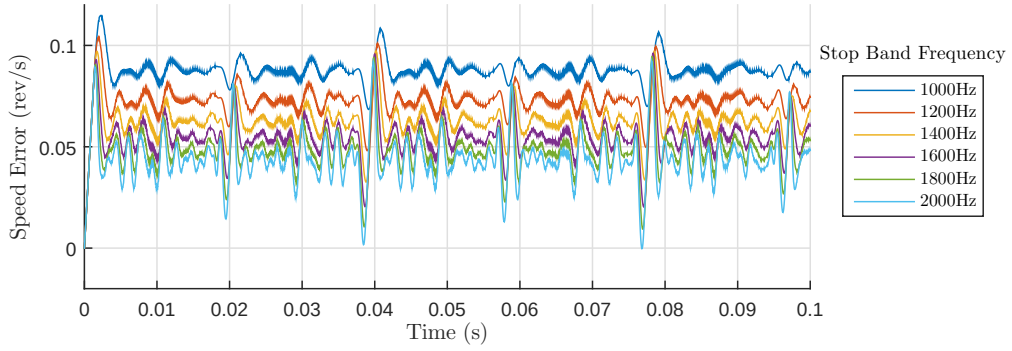

(C) 4^{th} order 60dB stop-band attenuation Chebyshev type 2 filter

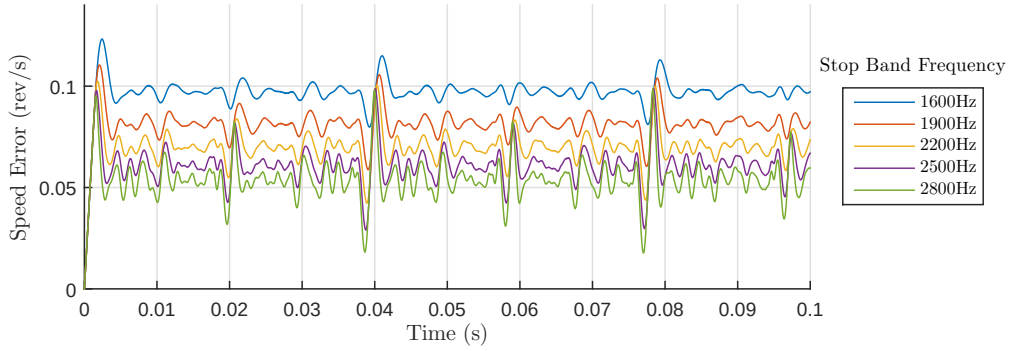

(D) 4^{th} order 80dB stop-band attenuation Chebyshev type 2 filter

FIGURE 3.32: Filtered speed measurements using Chebyshev type 2 filter with varying parameters

Figures 3.31, 3.32 shows that these conventional digital filters are not capable of reducing the quantization noise to an acceptable value, and the accuracy of the speed measurement is significantly reduced from the additional phase lag.

3.3.6.2 Steady State Linear Kalman Filter Design and Simulation

The Steady State Linear Kalman Filter technique introduce by 2.5.3.6 has several advantages over the conventional IIR filters. The filter is capable of estimating parameters with higher accuracy by taking the dynamical system and estimation error variance into account. The SSLKF design was based on a synthesized acceleration profile mimicking the capability of the CGESS mechanical system.

From Section 5.2, an acceleration control scheme has been developed to regulate the generator acceleration to roughly 2% steady state at 0.2 seconds with an input demand of 270 rad/s^2. This ideal response can be simulated with a transfer function expressed by:

$$H_{acc}(s) = 400 - \frac{100}{0.001344s^2 + 0.04033s + 1} \tag{3.16}$$

and its acceleration curve is shown in Figure 3.33. The 400 rad/s^2 acceleration seen at t=0 is caused by the lack of back pressure across the control valve from the near zero fluid flow, allowing the motor to utilize all the available pressure to transfer maximum acceleration to the shaft.

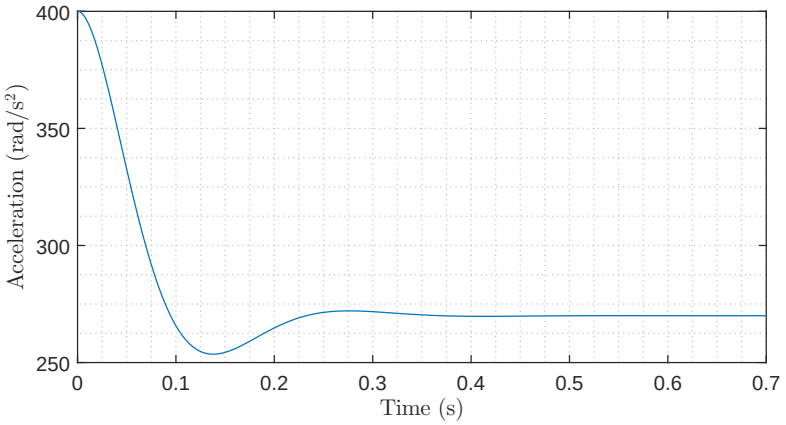

FIGURE 3.33: Simulated rotor acceleration

By integrating the acceleration profile shown in Figure 3.33, the speed and phase can be derived and shown by 3.34 and 3.35. The derived phase error can then be quantized with Equation 3.15 to simulate the encoder phase measurement at every sample, which

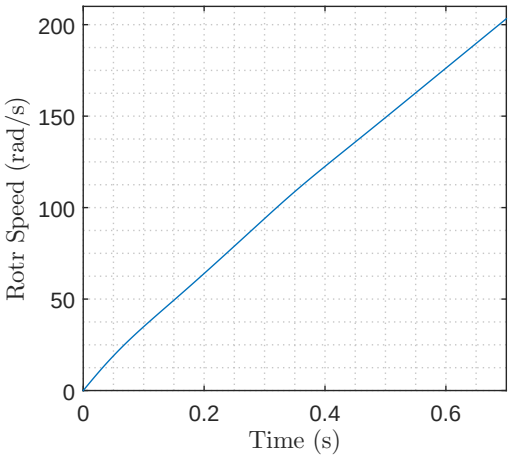

FIGURE 3.34: Simulated rotor speed

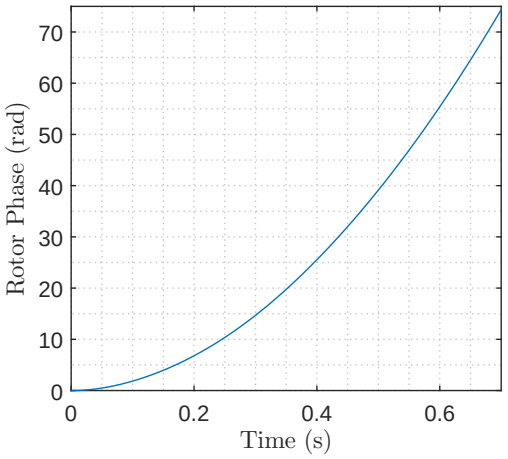

FIGURE 3.35: Simulated rotor phase

can be fed to the SSLKF algorithm expressed by Equations 2.78 and 2.79. Heuristically choosing $rho_0 = 550$, w $= 550$ and $\phi = 30$, the gain factors can be derived using Equations 2.81 to 2.92, giving:

$$g = \begin{bmatrix} g_1 \\ g_2 \\ g_3 \end{bmatrix} = \begin{bmatrix} 0.0535 \\ 29.43 \\ 8.093 \times 10^3 \end{bmatrix}$$

Passing the quantized encoder signals recursively through Equations 2.78 and 2.79, the pre-filtered and SSLKF filtered phase, speed and accelerations can be compared in Figure 3.36A, 3.37A and 3.38A.

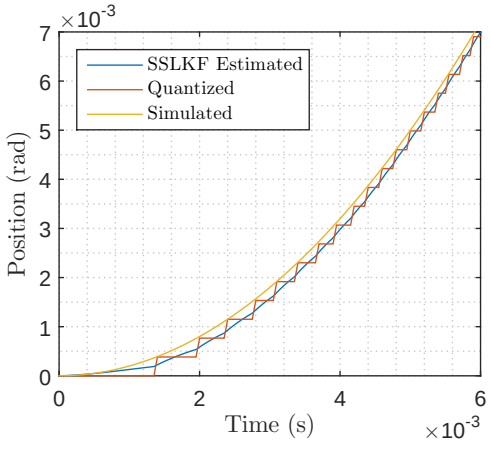

(A) Position estimation compared

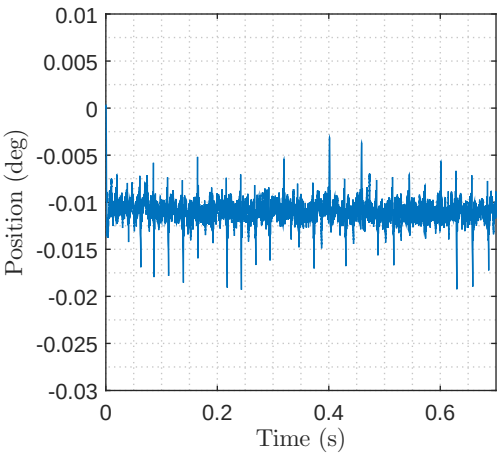

(B) Position SSLKF estimation error (SNR = 104.9 dB)

FIGURE 3.36: Filtered position measurements using SSLKF

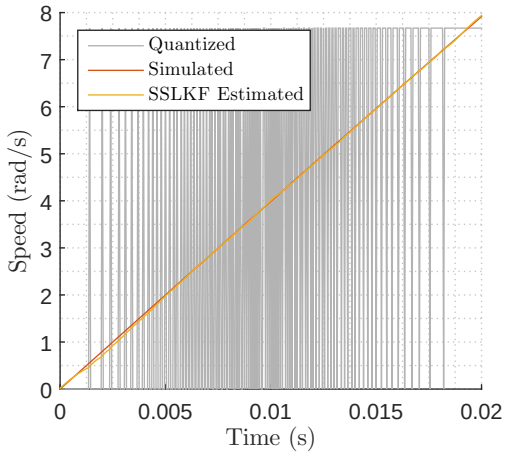

(A) Speed estimation compared

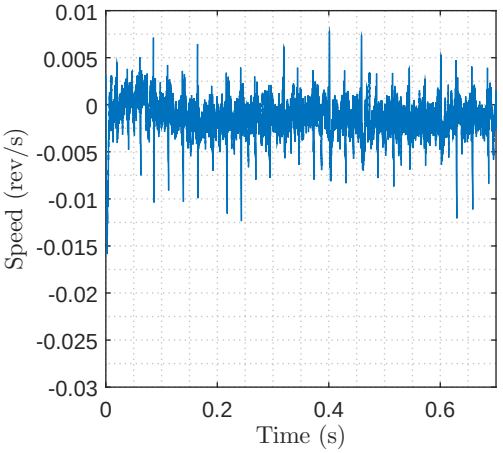

(B) Speed SSLKF estimation error (SNR = 93.8 dB)

FIGURE 3.37: Filtered speed measurements using SSLKF

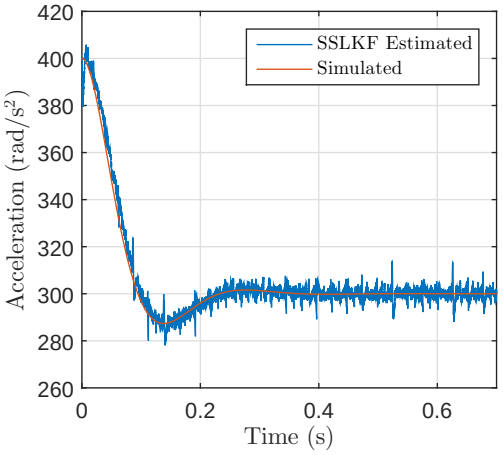

(A) Acceleration estimation compared

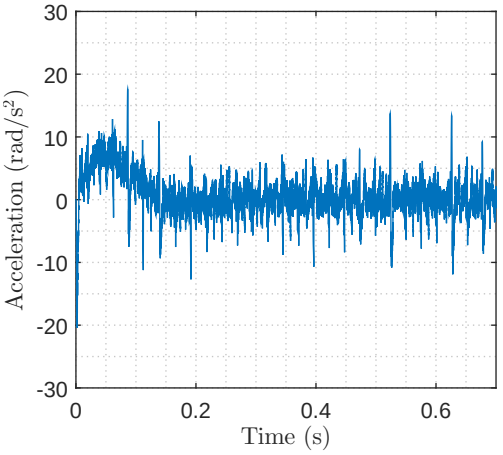

(B) Acceleration SSLKF estimation error (SNR = 39.0 dB)

FIGURE 3.38: Filtered acceleration measurements using SSLKF

Taking the error between the simulated ideal rotor parameters and the SSLKF filtered values, Figures 3.36B, 3.37B and 3.38B can be plotted. MATLAB SNR function showed that the SSLKF estimation of the simulated position, speed and acceleration SNR are 104.9 dB, 93.8 dB, and 39 dB respectively. Taking the normal distribution of the measurement errors, the average and standard deviation values of: -0.011^o and 0.0015^o was obtained for position measurement, and -0.0014 rev/s and 0.0024 rev/s was obtained for speed measurement. These benchmarks meet the accuracy requirements established by Table 3.5. Furthermore, the SSLKF filtered acceleration SNR also exceeded the 10 dB minimum SNR for an typical industrial process control suggested by [186] and can be used as an acceleration feedback without separate filtering.

3.3.7 RMS Voltage Estimation

It is well known that errors are introduced when a conventional digital RMS calculation is performed using a window length which is a non-integer multiple of the fundamental period of the measured signal frequency. As the CGESS generator is a highly dynamic system, it is our goal to ensure that the RMS calculation meets the performance criteria.

The RMS calculations are performed on a simulated 10kHz sampled voltage signal which has an linearly increasing frequency and amplitude, which is depicted by Figure 3.39. Figure 3.39 was plotted with the assumption that the generator field current is constant, which is possible if the AVR control was designed to exhibit relatively fast dynamics compared to the mechanical dynamics. The AVR was also assumed to regulate the field current to produce 1 p.u. peak power grid voltage at the nominal grid frequency, while the generator is accelerated at with 80% of maximum acceleration of 400rad/s^2.

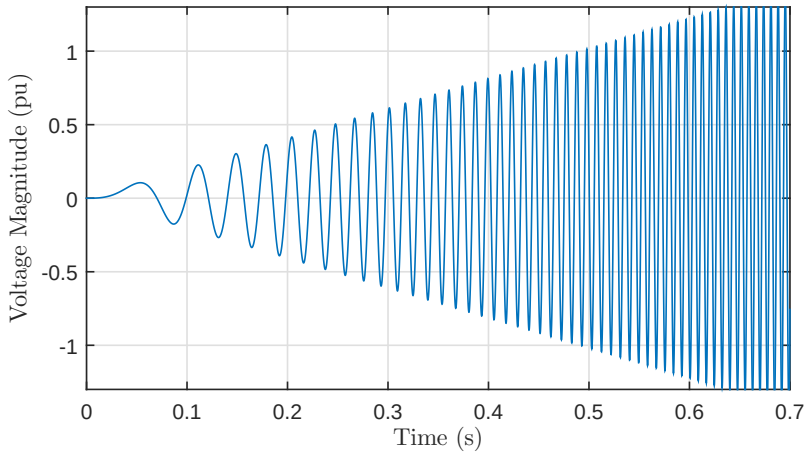

FIGURE 3.39: Simulated generator phase A voltage magnitude with a constant acceleration of 320rad/s^2

Through experimentation, a sliding window with the width of 150 samples (corresponding to 3/4 of the fundamental power grid nominal voltage cycle) and an calculation update rate of 100ms was chosen. The comparison between the simulated and calculated RMS is shown in Figure 3.40. For contrast, the tolerable synchronization voltage difference between the grid and the generator is illustrated by the amplitude of the green line, and the tolerable frequency deviation is illustrated by the horizontal distance between the green lines. The synchronization frequency in this case is 50Hz.

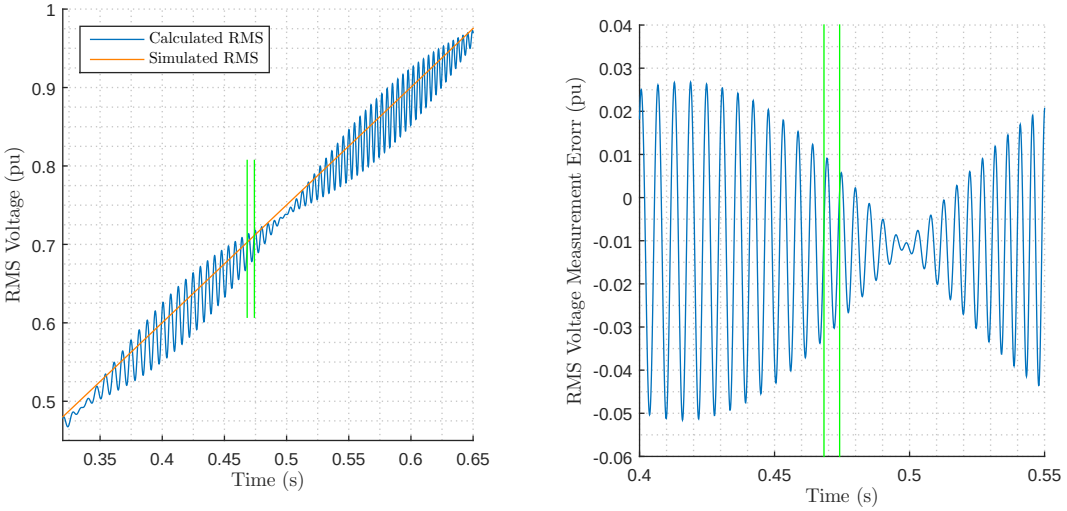

(A) Comparison between simulated and calculated RMS

(B) RMS calculation error

FIGURE 3.40: RMS calculated with a sliding window width of 150 samples

Figure 3.40 shows that the voltage measurement error obtained when the generator speed is within the acceptable speed deviation for synchronisation can vary between 1% to 3%, which is not within the error allowed by the accuracy limitation shown by Table 3.5. Figure 3.41 compares the effectiveness of using the typical Hanning, Hamming and Blackman windows on the generator voltages. The synchronization frequency is reduced down to 49Hz to simulate the most likely frequency scenario during the FIR period.

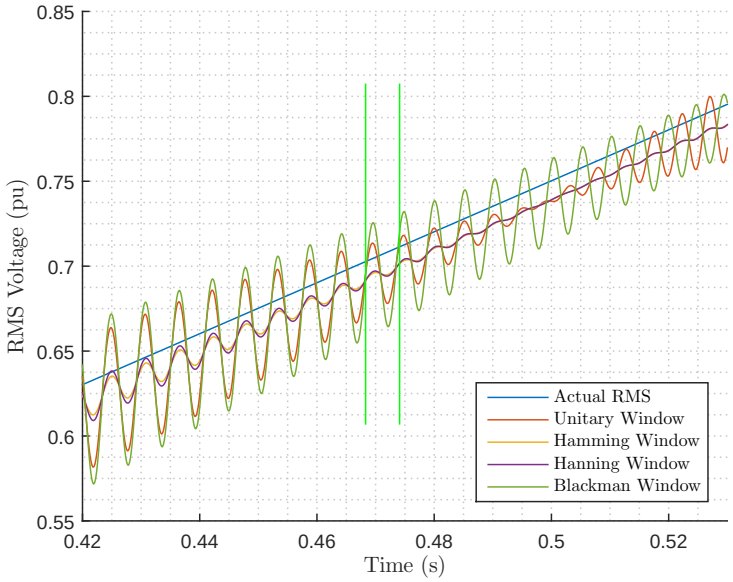

(A) Comparison between simulated and calculated RMS

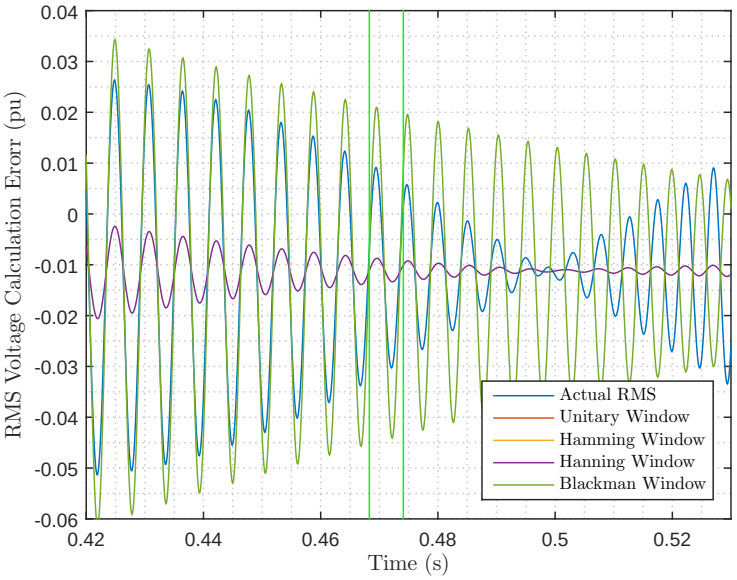

(B) RMS calculation error

FIGURE 3.41: RMS calculated with a sliding window width of 150 samples

Figure 3.41 showed that Hamming and Hanning windows gives the most accurate RMS calculation of around 1%, either Hanning or Hamming windows can be used in the RMS measurement algorithm.

This section shows the preliminary RMS calculation simulation assuming the hardware will not be a limitation and the quantization error is negligible. Although the windowing algorithms are included in the NI cRIO libraries, these methods are resource heavy due to the numerous multiplications required for each window. Section 2.5.3.8 proposes a few

alternative methods which can be used to replace the conventional windowing method if the hardware is less than capable during implementation.

Chapter 4

System Modeling and Identification

4.1 Chapter Structure

Process control plant modeling based on real-world system identification was carried out to ensure that the controller is able to perform as close to the expected simulated behavior as possible. For the control scheme validation process, a small scale, low powered CGESS test-rig was built in parallel with the 100 kW CGESS prototype assembly, and the majority of the control system testing was performed on the CGESS test-rig. The CGESS test-rig assisted in the selection of an appropriate PTV sizing, assess the valve dynamics, and describes the poor performance in control valve dynamics which the valve controller has to accommodate for.

4.2 Dynamic Model of Compress Gas Energy Storage System

4.2.1 Section Outline

From a process control view point, the sizing criteria for the proportional throttle valve was uncertain prior to the formulation of a feasible control strategy. While selecting a valve with larger orifice area reduces power loss through the valve during the power supplying stage, the fine pressure control is reduced during the synchronization stage due to the finite spool movement resolution. During the early stages of the project, the Parker TDA series NG-32 proportional throttle valve (PTV) was designated to be the main control apparatus. However, through characterization and simulation, the NG-32 PTV was shown to be insufficient to regulate the control output variable with satisfactory resolution; hence the replacement NG-16 valve was proposed.

This section documents the process of characterizing the pressure v.s. flow-rate behavior of the NG-32/NG-16 proportional throttle valve, the derivation of valve spool dynamics

from experimentation, the methodologies used to calculate the effect of spool dynamics on the process variable resolution, and selection of the more appropriate new control valve. The results obtained were used to improve the Simulink hydraulic model and to ensure the formulation of a robust controller design suited to the plant.

4.2.2 Proportional Throttle Valve Model Identification

4.2.2.1 NG-32 PTV Test Benches Overview

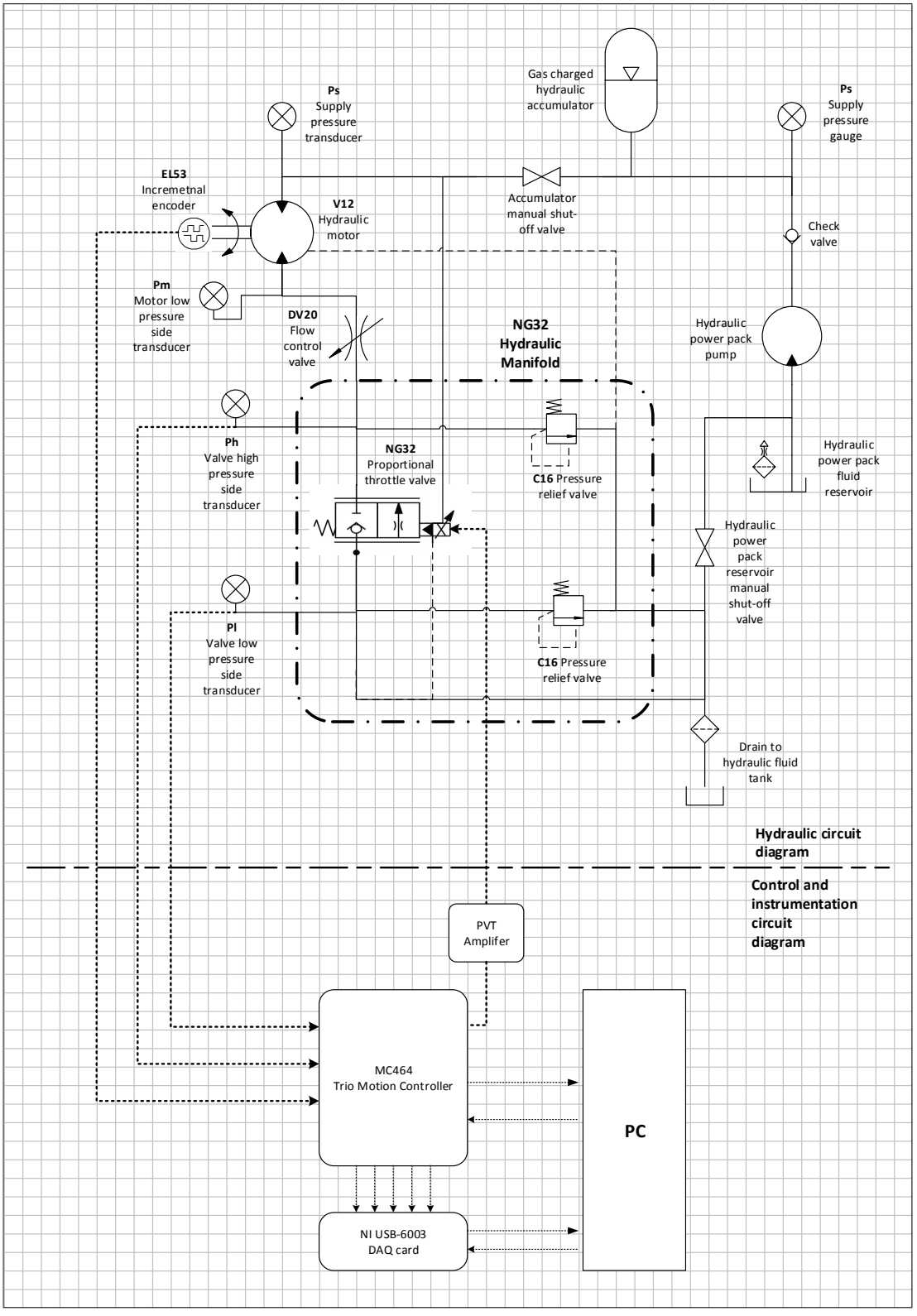

FIGURE 4.1: TDA NG-32 PTV characterization test-rig circuit diagram

The test rig depicted in Figure 4.1 is designed to evaluate the performance of the NG-32 PTV. The test rig initially was designed by EHL and the Callaghan team as a hydraulic load simulator, and was later modified to represent a scaled down CGESS prototype while the CGESS prototype was under construction. The supply pressure was limited to a maximum pressure of 250bar due to the limited output of the hydraulic power pack, and a minimum pressure of 80bar due to the fixed accumulator precharge. Although a flow-rate transducer was desired, space was not reserved for flow-meters in the original design. The flow-rate was calculated from the product of measured shaft speed and motor displacement. The volumetric efficiencies were approximated to be a constant 85 % from the datasheet.

The top section of Figure 4.1 shows the NG-32 test rig hydraulic diagram, which contains a drive circuit and charge circuit. The drive circuit consists of a Parker bladder type accumulator, an unloaded Parker V12-80 variable displacement hydraulic motor, Parker NG-32 PTV, a Stauff DV-20 manual rotary flow control valve (FCV) and a 300L air-vented fluid reservoir tank. The drive circuit was designed to regulate pressure and motor parameters by means of a control valve, which is similar to that in the CGESS prototype. The charge circuit consists of a hydraulic power pack, one way check valve and a manual shut-off valve. After isolating the accumulator from the drive circuit with a manual shut-off off valve, the power pack draws the hydraulic fluid from the reservoir, store the fluid within its internal fluid tank, and pressurizes the accumulator prior to each experiment. To quickly discharge the fluid stored in the accumulator, the hydraulic motor displacement was adjusted to be at its maximum value of 80cc/rev. The accumulator was prevented from fully discharging to 80 bars due to the damage caused by 1) the bladder rubbing on the fluid port and 2) the large destructive vacuum as the fluid fully empties [187].

For safety consideration, the NG-32 PTV was plumbed into a hydraulic manifold along with the pressure transducers and pressure relief valves to mitigate the large pressure spikes if the control valve were to suddenly close from testing. Furthermore, the DV-20 FCV was installed to prevent the motor from exceeding its maximum speed when the control valve is fully open. The manifold physical assembly is shown in Figure 4.2.

Figure 4.1 also outlines the instrumentation and controls circuit. The encoder and pressure signals were firstly processed by the MC464 TrioMotion Controller, then ported to the PC-connected DAQ card for data-logging due to the limited MC464 controller built-in memory. The valve poppet was driven by a Callaghan-Innovation built amplifier, which provides current depending on the MC464 control voltage signal. The PTV pilot supply was connected to the accumulator outlet to provide the pressure required for the

spool movement, and the pilot drain was connected to the tank return line internal to the manifold as instructed by the TDA series technical specification.

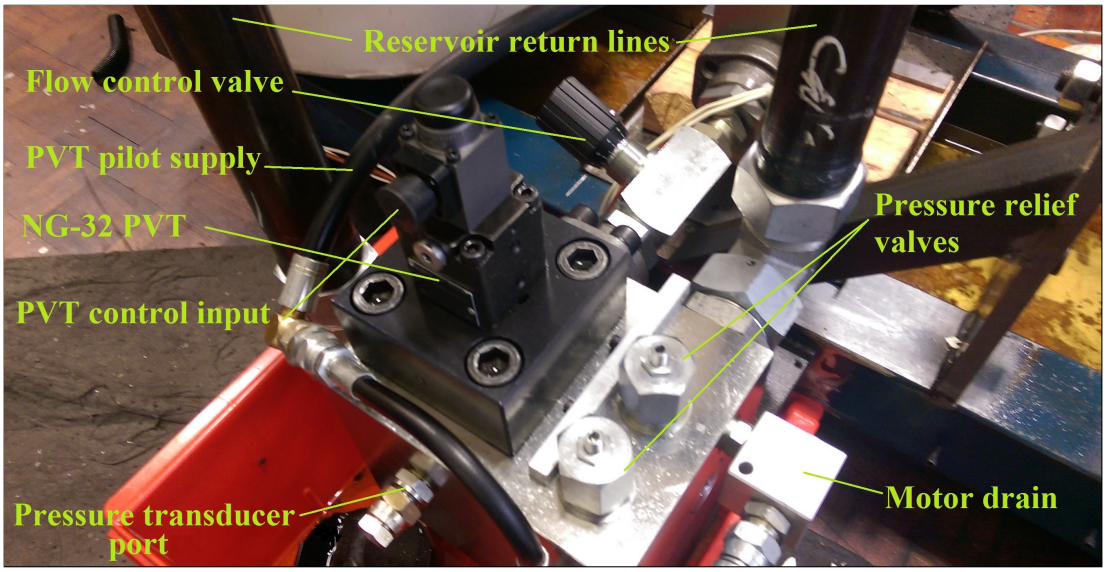

FIGURE 4.2: TDA NG-32 hydraulic manifold physical assembly (pressure transducers and control inputs yet to be wired)

The NG-32 test-rig parameters is compared with the CGESS prototype parameters in Table 4.1:

TABLE 4.1: CGESS and NG-32 Test Rig Comparison

Parameter	CGESS Prototype	NG-32 Test Rig
Max supply pressure	350 bar	250 bar
Max motor pressure	350 bar	250 bar
Motor displacement	115 cc/rev	80 cc/rev
Rotor inertia	1.545 kgm^2	4.4×10^{-3} kgm^2
Maximum torque	639 Nm	317 Nm
Maximum acceleration	400 rad/s^2	72.15 ×10^3 rad/s^2
Minimum servo period	1 ms	1 ms

4.2.2.2 NG-32 PTV Pressure Flow-rate Identification

The valve orifice pressure flow-rate characteristics were assessed by recording the motor speed and pressure measurements as the valve input was subjected to a step change. Due to the limited capacity of the accumulator, the pressure applied to the drive system naturally decreases from the volume of fluid vacating the accumulator, allowing the

valve flow-rate vs pressure behavior for a fixed control input to be recorded without the need for a adjustable pressure supply. The NG-32 PTV and DV-20 FCV pressure and flow-rate data recorded for a range of valve step inputs are shown in Figure 4.4, 4.5, 4.6 and 4.6. The recording time interval was set to 20ms.

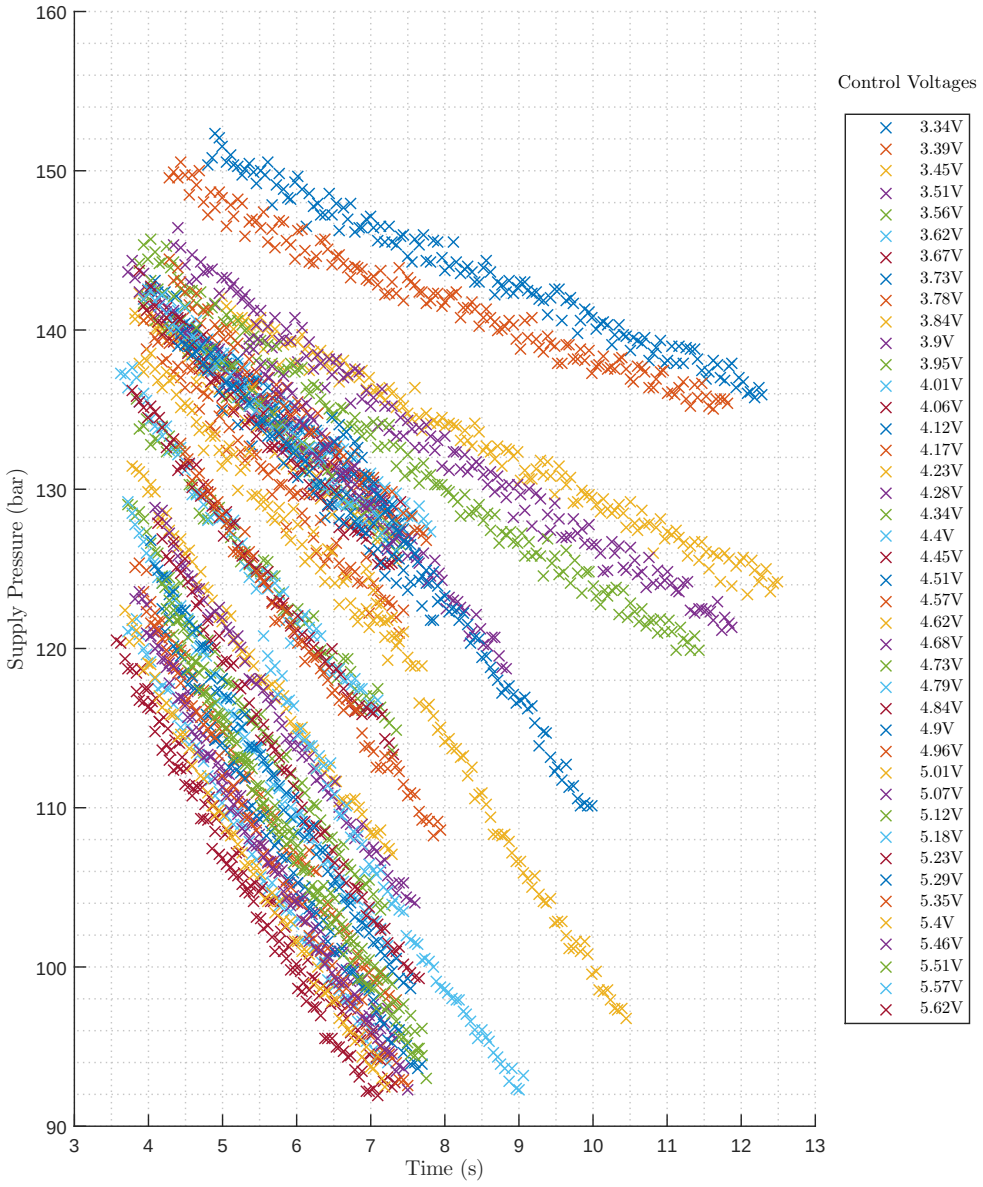

FIGURE 4.3: Recorded NG-32 test-rig motor low side pressure (labeled as P_M in Figure 4.1) in response to different PTV step input voltages

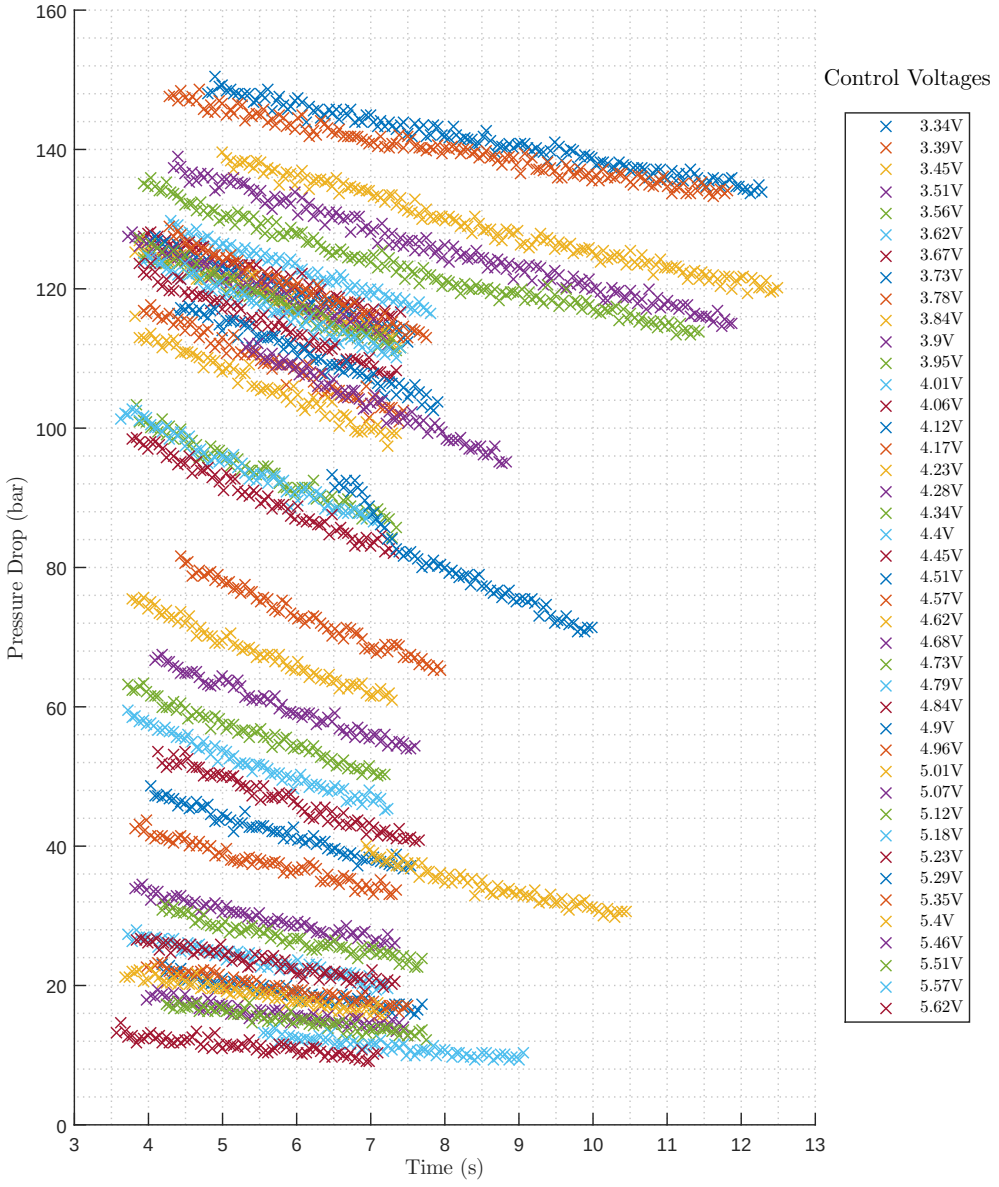

FIGURE 4.4: Recorded NG-32 PTV pressure drop(Calculated by subtracting P_l from P_h in Figure 4.1) in response to different PTV step input voltages

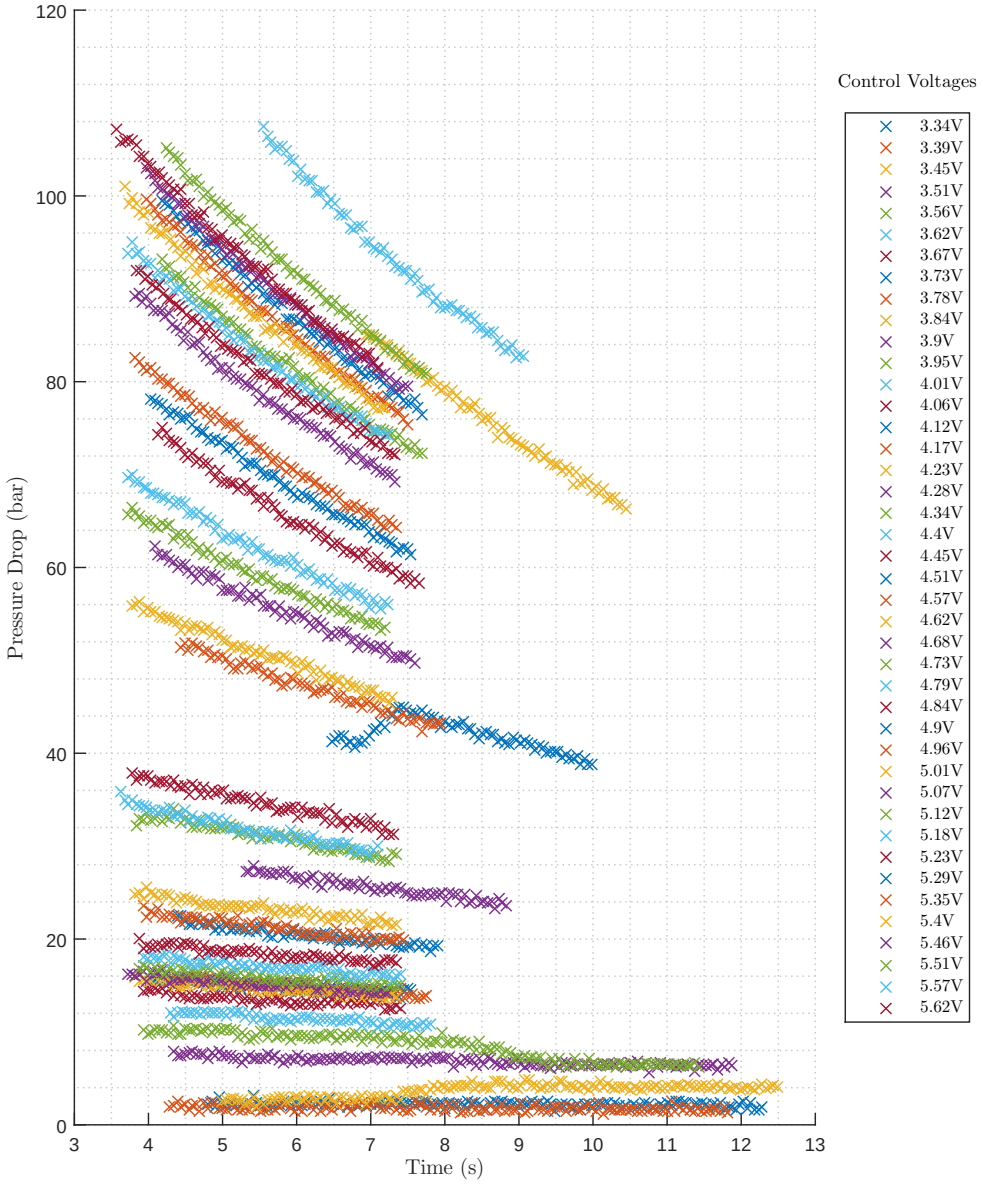

FIGURE 4.5: Recorded DV-20 FCV pressure drop (Calculated by subtracting P_h from P_m in Figure 4.1) in response to different PTV step input voltages

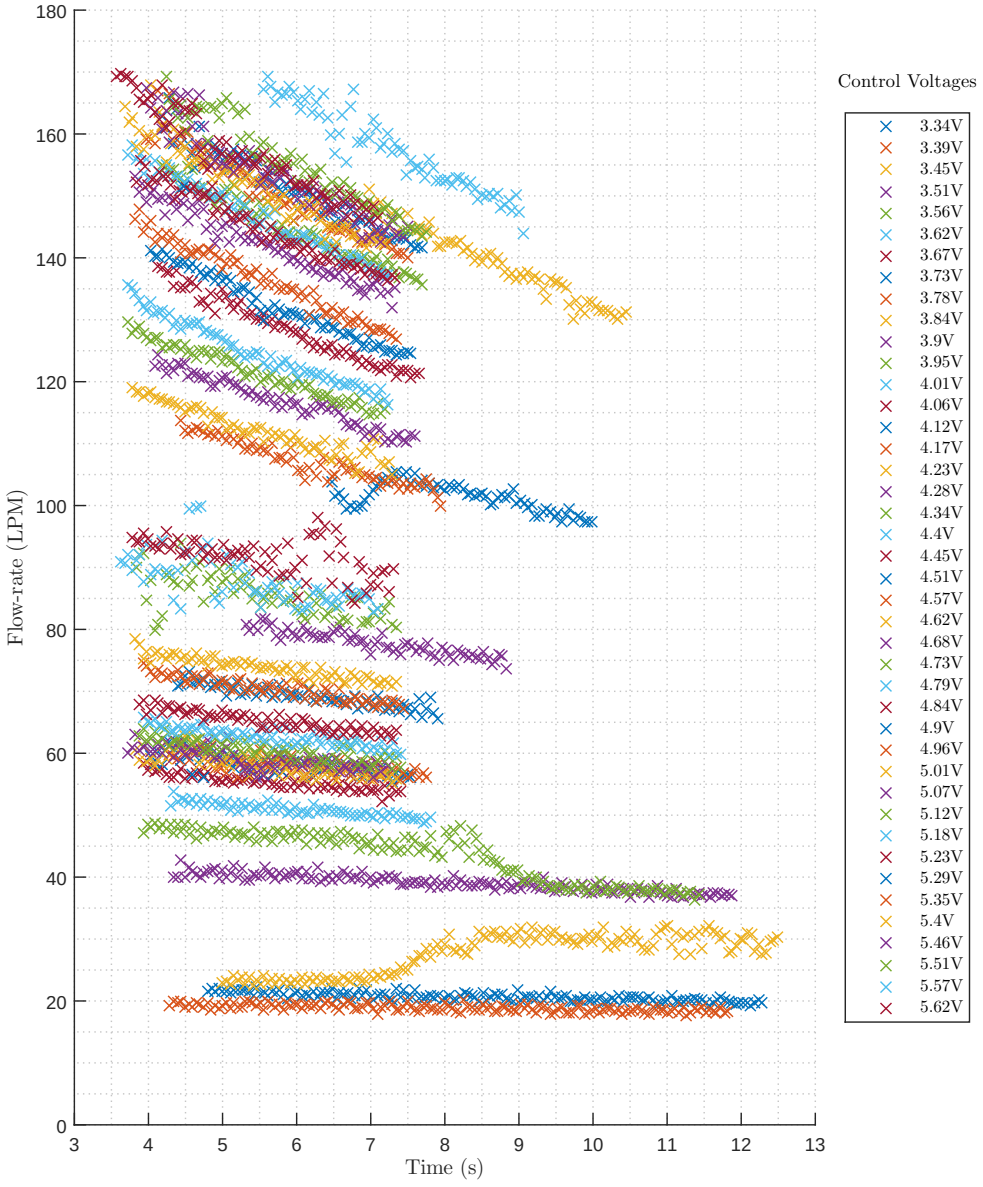

FIGURE 4.6: Recorded drive system flow-rate in response to different PTV step input voltages

It can be seen in Figures 4.4 to 4.6 that abrupt pressure and flowrate changes occur after some time, and the reason for these abnormalities have yet to be identified. For the purpose of CAESS control design, these changes was ignored due to the relatively short synchronisation control time.

Observing Equation 2.16, the flow-rate is linearly proportional to the square root of pressure by a constant flow coefficient K_v. By taking the square root of the pressure

measurements and plotting against the flow-rate, a first order polynomial $y = ax$ could be least squares fitted for each valve opening. The flow coefficient K_v equates to the parameter a in the fitted $y = ax$. The square-root of pressure vs flow-rate relationship of the FCV, PTV and the combined orifices (total pressure drop through both the FCV and the PTV) are shown in Figure 4.7, 4.8 and 4.9; their linearly fitted curves are also plotted for comparison.

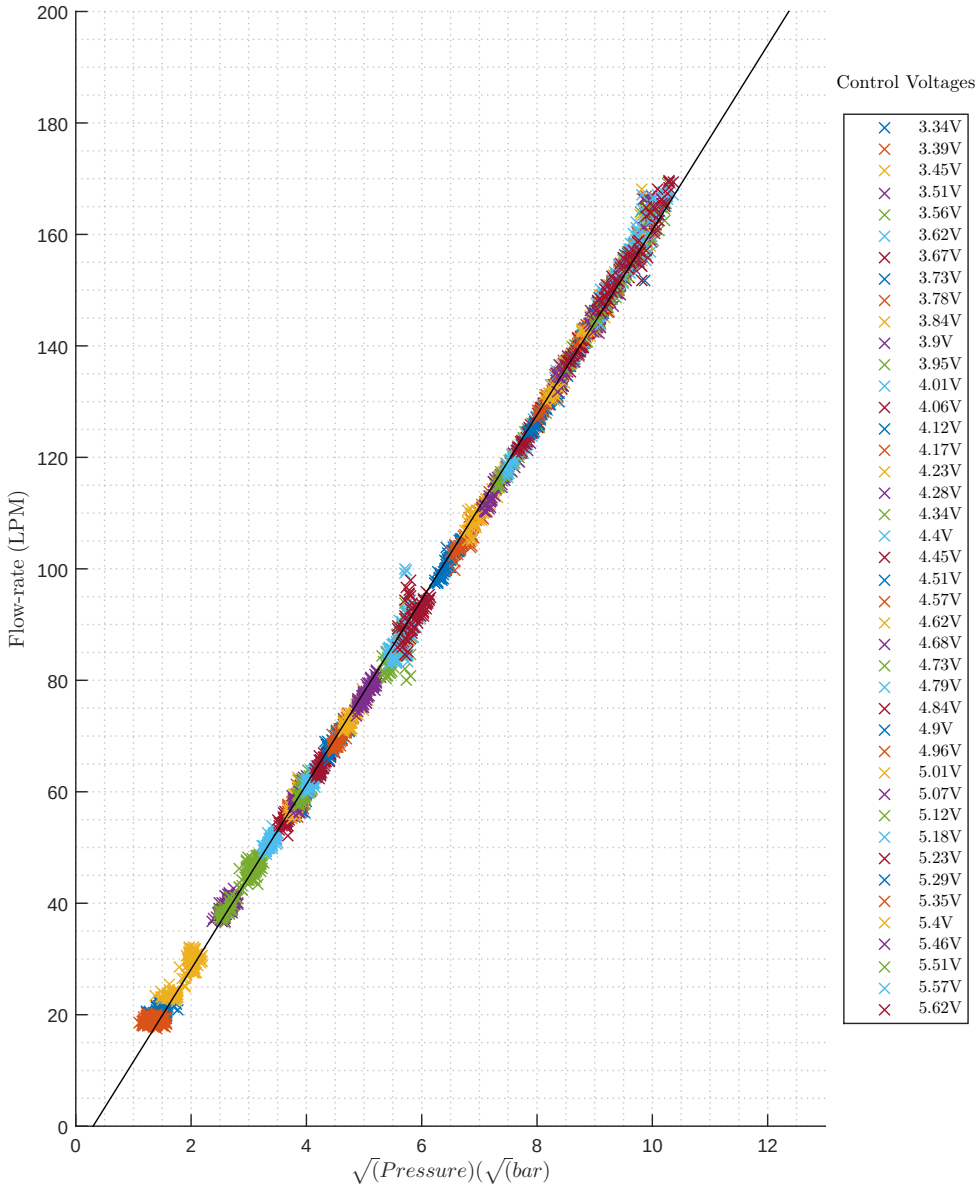

FIGURE 4.7: DV-20 FCV pressure v.s. flow-rate relationship with varying control inputs

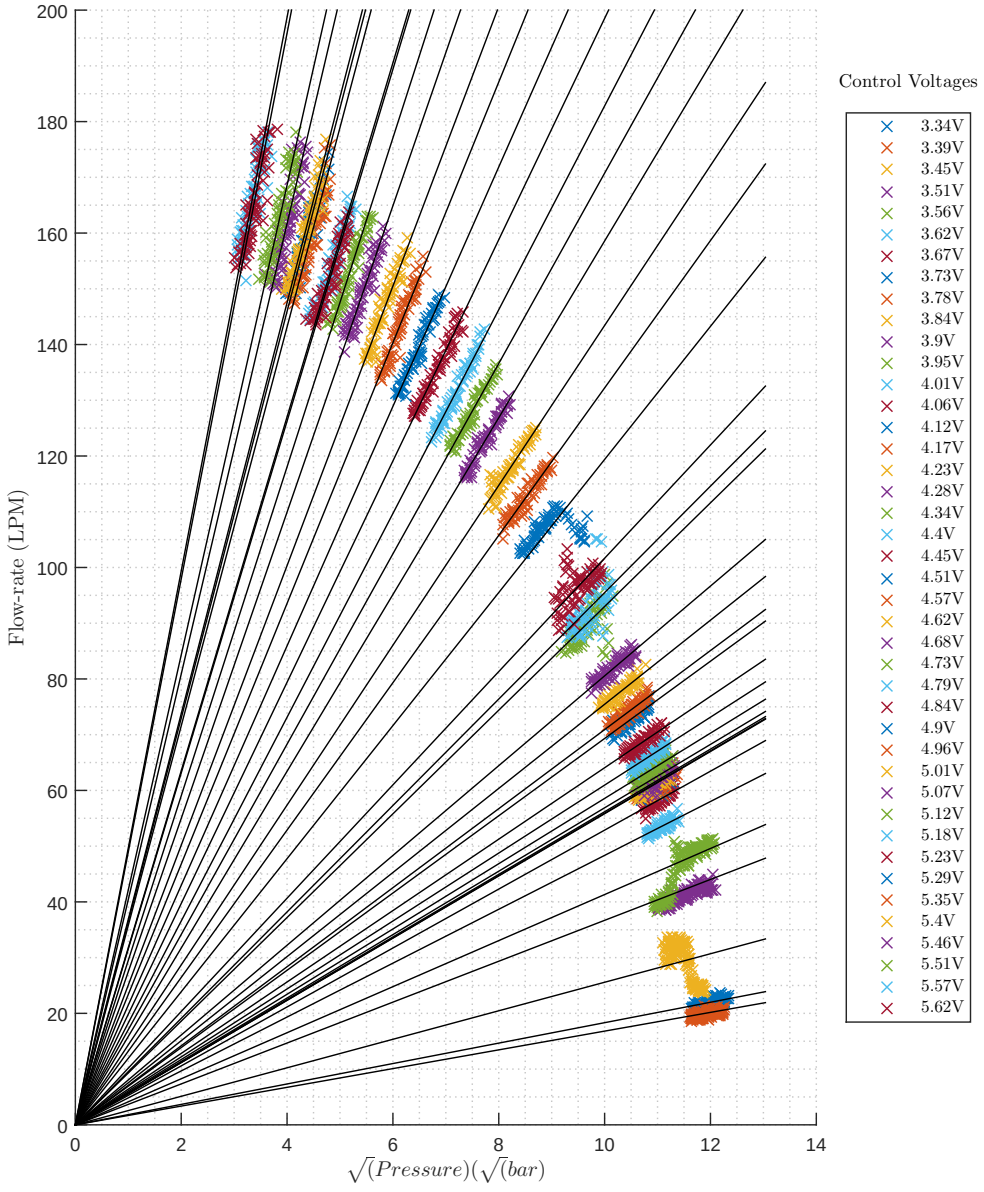

FIGURE 4.8: NG-32 PTV pressure v.s. flow-rate relationship with varying control inputs

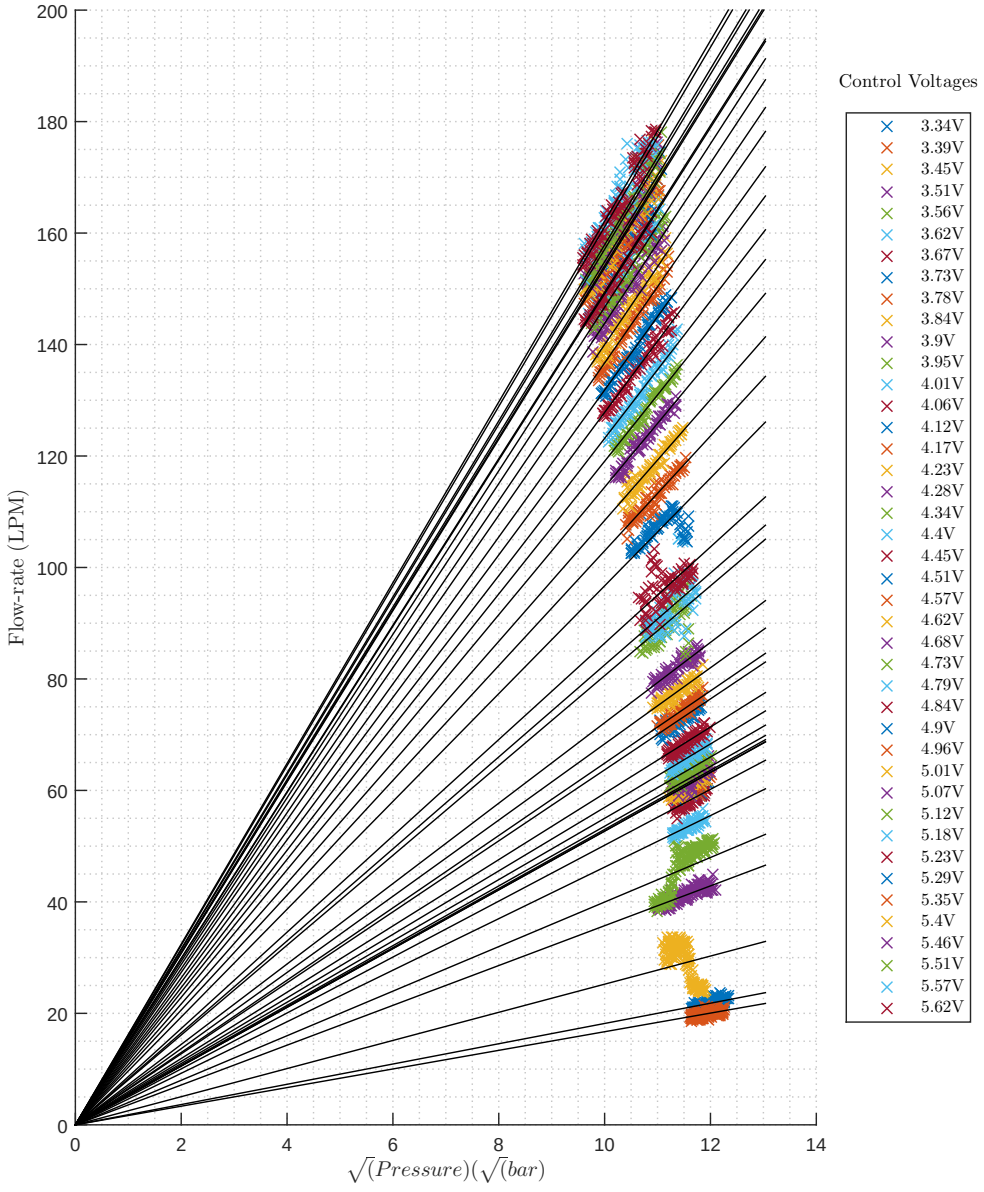

FIGURE 4.9: Combined orifices v.s. flow-rate relationship with varying control inputs

The control voltages mapped to the flow coefficient is shown in Figure 4.10

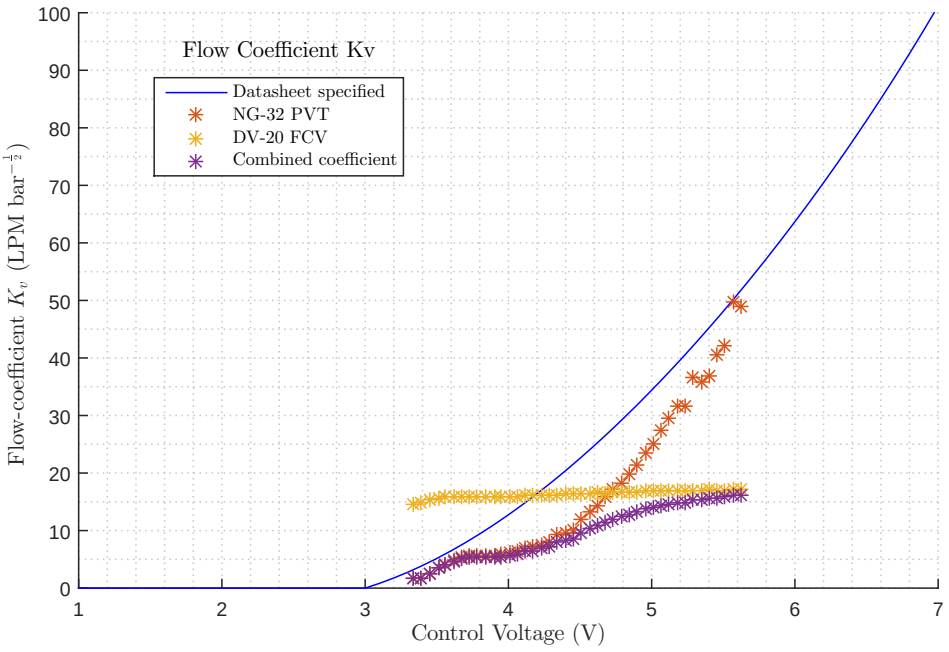

FIGURE 4.10: Control voltage to flow coefficient map

As expected, the flow coefficient of the DV-20 FCV shown in Figure 4.10 remains relatively constant. The NG-32 PTV flow coefficient curve however exhibits a region where the change in spool position is invariant to the input voltages between 3.6V to 4.4V. The cause for this region has yet to be found. It was proposed by the EHL that the extended amount of wear and tear from functioning on oil drilling platform could be the cause of this unexpected behavior. Figure 4.10 also showed that the flow coefficient did not completely agree with the manufacturer's datasheet. Regardless, the results shown in Figure 4.10 can used and extrapolated to tabulate the pressure, flow-rate and input parameters required for the Simulink variable orifice block.

4.2.2.3 NG-32 PTV Spool Dynamics Identification

During the early phase of the project, the valve spool dynamics were unknown and had to be approximated for the control design process. Using the standard spool model given by Equation 2.48, the NG-32 approximation is given by Equation 4.1 and its parameters are shown in Table 4.2. The graphical comparison of the approximate and the ideal response to a step input is shown in Figure 4.11B.

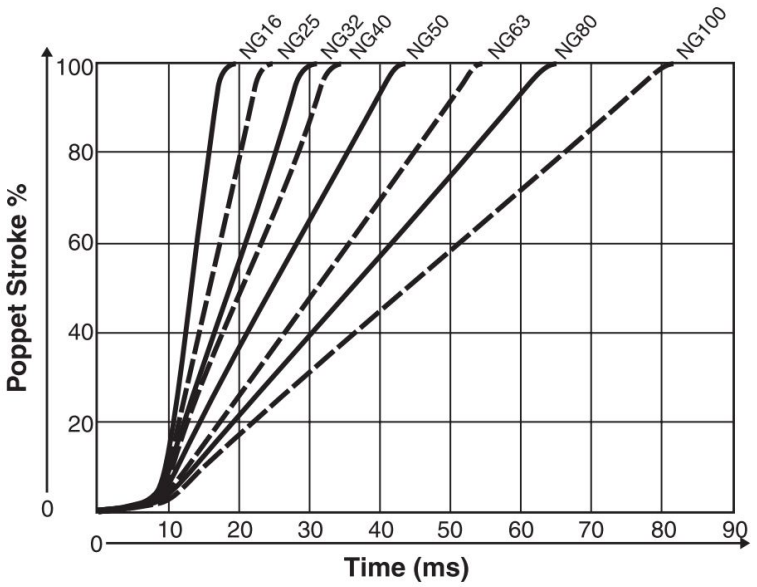

(A) NG-32 datasheet poppet response

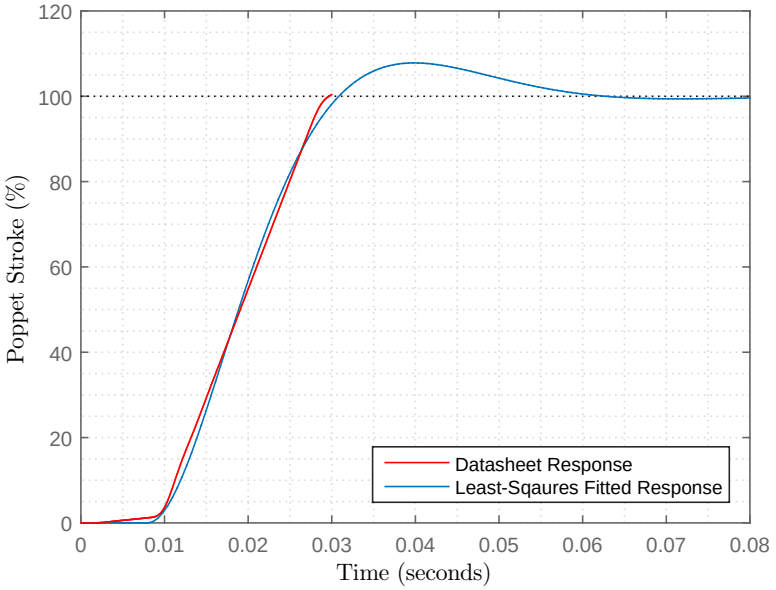

(B) NG-32 approximated valve poppet dynamics

FIGURE 4.11: NG-32 poppet dynamic approximation

$$H_{NG32}(s) = \frac{e^{-0.008s}}{0.00006202s^2 + 0.009922s + 1} \tag{4.1}$$

TABLE 4.2: Approximated NG-32 PTV spool transfer function parameters from datasheet

Parameter	Symbol	Value
Delay	t_d	0.008
Settling time	t_s	0.025
Damping coefficient	ζ	0.63
Natural frequency	ω_n	126

Observing the datasheet poppet stroke behavior shown in Figure 4.11A, a few valve dynamic parameters were unspecified. These identifiable uncertain quantities are:

1. **The dynamic response**. The response time shown in the datasheet lacks the damping coefficient, natural frequency and the rise time excluding the initial dead time as seen in the standard PTV model described by Equation 2.5
2. **The condition under which the dead band occurs.** It was uncertain whether the delay occurs whenever the valve input varies from one set point to another, or if the delay only occurs when the spool was directed to move from a fully closed position.
3. **The power amplifier and the solenoid dynamics.** The Callaghan built PTV amplifier characteristics has yet to be quantified, hence the direct transfer function between the input voltage to the actual spool position has yet to be modeled

Doubts about the amplifier emerged from the early NG-32 experiments, which are depicted by Figure 4.12. The Figure shows poor spool dynamic performance when the Parker recommended PCD00A-400 power amplifier was used as the PVT input driver. The RPM results obtained from the NG-32 test rig showed an initial and operating dead band of 50ms, and a RPM oscillation with a period exceeding 100ms. Furthermore, it appeared that the pilot pressure connection point was a major influence on the consistency of the spool dynamics, as early experimental evidence showed that the connecting the pilot at the same location as the PTV inflow port results in poor spool dynamics. It is necessary to identify the plant process as the measured dynamics greatly varied from the model provided by the manufacturer.

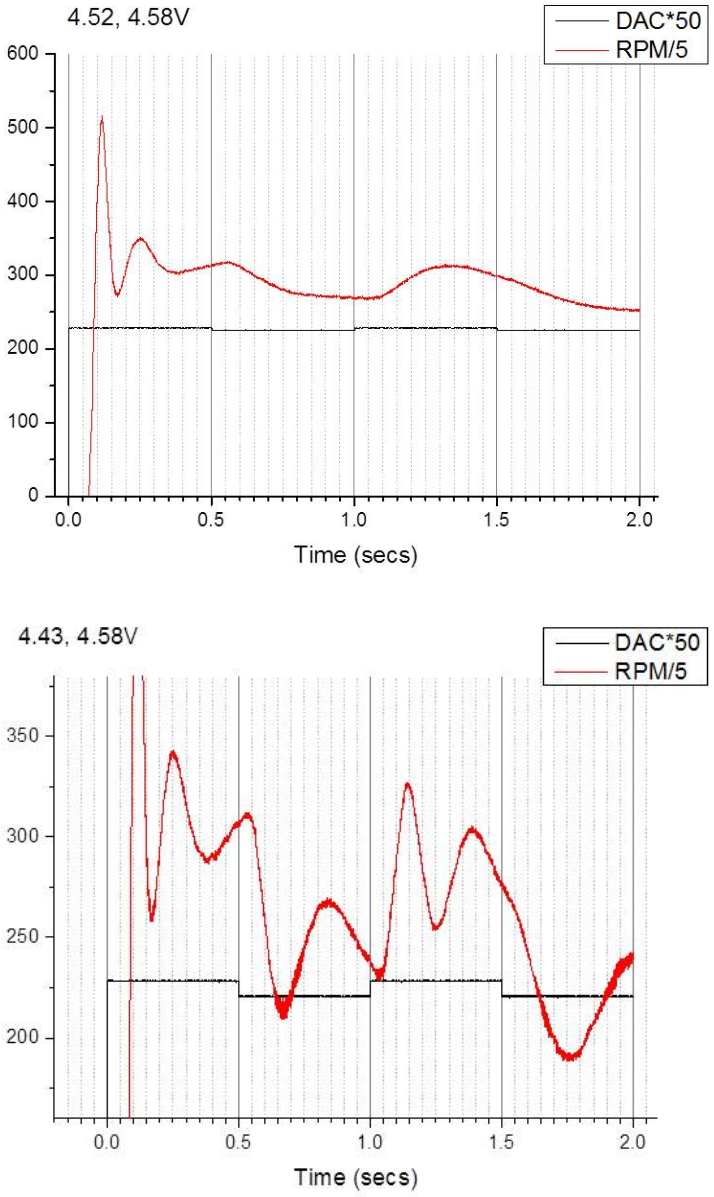

FIGURE 4.12: Early motor speed response to valve step voltage inputs (DAC = commanded digital values prior to digital to analog conversion)

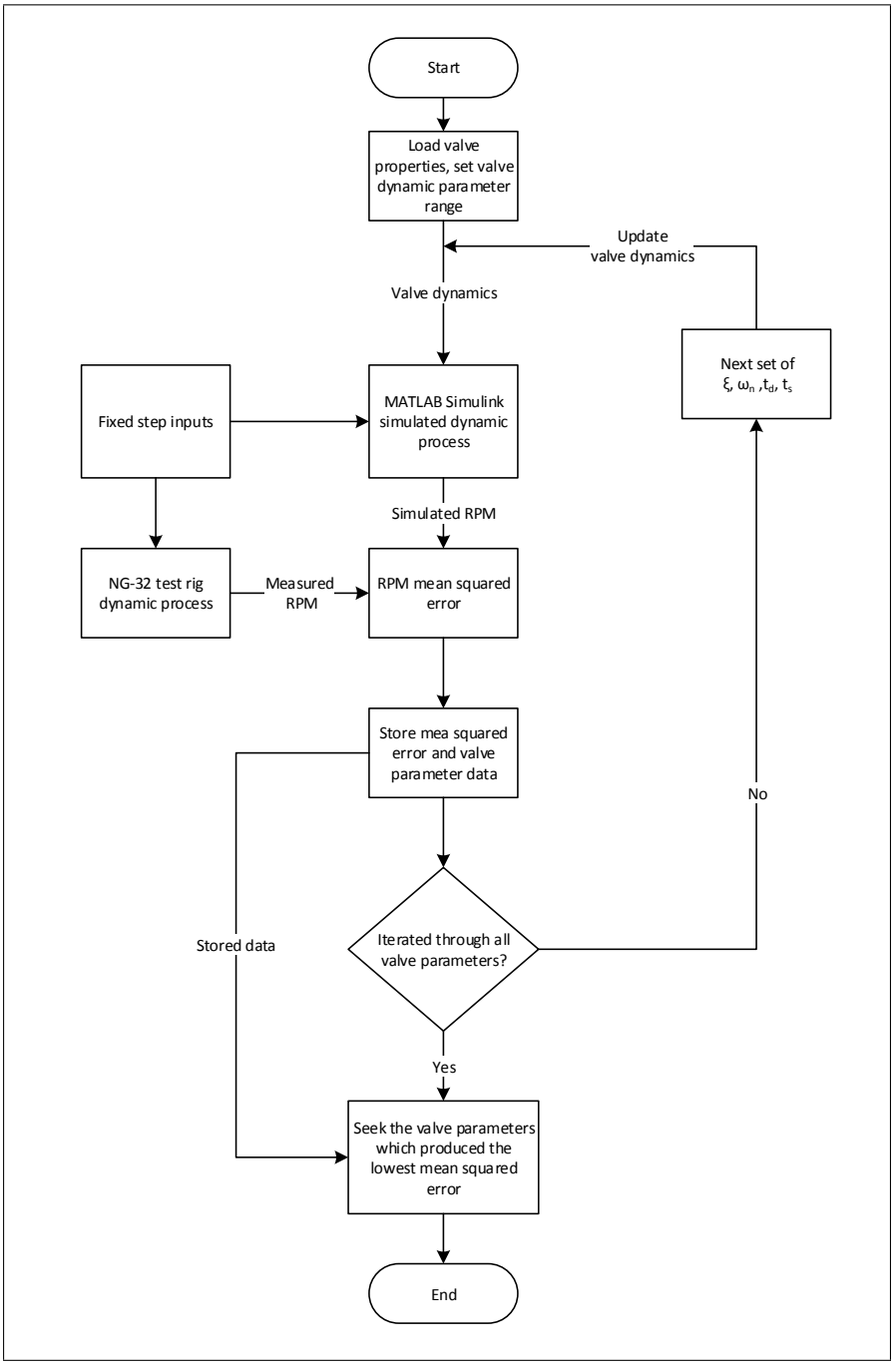

FIGURE 4.13: Least squared fit valve dynamic to measured RPM response process flow chart

Figure 4.13 depicts the approximation process used to obtain the spool dynamics. The free variables in the PTV spool dynamics parameters described by Equation 2.48 were varied through a range of values, and the squared errors between the measured and the simulated RPM generated from each combination of the parameters were collected. The optimal spool transfer function parameters were extracted from the field with the lowest mean squared error. The hydraulic motor parameters were entered according to Table

4.1, and the motor volumetric and overall efficiencies from the datasheet were estimated to be 90% and 87% respectively. The supply pressure was set to 80bars to agree with the experimental pressure. The Simulink dynamic process model used is shown in Figure 4.14.

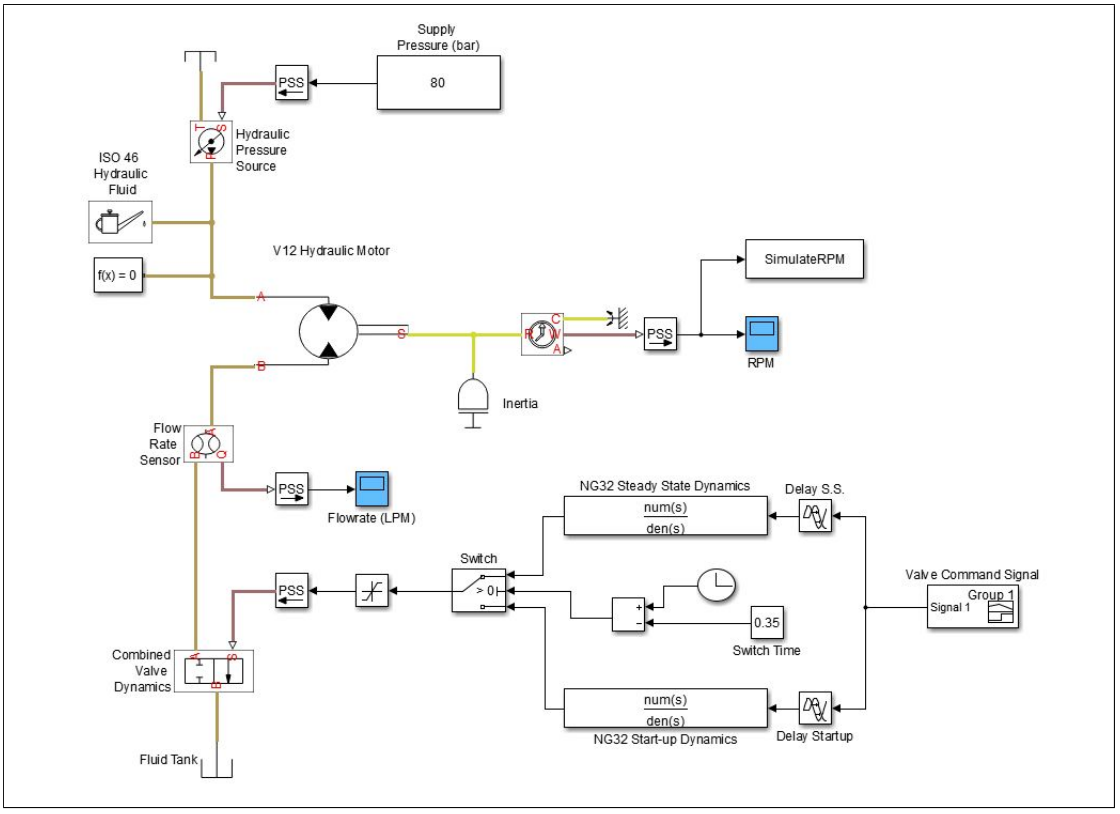

FIGURE 4.14: Matlab Simulink NG-32 dynamic model

The PTV dynamic fitting process was performed on four sets of RPM measurements, shown in Figure 4.15. The RPM measurement interval was set to the hardware minimum value of 1ms. Curves A), B) and C) in Figure 4.15 were produced by commanding the spool to move from the fully closed position at t=0.1s, and subsequently commanding to spool to move to a new position at t=0.35s. Curve D) was plotted by commanding the valve spool to step from fully closed position at t=0.15s to a new position at t=0.4s. Their step magnitudes are listed in the figure legends.

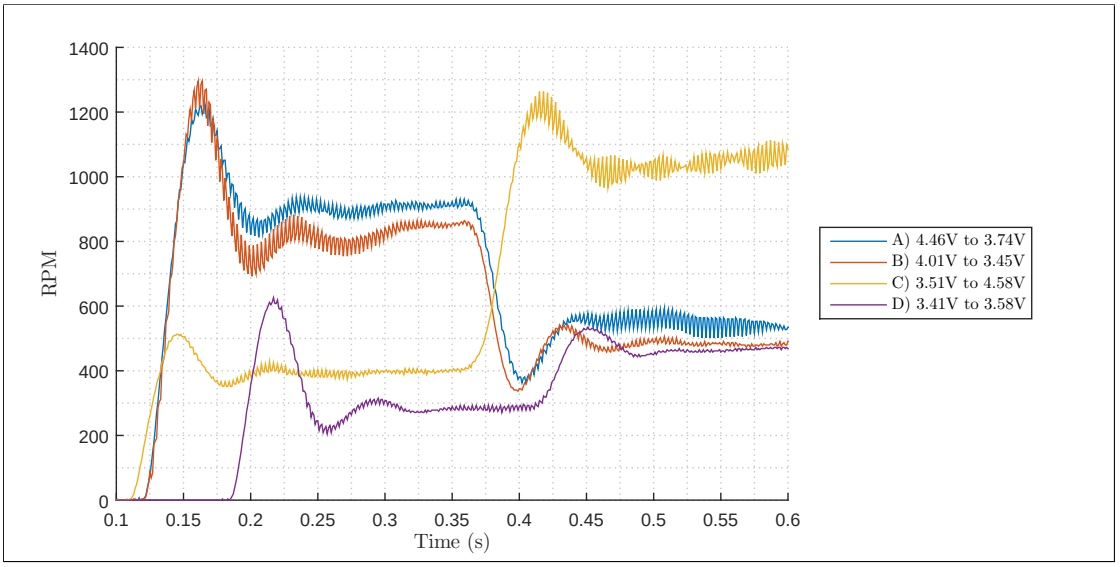

FIGURE 4.15: Matlab Simulink NG-32 dynamic model

Figure 4.15 shows that there is a discrepancy in dead time between opening the spool from a fully closed position and actuating the spool once the flow-rate reached steady state. The spool initializing dead time varied between 20ms to 80ms, and the steady state dead time varied between 9ms to 12ms.

The valve dynamics are approximated by fitting the simulated RPM outputs to the measured RPM observed after the spool has cleared the initial start-up dynamics, as the period of controller action takes place beyond the spool's initial dynamics. Figure 4.16 compares the truncated measured RPM outputs to the fitted simulated RPM using the method illustrated by Figure 4.13. The fitted spool dynamic parameters are tabulated in Table 4.3. Because the fitted parameters indicated that the valve dynamics vary with each voltage step experiment, the approximated dynamic used as a platform for controller design was chosen to be the average of the four step responses, which is shown in the last column of Figure 4.16.

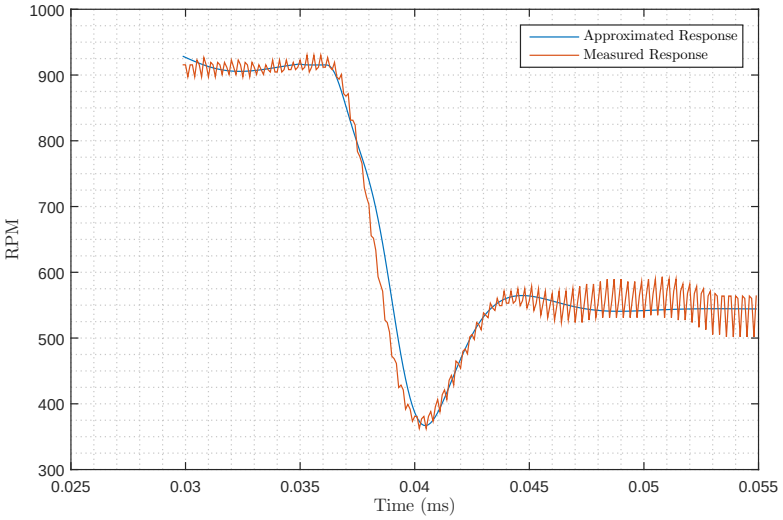

(A) Simulated RPM from least squared fitting vs measured RPM curves

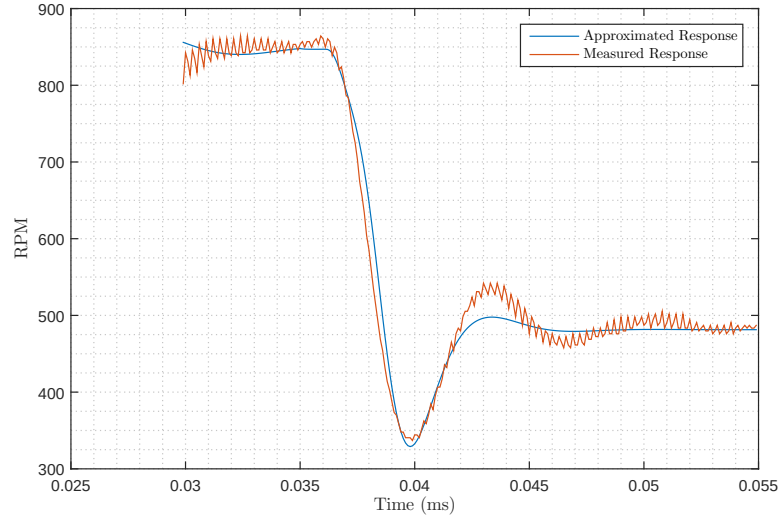

(B) Simulated RPM from least squared fitting vs measured RPM curves

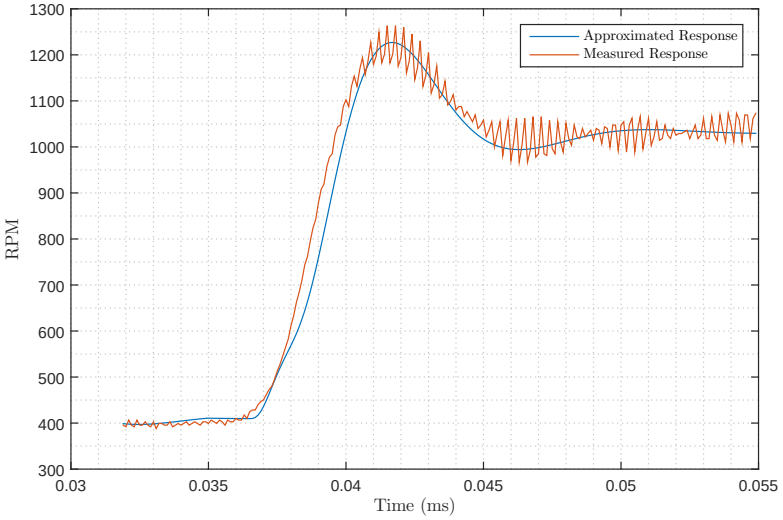

(C) Simulated RPM from least squared fitting vs measured RPM curves

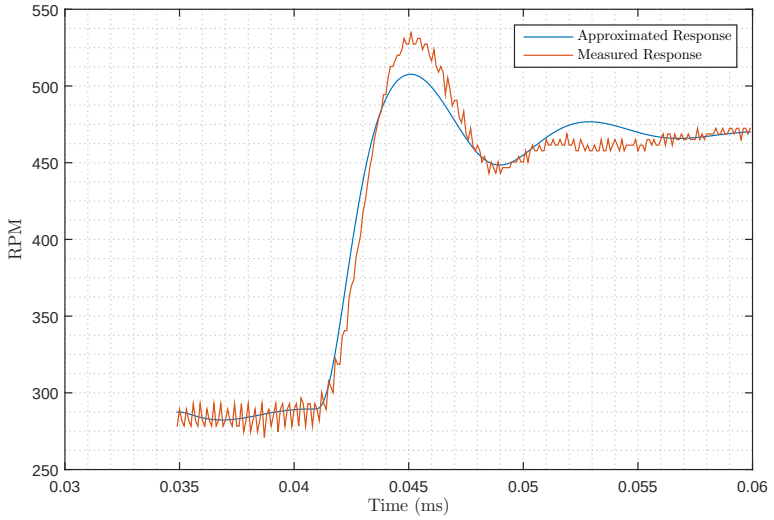

(D) Simulated RPM from least squared fitting vs measured RPM curves

FIGURE 4.16: NG-32 poppet dynamic approximations

TABLE 4.3: Fitted NG-32 valve spool standard transfer function parameters

Parameter	Delay (t_d)	Settling time (t_s)	Damping coefficient (ζ)	Natural frequency (ω_n)	Voltage steps	R^2
Figure 4.16A	0.011	0.068	0.51	86.51	4.12V to 3.49V	0.979
Figure 4.16B	0.011	0.053	0.54	104.82	4.01V to 3.45V	0.975
Figure 4.16C	0.015	0.084	0.44	75.98	3.51V to 4.58V	0.983
Figure 4.16D	0.009	0.133	0.27	83.54	3.41V to 3.58V	0.965
Average	0.012	0.085	0.44	87.7		

Finally, the NG-32 PTV spool dynamics is approximated by Equation 4.2:

$$H_{NG32aprox}(s) = \frac{e^{-0.012s}}{0.0001377s^2 + 0.01033s + 1} \tag{4.2}$$

4.2.2.4 NG-32 Replacement Proposal

An important factor in assessing the feasibility of utilizing the NG-32 PTV was the influence of the valve spool resolution on the controllable motor acceleration resolution. There is a minimum resolution in spool movement, which in turn affects the minimum quantum of acceleration which could be regulated. Prior to the formulation of an acceleration control scheme, the operating range of the valve was unknown, hence the valve performance adequacy was undetermined. After the NG-32 valve characterization process, which took place simultaneously with control scheme development, it was discovered that the NG-32 PTV spool resolution was insufficient to control the acceleration process variable. This section details the shortcomings of the ideal NG-32 PTV and compares the results with the newly selected NG-16 PTV by MATLAB simulation.

The valve pressure drop characteristics depend on the instantaneous flow-rate and the spool position. If the valve spool is set to stay stationary, an increase in flow-rate from the accelerating motor also increases the valve pressure drop. To maintain constant pressure drop across the motor, the spool must open incrementally to maintain a constant pressure drop through the valve. Comparing the control input range of a valve rated at a higher LPM with a valve rated at a lower LPM (i.e. large vs small orifice area), the valve with higher rated LPM must operate at a relatively smaller input range to provide the same orifice area as the valve rated at a lower LPM. This shorter range of valve input operating range combines with a fixed spool resolution results in a less resolvable pressure regulation.

To initiate the simulation describing the valve spool operating range, we first establish a PTV operating environment designed for the CGESS prototype. The hydraulic system operating variables are enumerated as follows:

1. The motor was set to accelerates at 320 rad/s^2 (80% of full acceleration)
2. The hydraulic motor displacement was set to 115cc/rev to drive the generator with the rated torque of 640Nm
3. The supply pressure was charged to the designed 350bar
4. The PTV was designed to dissipate 70bar of pressure

As shown in Figure 2.9, the datasheet specified flow coefficient mapped to the input voltages of the TDA NG series PTV has been derived. With the flow-coefficient tabulated, the input voltages can be obtained by solving Equation 2.16 with incrementing flow-rates at a constant pressure drop of 70 bar. The input voltages plotted against

rotor speed for the NG-32 and the NG-16 PTV is shown in Figure 4.17

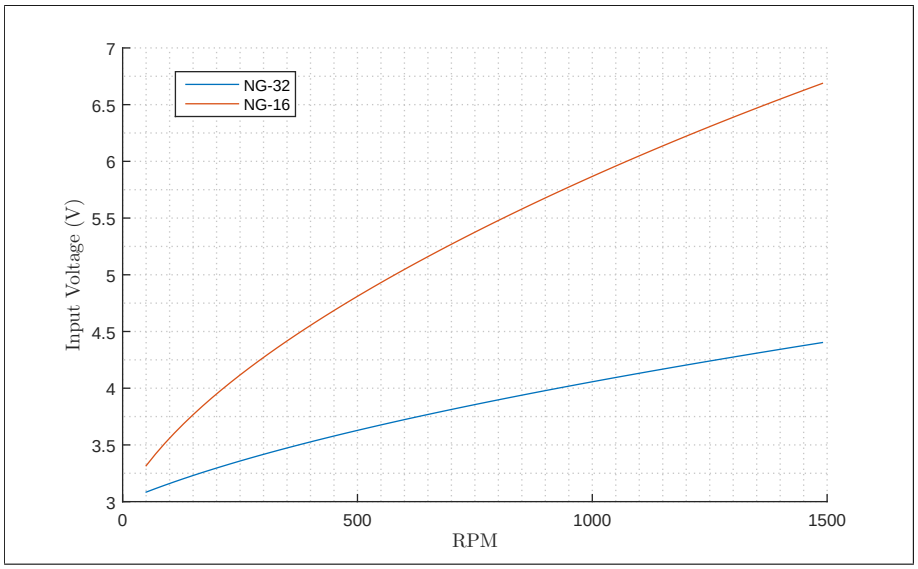

FIGURE 4.17: NG-32 PTV input required to maintain 320bar motor pressure

Figure 4.17 illustrates the difference between the voltage range using a NG-16 PTV and a NG-32 PTV to achieve the same 70bar of pressure drop. The NG-32 PTV operating input range spans from 3V to 4.4V, whereas the NG-16 utilizes a wider range of spool movements, ranging between 3V to 6.75V. The voltage range however cannot convey the PTVs' ability to resolve the acceleration variable, thus a numerical method was developed to study the change in pressure due to a small deviation in spool position from the steady state input. With each small signal spool perturbation, the flow-rate was assumed constant. The assumption was reasonable as the flow-rate cannot change instantaneously due to rotor inertia. This process is similar to small signal linearization, and the graphical illustration is shown in Figure 4.18.

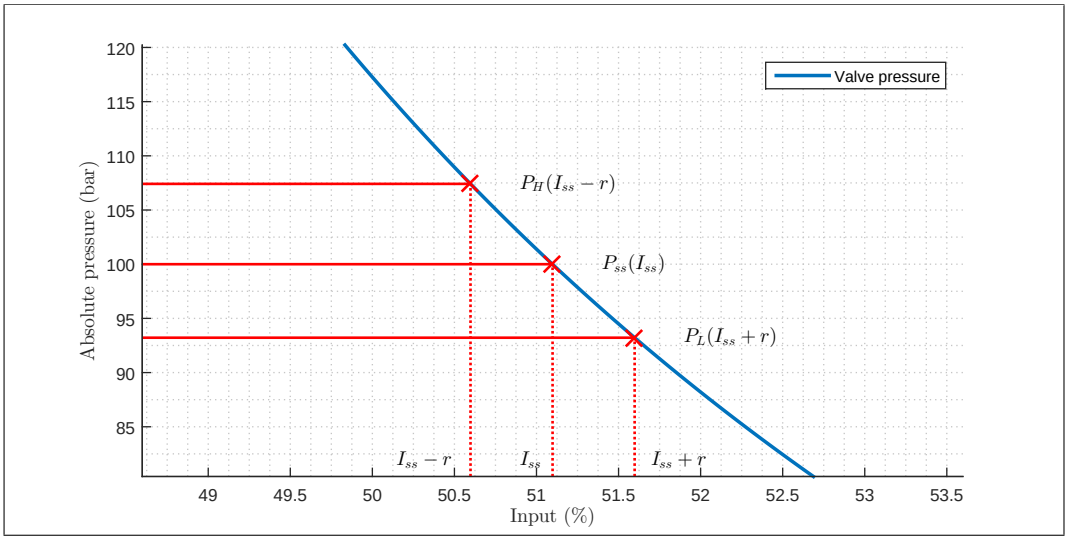

FIGURE 4.18: Example of an PTV pressure resolution derivation (I_{ss} = steady state input, r = minimum resolvable spool distance (%), P_{ss} = steady state pressure, P_H = pressure evaluated at low spool displacement, P_L = pressure evaluated at high spool displacement)

Figure 4.18 depicts the numerical differentiation method to determine the minimum change in pressure $P_H - P_L$ that is capable of being resolved by the spool. It is achieved by plotted the pressure vs percentage inputs expressed at a fixed LPM, and taking the difference between the pressures evaluated at two inputs displaced at a higher and lower point than the steady state input by the minimum resolvable spool movement. The steady state input in this case is taken at the established constant PTV pressure drop. With elapsing time, the LPM increases and so does dynamics of the pressure curve, thereby altering the change in pressure per spool resolution.

Since the motor pressure and valve pressure sums to the supply pressure, the loss of valve pressure is equal to the gain of the motor pressure; thus, the PTV pressure gradient value equates to the negative of motor pressure gradient value. The absolute change in acceleration is obtained by multiplying the pressure by the motor displacement using Equation 2.18) to get shaft torque, and divide the torque by the total CGESS shaft inertia. The percentage change in acceleration could then be obtained by normalizing the absolute change in acceleration with the desired motor acceleration.

As the Parker TDA series valve resolution was unspecified, 0.5% (which translates to voltage input resolution = 0.05V) of the maximum spool position was assumed to be the minimal be resolvable spool displacement, as suggested in Section 2.2.7.5. The resolvable acceleration v.s. the increasing flow-rate using the method outlined is shown Figure 4.19.

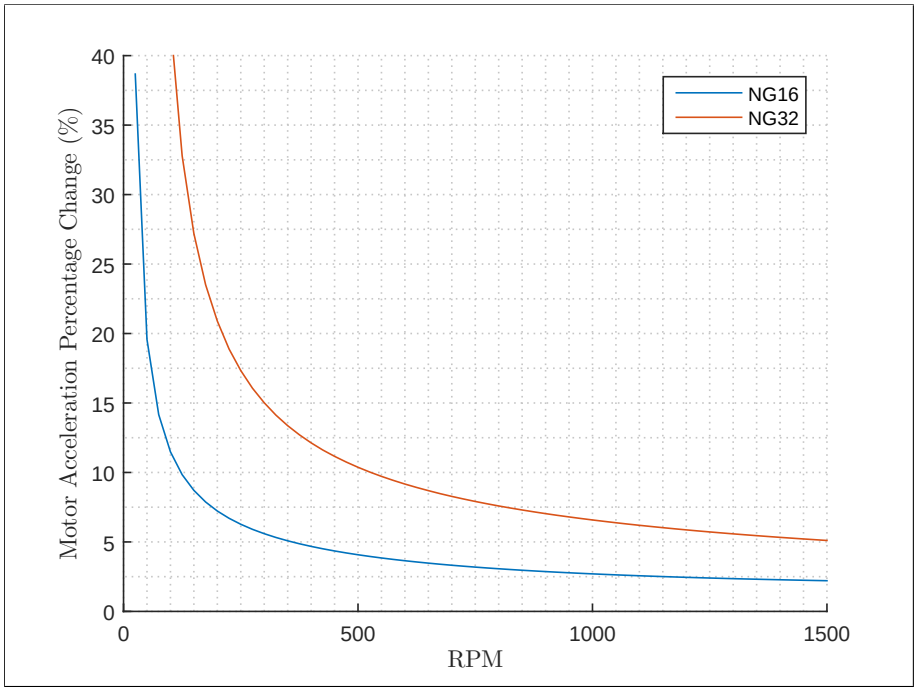

FIGURE 4.19: Percentage change in resolvable acceleration due to 0.5% change in spool movement deviated from steady state

Observation of Figure 4.19 suggests that the resolvable acceleration using the NG-32 valve is relatively unsatisfactory at lower RPM, where the control action takes place. The curve shows the NG-32 PTV attained acceleration resolution values of no better than 5% at half of the synchronization speed. The NG-16 PTV on the other hand improves the resolvable acceleration by a factor of 2. A suggestion was made to the EHL hydraulic engineer to replace the NG-32 with the NG-16 PTV and install a second PTV in series to extend the operating range, if the NG-16 acceleration resolution performance is found to be inadequate.

4.2.2.5 NG-16 PTV Test Benches Overview

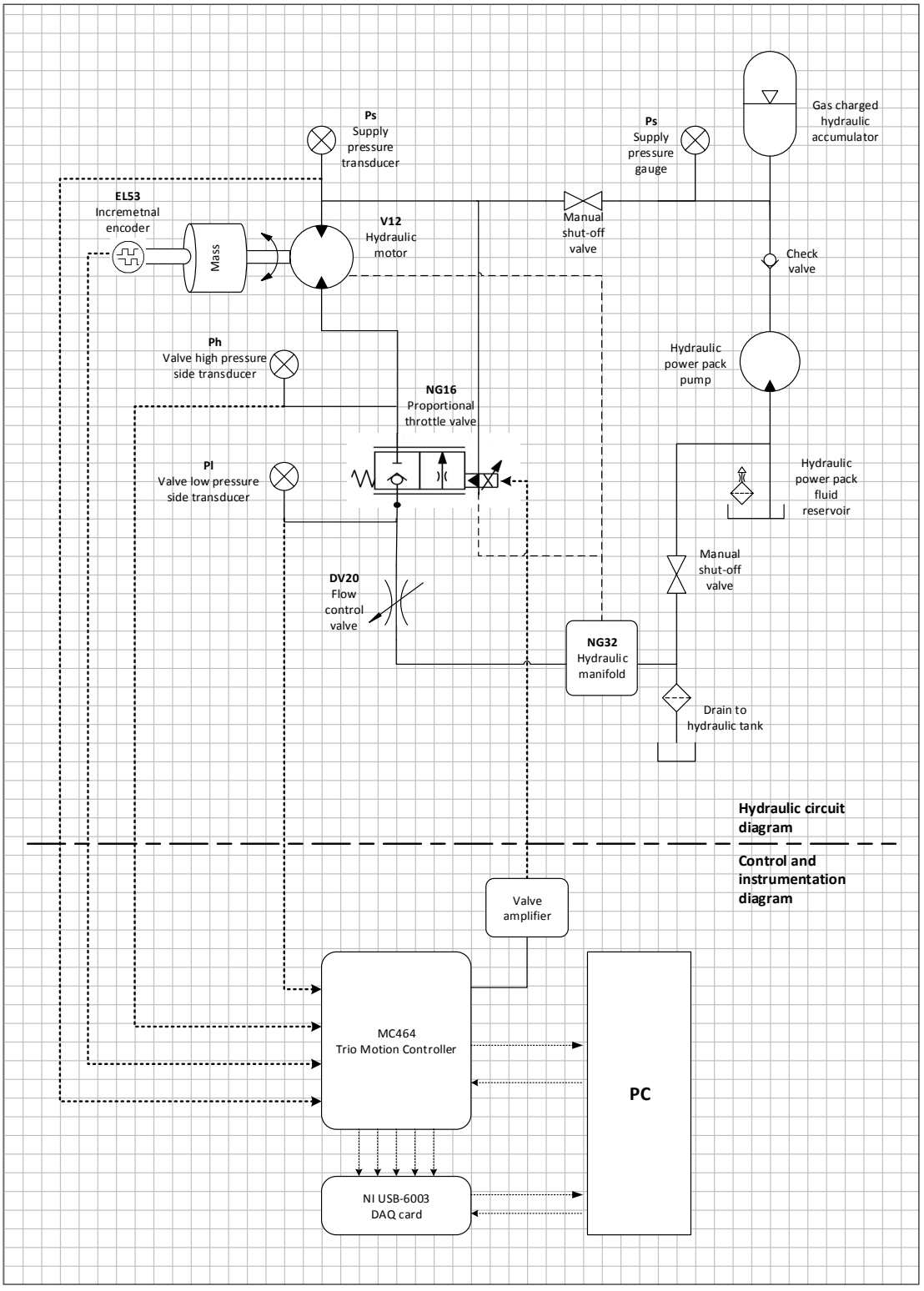

FIGURE 4.20: NG-16 valve characterization test-rig circuit diagram

As depicted by Figure 4.20, the NG-16 test trig was a modified NG-32 test rig designed to exhibit dynamics comparable with a scaled down CGESS system. Although the NG-32 hydraulic manifold was in already place, the valve housing dimensions on the manifold proved un-suitable for the smaller NG-16 valve. The original manifold block remained in the hydraulic circuit as the manifold was a part of the return path for the fluid. Thus, the NG-16 valve manifold was plumbed upstream to the DV-20 FCV while the poppet inside the NG-32 valve was removed. The pressure transducers were repositioned to measure the pressure differential across the NG-16 valve. The NG-16 manifold physical set-up is shown in Figure 4.21.

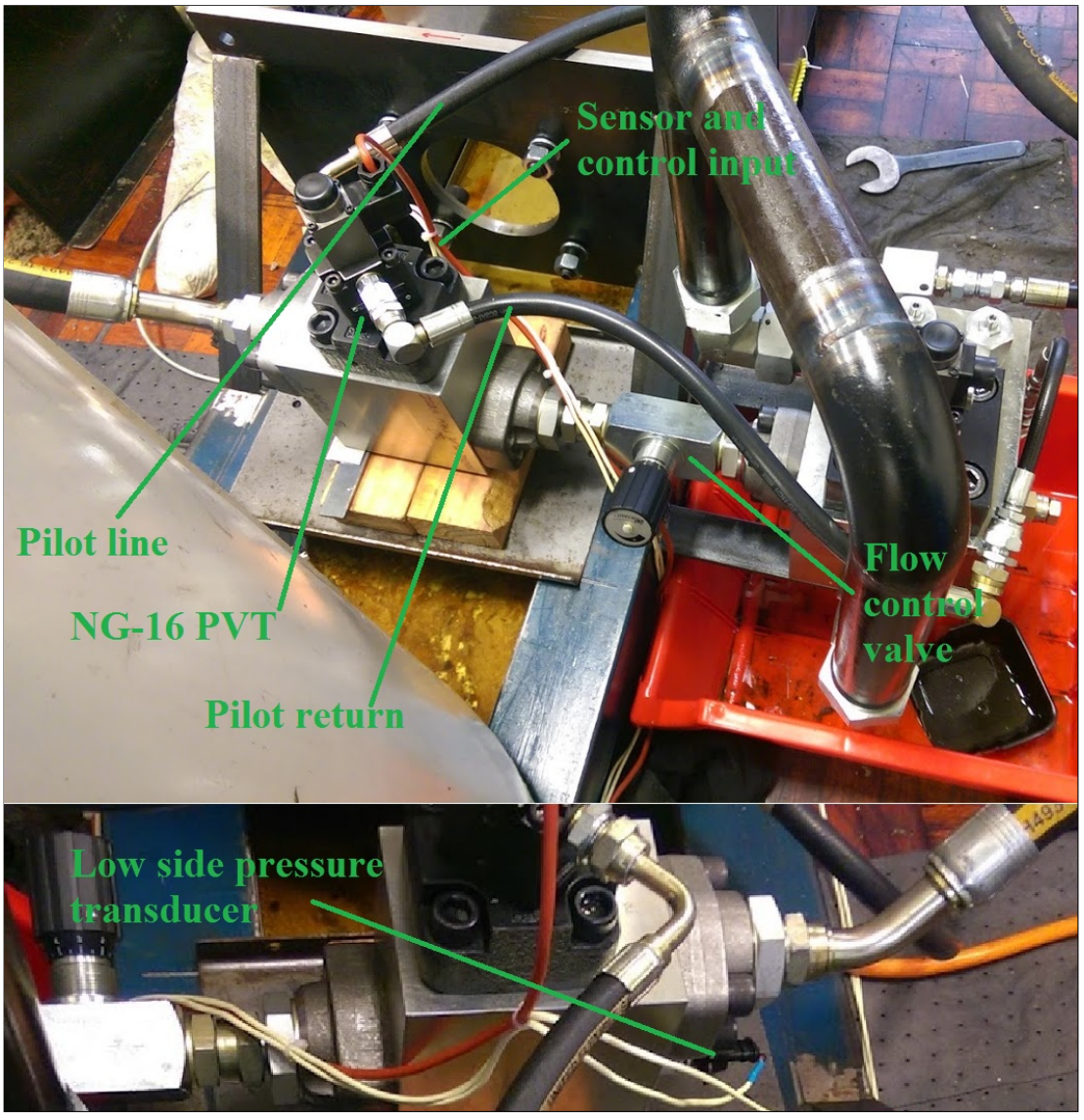

FIGURE 4.21: NG-16 valve hydraulic manifold physical assembly

Since the hydraulic motor shaft was uncoupled, the acceleration was expected to be extremely large; thus it was necessary to provide the motor with inertial load to reduce the acceleration. Observing Table 4.1, the NG-32 test-rig hydraulic motor acceleration

exceeds the CGESS prototype by a factor of 180. Without additional rotor inertia, the shaft speed reaches 1500rpm within 3ms*. Although fast acceleration results in quicker synchronization, which was the goal of this control algorithm; the hardware was incapable of controlling the drive system.

To suppress the excessive acceleration, the motor displacement was reduced to 16cc/rev, the supply pressure was reduced to 180 bar, and a steel cylinder with an inertia of 0.144kgm^2 was coupled to the shaft. Using the same technique illustrated in Section 4.2.2.4, the percentage resolvable acceleration was also plotted for this modified system, with the desired acceleration selected at 85 % of its maximum value. The parameter comparison between the CGESS prototype and the NG-16 test rig is are shown in Table 4.4, and the NG-16 resolvable acceleration relative to LPM is shown in Figure 4.22.

TABLE 4.4: CGESS prototype and NG-16 Test Rig Comparison

Parameter	CGESS Prototype	NG-16 Test Rig
Supply pressure	350 bar	180 bar
Max motor pressure	350 bar	180 bar
Motor displacement	115 cc/rev	16 cc/rev
Rotor inertia	1.545 kgm^2	0.144 kgm^2
Maximum torque	639 Nm	45.71 Nm
Maximum acceleration	400 rad/s^2	317 rad/s^2
Minimum servo period	1 ms	1 ms

*Under the assumption that the valve spool dynamics had infinite bandwidth

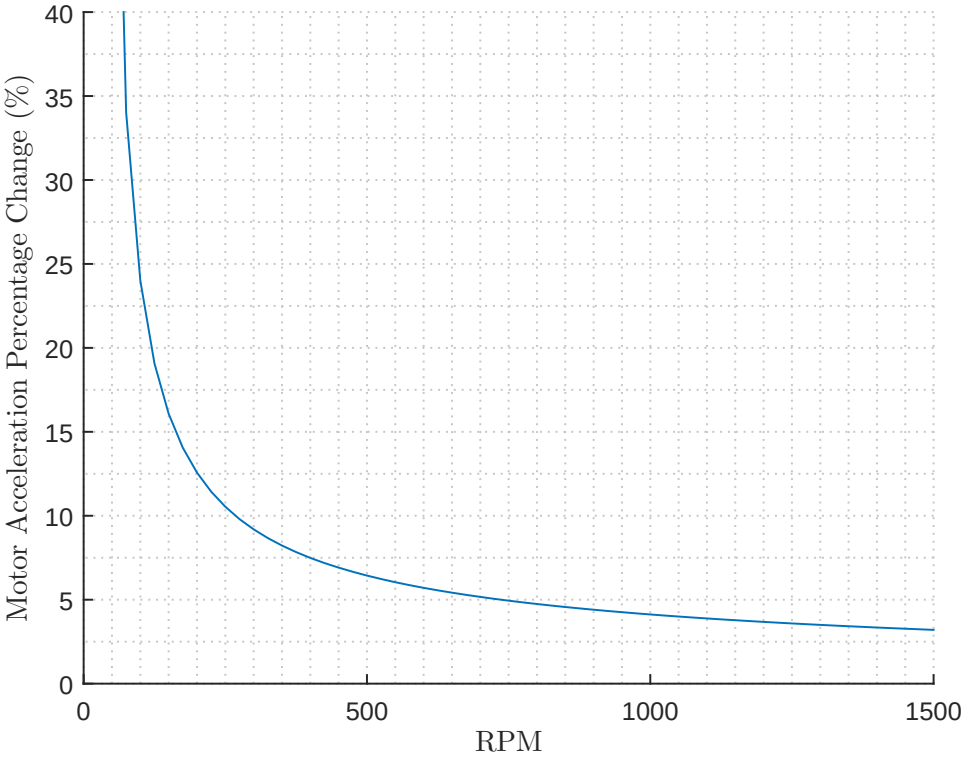

FIGURE 4.22: TDA NG-16 test-rig resolvable acceleration relative to flow-rate

The complete NG-16 test rig physical assembly is shown in Figure 4.23.

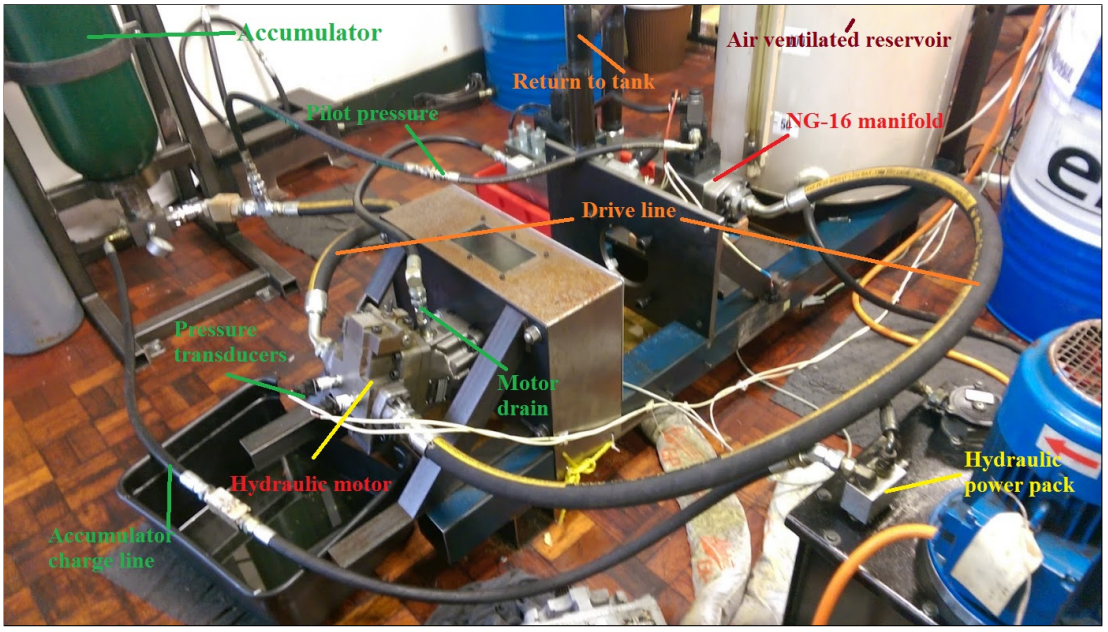

FIGURE 4.23: TDA NG-16 test-rig assembly without shaft inertia

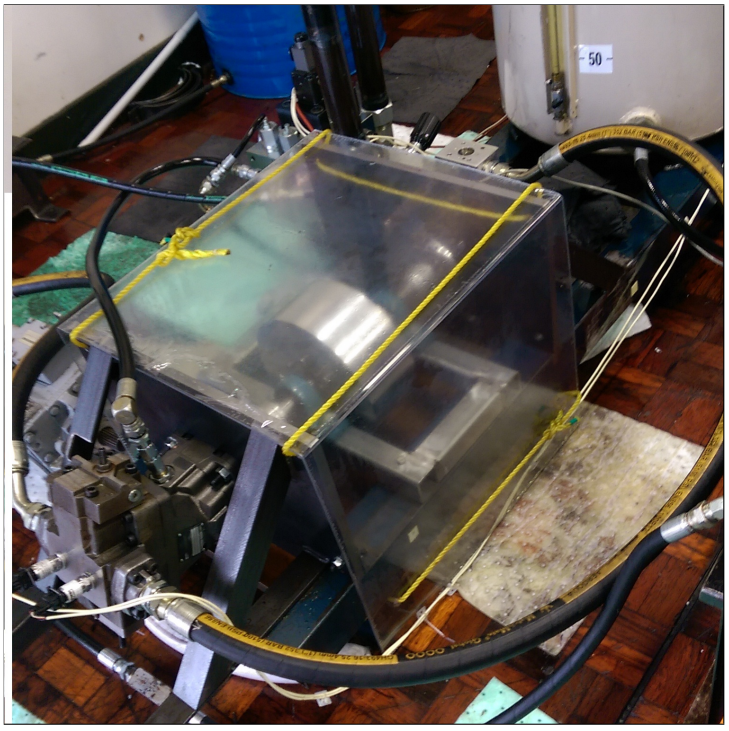

FIGURE 4.24: TDA NG-16 test-rig assembly with inertia

To avoid over-speeding the hydraulic motor, the DV-20 FCV was added to the drive system. Although the maximum hydraulic motor speed was rated at 6000 RPM, the audible noise due to the vibrating test rig was a major concern to the Callaghan team, thus the FCV orifice setting was allocated a much higher restriction than was required to limit the motor speed. The additional FCV orifice not only alters the pressure v.s. flow-rate relationship, but the rate of decay in available motor pressure is also increased, which may lead to the exhaustion of acceleration before the end of synchronization control can be reached. To ensure the pressure resource is adequate during the control period, the appropriate FCV setting had to be determined.

Within each test iteration, the FCV position was set and the RPM was recorded as the PTV was commanded to fully open. The final FCV gate was set at the level such that the recorded acceleration was not able to decay to less than 250rad/s^2 (80% of maximum motor acceleration) after 0.6 seconds (the time to reach synchronization speed at the designated acceleration). The RPM result measured with the final fixed FCV setting is shown in Figure 4.25, and the acceleration obtained from filtering the speed with a 50Hz cut-off 4th order low pass Butterworth filter is shown in Figure 4.26. A total of 7 experiments using the same FCV setting were performed to assess the consistency of the results.

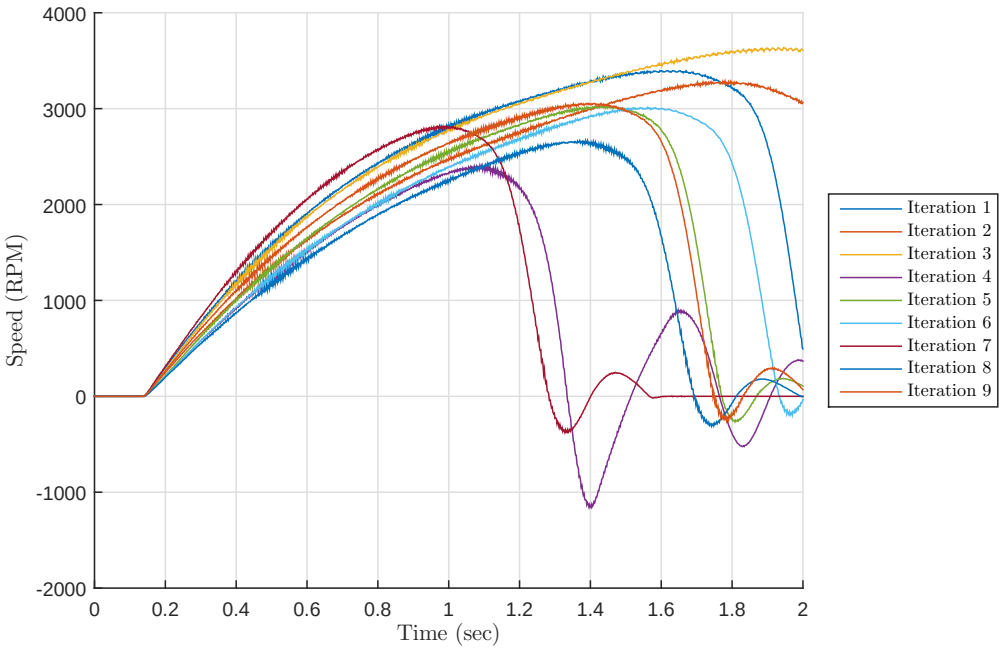

FIGURE 4.25: Repeated RPM responses from step opening NG-16 FCV to maximum position

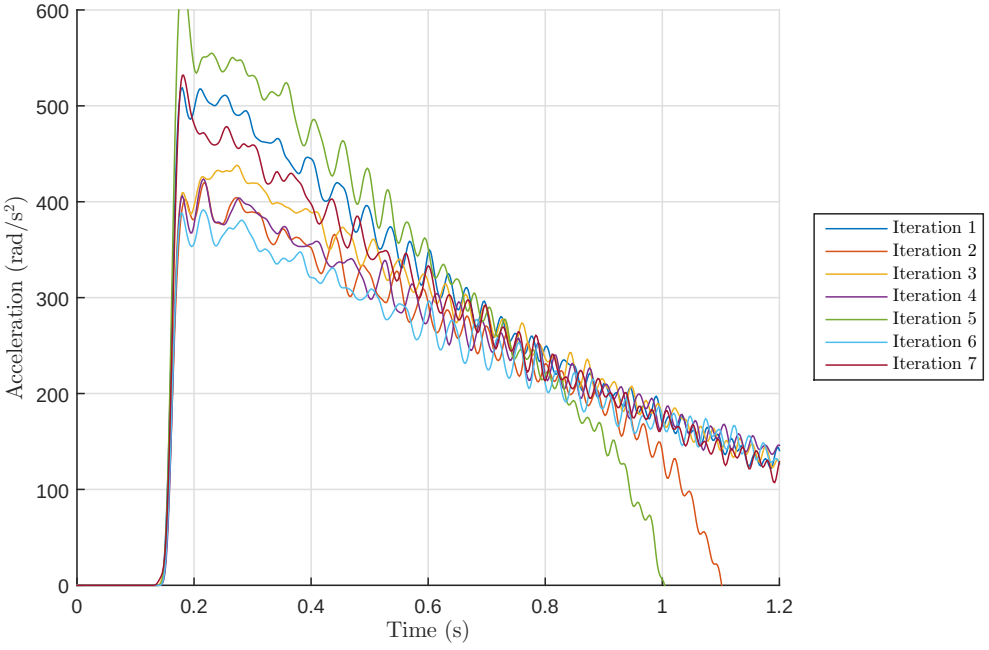

FIGURE 4.26: Motor shaft acceleration

Figures 4.28 and 4.25 demonstrated that the process repeatability was extremely poor. Despite commanding the valve to fully open with the same input, the peak and the decay in acceleration varied. Observing the pressure measurements shown in Figures

4.27 and 4.28, the culprit of the acceleration fluctuation appeared to be the FCV, which exhibited dynamics similar to an inconsistent orifice area. Although it may be necessary to replace the FCV, due to the limited funding and time of the project, the FCV stayed in the drive system. The inconsistent behavior of the test system wasn't expected to be transfered to the final system.

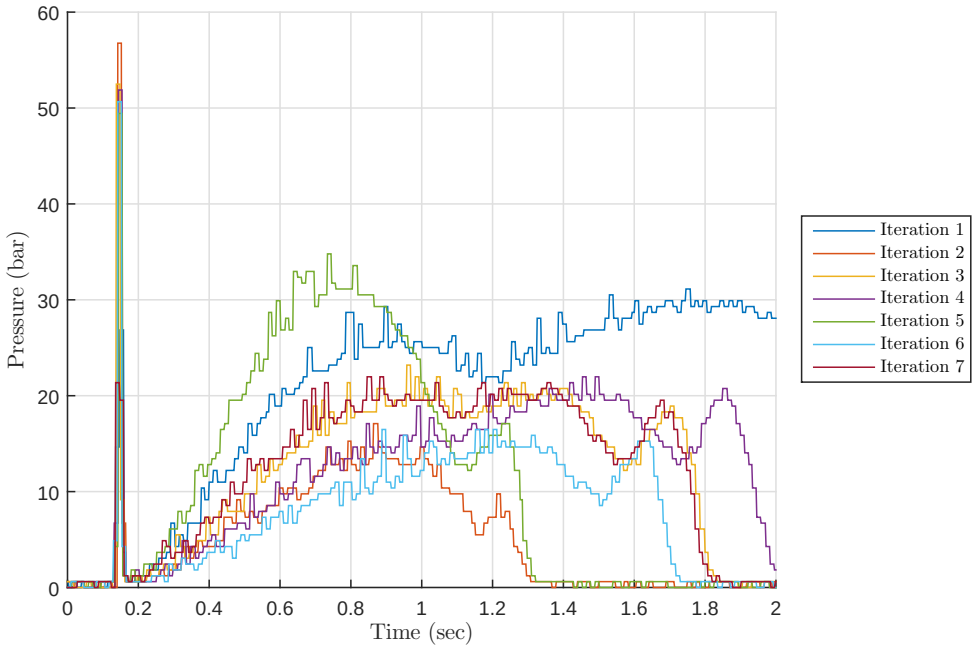

FIGURE 4.27: DV-20 FCV pressure drop tested with max PTV opening

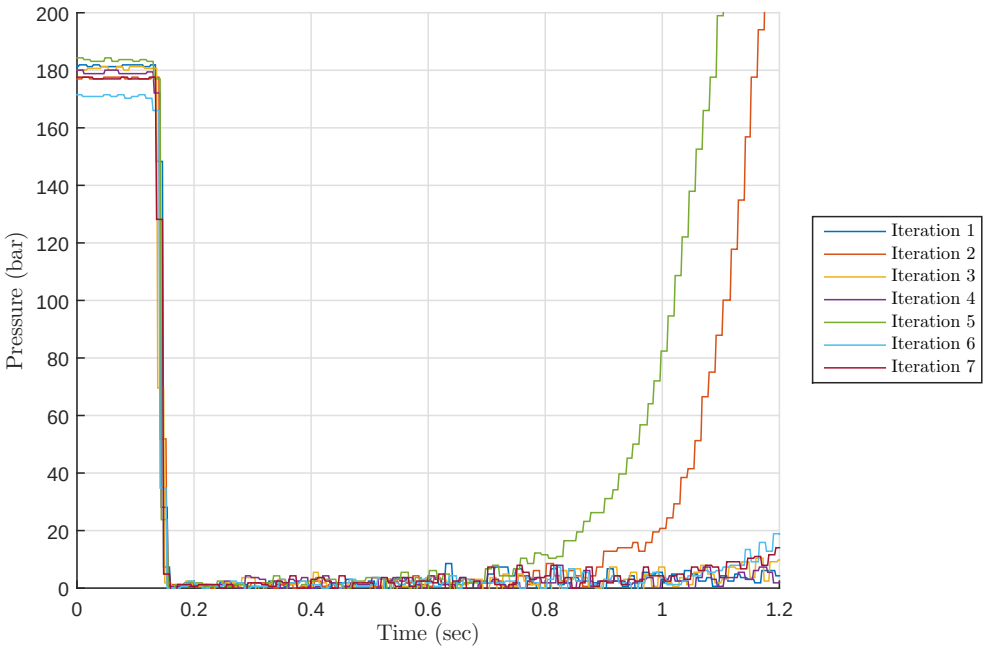

FIGURE 4.28: NG-16 PTV pressure drop test with max PTV opening

4.2.2.6 NG-16 PTV Pressure Flow-rate Identification

With the same methodology used in the NG-32 PTV characterization, the NG-16 PTV behavior was also recorded. The pressure dynamics of the NG-16 PTV, the fixed setting DV-30 FCV and the combination of the two orifices are shown in Figures 4.29, 4.30 and 4.31. The flow-rate through both orifices is shown in Figure 4.32.

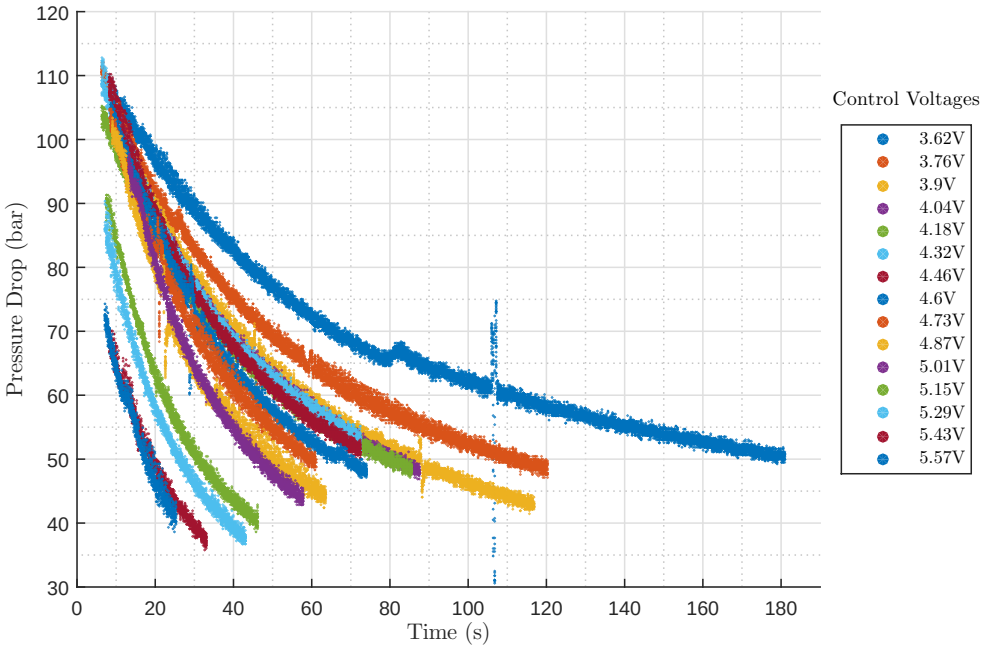

FIGURE 4.29: TDA-NG16 pressure drop vs time

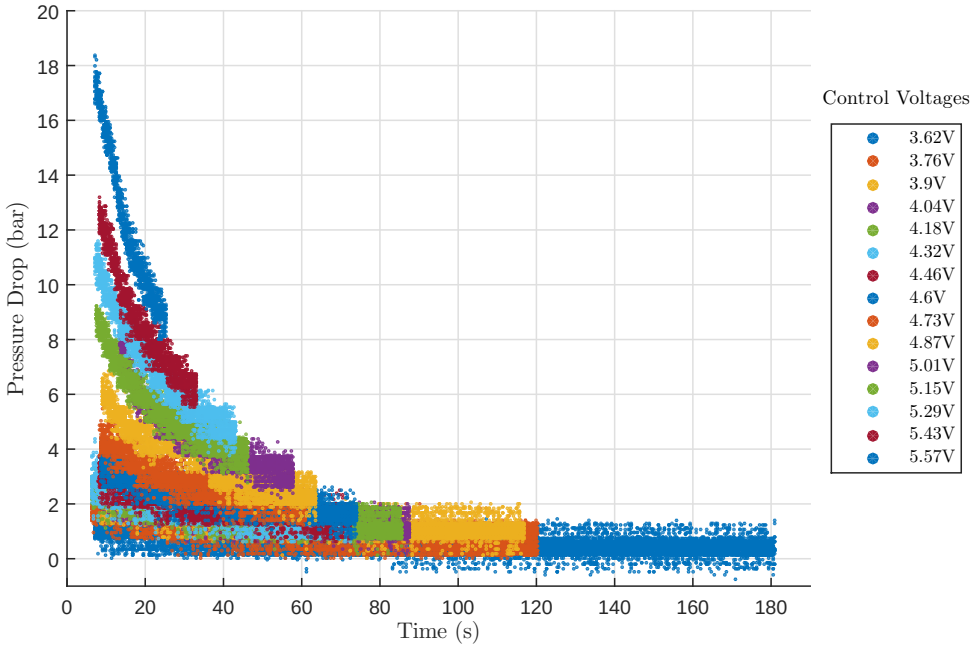

FIGURE 4.30: DV20 flow control valve pressure differential curve measured with varying TDA-NG16 control input voltages

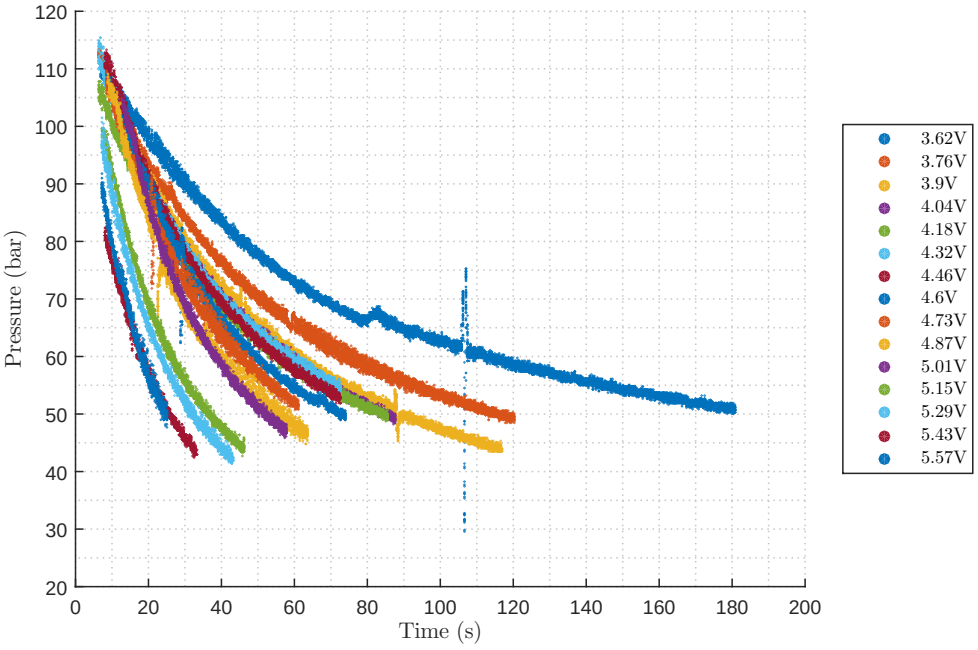

FIGURE 4.31: Motor low pressure side

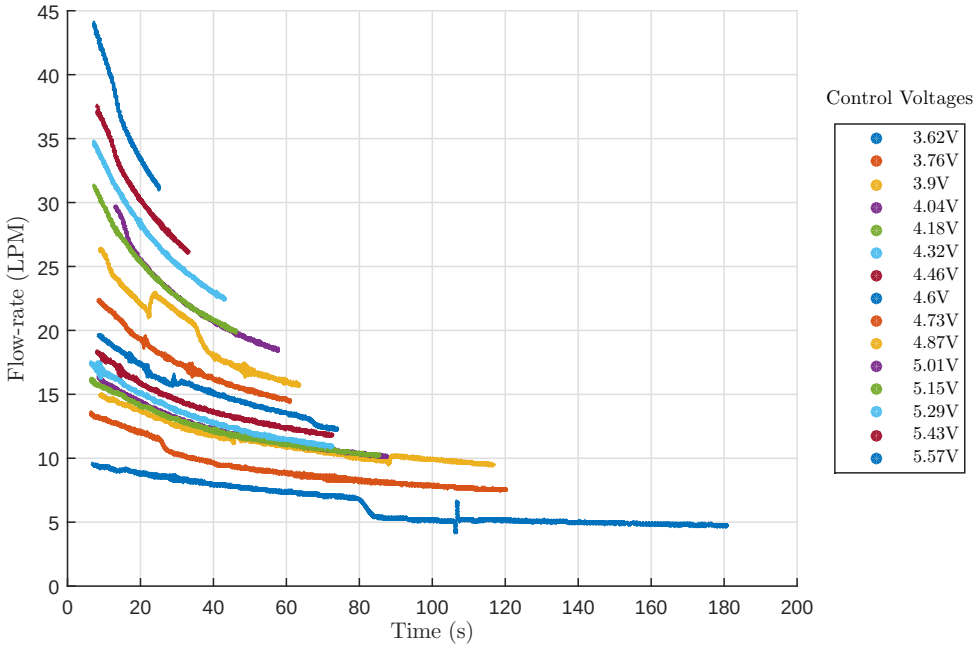

FIGURE 4.32: Flow-rate measured with varying TDA-NG16 control input voltages

The control voltage range was originally intended to span up to 10 volts, as this was the range specified by the NG-16 datasheet. The limited control voltage steps shown in Figures 4.32,4.29, and 4.30 were due to the catastrophic failure of the test rig from the inappropriate design of the over-speed shut-down sequence, where the valve was step shut when over-speed was detected. Unlike the original hydraulic assembly where the fluid inertia was negligible due to the lack of a coupled shaft mass and the inclusion of pressure bypass valves, the damage generated by the hydrostatic shock from the sudden closure of the PTV blew the NG-16 poppet and solenoid out of its housing manifold and fractured the encoder flex-coupling. The shut down sequence resulted in a permanently incapacitated test rig and prevented any future experiments allowed by the thesis time frame. The damaged manifold is shown in Figure 4.33.

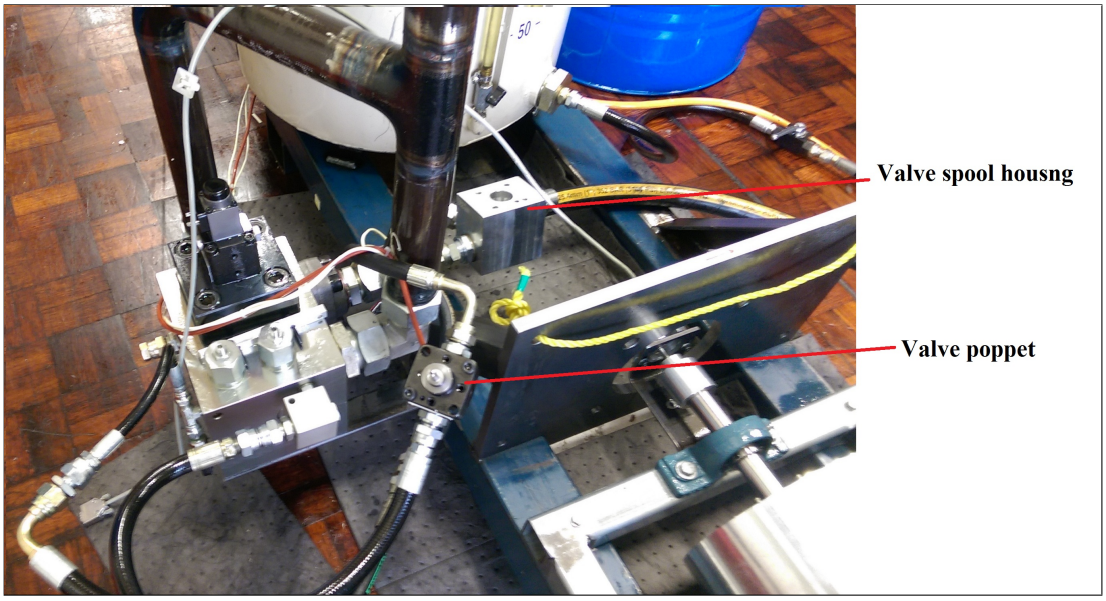

FIGURE 4.33: NG-16 valve poppet and bolts stripped out of it's housing manifold socket due to over pressure

Nevertheless, combining the data shown in 4.32 and 4.29, the partially recorded pressure v.s. flow-rate can be calculated and plotted. The results are shown in Figures 4.34, 4.35 and 4.36.

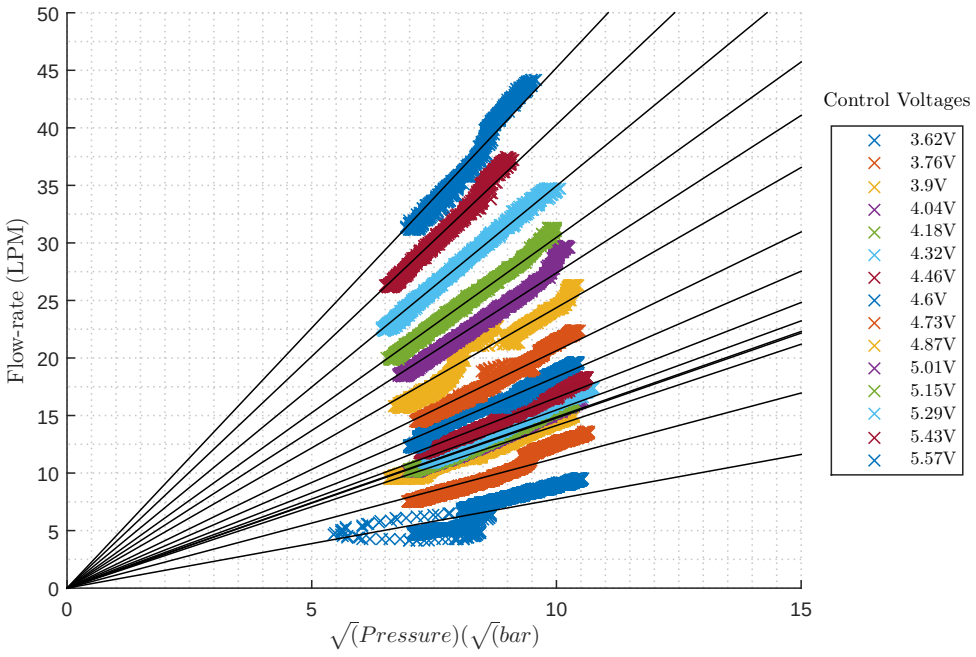

FIGURE 4.34: Combined pressure vs flow-rate relationship

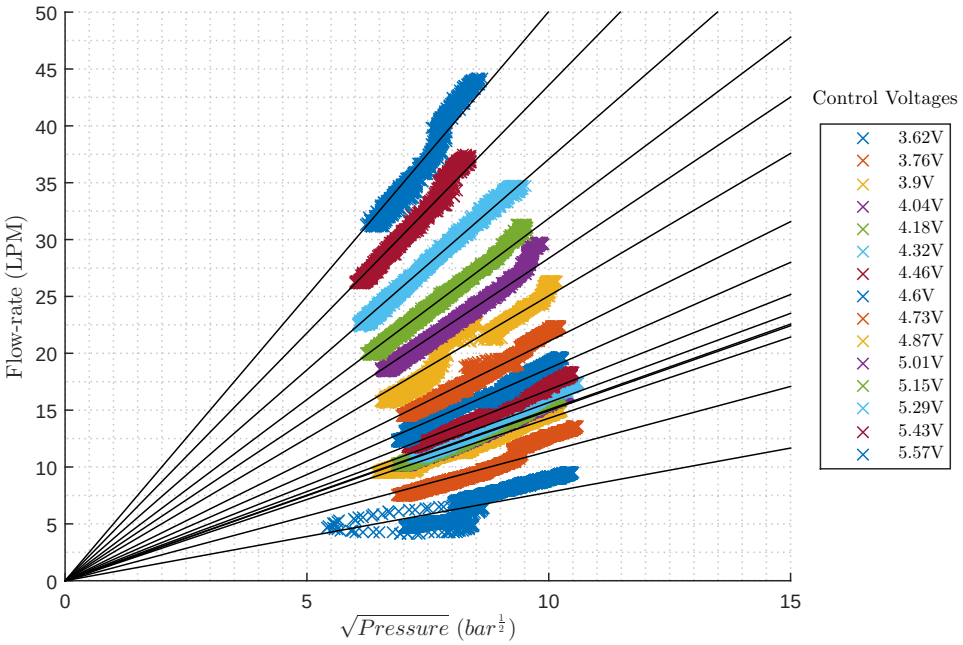

FIGURE 4.35: Scaled NG-16 PTV pressure v.s. flow-rate

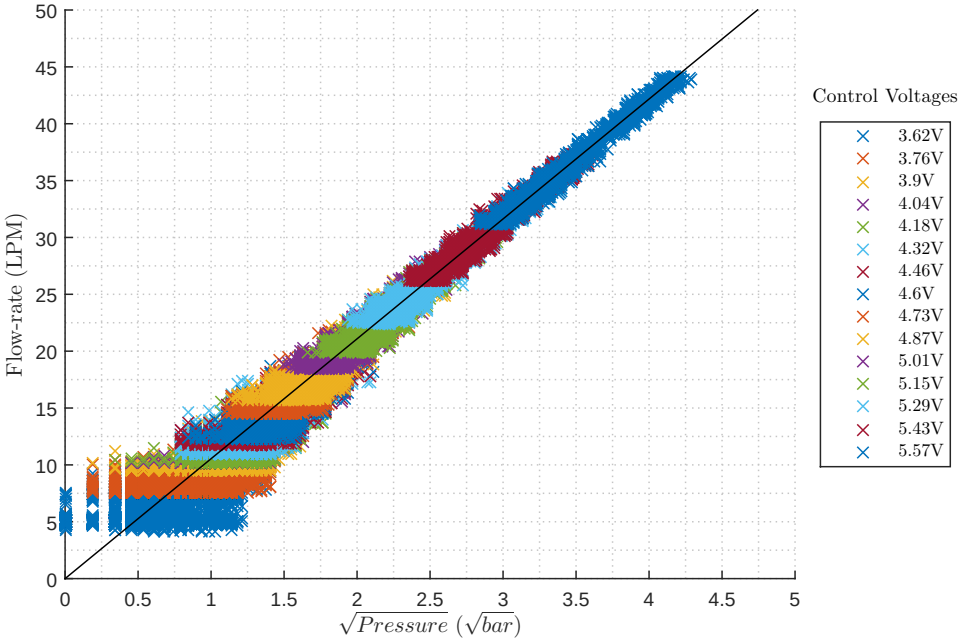

FIGURE 4.36: DV-20 FCV pressure flow profile

Figure 4.36 indicated that with lower PTV inputs, the pressure drop was almost constant regardless of flow-rate. Figure 4.37 compares the NG-16 datasheet flow coefficients and the results from of mapping the input voltage to the flow coefficient obtained from measurement data.

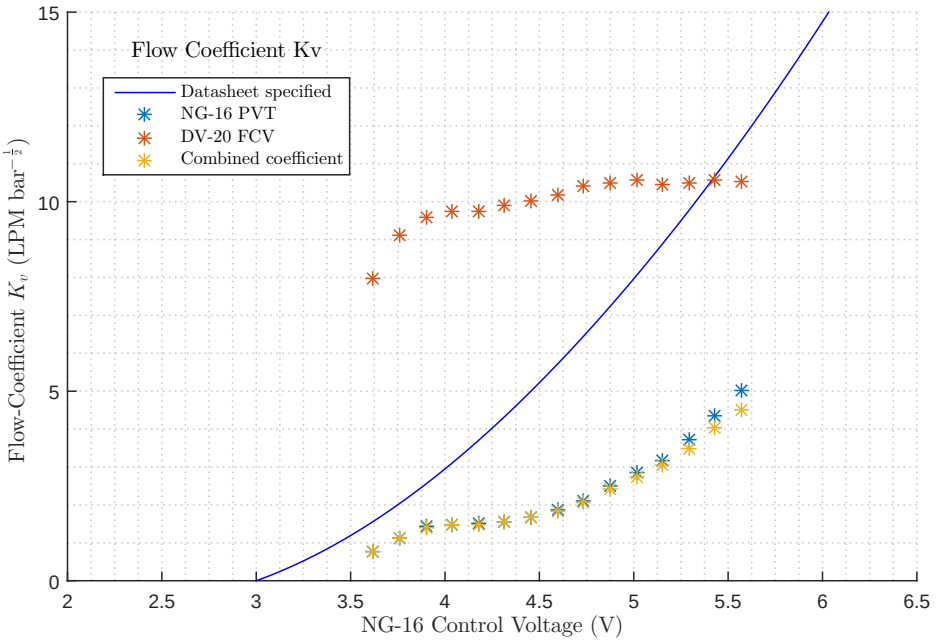

FIGURE 4.37: Flow coefficient to control voltage map

Two non-ideal behaviors can again be observed in Figure 4.37. Firstly, the poppet movement between the control input of 3.9 to 4.2 V is seen unresponsive and secondly, the ideal flow coefficient seemed much higher than the measured coefficient. The difference between the flow-coefficients suggested that 1) the orifice area appears to be less than the specified value, or 2) the current output of the Callaghan made amplifier did not directly scale to spool position according to the datasheet. Other possible causes of the perturbation from the ideal valve characteristics could be attributed by the valve manifold construction, decaying pilot pressure, and errors due to varying volumetric efficiencies of the motor. Regardless of the results, the flow coefficient derived from the measurement can also be use for hydraulic system modeling in Simulink.

4.2.2.7 NG-16 PTV Poppet Dynamic Identification

Unfortunately, no data with sufficient time resolution was recorded prior to the destruction of the test rig. The RPM values recorded to validate the functionality of the drive system and instrumentation were recored with 10ms time intervals, and was too sparse to capture the dynamics of the NG-16 PTV spool. The NG-16 spool dynamics was approximated by the NG-32 dynamics, which is shown in Equation 4.2. The datasheet specified NG-16 dynamics are shown in Figure 4.38, its transfer function is given by Equation 4.3, and its standard second order parameters are tabulated in Table 4.5.

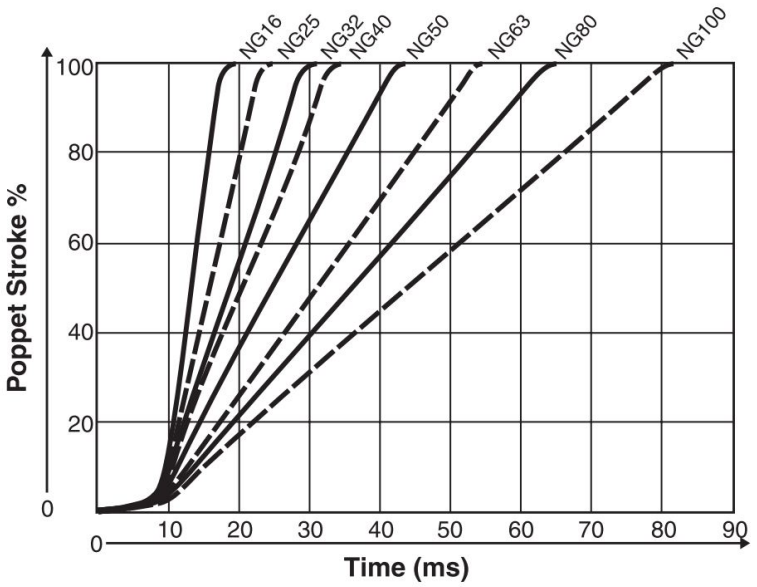

(A) NG-16 datasheet poppet response

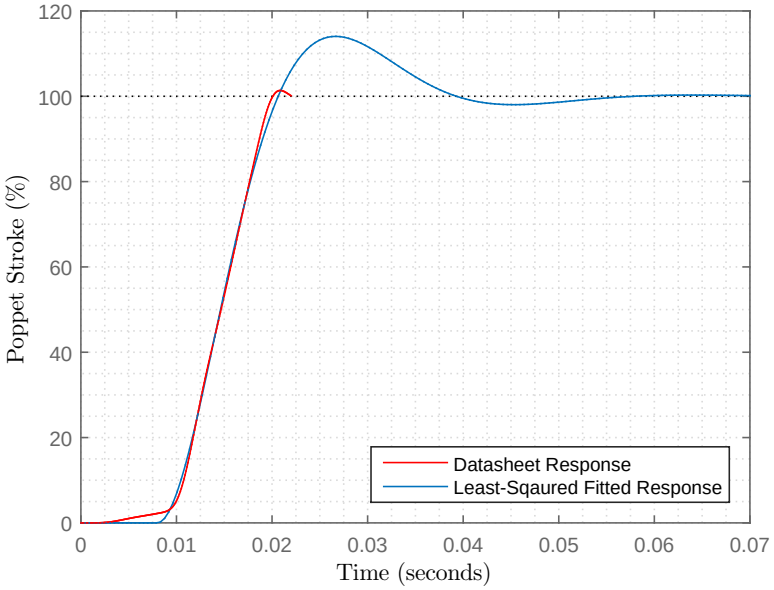

(B) NG-16 approximated valve poppet dynamics

FIGURE 4.38: NG-16 poppet dynamic approximation

$$H_{NG16aprox}(s) = \frac{e^{-0.008s}}{0.00002535s^2 + 0.005337s + 1} \tag{4.3}$$

TABLE 4.5: Approximated NG-16 PTV spool transfer function parameters from datasheet

Parameter	Symbol	Value
Delay	t_d	0.008
Settling time	t_s	0.019
Damping coefficient	ζ	0.53
Natural frequency	ω_n	199

Chapter 5

Synchronization Controller Design

5.1 Chapter Structure

This chapter first introduces the concepts behind the acceleration control, describes the small signal modeling of the hydraulic power drive system and controller design methodology, and concludes with a set of successful synchronisation results simulated with a wide range of simulation conditions and hydraulic component behaviors.

5.2 Acceleration Control Scheme

5.2.1 Introduction

An earlier synchronization control scheme was based on modify traditional synchronisation procedure. By firstly fully opening the PVT, then switching to an active phase tracking control once the generator frequency is near synchronous speed, the time the for phase difference to converge to zero is reduced. Using this method however introduces an unpredictable step torque change related to the phase difference at the switchover point. Furthermore, since the generator acceleration is already at maximum value prior to phase control, the only possible control effort was to decelerate the generator, which requires negative pressures across the hydraulic motor. As the PTV rated pressure is exceeded to achieve the negative motor pressure, this approach cannot be employed. Instead, a constant generator acceleration demand can be calculated to continuously track the EPS from the start such that the step torque variation can be eliminated.

5.2.2 Optimal Acceleration Derivation

The acceleration demand scheme is based on calculating a fixed shaft torque such that the error between the grid and the generator phase angles is zero at the time when

the generator frequency matches the grid frequency. The graphical visualization of this concept is illustrated by Figure 5.1.

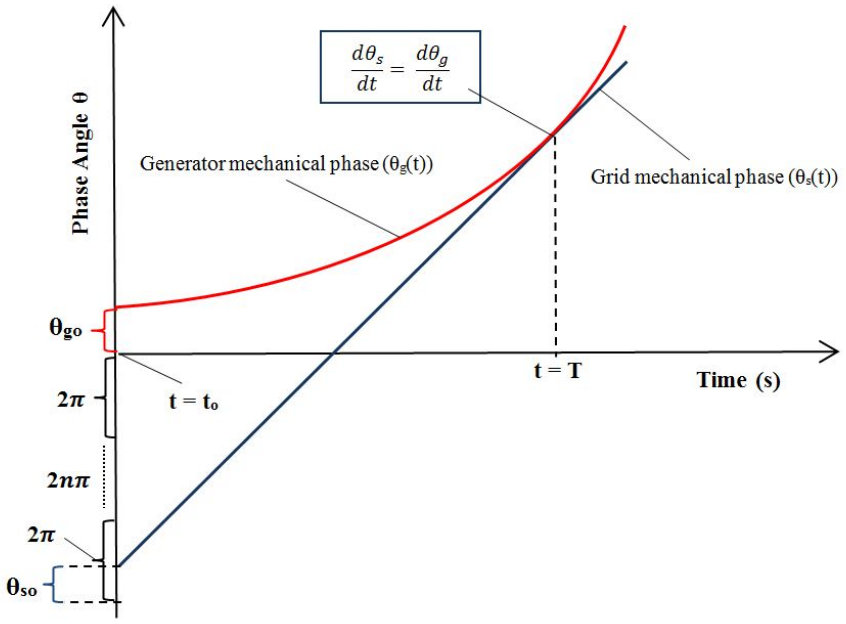

FIGURE 5.1: Acceleration Control Visual Representation

The acceleration demand formula is derived from the fundamental rotational kinematic equations given by Equations 5.1 and 5.2:

$$\theta_f = \int_0^T \omega(t)\,\mathrm{d}t + \theta_i \tag{5.1}$$

Where	θ_f	is the angular displacement at final time T	(rad)
	θ_i	is the initial angle	(rad)
	$\omega(t)$	is the rotational speed as a function of time t	(rad/s)
	T	is the final time	(s)

$$\omega_f(t) = \int_0^T \alpha(t)\,\mathrm{d}t + \omega_i \tag{5.2}$$

Where	ω_f	is the rotational speed at final time T	(rad/s)
	ω_i	is the initial rotational speed	(rad/s)
	$\alpha(t)$	is the rotational acceleration as a function of time t	(rad/s^2)

The mathematical expressions describing the equivalence in frequency and phase of the power grid and the generator after some time T_{sync} are given in Equations 5.3 and 5.4*.

$$\omega_g(t_0) + \int_{t_0}^{T_{sync}} \alpha_g(t)\,\mathrm{d}t = \omega_s(t_0) + \int_{t_0}^{T_{sync}} \alpha_s(t)\,\mathrm{d}t \tag{5.3}$$

$$\theta_g(t_0) + \int_{t_0}^{T_{sync}} \omega_g(t)\,\mathrm{d}t = \theta_s(t_0) + \int_{t_0}^{T_{sync}} \omega_s(t)\,\mathrm{d}t \tag{5.4}$$

Where	t_0	is the current sampling time	(s)
	T_{sync}	is the time the phase and frequency errors will be zero	(s)
	$\omega_s(t_0)$	is the grid speed sampled at t_0	(rad/s)
	$\omega_g(t)$	is the generator speed as a function of time t	(rad/s)
	$\omega_s(t)$	is the grid speed as a function of time t	(rad/s)
	θ_{go}	is the generator phase sampled at the current time t_0	(rad)
	θ_{so}	is the grid phase sampled at the current time t_0	(rad)
	$\alpha_g(t)$	is the generator acceleration at time t	(rad/s^2)
	$\alpha_s(t)$	is the grid acceleration at time t	(rad/s^2)

Several assumptions were made to simplify the above expressions. The generator initial speed was set to zero since the rotor is at rest prior to applying shaft torque, the grid frequency variation is negligible within the control time period, and the generator acceleration can be regulated to a constant value. These assumptions translate to: $\alpha_s(t) = 0$, $\omega_s(t) = \omega_{so}$, and $\alpha_g(t) = \alpha_g$. Furthermore at time T_{sync}, the grid and the generator mechanical speeds are equal. Substituting these equalities into Equation 5.3 and 5.4, the expressions are:

$$\omega_{go} + \alpha_g T_{sync} = \omega_{so} \tag{5.5}$$

$$\theta_{go} + \int_{0}^{T_{sync}} \omega_g(t)\,\mathrm{d}t = \theta_{so} + \omega_{so} T_{sync} \tag{5.6}$$

Since the generator acceleration is constant and the initial rotor speed is zero, the speed of the generator experiencing an constant acceleration of α_g at time t:

$$\omega_g(t) = \alpha_g t \tag{5.7}$$

*All angular variables are converted to mechanical quantities

Substituting Equation 5.7 into Equation 5.6, evaluating the integral and eliminating T_{sync} using Equation 5.5, we have:

$$\theta_{go} + \frac{1}{2}\frac{\omega_{so}^2}{\alpha_g} = \theta_{so} + \frac{\omega_{so}^2}{\alpha_g} \tag{5.8}$$

Rearranging Expression 5.8, the optimal generator acceleration α_{opml} to guarantee zero phase and frequency error between the grid and the generator at T_{sync} is given by:

$$\alpha_{opml} = \frac{1}{2}\frac{\omega_{so}^2}{\theta_{go} - (\theta_{so} - 2n\pi)} \tag{5.9}$$

The $2n\pi$ in Equation 5.9 determines which electrical period is selected for the synchronisation target, and this choice strongly determines the optimal acceleration. The approximate acceleration ceiling was chosen to be 85% of the maximum value to take the error in motor displacement setting control, motor nonlinearities and variation in supply pressure into account. Furthermore, Equation 5.9 can be used to re-calculate demand acceleration as grid and generator parameters vary.

As the control valve has dead time ranging between 20ms to 50ms, the calculated acceleration is expected to increase from its calculated initial value. It is necessary to implement a recalculation scheme once the derived acceleration exceeds the selected threshold. The effect of continuous optimal acceleration calculation for the EPS phase target while the generator is staying stationary is illustrated by Figure 5.2, which shows the re-setting of the synchronisation phase angle target by a step down in the derived acceleration.

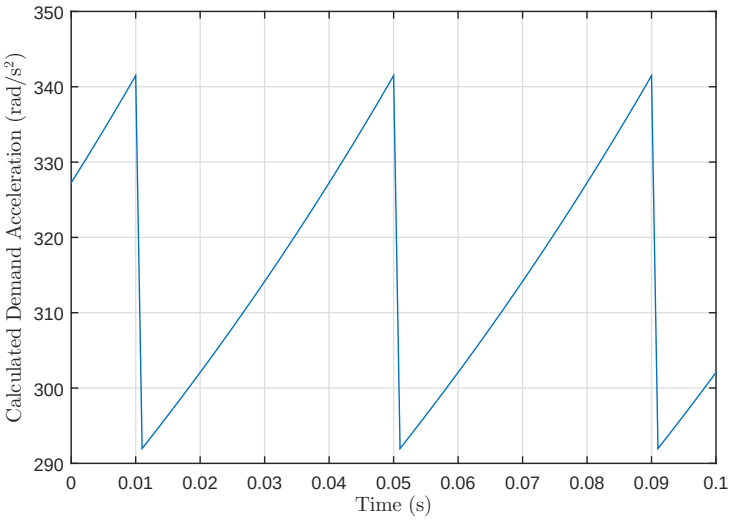

FIGURE 5.2: Effect of acceleration derivation grid offset reset due to control valve dead time ($\theta_{go} = 0, \theta_{so} = 0$)

The subsequent sections describe the process used accomplish this proposed acceleration control goal.

5.2.3 Control Topology and Simulink Model

The acceleration control simulation is performed with MATLAB Simulink using the fixed step ODE4 (Runge-Kutta) solver with an fixed calculation time interval of 0.1ms. Figure 5.3 shows the proposed acceleration feedback control process topology. The power grid and generator quantities are fed into the acceleration derivation block to compute the optimum acceleration upon receiving the IR demand signal. As the goal of the controller is to maintain a constant acceleration, a feedforward block is designed to create a constant valve pressure loss using flow-rate as a variable. To trigger the valve opening signal which is independent of the flow-rate, a constant voltage is first generated upon receiving the IR demand signal in the feedforward block.

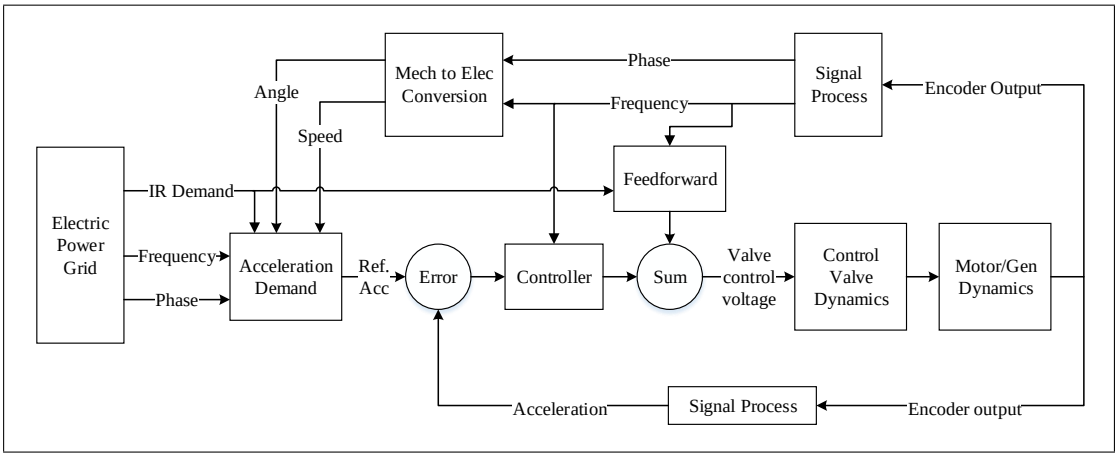

FIGURE 5.3: Proposed CGESS acceleration feedback control system topology

The control block contains the controller and the gain scheduler. The valve pressure flow-rate linearization is accomplished by utilizing the shaft speed feedback. By estimating the input voltage to valve pressure gain evaluated at various shaft speeds, a gain trajectory can be synthesized to dynamically vary the controller gain on the fly, therefore preserving the control loop stability.

The equivalent Simulink model topology is shown in Figure 5.4, which shows that the core of the feedback system is divided into the acceleration derivation block, the controller block and the hydraulic power drive system block. These expanded subsystems are shown in Figure 5.5, Figure 5.6 and Figure 5.7. The detailed acceleration block design is described in Section 5.2.4, and the controller block design is described in Sections

5.2.5 and 5.2.6. The conceptual formulation of the plant dynamics and the controller design process is documented in Section 5.2.7.

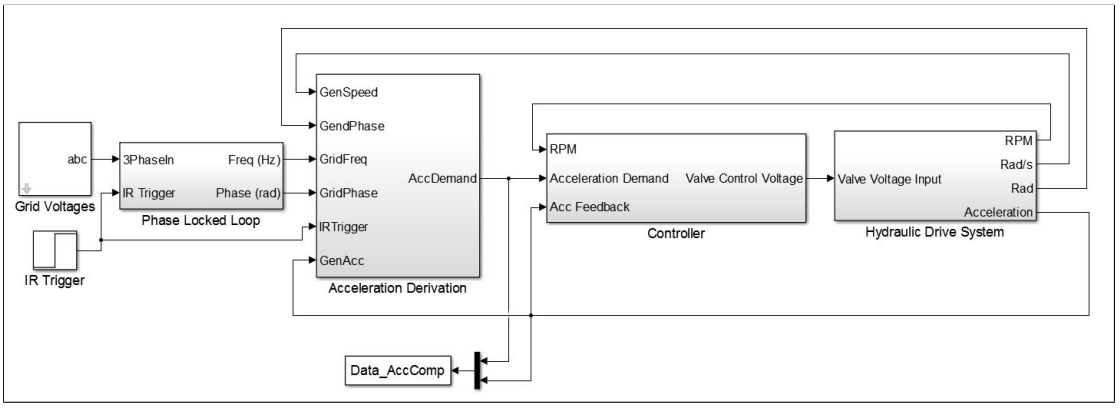

FIGURE 5.4: Simulink CGESS acceleration feedback control system topology

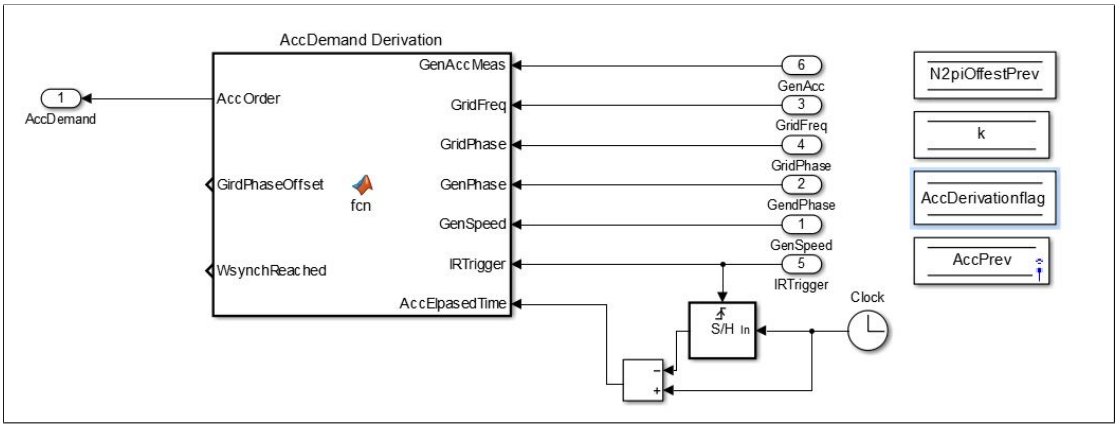

FIGURE 5.5: Acceleration derivation block

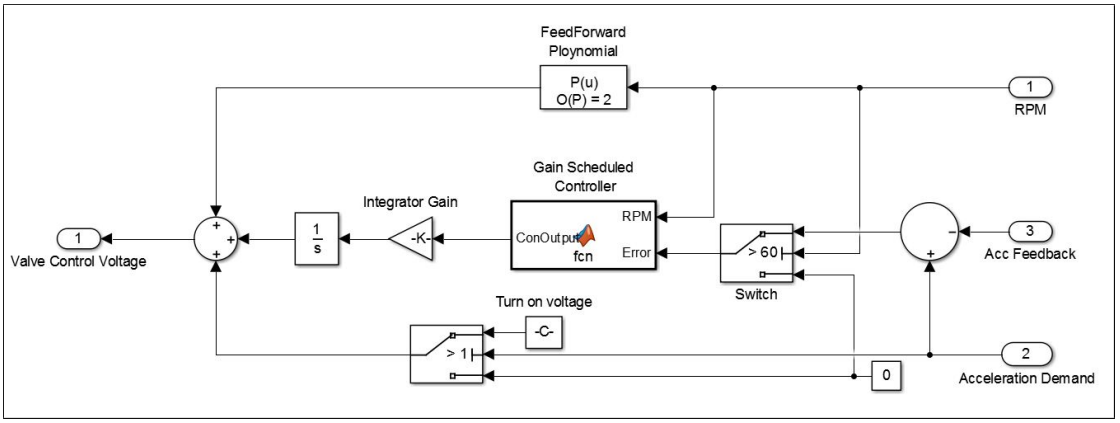

FIGURE 5.6: Controller block

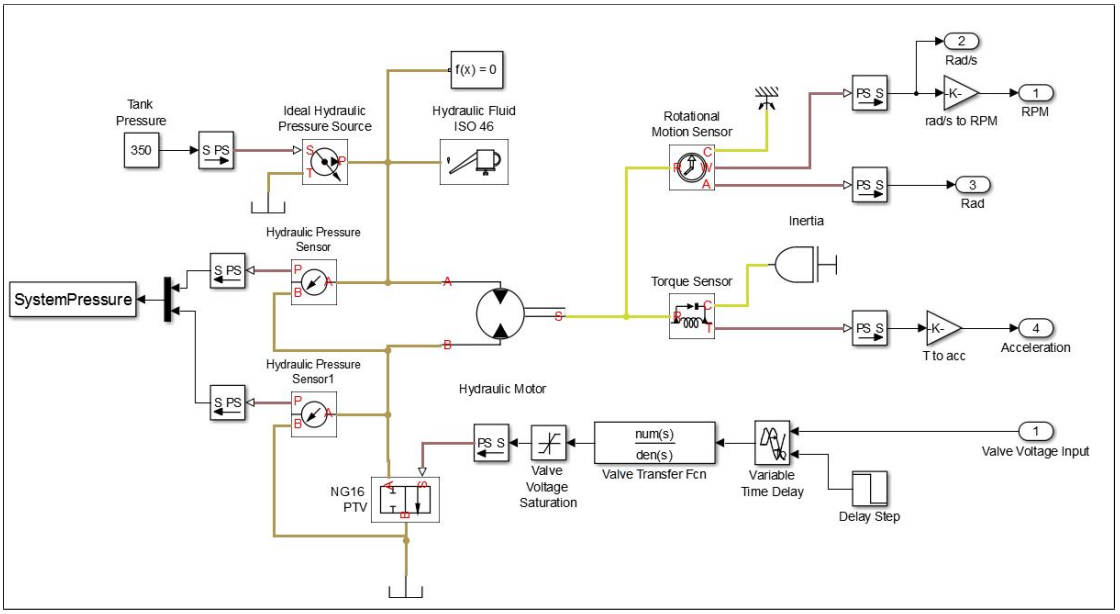

FIGURE 5.7: Hydraulic system block

The hydraulic mechanical system parameters were based on datasheet specifications and entered according to Table 5.1. As the opposing torque of a unloaded synchronous generator is insignificant to the hydraulic system, only the generator inertia was considered. The valve dynamics were intentionally omitted from the table as varying the valve dynamics was necessary to test the closed loop control system stability. To mimic the variable valve spool dead time during start up, a variable delay Simulink block was used to separate the start up delay and the operating delay.

TABLE 5.1: CGESS prototype system Simulink model mechanical parameters

Parameter	Value
Motor displacement	0.120 L/rev
Motor volumetric efficiency	95%
Motor total efficiency	92%
Motor nominal pressure	350 bar
Motor nominal speed	1500 RPM
Motor nominal kinematic viscosity	46 cSt
Motor nominal fluid density	861 kg/m^3
Total shaft inertia	1.545 kgm^2
Supply pressure	350 bar

5.2.4 Acceleration Derivation Block Design

Once the acceleration derivation is triggered by the FIR demand signal, additional steps are activated to ensure control stability. These steps are:

- New phase trajectory seeking is halted when the demand acceleration hits the acceleration ceiling after 0.2 seconds has elapsed. From simulation, seeking a new grid phase trajectory results in stepping the acceleration demand to a lower magnitude and subsequently instigates instability
- Hold the acceleration constant if the mechanical frequency difference is less than 1Hz, as the derived acceleration is sensitive to measurement noise within this period
- When speed and phase synchronisation conditions are met, generate a synchronisation signal

The implemented MATLAB function is attached in Appendix B

5.2.5 Feed-forward Trajectory Design

Since the generator acceleration is proportional to the motor pressure, the objective is to maintain a constant motor pressure regardless of the flow-rate. For the conditions shown in Figure 5.2, the valve operating pressure is roughly between 50 and 95 bar.

The control valve is characterized around 83 bar pressure drop across the valve. As the motor accelerates, and the flow through the valve increases, a feed-forward valve input trajectory is generated as shown in Figure 5.8 so the controller dynamics do not have to follow this change.

As the valve pressure loss is flow-rate dependent for a fixed orifice area, the valve voltage input required to attain constant valve pressure drop could be achieved by using RPM as a parameter. The control voltage trajectory was constructed by substituting 83 bar valve pressure and the incrementing flow-rates using Equation 2.16, extracting the flow-coefficient using NG-16 datasheet values, and mapping the flow coefficient to the control voltage. By least squared fitting a second order polynomial to the curve, the feedforward voltage as a function of RPM was derived. Figure 5.8 depicts the comparison between the ideal and fitted feedforward voltage.

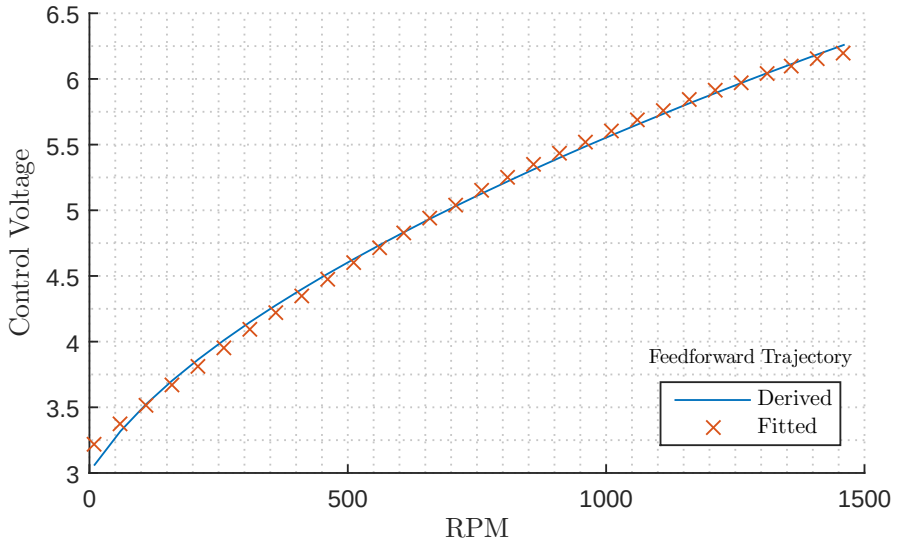

FIGURE 5.8: Feed-forward NG-16 valve input

The fitted feedforward voltage shown in Figure 5.8 is expressed by Equation 5.10:

$$V_{FF}(RPM) = -7.45 \times 10^{-7} \cdot RPM^2 + 0.0032 \cdot RPM + 3.18 \qquad V \tag{5.10}$$

This method is an attempt to bring the PTV poppet closer to a position which will result in the desired PTV pressure drop. Since there is a delay from control input to poppet movement, the actual PTV pressure drop will lag behind ideal pressure drop without additional compensation methods such as the Smith predictor [188].

5.2.6 Gain Scheduled Function Design

Similar to the feedforward block, a variable gain block was implemented to linearize the effect of flow-rate. Figure 5.9 illustrates the effect of increasing flow-rate on the input-to-pressure gain of the valve. The decrease in input voltage to pressure gain slope (shown as red dashed lines) observed at the intersects between the desired fixed valve pressure and the dynamic valve pressures shows nonlinear dynamics related to flow-rates.

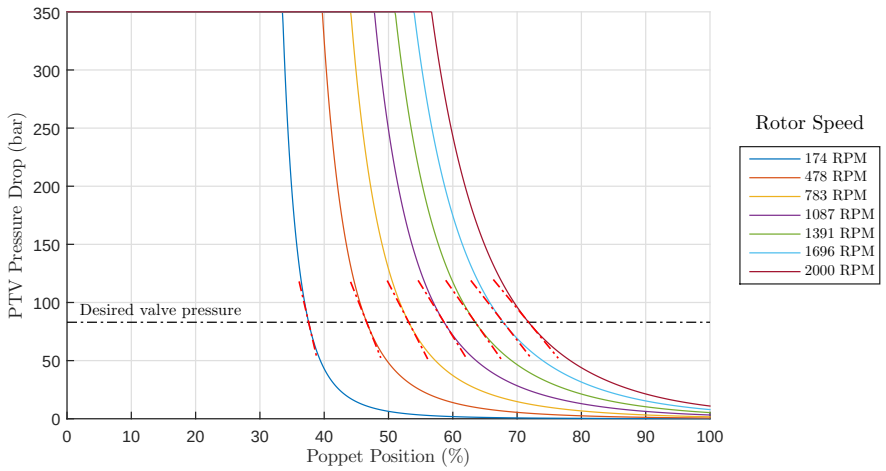

FIGURE 5.9: Visualization of control valve voltage to pressure gain relative to increasing rotor speed

To approximate this nonlinearity, a input displacement of 1% was used to small signal linearize the input to pressure dynamics. Figure 5.10 shows the negative value of the linearized input to pressure gain around the nominal loss of 83 bar plotted as a function of shaft speed. The red crosses shown in Figure 5.10 are the results evaluated from the second order polynomial fitted to the derived input to pressure gain.

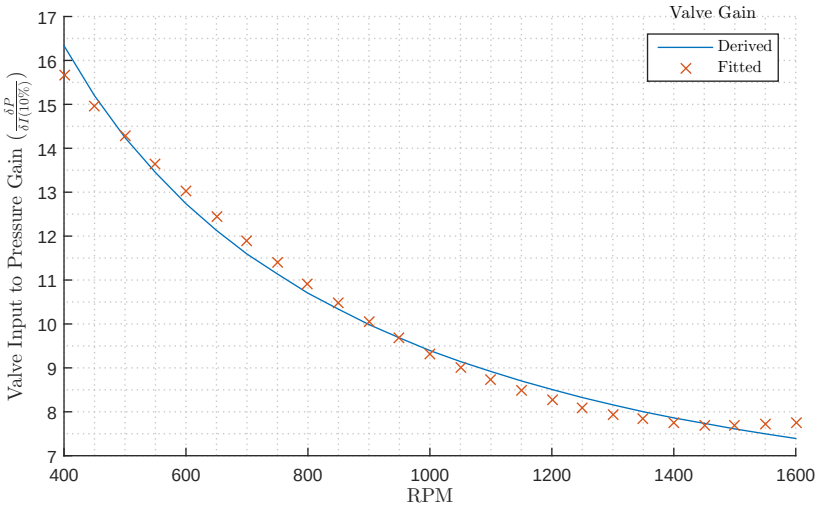

FIGURE 5.10: NG-16 PTV input to pressure gain trajectory plotted as a function of RPM

The fitted polynomial describing the curve shown in Figure 5.10 is expressed by Equation 5.11;

$$V_{GainSlope}(RPM) = 6.62 \times 10^{-6} \cdot RPM^2 - 0.0198 \cdot RPM + 22.55 \tag{5.11}$$

Having described the nonlinearity with Equation 5.11, a scaling factor can be applied to linearized the input to pressure dynamics base on shaft speed. To ensure that the controller is able to track the acceleration at an early stage, the desired input to pressure gain for normalization is chosen to be around 600RPM. Figure 5.10 suggests that the PTV input to pressure gain at 600RPM is around -13.15 bar per percent input. By normalizing the fitted elements with 13.15 and inverting the results, the gain scheduled function block can be derived and shown in Figure 5.11:

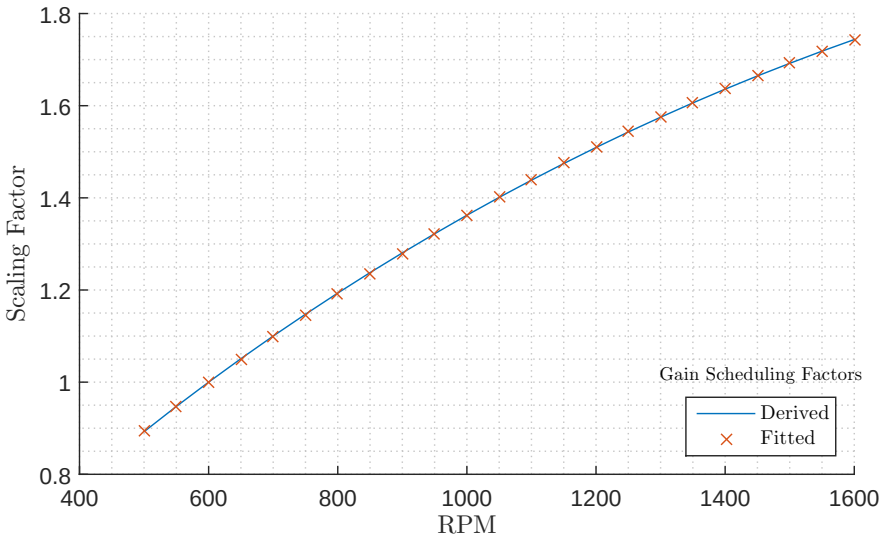

FIGURE 5.11: Gain scaling factors with schedule with RPM as scheduled variable

The gain scheduling function is described by fitting the curve with:

$$V_{GainSche}(RPM) = -2.86 \times 10^{-7} \cdot RPM^2 + 0.00135 \cdot RPM + 0.29 \tag{5.12}$$

5.2.7 Controller Design

The feedback control block diagram is shown in Figure 5.12. By actuating the control valve poppet, the valve pressure loss can be varied, thereby regulating the motor pressure and the resultant acceleration.

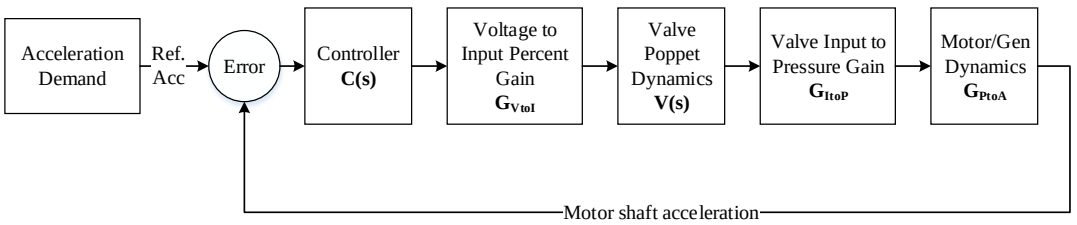

FIGURE 5.12: Feedback controller block diagram

In Figure 5.12, the scaling factor which converts the valve input voltage (from 0-10V) to the percentage in poppet movement (0-100%) is shown as G_{VtoI}, which has a value of 10.

It was stated earlier that a NG-16 PTV was chosen as the pressure regulating component for the CGESS prototype, and its dynamics were to be described by Equation 4.2 as the NG-16 valve dynamic model data was missing. As classical control design algorithm requires the plant transfer function to be a rational, the irrational ideal time delay seen in Equation 4.2 is transformed by a third order Padé approximation. The control valve poppet dynamic approximation is given by:

$$V(s) = \frac{-s^3 + 1000s^2 - 4.167 \times 10^5\,\mathrm{s} + 6.944 \times 10^7}{0.00013s^5 + 0.1401s^4 + 65.21s^3 + 1.421 \times 10^4\,\mathrm{s}^2 + 1.113 \times 10^6\,\mathrm{s} + 6.944 \times 10^7} \tag{5.13}$$

The step responses of the characterized poppet model given by Expression 5.13 and the approximated poppet model given by Equation 4.2 are compared in Figure 5.13.

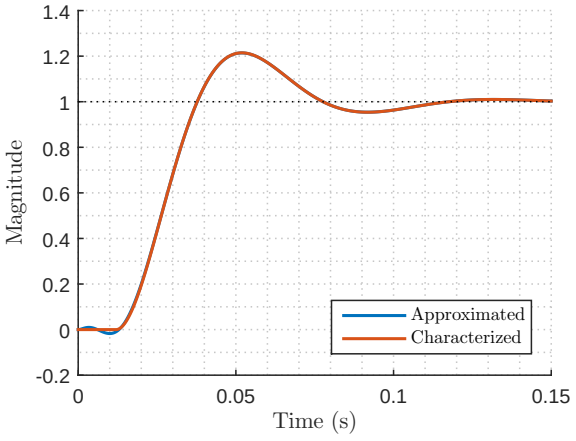

FIGURE 5.13: Third order Padé approximation of characterized control valve model

Since a reduction in the valve pressure drop results in an increase of motor pressure drop, the motor pressure gain was taken to be the negative of the control valve pressure gain. As the control valve input to pressure change was linearized to be -13.15 bar per percentage input in the previous section, the G_{ItoP} block has the value of 13.15.

Using Table 5.1, Equation 2.18 and Equation 2.20, the motor pressure differential to acceleration conversion is described by:

$$G_{PtoA} = \frac{D \cdot \eta}{63 \cdot J} = \frac{115 \cdot 0.92}{63 \cdot 1.55} = 1.087 \tag{5.14}$$

The acceleration control plant model is therefore:

$$\begin{aligned} H_{aop} &= G_{VtoI} \cdot V(s) \cdot G_{ItoP} \cdot G_{PtoA} \\ &= \frac{-150.1s^3 + 1.501 \times 10^5\,\mathrm{s}^2 - 6.253 \times 10^7\,\mathrm{s} + 1.042 \times 10^{10}}{0.00013s^5 + 0.1401s^4 + 65.21s^3 + 1.421 \times 10^4\,\mathrm{s}^2 + 1.113 \times 10^6\,\mathrm{s} + 6.944 \times 10^7} \end{aligned} \tag{5.15}$$

With an uncontrolled plant and unity gain negative feedback, the closed loop transfer function is described by Equation 5.16, whose the pole zero map is shown in Figure 5.14. The right hand side poles indicate that the uncontrolled acceleration feedback system is unstable.

$$H_{ucl} = \frac{-150.1s^3 + 1.501 \times 10^5\,\mathrm{s}^2 - 6.253 \times 10^7\,\mathrm{s} + 1.042 \times 10^{10}}{0.00013s^5 + 0.1401s^4 - 84.86s^3 + 1.643 \times 10^5\,\mathrm{s}^2 - 6.141 \times 10^7\,\mathrm{s} + 1.049 \times 10^{10}} \tag{5.16}$$

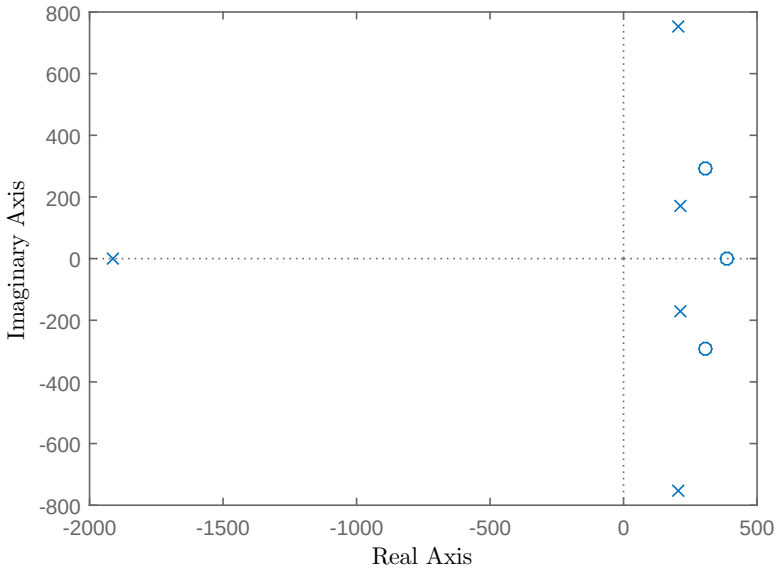

FIGURE 5.14: Pole zero map of uncontrolled acceleration control system with unity feedback

The controller was designed using the Root Locus design tool in MATLAB. The open loop CGESS acceleration plant model using loot locus analysis is shown in Figure 5.15:

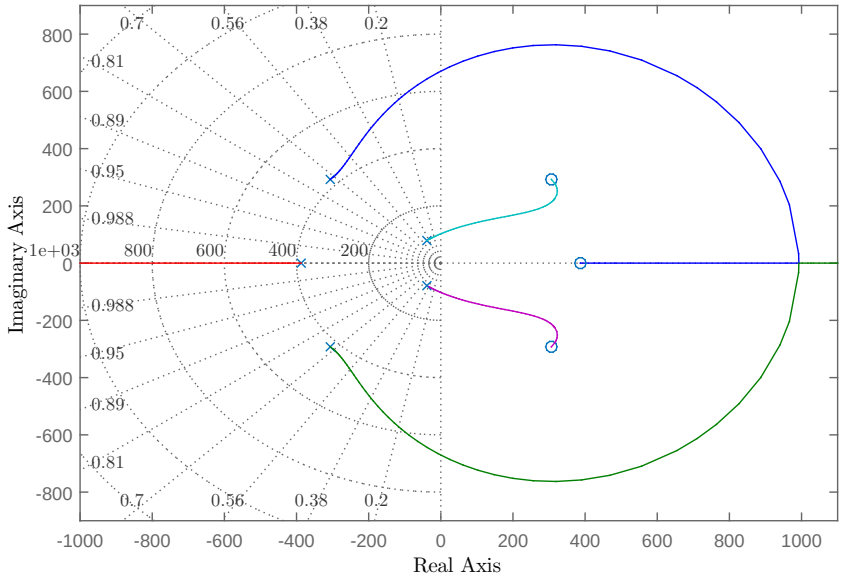

FIGURE 5.15: Root locus plot of the uncontrolled open loop acceleration system

In order to eliminate steady state error, the controller begins with an integrator. Given that 0.4 seconds will be the fastest time the shaft can reach synchronization speed and

excessive oscillation is likely to cause the control valve to fully shut near the early period of acceleration control, it is reasonable to select a 0.2 second settling time and a 10% maximum overshoot to allow for a degree of stability margin. The effect of adding an integrator is demonstrated by the root locus plot shown in Figure 5.16. The poles which meet settling time and the overshoot (in %) criteria are denoted by the vertical black line and the radial black lines. The region of acceptable pole locations capable of satisfying/reducing the settling time and overshoot is shown as the white region in Figure 5.16

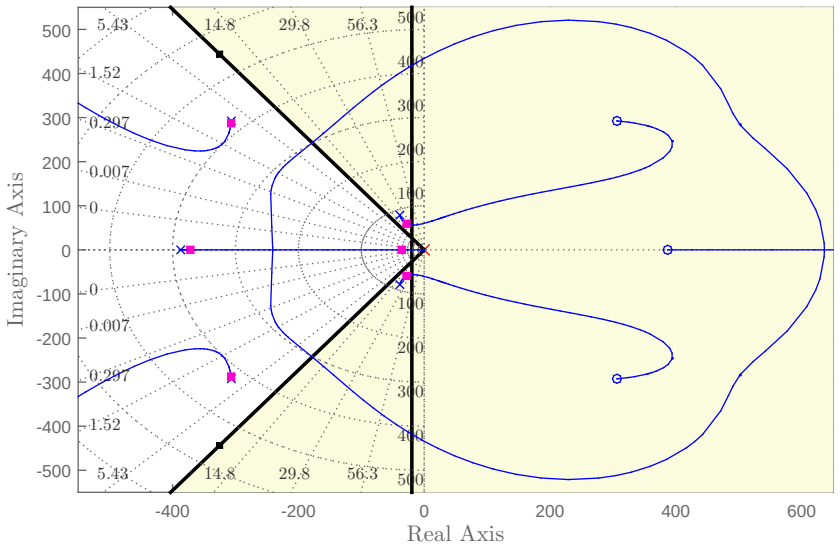

FIGURE 5.16: Acceleration controller design with Root Locus analysis

The graphical gain placement method based on the Root Locus analysis tool is shown in Figure 5.17. The integrator gain was chosen to be 0.125 in order to position the poles within the white region. The controller C(s) in Figure 5.12 is therefore defined by Equation 5.17. The acceleration step response shown in Figure 5.18, and the resulting closed loop Bode plot is shown in Figure 5.19.

$$C(s) = \frac{0.125}{s} \tag{5.17}$$

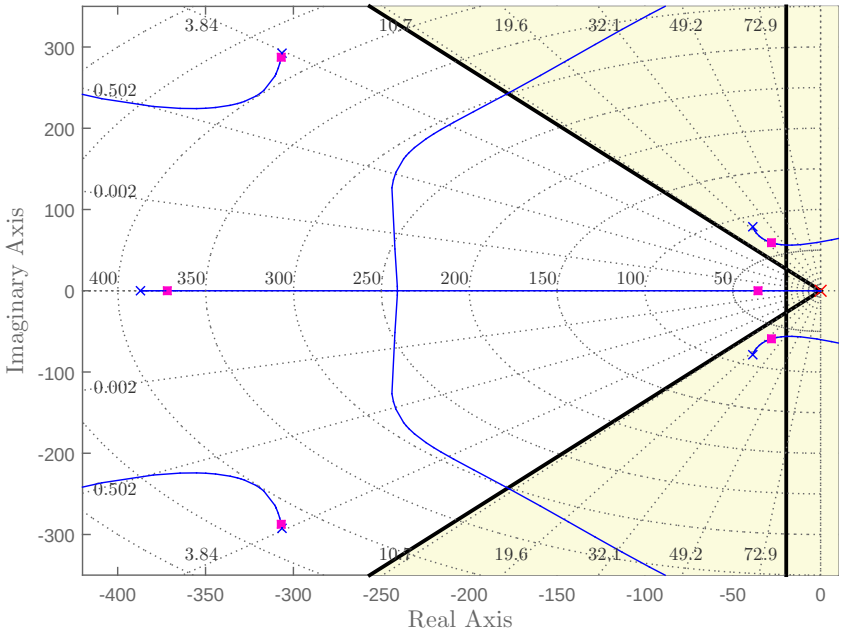

FIGURE 5.17: Acceleration controller design with Root Locus analysis

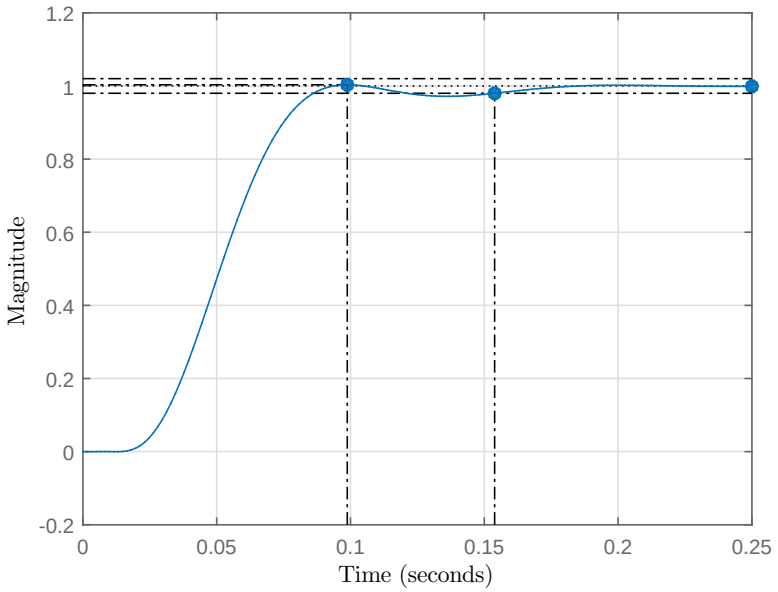

FIGURE 5.18: Acceleration control step response (0.3% overshoot at t = 0.1s, settling time to 2% error at 0.15s

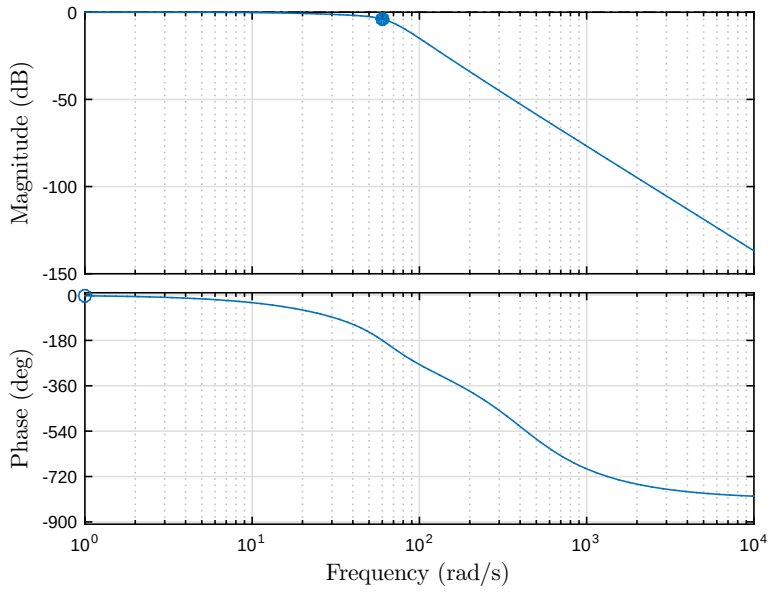

FIGURE 5.19: Bandwidth of feedback acceleration control system using Bode plot with a closed loop transfer function (Band Width = 54.2rad/s)

Figure 5.18 and 5.19 demonstrate that the specified control performance could be met using a single integrator with a scaling factor. As valve dead time will saturate the integrator, the integral control is only activated when the motor shaft starts moving. The triggering speed is 1rev/s, and its MATLAB implementation is seen in Figure 5.6. To check closed loop stability, Figure 5.20 and Figure 5.22 was obtained.

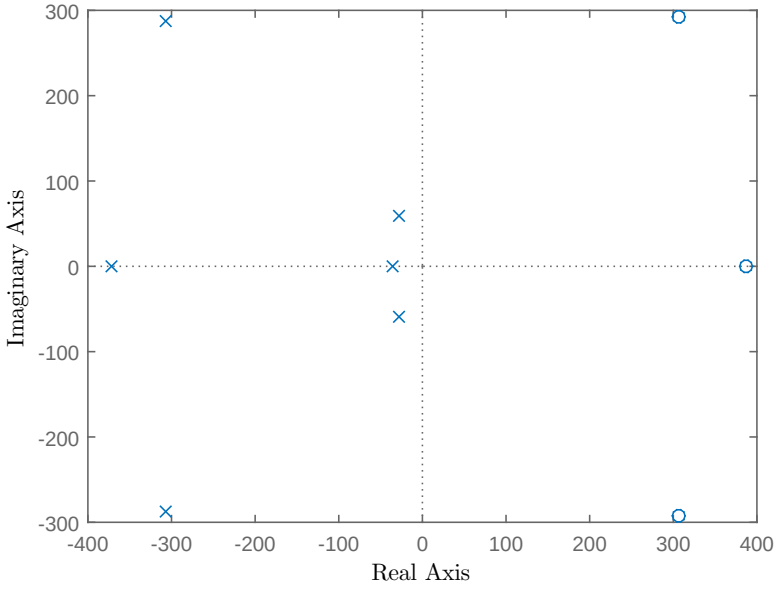

FIGURE 5.20: Acceleration controlled closed loop pole zero map

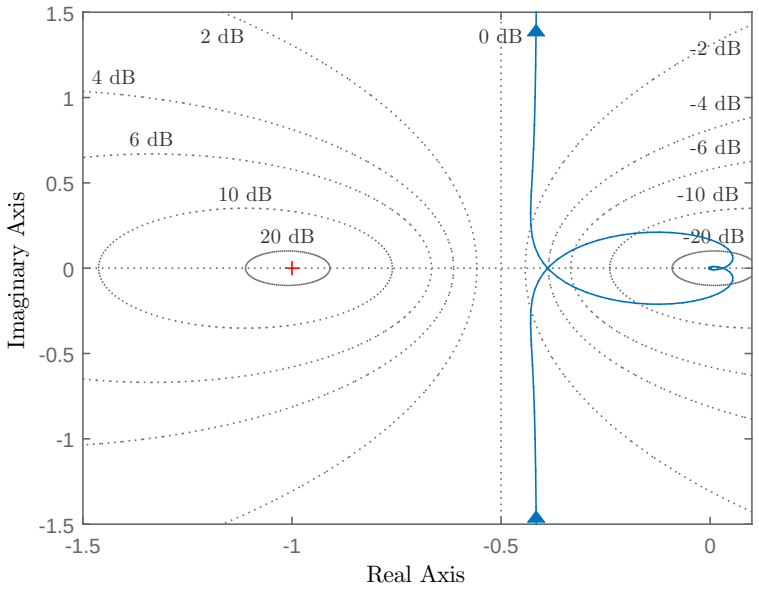

FIGURE 5.21: Stability analysis of feedback acceleration control using Nyquist plot with an open loop transfer function

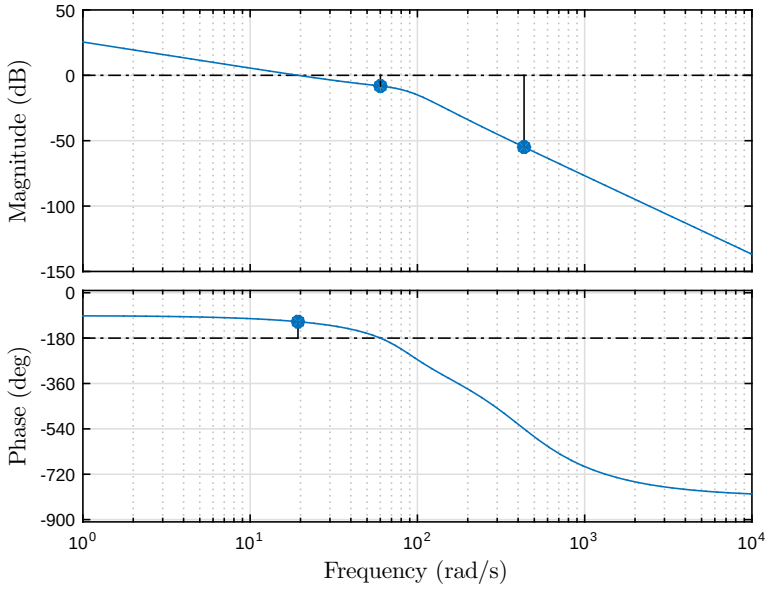

FIGURE 5.22: Stability analysis of acceleration controller using Bode plot with an open loop transfer function (gain margin: 8.21dB; phase margin: 65.2^o)

The pole zero map and the Nyquist plot shown in Figure 5.20 and 5.21 validate the stability of the closed loop acceleration control system. The pole-zero plot shows all the closed loop system poles in the left hand plane, and the Nyquist plot shows that there is a zero encirclement of the -1 point when there are no open loop poles in the right

hand plane. Figure 5.22 shows that the additional plant degradation cannot impose more than 65 degrees delay, and the input to pressure gain cannot exceed an factor of 2.5. These stability margins implies that the control valve pressure flow and dynamics mathematical approximation had to be relative accurate.

5.2.8 Simulation and Results

To account for the random shaft resting position and the unpredictable reserve demand time instant into consideration, the simulations were performed with various initial shaft positions. Varying the resting generator phase will have the same effect as changing the initial grid phase as they are relative measures.

Firstly, the acceleration control strategy concept shown in Figure 5.1 was validated using the results from Simulink model which is shown in Figure 5.23. The phase comparison is plotted with the initial mechanical shaft position of 180^o and power grid phase of 0^o.

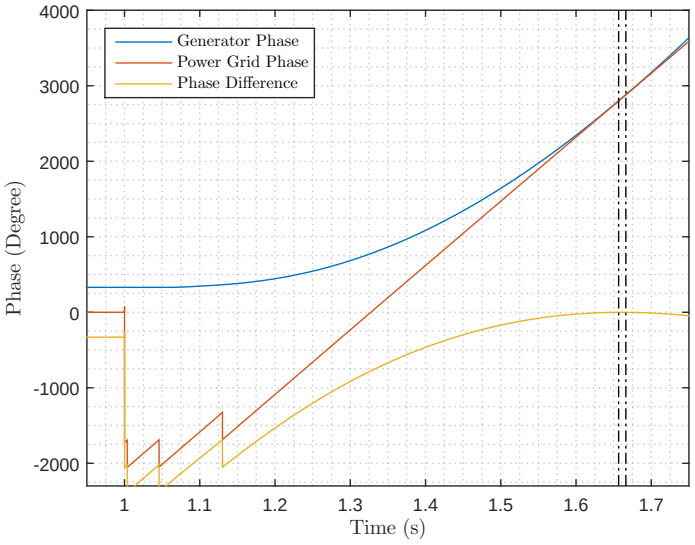

FIGURE 5.23: Acceleration controlled mechanical phase progression (initial shaft angle = 180^o),(dashed vertical black lines indicates the speed difference is within 0.3Hz)

The acceleration control stability was validated by plotting the demand v.s. feedback shaft acceleration for various shaft initial positions. The acceleration comparison are shown by Figure 5.24. To ensure the control valve pressure does not exceed the protective setting on the pressure relief valve and result in loss of pressure regulation, the control valve and motor pressure dynamics are shown in Figure 5.25, which shows that as long as the motor shaft acceleration is positive during the control period, the valve pressure cannot exceed the supply pressure.

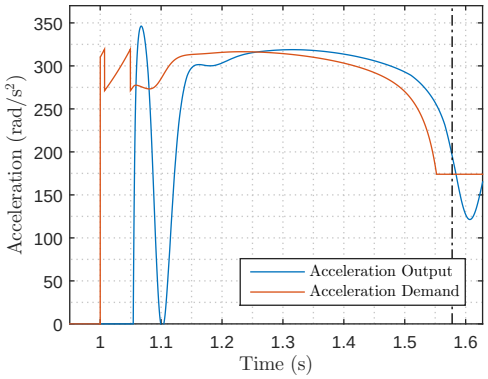

(A) Initial motor phase = 0^o

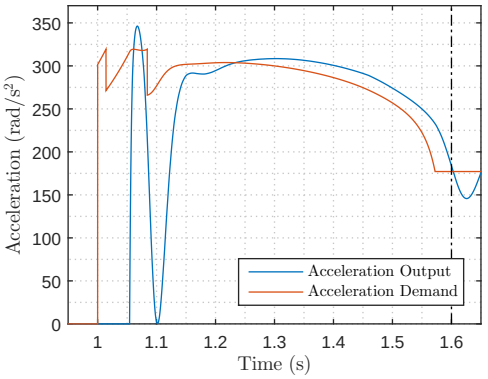

(B) Initial motor phase = 60^o

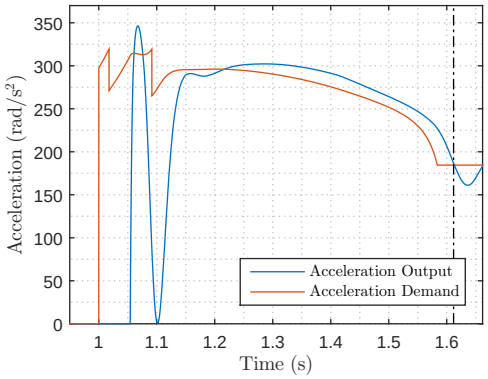

(C) Initial motor phase = 90^o

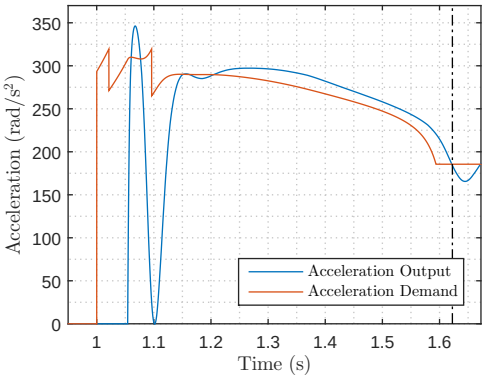

(D) Initial motor phase = 120^o

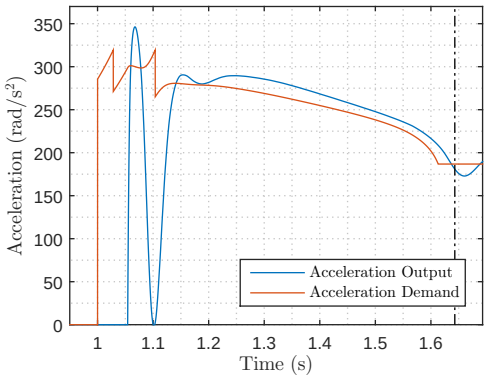

(E) Initial motor phase = 180^o

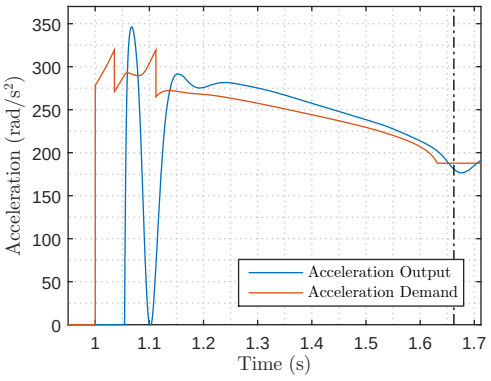

(F) Initial motor phase = 240^o

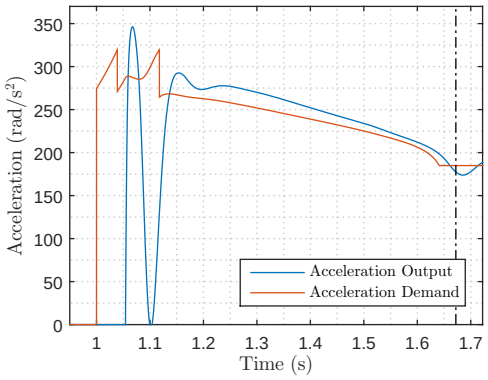

(G) Initial motor phase = 270^o

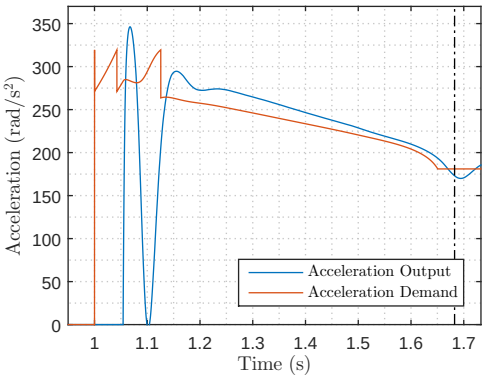

(H) Initial motor phase = 300^o

FIGURE 5.24: Demand and motor acceleration comparison simulated with acceleration control (dashed line indicates when frequency difference is within 0.3Hz)

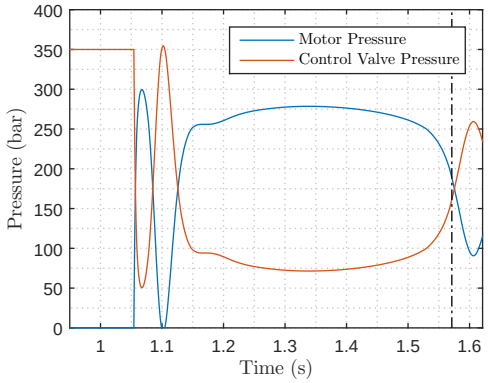

(A) Initial motor phase = 0^o

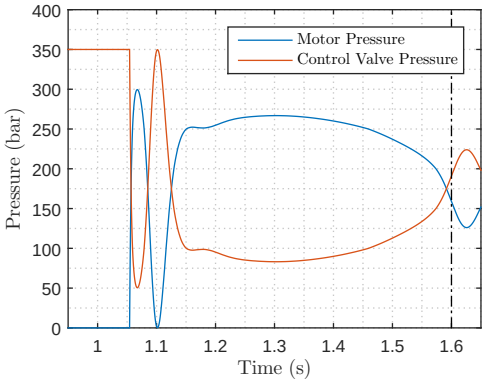

(B) Initial motor phase = 60^o

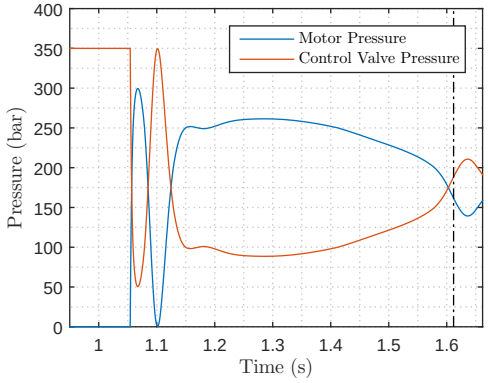

(C) Initial motor phase = 90^o

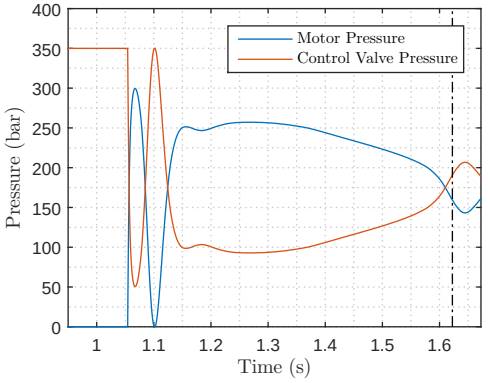

(D) Initial motor phase = 120^o

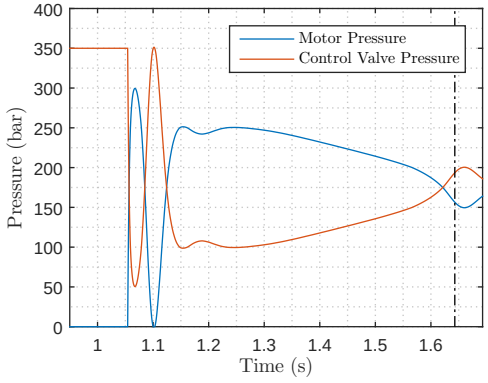

(E) Initial motor phase = 180^o

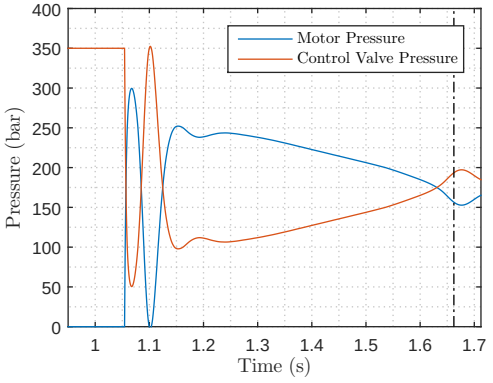

(F) Initial motor phase = 240^o

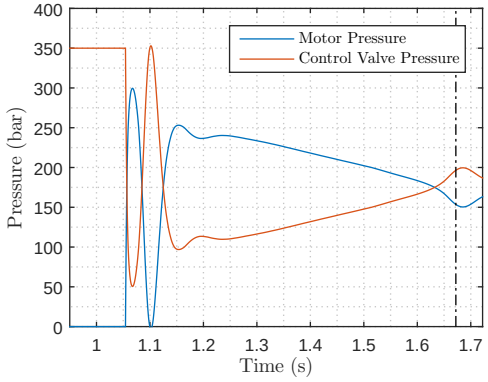

(G) Initial motor phase = 270^o

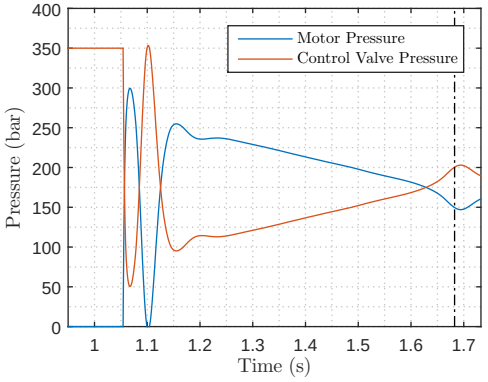

(H) Initial motor phase = 300^o

FIGURE 5.25: Motor and control valve pressure dynamics from acceleration control (dashed line indicates when frequency difference is within 0.3Hz)

Figure 5.24 shows that although the controller is stable, following errors are present. The consequent mechanical phase error produced by this control scheme is shown in Figure 5.26, which indicated that it is possible for the phase error to be as low as -2.8^o when the speed is within synchronization limit.

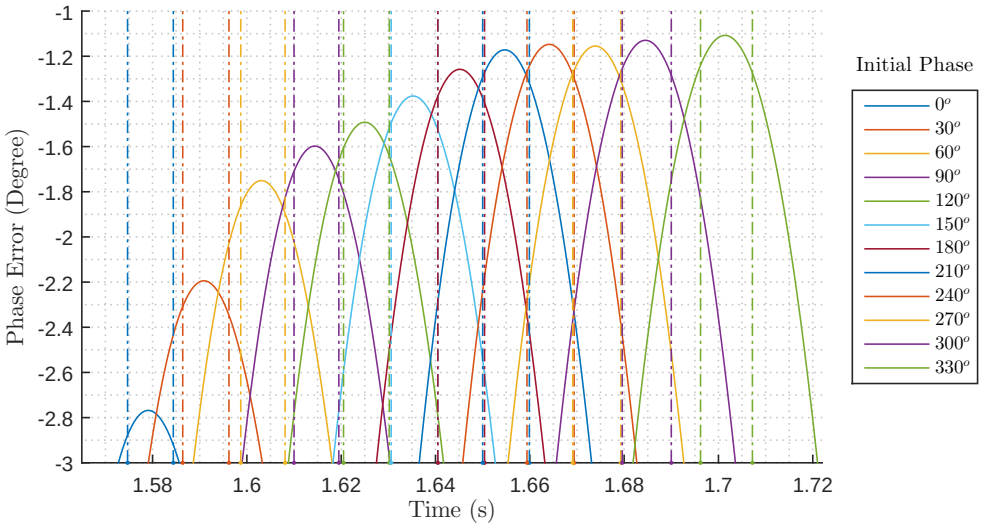

FIGURE 5.26: Simulated mechanical phase errors obtained with various shaft resting phase angle using theoretical controller and characterized valve dynamics (dashed line indicates when the speed difference is within ±0.3Hz)

Figure 5.24 and 5.26, show that using the derived feedforward and gain scheduling gain described by Equation 5.12 and 5.10 results in a moderate phase error near synchronization speed due to the constant acceleration tracking error.

Because of the PTV dead time, the actual position of the PTV poppet is always lagging behind the ideal feedforward position calculated from flowrate. By heuristically experimenting with the parameters of the feedforward and gain scheduling functions, the synchronization performance was improved by using the following feedforward, gain scheduler and controller expressions:

$$V_{F.F.}(RPM) = -1.25 \times 10^{-6} \cdot RPM^2 + 0.0035 \cdot RPM + 3.5 \qquad V \tag{5.18}$$

$$V_{G.S.}(RPM) = 0.0023 \cdot RPM + 0.2 \qquad V \tag{5.19}$$

$$C(s) = \frac{0.12}{s} \tag{5.20}$$

To benchmark the closed loop performance using the improved controller, the following systems were used to investigate the closed loop stability to accommodate for the real world mechanical system dynamic variation, which is summarized by Table 5.2:

TABLE 5.2: CGESS System Plant Dynamic Variation

System Type	Description
Characterized	The control valve dynamics described by parameter identification obtained from experiments using the test rig
Polluted	The acceleration feedback signal is distorted by measurement noise
Ideal	The control valve dynamic is described by the manufacturer datasheet
Deteriorated	The control valve dynamic performance is decreased by additional response time and reduced damping

5.2.8.1 Characterized Dynamic System

Similar to the simulations performed in the previous section, the characterized system Simulink model uses the valve dynamics expressed by Equation 4.2. The shaft accelerations obtained under various initial rotor positions are depicted by Figure 5.27, which shows that although the controller cannot regulate the generator acceleration with zero error, the shaft acceleration follows the demand acceleration closely and the rate of demand acceleration decay is less prominent when compared to Figure 5.24. Moreover, reduction in the initial acceleration oscillation can be seen.

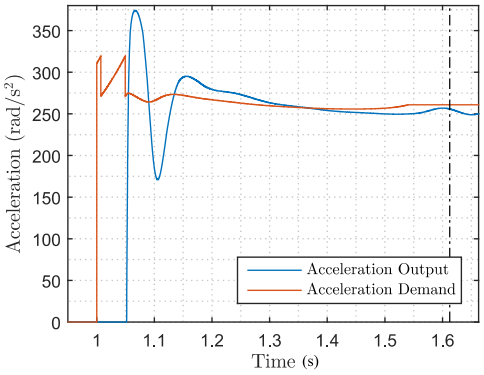

(A) Initial motor phase = 0^o

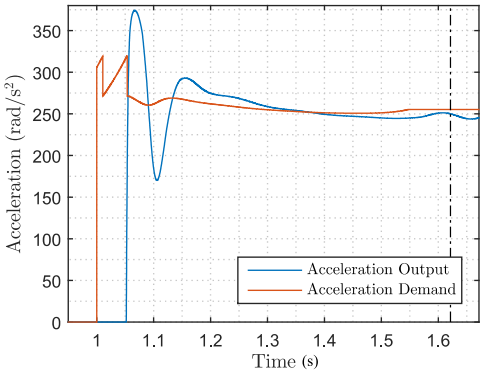

(B) Initial motor phase = 30^o

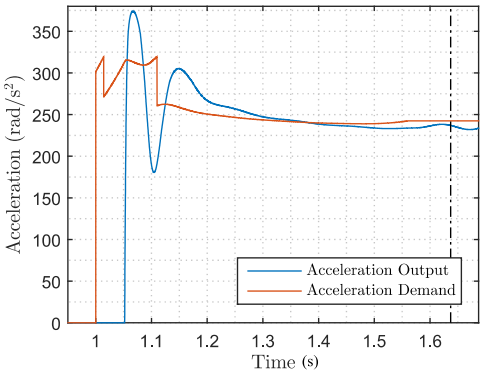

(C) Initial motor phase = 60^o

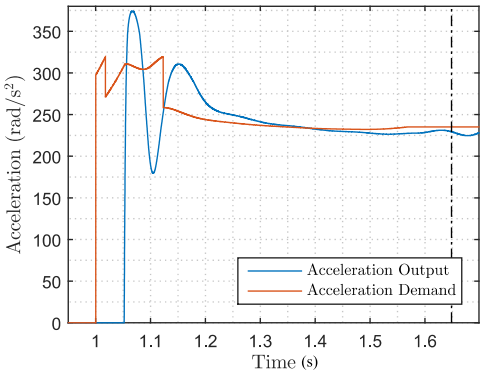

(D) Initial motor phase = 90^o

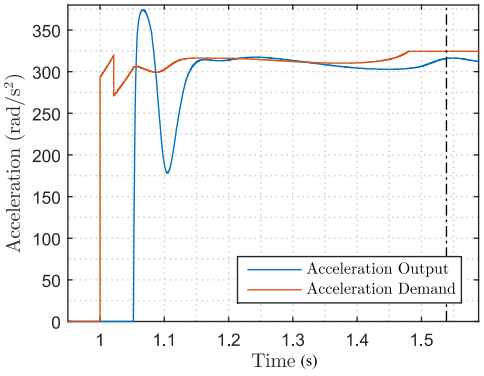

(E) Initial motor phase = 120^o

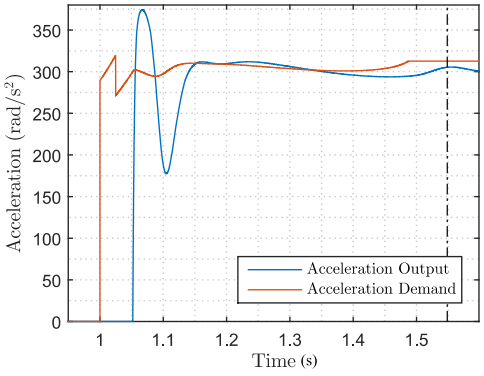

(F) Initial motor phase = 150^o

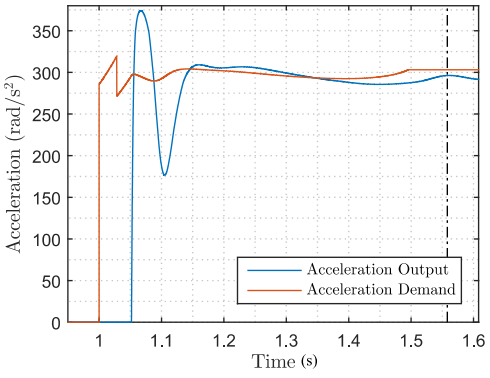

(G) Initial motor phase = 180^o

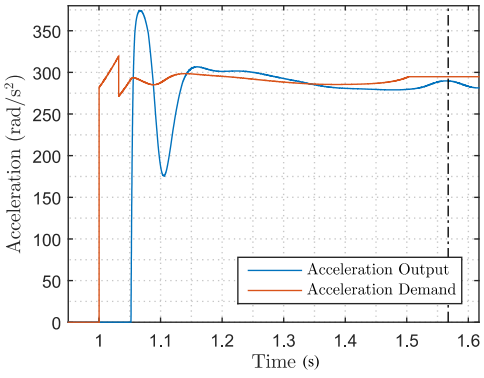

(H) Initial motor phase = 210^o

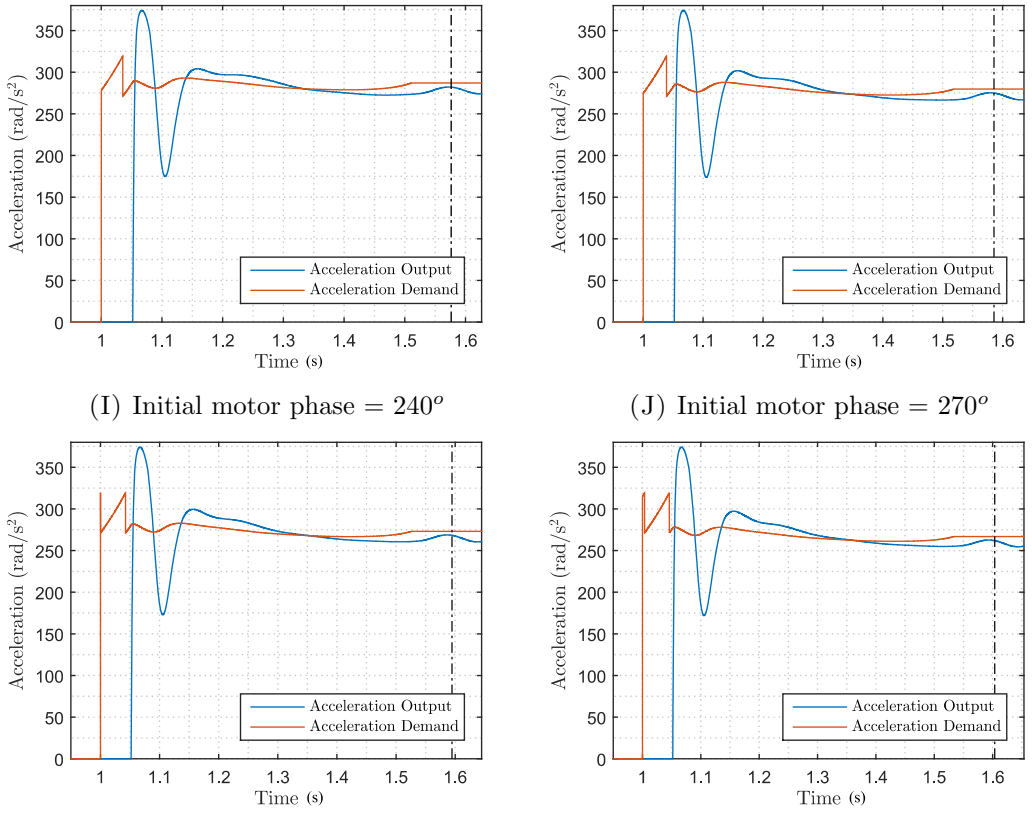

(I) Initial motor phase = 240^o

(J) Initial motor phase = 270^o

(K) Initial motor phase = 300^o

(L) Initial motor phase = 330^o

FIGURE 5.27: Demand and motor acceleration comparison simulated with parameter characterized valve (dashed line indicates the instance the electrical frequency difference is within 0.3Hz)

Figure 5.28 shows the phase difference simulated with various shaft positions and it demonstrated that the electrical angular error of $\pm 1^o$ could be achieved when the generator/power grid frequency difference is within $\pm$0.3Hz. These results satisfy the synchronization limitation criteria and confirm the legitimacy and the performance of the controller despite the initial generator phase. The synchronization window lasts between 5 to 7 ms.

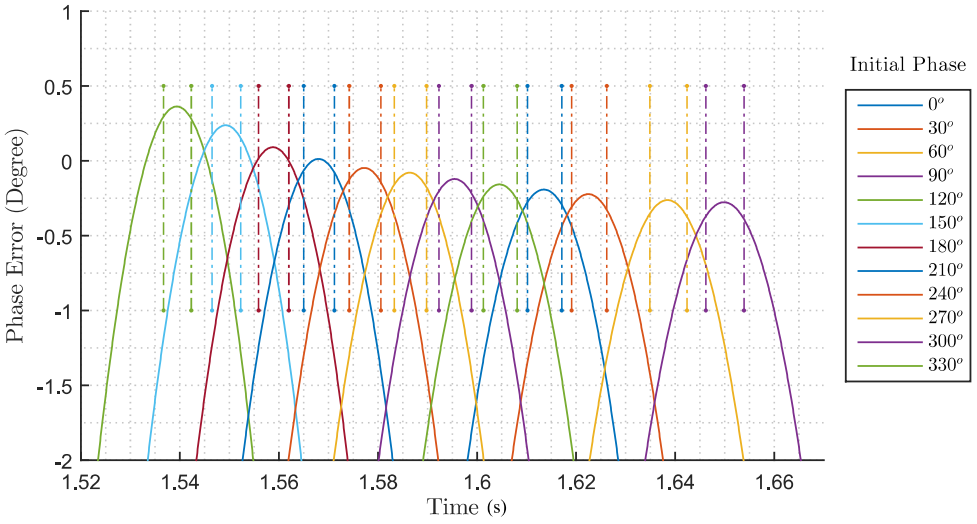

FIGURE 5.28: Phase error plot obtained with various shaft resting positions (dashed line indicates the time span the speed difference is within ±0.3Hz)

5.2.8.2 Distorted Dynamic System

To evaluate the stability of the closed loop system modeled with noisy measurements, Gaussian noise with 10rad/s^2 variance was added to the acceleration input, and harmonics (3% 5^{th} and 5% 7^{th}) were added to the power grid voltages. In addition, -1.2Hz/s frequency decrease was added to the power grid voltage to simulate under-frequency events. Figure 5.29 depicts the acceleration profile simulated with various initial phase conditions, and the phase error near the synchronization speed is shown in Figure 5.30. By showing the stable output generator acceleration behavior as a result demanding maximum and minimal input acceleration (occurs at initial phase angles of 90^o and at 150^o), it can be concluded that stability is achieved throughout the intermediate acceleration values.

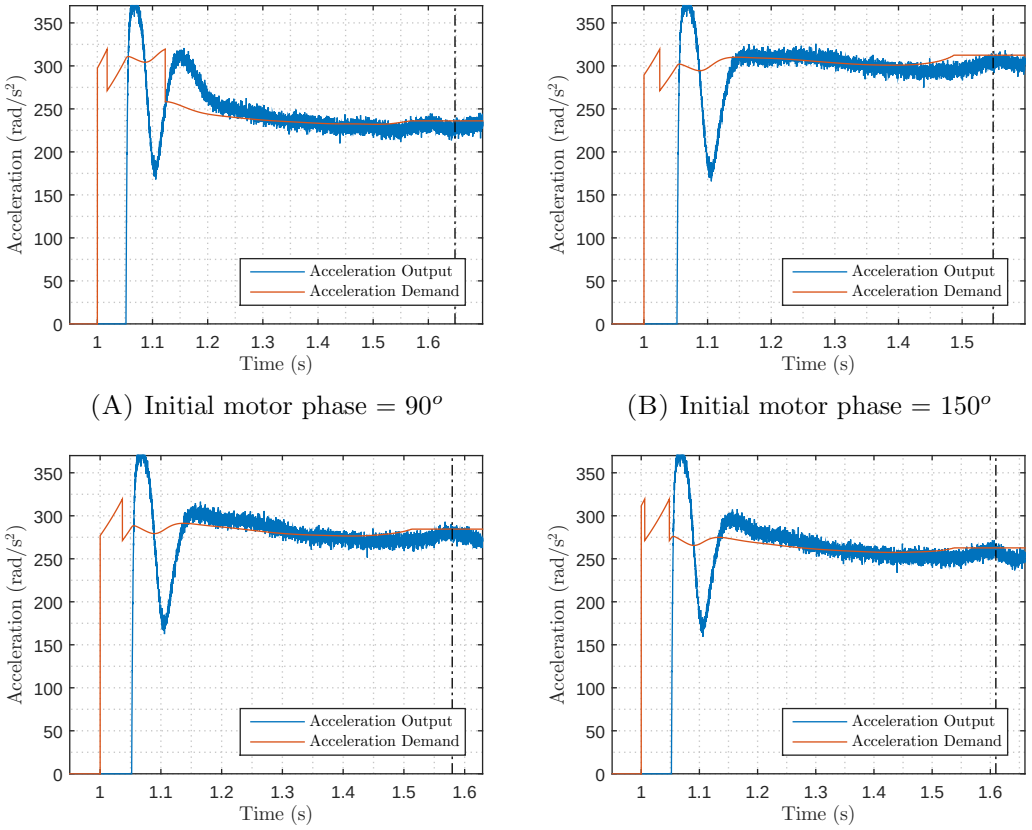

(A) Initial motor phase = 90^o

(B) Initial motor phase = 150^o

(C) Initial motor phase = 250^o

(D) Initial motor phase = 350^o

FIGURE 5.29: Demand and motor acceleration comparison simulated with distorted acceleration input (dashed line indicates the instance the electrical frequency difference is within 0.3Hz)

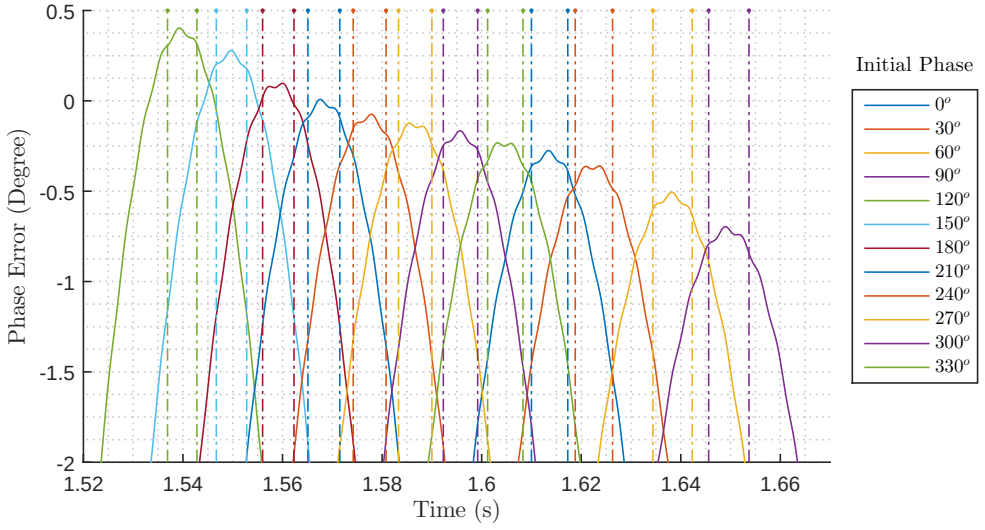

FIGURE 5.30: Generator and power grid phase error obtained with various shaft resting positions and distorted EPS parameters (dashed line indicates the time span the speed difference is within ±0.3Hz)

5.2.8.3 Ideal Dynamic System

As the test-rig was constructed with used hydraulic motor and conduits, the dynamics may be more predictable when the controller is implemented on the CGESS prototype; therefore it is essential to test the control system with the ideal control NG-32 valve dynamics specified by the datasheet. The acceleration profile using the Simulink control valve model described by Equation 4.1 is shown in Figure 5.31, and the resulting phase error plot is shown in Figure 5.32. Similarly, the acceleration demand input v.s. shaft acceleration using an ideal NG-16 PTV model expressed by Equation 4.3 is shown in Figure 5.33 and the obtained phase error is shown in Figure 5.34.

The results from both ideal valve models show that the motor acceleration appeared to be less oscillatory at the beginning, and the demand acceleration remains within between the maximum and the minimum acceleration saw-tooth suggested by Figure 5.2. Again, the simulations show the synchronization criteria can be met with the same acceleration controller.

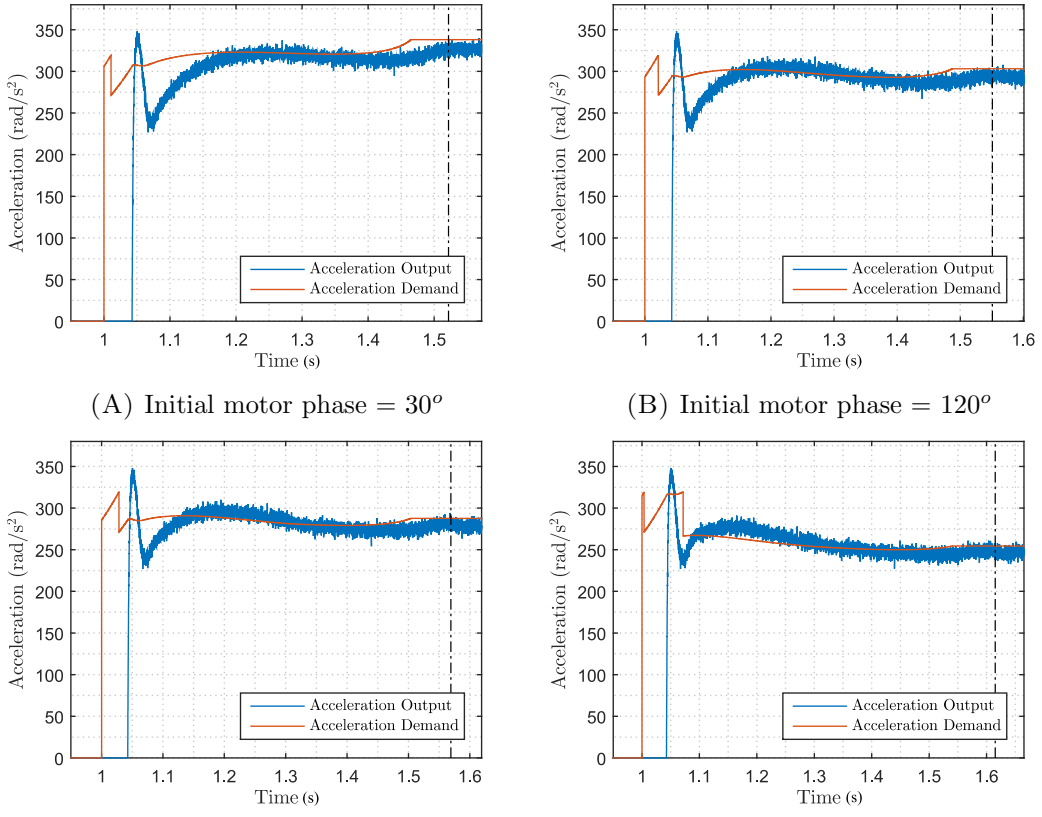

(A) Initial motor phase = 30^o

(B) Initial motor phase = 120^o

(C) Initial motor phase = 180^o

(D) Initial motor phase = 330^o

FIGURE 5.31: Demand and motor acceleration comparison simulated with datasheet approximated NG-32 PTV (dashed line indicates the instance the frequency difference is within 0.3Hz)

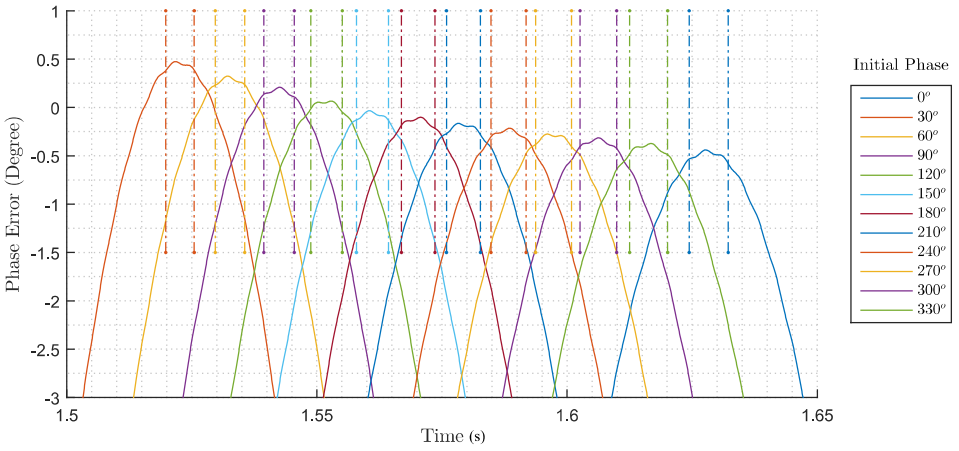

FIGURE 5.32: Phase angle errors obtained with various shaft resting positions using datasheet approximated NG-32 PTV dynamics (dashed line indicates the time span the speed difference is within ±0.3Hz)

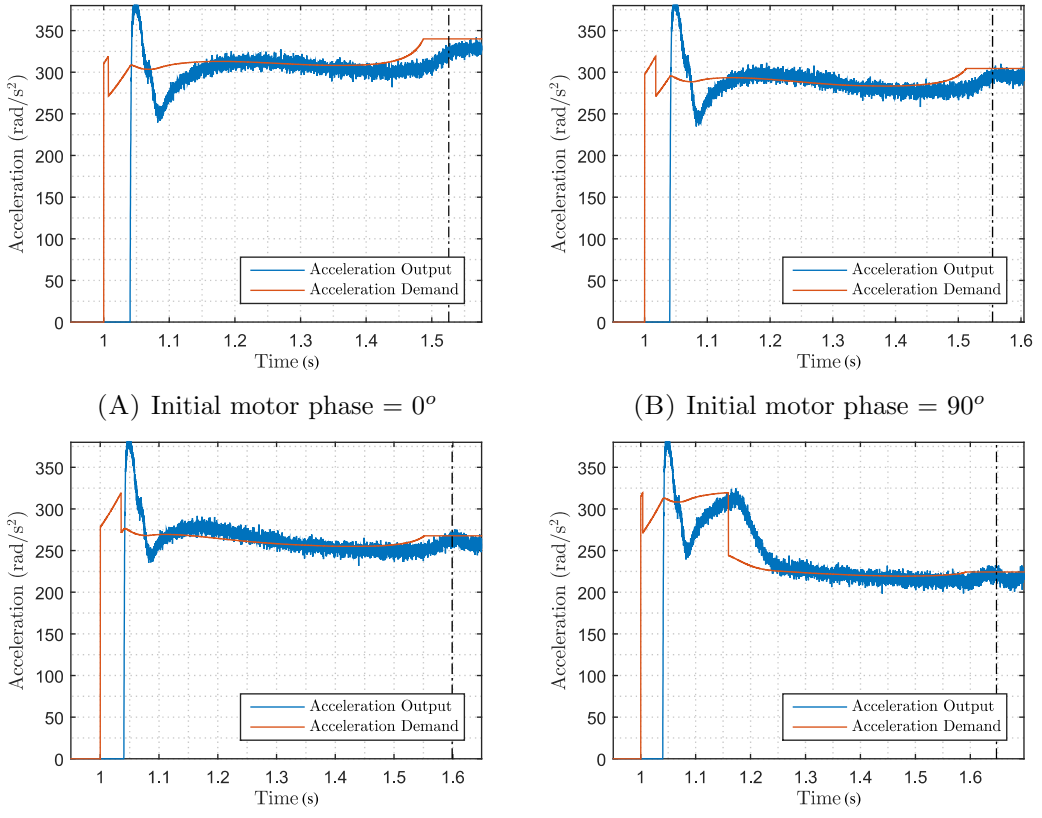

(A) Initial motor phase = 0^o

(B) Initial motor phase = 90^o

(C) Initial motor phase = 240^o

(D) Initial motor phase = 330^o

FIGURE 5.33: Demand and motor acceleration comparison simulated with datasheet approximated NG-16 PTV (dashed line indicates the instance the frequency difference is within 0.3Hz)

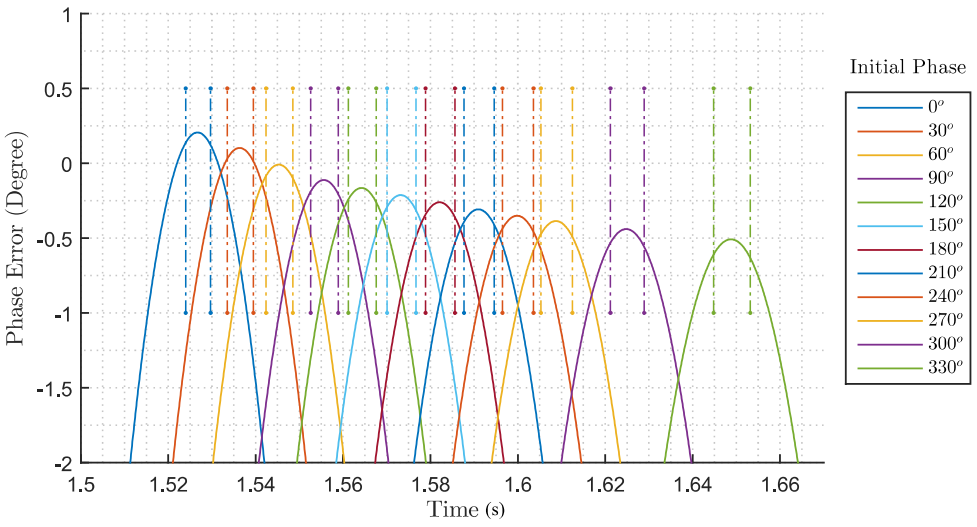

FIGURE 5.34: Phase angle errors obtained with various shaft resting positions using datasheet approximated NG-16 PTV dynamics (dashed line indicates the electrical frequency difference is within ±0.3Hz)

5.2.8.4 Deteriorated Dynamic System

The valve settling time and damping is further deteriorated to $t_s = 120$, $\zeta = 0.35$, $\omega_n = 3/(t_s\zeta)$ in order to check the closed loop stability if a degraded valve was to be used. The acceleration comparison is depicted by Figure 5.35, and the phase errors simulated with various shaft position is shown in Figure 5.36. Although the phase error is acceptable near the synchronization speed for all initial shaft position, Figure 5.35B shows minor oscillation at higher RPM, indicating the beginning of unstable behavior. Regardless, the simulation shows the controller is sufficient and is able to satisfy the synchronization criteria, as demonstrated by Figure 5.36 .

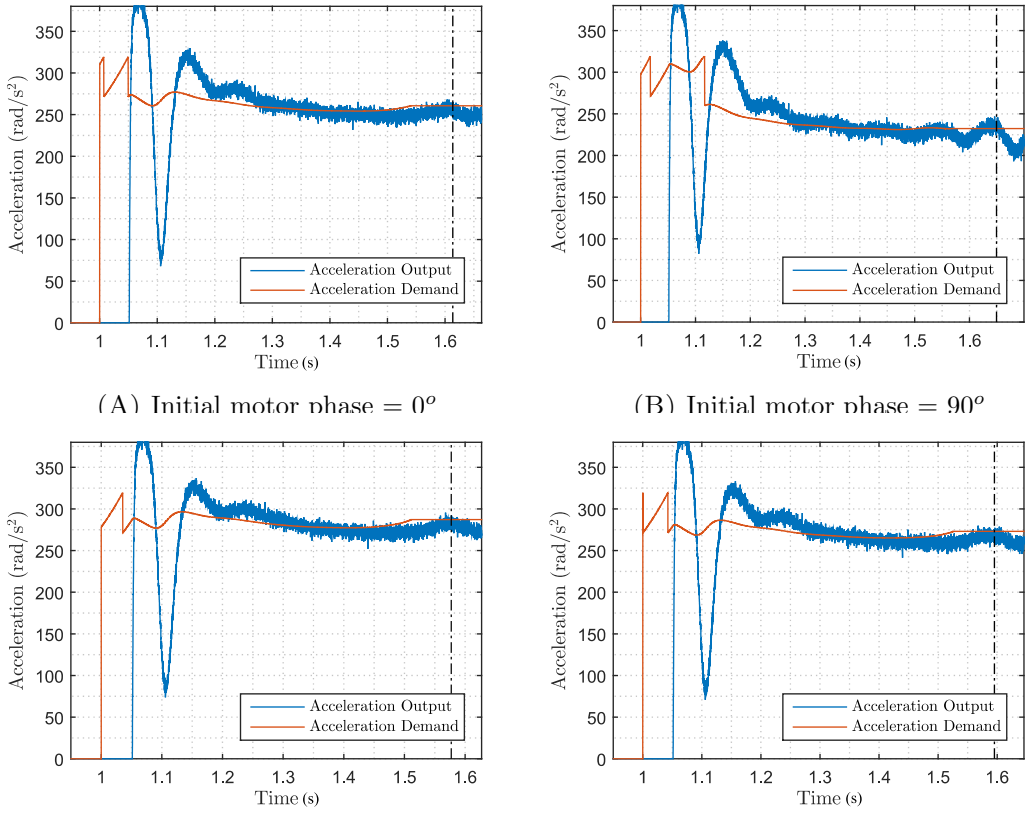

(A) Initial motor phase = 0^o (B) Initial motor phase = 90^o

(C) Initial motor phase = 240^o (D) Initial motor phase = 300^o

FIGURE 5.35: Demand and motor acceleration comparison simulated with poor performing valve (dashed line indicates the instance the frequency difference is within 0.3Hz)

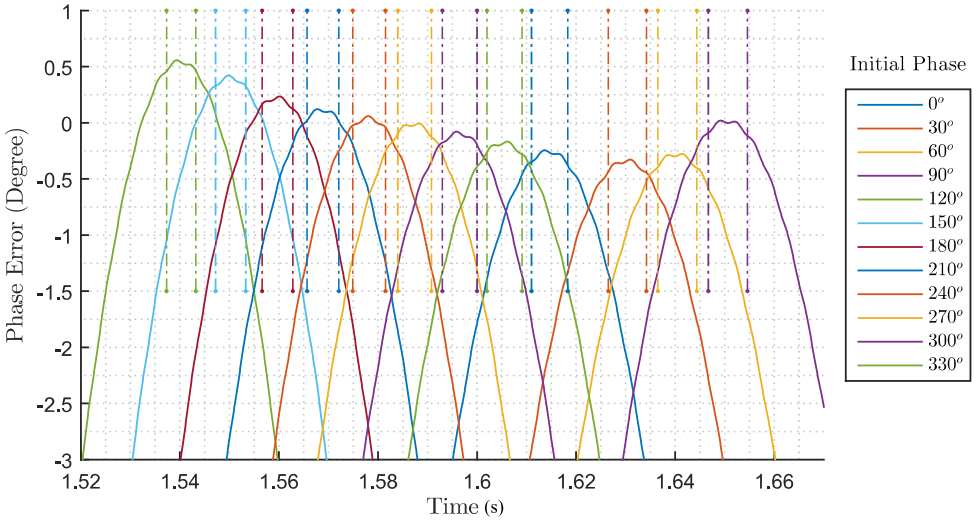

FIGURE 5.36: Phase error plot obtained with various shaft resting positions using poor valve dynamics (dashed line indicates the time span the speed electrical frequency difference is within ±0.3Hz)

5.2.9 Synchronisation Relay Implications

Figures 5.26, 5.28, 5.30, 5.32, 5.34, and 5.36 showed that the time generator stays in the synchronisation for a duration of between 5ms and 7ms, which is much shorter than an typical electromechanical relay turn on time. There are two viable implementations which can ensure the breaker closes precisely: 1) utilize the fast <1ms turn-on time of a conventional solid state relay [189] [190] [191] [192] [193] such that no preemptive breaker closure command generation is needed; or 2) chose an electromechanical relay [194][195] which has a high consistency in breaker turn-on time, and build an advancing signal generation procedure. At the moment, the synchronisation signal generation procedure has yet to be implemented.

Chapter 6

Synchronization Stability Analysis

6.1 Chapter Structure

In a conventional EPS synchronisation process, the generator is speed controlled such that the net torque delivered is always just enough to match the rotational losses and the wait for synchronisation is not critical. As the CGESS generator is always accelerating due to the acceleration control strategy, a net torque is present on the rotor upon breaker closure. Furthermore, the EPS voltage magnitude isikely to be off-nominal and this leads to a reduction in the available damping force on the generator. Therefore, the rotor's ability to reach steady state cannot be guaranteed if the synchronisation parameters are entirely dependent on the IEEE recommendations [97] and the ABB manual [96], whose guidelines are based on conventional synchronisation process. The amount of electromagnetic damping available for rotor deceleration as well as the acceptable range of frequency-phase angle difference synchronisation has to be addressed.

6.2 Synchronization Stability

6.2.1 Section Outline

The stability analysis is performed on a simplified model of the CGESS/EPS electrical interconnection, which is introduced in the first section. Since the generator rotor stability and torque progression depends strongly on the frequency, synchronisation angle, and the generator/EPS terminal voltage magnitudes, the effect varying of all three parameters are investigated. Drawing from the findings, the acceptable range of synchronisation is defined such that the breaker can be closely safely without exceeding the mechanical limitations upon synchronisation.

6.2.2 Stability Study using Classical Model

Whether a generator will stay in synchronism with a large interconnected power system following a disturbance is traditionally studied with the equal area criterion method, which was introduced in Section 2.3.7.4. In this section, a model is developed to facilitate the equal area criterion study.

The interconnected machine generator electrical circuit diagram used to model the CGESS generator synchronisation environment is depicted by Figure 6.1.

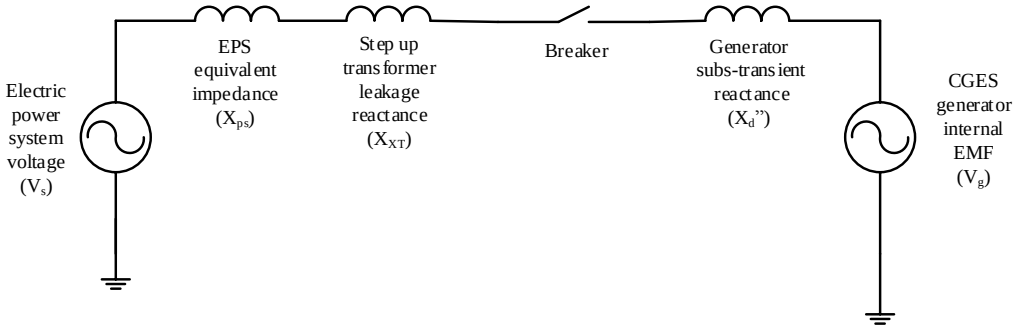

FIGURE 6.1: Synchronisation electrical circuit diagram

In this study, the power grid modeled by its Thévenin equivalent circuit (i.e. ideal voltage source behind an impedance). The generator winding and step up transformer are modeled as the subtransient reactance and leakage reactance respectively , which is commonly used in power system transient stability studies [196]. The per unit base values are defined in Table 6.1.

TABLE 6.1: Synchronization Stability Study Per Unit Base Values

Parameter	Symbol	Value
Power	$S_{gen.base}$	100kVA
Voltage (LV side)	$V_{genLV.base}$	400V
Voltage (HV side)	$V_{genHV.base}$	11,000V
Current (LV side)	$I_{genLV.base}$	144.34A
Current (HV side)	$I_{genHV.base}$	9.091A
Impedance (LV side)	$Z_{genLV.base}$	1.6 Ω
Impedance (HV side)	$Z_{genHV.base}$	1210 Ω

Leakage reactance is typically used to simulate transformer behavior in power stability studies. As the Callaghan campus distribution transformer could not be accessed at the time, the leakage reactance was approximated to be 0.051 p.u.[68], which is a

typical value for a <10MVA, 11kV rated distribution sized transformer. Given that a typical distribution transformer rarely exceeds 1MVA in commercial buildings [197], the Callaghan distribution transformer was also approximated to be 250kVA. Converting the impedance to the 100kVA base with Equation 2.28, we have:

$$X_{XT(p.u.)} = 0.051 \cdot \left(\frac{1}{1}\right)^2 \frac{100\text{kVA}}{250\text{kVA}} = 0.0204\, p.u. \tag{6.1}$$

Similarly, the power system Thévenin equivalent impedance was approximated. In practice, power systems are designed with a maximum short circuit level such that the current through the existing distribution equipment cannot exceed their maximum ratings during a fault, and the Transmission Line Planning Guideline [198] references the maximum short circuit level of a 11 kV transmission system to be 475MVA. Assuming a short circuit level of 400MVA (85% of planned value) is seen at the high voltage side of the step up transformer, the power system Thévenin equivalent impedance can be derived with equation 2.25:

$$\begin{aligned} X_{ps} &= \frac{V_{EPS}^2}{S_{EPS}} \\ &= \frac{(11 \times 10^3)^2}{400 \times 10^6} \\ &= 0.3025\Omega \end{aligned} \tag{6.2}$$

Using Equation 2.27, X_{ps} can be converted into per-unit expression with 11kV, 100kVA base:

$$\begin{aligned} X_{ps(p.u.)} = \frac{Z_{actual}}{Z_{base}} = \quad &= \frac{0.3025}{1210} \\ = 0.00025\, p.u. \end{aligned} \tag{6.3}$$

The power grid impedances are approximated by pure reactances without the resistance, as transmission lines and transformers are dominantly inductive. The generator saturated d-axis subtransient reactance was used for transient simulation as suggested by protection studies handbooks [90], [199], [200], [201]. The per unit reactances are summarized by Table 6.2.

TABLE 6.2: Synchronization Stability Study Per Unit Base Values

Impedance	Symbol	Value
Electric power grid equivalent reactance	X_{ps}	0.00025 p.u.
Step up transformer leakage reactance	X_{XT}	0.0204 p.u.
Generator d-axis subtransient reactance	X_d"	0.1830 p.u.
Generator q-axis transient reactance	X_q	1.446 p.u.
Applied generator mechanical power	P_m	1 p.u.

In this study, the mechanical power was set to be the highest possible synchronisation machine power input of 1 p.u. and the electrical power output is modeled by Equation 2.37. To provide a better visualization of how close the generator is to instability, equation 6.4 can be written:

$$A_{ratio} = \frac{\text{Decelerating Area}}{\text{Accelerating Area}} \tag{6.4}$$

which indicates the relative stability margin where the value of 1 represents the border of instability.

The power angle relationship of the CGESS generator with 1 p.u. voltage synchronized to the EPS with 1 p.u. voltage with 0 degree angular error is shown in Figure 6.2, which showed that the generator will be stable if perfectly synchronized to an 1 p.u. EPS with the expected impedances.

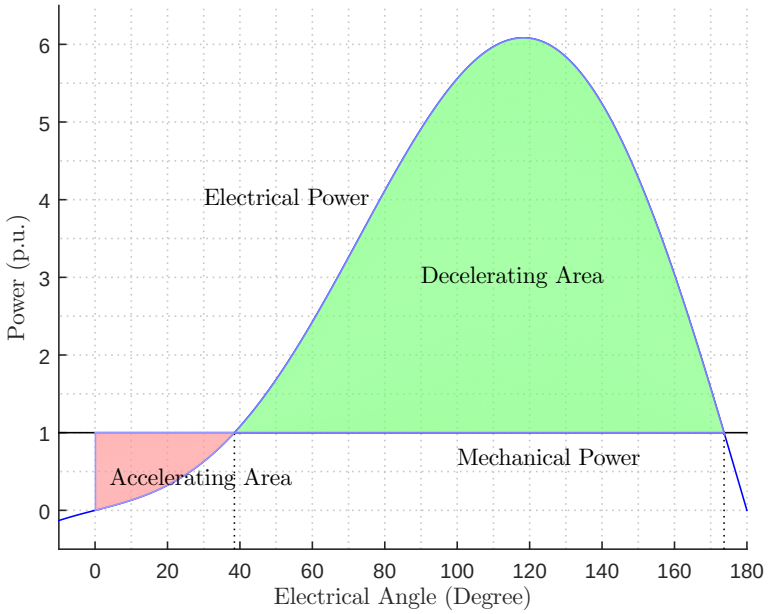

FIGURE 6.2: Equal area criterion graphical illustration simulated with expected impedances and perfect angle synchronisation ($A_{ratio} = 16.96$)

6.2.3 Effect of Power System Voltage Dip

From equation 2.37, the delivered generator electrical power decreases as the EPS voltage magnitude sags. Because the synchronisation recommendation requires the generator terminal voltage to be within the percentage error of the EPS voltage, the reduction in electrical damping force is due to voltage sag is raised to the power of 2. Using the area ratio expressed by Equation 6.4, Figure 6.3 can be plotted to study the effect of voltage dips on the stability, with a 15^o synchronisation angle even.

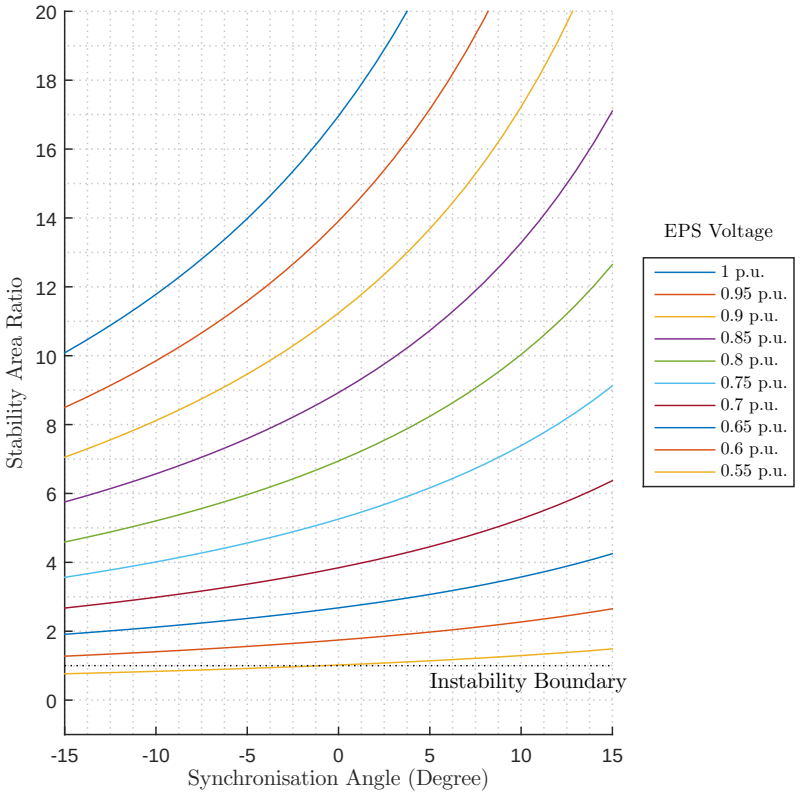

FIGURE 6.3: Stability analysis using equal area criterion when $V_{grid} = V_{gen}$

Figure 6.3 suggests that successful synchronisation can still be achieved following the $\pm 15^o$ synchronisation angle error if the EPS voltage is above 0.6 p.u..

Since the EPS voltages will be off the nominal magnitude seen in a typical CGESS synchronisation process, the rotor torque is also studied to ensure the imposed torque does not exceed its rated value. Figure 6.4 contains a set of the electromagnetic torque progression obtained under various synchronisation angles. The plot is achieved through using the transient torque dynamics equation described by Equation 2.41 and treating X_D as the combination of X_{ps}, X_{XT}, X_d" that are depicted in Table 6.2.

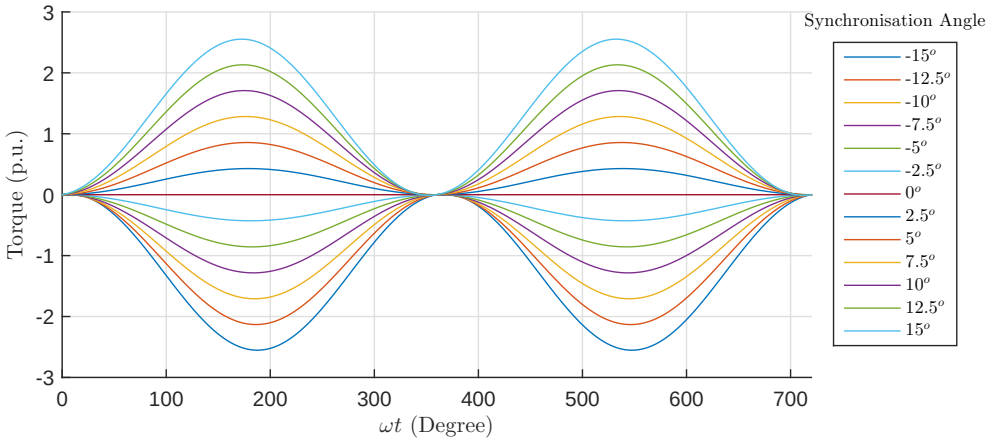

FIGURE 6.4: Torque transient as a function of synchronisation angle

Expectedly the largest peak transient torque occurs when the synchronisation angle is at its extrema. To study the peak transient torque behavior due to decreased EPS voltage magnitude, the torque was considered only using $\Delta\delta = \pm 15^o$. The respective torque dynamics are shown in Figures 6.5A and 6.5B, which shows even with nominal EPS voltages, synchronizing at $\Delta\delta = \pm 15^o$ will result in peak torque exceeding the generator rated value. Figures 6.5A and 6.5B also show that the peak torque is reduced as the EPS voltages dip becomes more severe.

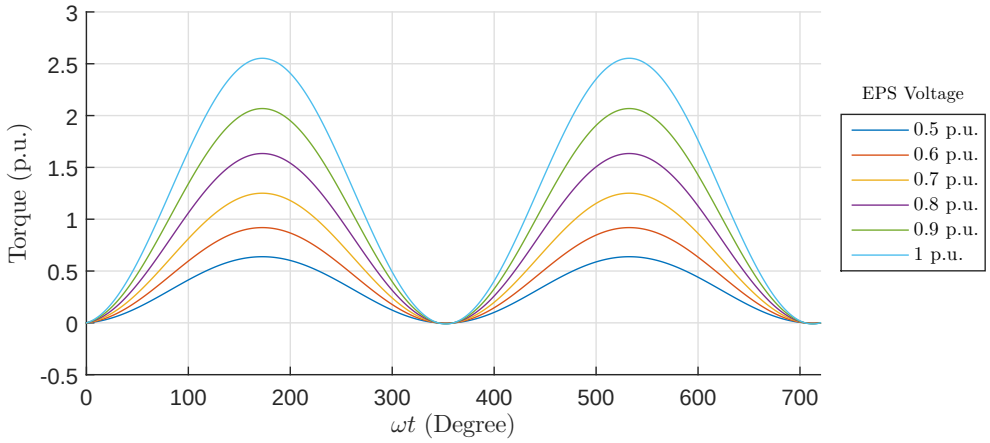

(A) Torque transient when $\Delta\delta = 15^o$

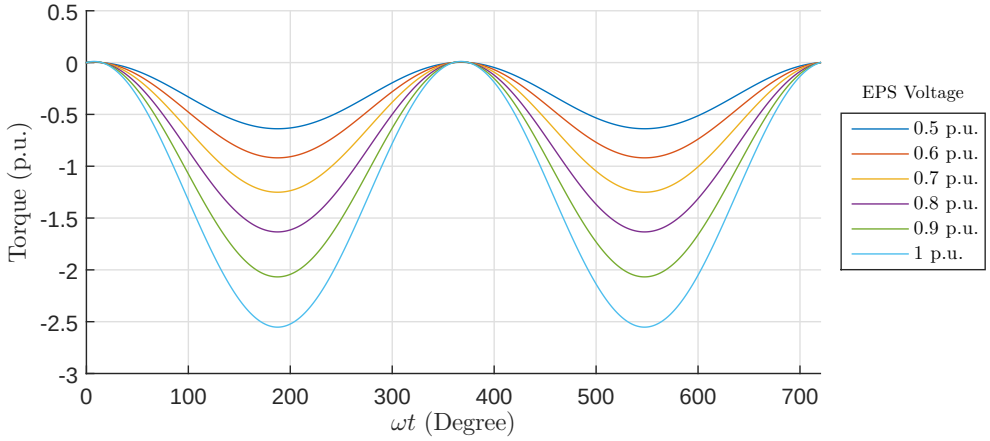

(B) Torque transient when $\Delta\delta = -15^o$

FIGURE 6.5: Synchronisation peak torque transients

Observing Figure 6.5A and 6.5B, the transient torque increases with the EPS voltages magnitude and the synchronisation angle error, which is expected. However, the exact voltage and synchronisation angle error range within which the breaker can be safely closed without overstepping rated torque is unclear. Using the symmetrical nature shown in Figure 6.5A and 6.5B, the absolute peak torque using only the positive synchronisation angle differences are plotted against the EPS voltages, and the result is shown in Figure 6.6.

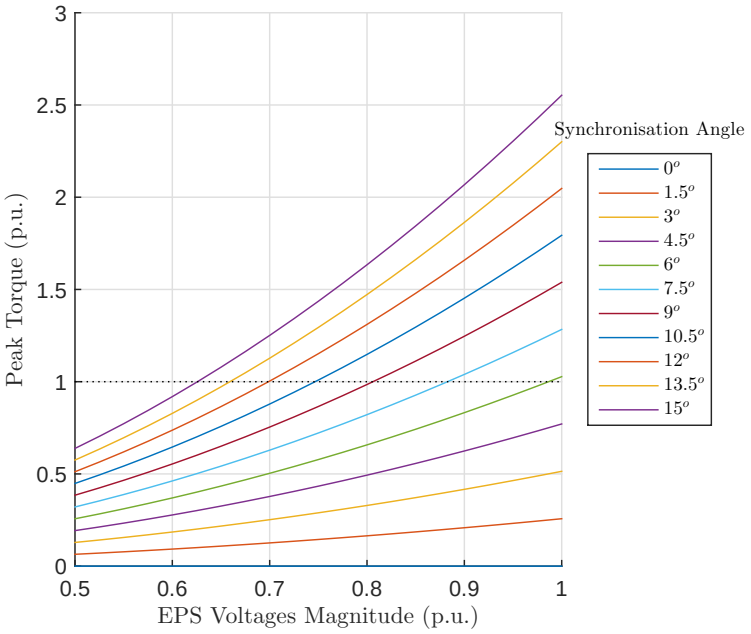

FIGURE 6.6: Peak transient torque as a function of EPS voltage variation

Figure 6.6 demonstrates that the breaker can be closed safely if the synchronisation angle is less than 6^o regardless of the EPS voltage magnitude, as the peak torque will not exceed 1 p.u. any time after the breaker closure. Since the simulations shown in Chapter 5 proposed that the controller is capable of synchronizing the CGESS to the EPS with an angle difference of less than 1^o, the wide range of allowable synchronisation phase angle error provides the controller with a significant amount of control error margin.

6.2.4 Effect of Impedance Modeling Error

Because the strength of the power system at the connection point and the step up transformer characteristics shown in the previous sections have been approximations based on textbooks and planing criteria the effect of impedance modeling error is also investigated. Figure 6.7 is a plot of the effect of transformer/EPS impedance modeling error on the stability area ratio using nominal EPS and CGESS generator voltages.

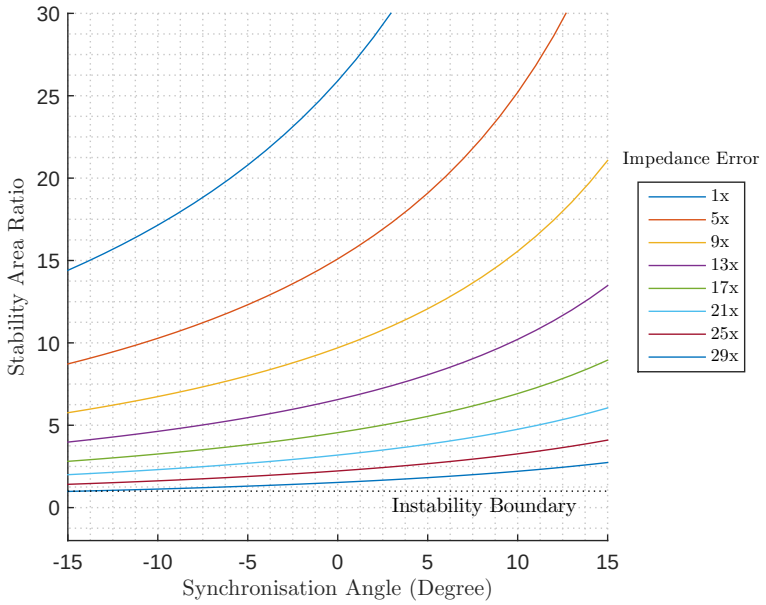

FIGURE 6.7: Effect of impedance modeling error on stability

Figure 6.7 shows that the tolerable transformer impedance and the EPS equivalent impedance sum cannot be higher than 25 times the expected value. Since the transformer impedance is around 100 times the EPS impedance, it is recommended that the CGESS is installed with a step up transformer which has an impedance less than 0.51 p.u..

6.2.5 Summary and Development of Synchronisation Limitations

Studies shown in Sections 6.2.4 and 6.2.3 advised that the CGESS generator cannot synchronize to the EPS based on the IEEE synchronisation phase angle recommendation, and this leads to the development a new set of synchronisation limitation. Following the instant that the generator speed crosses over the threshold of -0.3 Hz difference from the EPS frequency, the developed synchronisation algorithm should ensure:

1. the generator open circuit voltage is measured with the same voltage magnitude as the EPS.

2. synchronisation angle error is within $\pm 6^o$

before sending the breaker closure command. These steps were set to alleviate the effect of impedance modeling error and to accommodate for the measurement angle error contributed by the phase locked loop design and the encoder measurement signal processing algorithm.

Chapter 7

Conclusion

7.1 Thesis Summary

This thesis documents the design and simulation of control and instrumentation to achieve the rapid compressed gas energy storage system grid synchronisation goal proposed by Callaghan Innovation. The traditional synchronisation method, off-the shelf synchronisation hardware specifications, and the power grid dynamics during a contingent event are firstly studied to define the desired instrumentation accuracy. Then, appropriate signal processing algorithms such as the PLL and Kalman filter are designed to meet the accuracy specifications. Using the developed hydraulic model, an acceleration control strategy is formulated to eliminate the switchover from maximum acceleration to phase control which is limited by hydraulic valve capability. Although a system identification process was carried out, the test-rig sustained irrecoverable damages part way through the tests. The partially characterized PTV provided sufficient information on the valve dynamics which are unlike the manufacturers specification, and allowed a more robust controller to be designed.

Using a wide range of realistic power grid and generator conditions, simulation results demonstrate solid control performance by meeting both the synchronisation frequency and phase limitation simultaneously, even with a deteriorated control valve. In addition, post breaker closure transient stability studies have been conducted to test the novel acceleration control technique. The stability study resulted in a more restricted synchronisation limitation, which the controller is capable of accomplishing.

Overall, much work was put into analyzing the viability of rapidly synchronizing a hydraulic powered generator and provide the control development framework using well understood classical techniques without access to the full CAESS system. The simulations verified the suitability of the proposed rapid synchronisation approach. Should the project wish to expand and increase the CAESS power output, this thesis sets the foundations for hydraulic powered system modeling and rapid synchronisation control.

7.2 Limitations and Future Work

Although the simulations were comprehensive, the control performance cannot be guaranteed on the compressed gas hydraulic system since the simulations were based on a very limited amount of practical testing. Many process disturbances and unforeseen variations in process variables such as accumulator pressure, additional hydraulic orifice constrictions, motor efficiency, inertial mass, as well as fluid temperature, are likely to deviate the system from the intended controller operating range. It is not possible to cover every scenario within the scope of this thesis. Moreover, the gain scheduled controller was not designed considering the processing hardware limitations. In reality, the scheduled gain change will be triggered as the flowrate crossover a threshold instead of being continuously computed with each sample period. In the future, the controller must be converted to machine appropriate software and tested in a real environment.

In terms of practical implementation, the calibration of rotor position to terminal emf has yet to be validated. Despite the textbook definition which states that the generator terminal voltage is directly proportional to rotor position, the description only refers to the generator operating in steady state. For the CAESS system, the rapid acceleration may cause unforeseen hurdles for a commercial automatic voltage regulator, as the steady excitation field establishment time has not traditionally been a constraint prior to grid synchronisation. Whether this is a trivial problem or not for the automatic voltage regulator remains to be investigated.

Appendix A

Compressed Gas Energy Storage Hydraulic Circuit Diagram

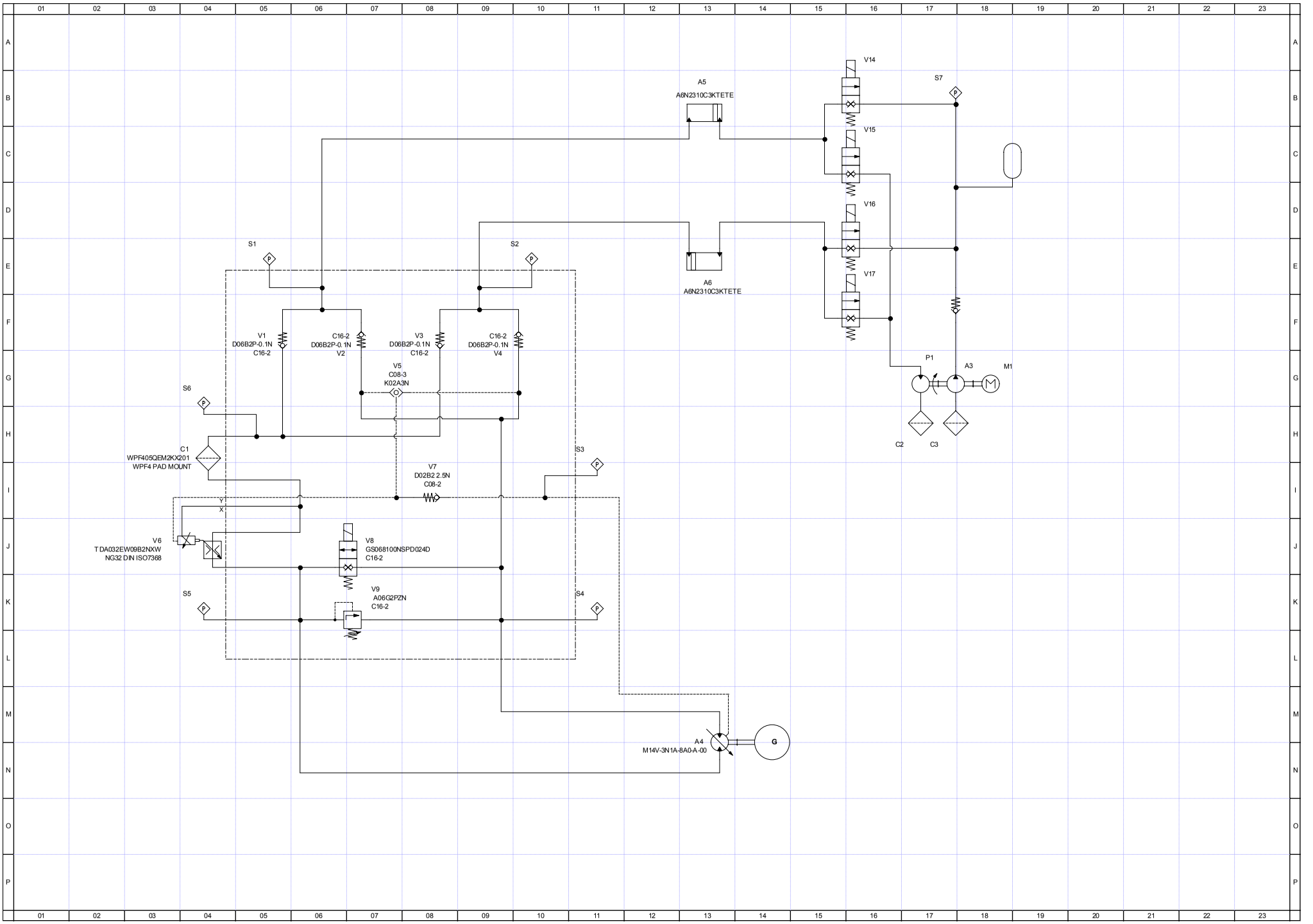
A5
A6N2310C3KTETE
A6
A6N2310C3KTETE
V14
V15
V16
V17
S7
S1
S2
V1
D06B2P-0.1N
C16-2
C16-2
D06B2P-0.1N
V2
V3
D06B2P-0.1N
C16-2
C16-2
D06B2P-0.1N
V4
V5
C08-3
K02A3N
P1
A3
M1
C2
C3
S6
C1
WPF405QEM2KX201
WPF4 PAD MOUNT
S3
V7
D02B2 2.5N
C08-2
Y
X
V6
T DA032EW09B2NXW
NG32 DIN ISO7368
V8
GS068100NSPD024D
C16-2
S5
V9
A06G2PZN
C16-2
S4
A4
M14V-3N1A-8A0-A-00
G

Appendix B

Controller Design

```
function [AccOrder,GirdPhaseOffset,WsynchReached]...
  = fcn(GenAccMeas,GridFreq,GridPhase,GenPhase,GenSpeed,IRTrigger)

%Process Elec to Mech Quantities
GridMechRadPerS = GridFreq*2*pi/2;      %Convert to Mechanical Frequency
GridPhz = GridPhase/2;
%Hydraulic System Variables
PmMax = 350;    %250 bars of pressure drop accross motor
MotorDis = 115;     %motor displacement 115cm^2/rev
%Mechanical
Tmax = MotorDis*PmMax/63;
Accmax = Tmax/1.6;  %T = Ja a = Tmax/Jestimate;

%Initialize Variables
GirdPhaseOffset = 0;
N2piOffest = 0;
WsynchReached = 0;
LastCycleFlag=0;
Aorder = 0;
AccOrder = AccPrev;

% Desgin Limitations
Alim = 0.8*Accmax;
FsyncLimit = 0.1;
WsyncLimit = FsyncLimit*pi;     %not by 2pi because mech speed

if IRTrigger == 1;
    if AccDerivationflag == 1;
        for n = 2:1:20
            ACCorder = 1/2*(GridMechRadPerS-GenSpeed)^2...
            /(GenPhase-GridPhz+n*2*pi);
            if ACCorder < Alim
                k = n;
                AccDerivationflag = 0;
                break;
            end
        end
```

```
38      end
39      N2piOffest = k;
40      Aorder = 1/2*(GridMechRadPerS-GenSpeed)^2/(GenPhase-GridPhz+k*2*pi);
41      GirdPhaseOffset = GridPhz - N2piOffest*2*pi;
42      %Derivation conditions
43
44      if (GridMechRadPerS - GenSpeed) < 1*2*pi;
45          AccDerivationflag = 0;
46          LastCycleFlag = 1;
47          Aorder = AccPrev;
48      end
49      if Aorder > Alim | Aorder < 0;
50          AccDerivationflag = 1;
51      end
52      if AccElpasedTime>0.2
53          AccDerivationflag = 0;
54      end
55      if (GridMechRadPerS-GenSpeed)<WsyncLimit ...
56      & abs(GenPhase-GirdPhaseOffset)<(10*pi/180)
57          WsynchReached = 1;
58      end
59
60      AccPrev = Aorder;
61
```

Appendix C

ABB AMG0250AA04-DBSI Synchronous Generator Specification

TECHNICAL SPECIFICATION

Type designation: **AMG 0250AA04**
Application: Diesel/Gas engine Industrial Application Series
Site criteria: Land use

NOTES

CONTENTS

SECTION:

*Type definition:

AMG0250AA04 DBSI

IC/IP combination
Bearing type
Excitation type
Industrial generators

Bearing type: A-Double bearing, B-Single bearing
Excitation type: S-Shunt, A-Auxiliary winding, P-PMG

1 PERFORMANCE DATA (Calculated values)

TYPE

Type designation: AMG 0250AA04

PERFORMANCE DATA

Main standard	IEC 60034							
Rated power factor	0.8							
Insulation class	H							
Temperature rise	H							
Ambient temperature	40 ℃							
Altitude over sea level	≤ 1000 m							
Cooling/Protection	IC0A1/IP23							
	Single bearing				Double bearing			
Mounting arrangement	IM 2105				IM 1001			
Weight without/with PMG	405/415 kg				420/430 kg			
Inertia without/with PMG	1.45/1.46 kgm^2				1.39/1.40 kgm^2			
Direction of rotation	CW (Facing drive end)							
Maximum overspeed	2250 rpm							
Winding pitch	Two thirds (2/3)							
Stator winding resistance	0.0531Ω per phase at 20℃ series star connection							
Rotor winging resistance	1.211 Ω at 20℃							
Ex. stator winding resistance	9.22 Ω at 20℃							
Ex. rotor winding resistance	0.200 Ω at 20℃							
Total Harmonic Distortion	At no load<2%, at rated Linear balanced load <5%							
Voltage regulation	±1 %							
Telephone Interference	THF<2%				TIF<50			
Frequency	50 Hz				60 Hz			
Speed	1500 rpm				1800 rpm			
Cooling Air	0.17 m³/sec				0.20 m³/sec			
Voltage series star 3ph.	380/220	400/231	415/240	440/254	415/240	440/254	460/266	480/277
Voltage parallel star 3ph.	190/110	200/115	208/120	220/127	208/120	220/127	230/133	240/138
Voltage series delta 3ph.	220	230	240	254	240	254	266	277
Voltage parallel delta 3ph.	110	115	120	127	120	127	133	138
Rated continuous output	95 kVA	100 kVA	100 kVA	90 kVA	108 kVA	115 kVA	120 kVA	125 kVA
Xd(u)	3.024	2.873	2.669	2.137	3.459	3.276	3.128	2.992
Xd(s)	2.352	2.109	1.851	1.312	2.863	2.626	2.414	2.196
Xq(u)	1.522	1.446	1.343	1.076	1.741	1.649	1.574	1.506
X'd(u)	0.317	0.301	0.280	0.224	0.362	0.343	0.328	0.314
X'd(s)	0.288	0.274	0.255	0.204	0.329	0.312	0.298	0.285
X"d(u)	0.212	0.201	0.185	0.146	0.245	0.231	0.220	0.210
X"d(s)	0.193	0.183	0.168	0.133	0.223	0.210	0.200	0.191
X"q(u)	0.162	0.154	0.143	0.114	0.185	0.175	0.167	0.160
X"q(s)	0.147	0.140	0.130	0.104	0.168	0.159	0.152	0.145
X1(u)	0.079	0.076	0.070	0.056	0.091	0.086	0.082	0.079
X2(u)	0.187	0.177	0.164	0.130	0.215	0.203	0.194	0.185
X2(s)	0.170	0.161	0.149	0.118	0.195	0.185	0.176	0.168
X0(u)	0.033	0.031	0.029	0.023	0.038	0.036	0.034	0.032
Xp(s)	0.238	0.226	0.210	0.168	0.271	0.257	0.246	0.236
SCR (short circuit ratio), Ir0/Xd (u)	0.43	0.47	0.54	0.76	0.35	0.38	0.41	0.46
s=saturated value, u=unsaturated value, values are p.u. at rated voltage and power								
Td0'	1.645 s							
Td'	0.076 s							
Td''	0.0063 s							
Ta	0.0135 s							
CE-Marking	Generator fulfills the requirements of Low Voltage Directive (2006/95/EC) Generator supplied to EEA-area will be CE-marked							

2 PERFORMANCE CURVES

THREE PHASE EFFICIENCY CURVES, 50 Hz/380–440 V

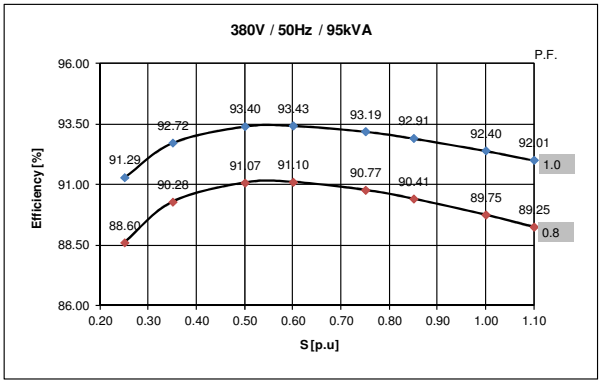

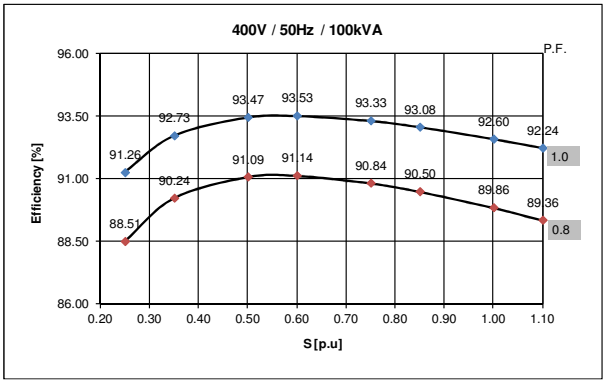

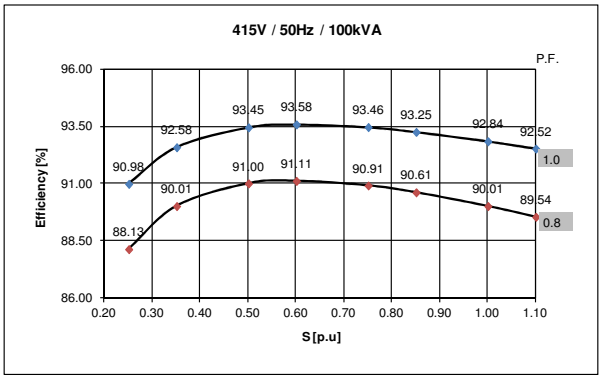

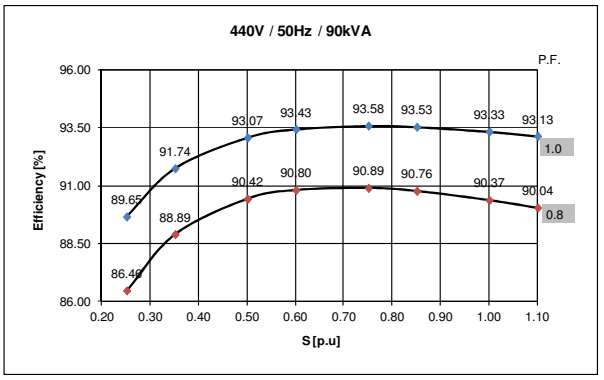

THREE PHASE EFFICIENCY CURVES, 60 Hz/415–480 V

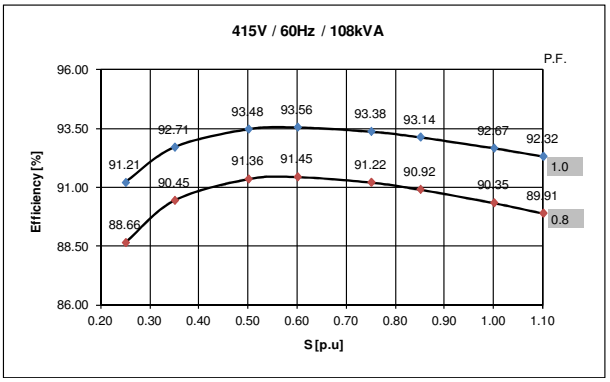

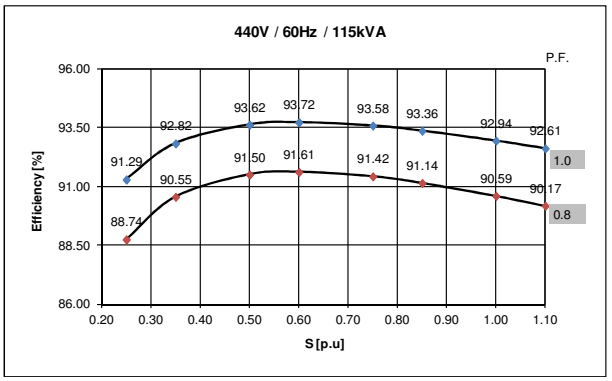

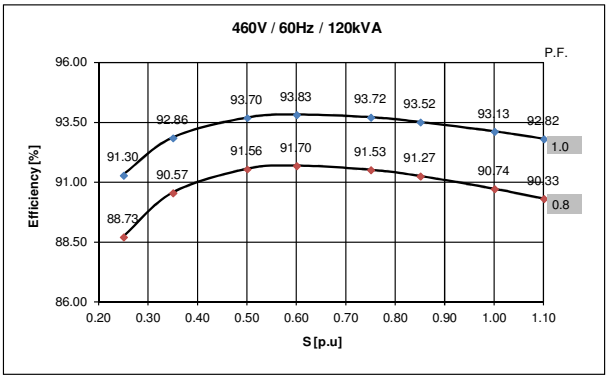

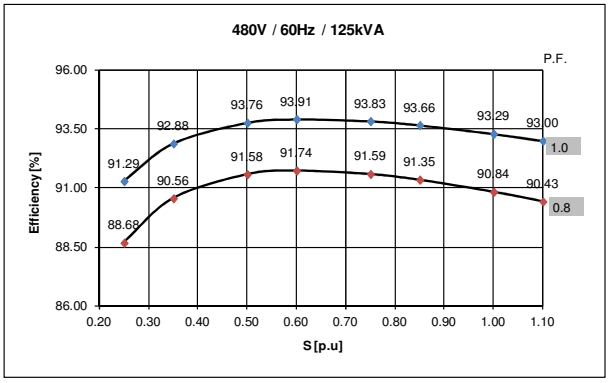

TRANSIENT VOLTAGE REGULATION CURVES

Load application (Shunt excitation):

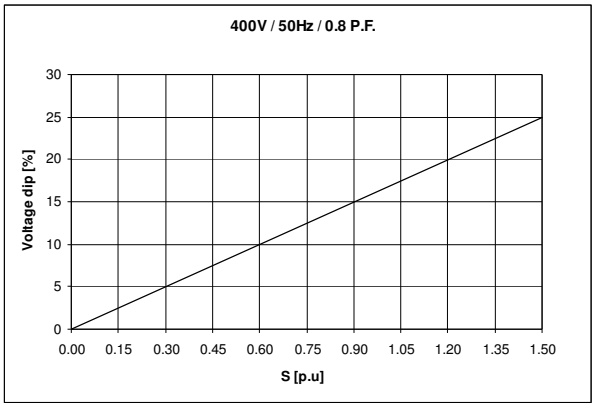

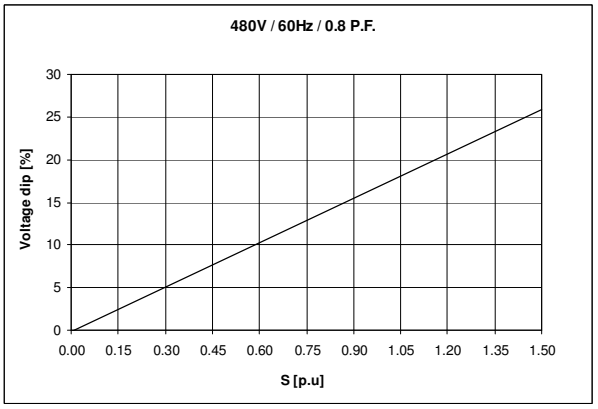

Load application (Auxiliary winding or PMG excitation):

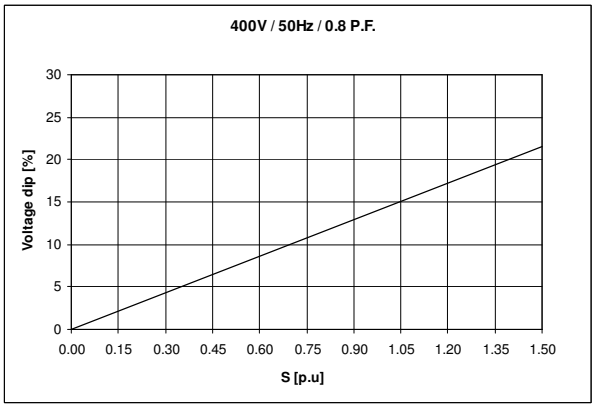

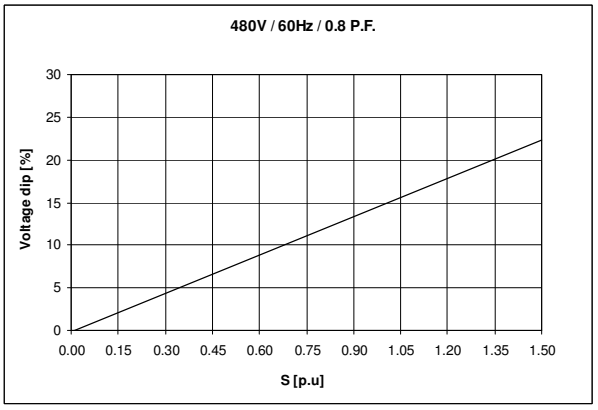

Load rejection (Shunt excitation):

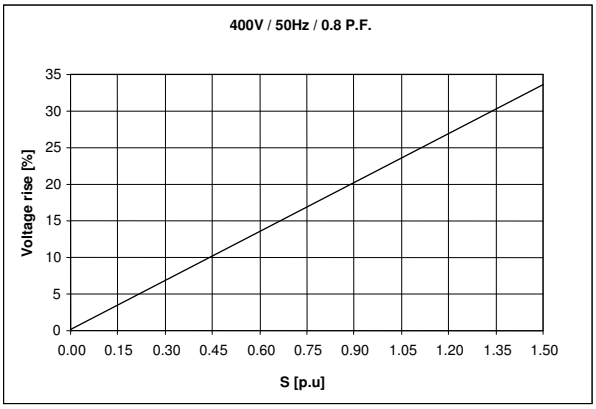

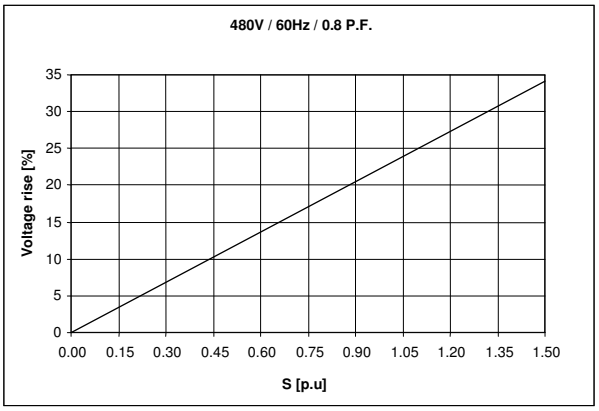

TRANSIENT VOLTAGE REGULATION CURVES

Load rejection (Auxiliary winding or PMG excitation):

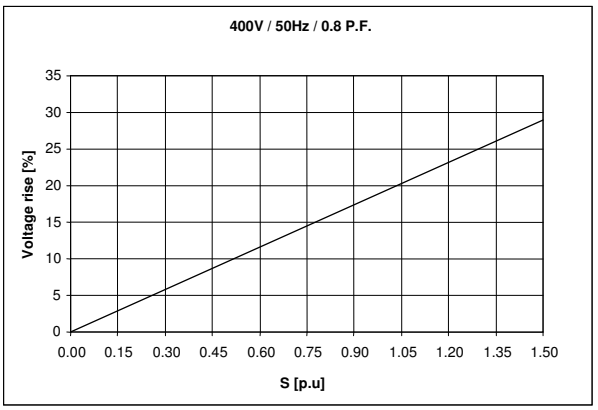

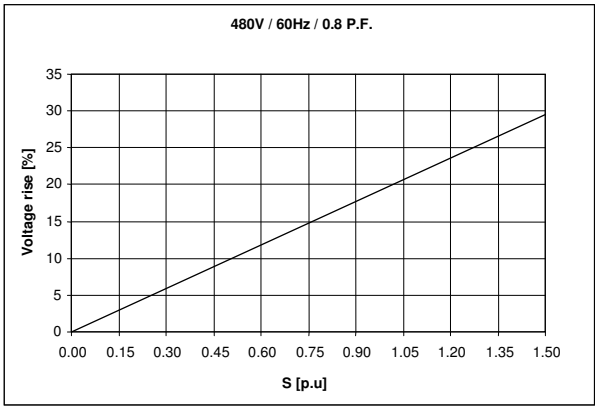

Locked Rotor Motor Starting Curve (Shunt excitation):

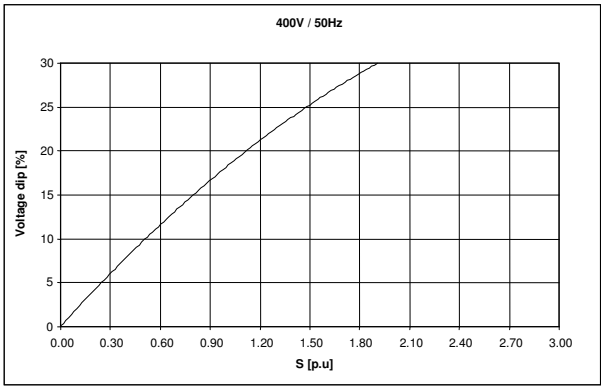

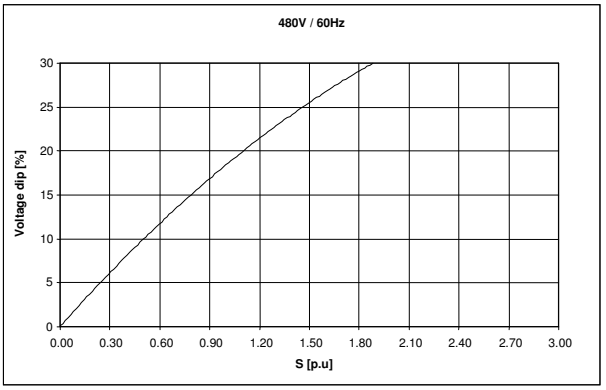

Locked Rotor Motor Starting Curve (Auxiliary winding or PMG excitation):

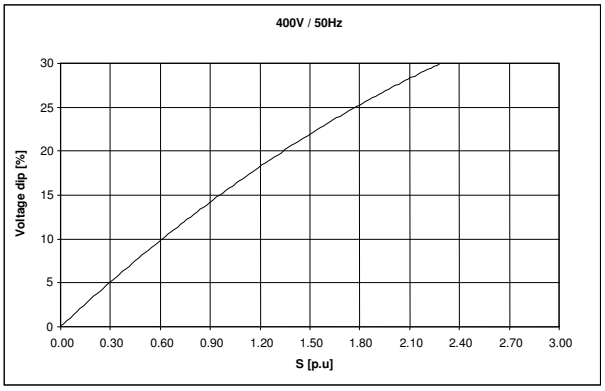

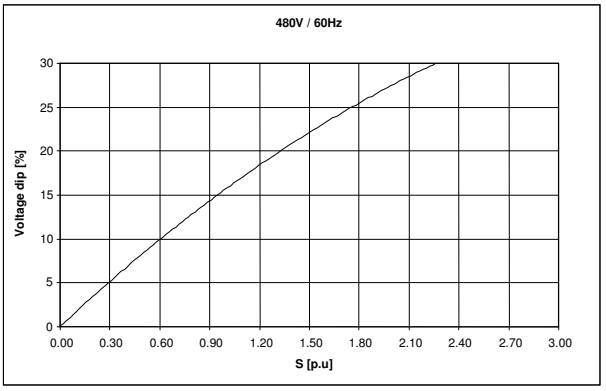

Note1

S [P.U] =S/S(Rated), S stands for the actual operation capacity, S(Rated) stands for the generator rated output capacity.

THREE PHASE SHORT-CIRCUIT CURVES (At no-load and rated speed, base on star connection)

50Hz

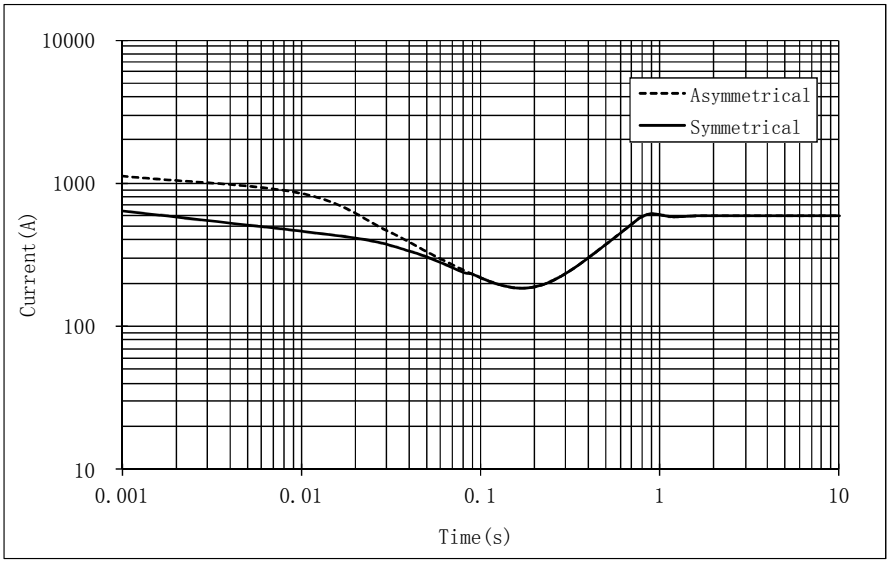

60Hz

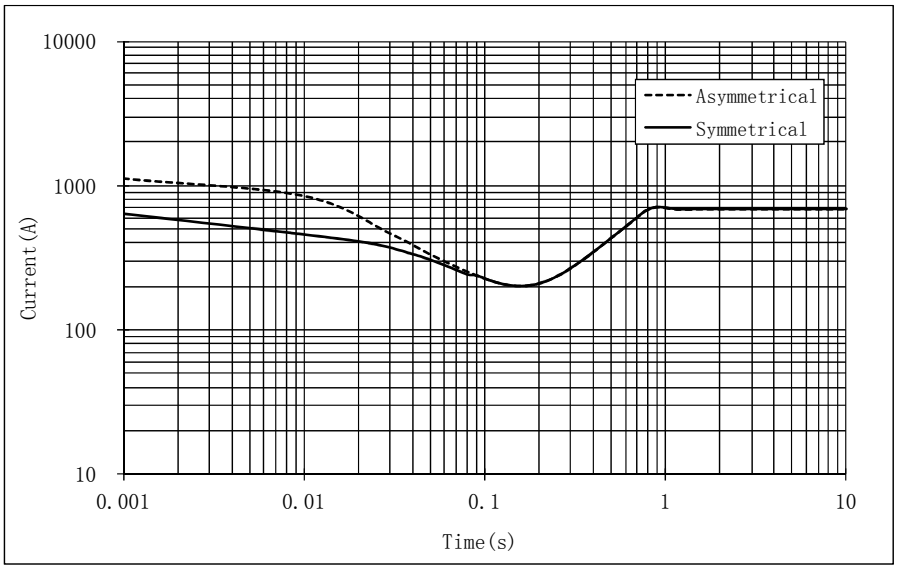

Note2

Curves are for star connection. For other connection, please use following multiplication factors:
Series delta: Current values x 1.732
Parallel star: Current values x 2

Curves are for 3-phase short-circuit. For other types of short-circuit, please use following multiplication factors:

	Instantaneous	Continuous	Maximum duration
3-phase	1	1	10 sec.
2-phase L/L	0.87	1.5	5 sec.
1-phase L/N	1.3	2.2	2 sec.

3 CONFIGURATION AND SCOPE OF SUPPLY

GENERAL

The generator is designed to operate together with a diesel or gas engine.

CONSTRUCTION

The stator frame is a rigid welded steel structure construction. The stator core is built of thin electric sheet steel laminations which are insulated on both sides with heat-resistant inorganic resin.

The rotor consists of a shaft and a star shape rotor core. The shaft is machined of rolled steel. Special heat treatment is used if shaft operates under heavy conditions. The poles are manufactured of 0.5 mm sheet steel. The pole laminations are pressed and welded together with steel bars. These bars are then welded to the end plates. Rotor balancing is done acc. to ISO 1940/1. The standard balancing quality grade is G2.5.

All windings are completely vacuum pressure impregnated with high quality resin. The windings are provided with very strong bracing which withstands all expected mechanical and electrical shocks and vibrations as well as chemicals.

End shields are made of casted steel, The stator frame and stator core are welded together, and bolted with end shields.

MAIN TERMINAL SPACE

Protection class IP44, Integrated into the top module of the generator.

Supply cable entries: Closed terminal box. Cable inlet to the main terminal box to be done by the customer.

Twelve (12) leads T1 – T12 brought into the terminal box to enable internal series star, parallel star, series delta and parallel delta connection, Main terminals U, V, W and neutral point N in the main terminal box for external connection

Terminal marking acc. to IEC.

Designed for continuous current load.

FOUNDATION

The machine can be mounted using shimming, machined blocks, chock fast or on grouted sole plates or bed plate. Before using other mountings, contact us.

CONTROL SYSTEMS

General

Brushless excitation.

Automatic Voltage Regulator System

Mounted inside the main terminal box.

Analog type AVR.

Functions:

a) 1-channel AVR.
b) Excitation power can be from phase voltage of main terminal or auxiliary winding, PMG.
c) Voltage set-point adjustment (local).
d) U/f limiter.
e) Parallel operation.

Static voltage regulation accuracy +/- 1.0 %.

Voltage recovery time after transient<1.5 s, +/- 3.0 % (acc. to IEC 60034).

Nominal Um, range: < 90 VDC at 110 VAC input, 170 VDC at 220 VAC input.

Nominal Im, range: continuous 5 ADC.

BEARINGS

Non Drive-end: Rolling, sealed, free. Drive-end: Rolling, sealed, locked.(Double bearing)

Maximum bearing temperature 90 °C at ambient 40°C.

TESTING

Testing is according to IEC and ABB internal requirements. The test may be observed by the customer without extra charges. The test procedures are described in the following documents which are available on request:

-Routine tests: MDD 8006327 (for all machines).
-Type tests: MDD 8006328 (optional, to be agreed separately).
-Special tests: MDD 8006329 (optional, to be agreed separately).

PERFORMANCE CHARACTERISTICS AND OPERATIONAL LIMITS

Rating for continuous running duty:
Duty type S1.

Rating for short-time duty:
10 % overload at nominal power factor for one hour at twelve hour intervals.

Overcurrent withstand capability:
1.5 times nominal current for 2 minutes.

Sustained short-circuit current:
More than 3 times nominal current for 10 seconds.

Generator shall be suitable for supplying circuits which, when supplied by a system of balanced and sinusoidal voltages:

Result in currents not exceeding a harmonic current factor of 0,05 and

Result in a system of currents where neither the negative-sequence component nor the zero-sequence component exceed 5% of the positive-sequence component

Maximum voltage unbalance is 0.5 %.

Maximum I2/IN value for continuous operation is 8 %.

Maximum $(I2/IN)^2$ x t in seconds for operation under fault conditions is 20

Maximum continuous voltage variation with rated output is ±5 %.

Maximum continuous frequency variation with rated output is ±2 %.

Maximum combined voltage and frequency variation and maximum short-time limits are acc. To IEC 60034-1:2004, Section 7.3.

Electromagnetic Compatibility (EMC)

Radiated and conducted emissions comply with the requirements of CISPR 11, Class B, Group 1, Table B.1. (IEC 60034-1, Annex B).

TOLERANCES

Efficiency η	
Machines up to and including 150 kW (or kVA)	–15 % of (1–η)
Machines above 150 kW (or kVA)	–10 % of (1–η)
Total losses (applicable to machines with ratings >150 kW or kVA)	+10 % of the total losses
Peak value of short-circuit current under specified conditions	±30 % of the value in the technical specification
Steady short-circuit current at specified excitation	±15 % of the value in the technical specification
Moment of inertia	±10 % of the value in the technical specification

SURFACE TREATMENT

Grade: C2, Standard color

Surface treatment C2 according to the ISO 12944 standard, for standard industrial environment.

4 ACCESSORIES

OPTIONAL ACCESSORIES

No pc/pcs	Item	Note
1	Anti-condensation heater	
1	Current transformer	For parallel operation with other generators
3	PT100 for stator winding	
1	PTC sensor (triple)	
1	PMG	

5 DIMENSIONS

MAIN DIMENSIONS

Single bearing **Double bearing**

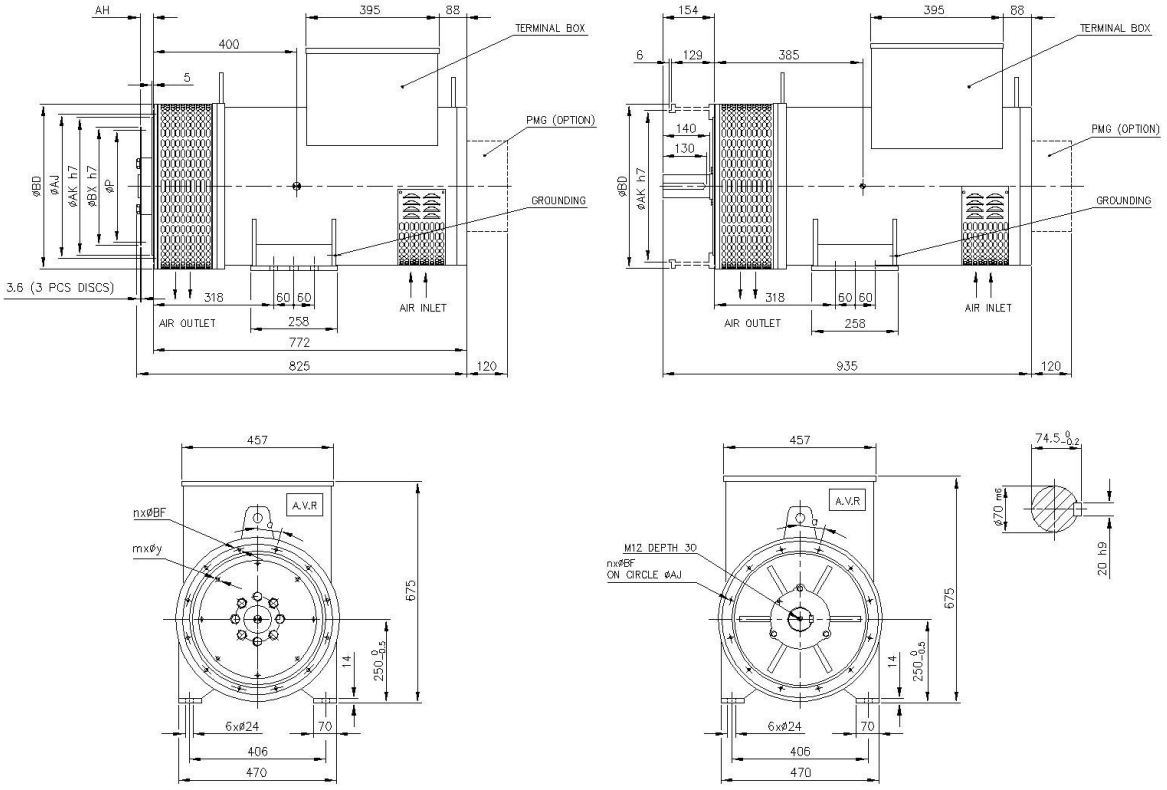

Flange dimensions

S.A.E	AK	AJ	BD	BF	n	a
3	409.58	428.6	490	11	12	15°
2	447.67	466.7	528	11	12	15°

Flex disc dimensions

S.A.E	BX	P	AH	Y	m
$11^{1/2}$	352.43	333.38	39.6	11	8

ROTOR DRAWINGS

Single bearing

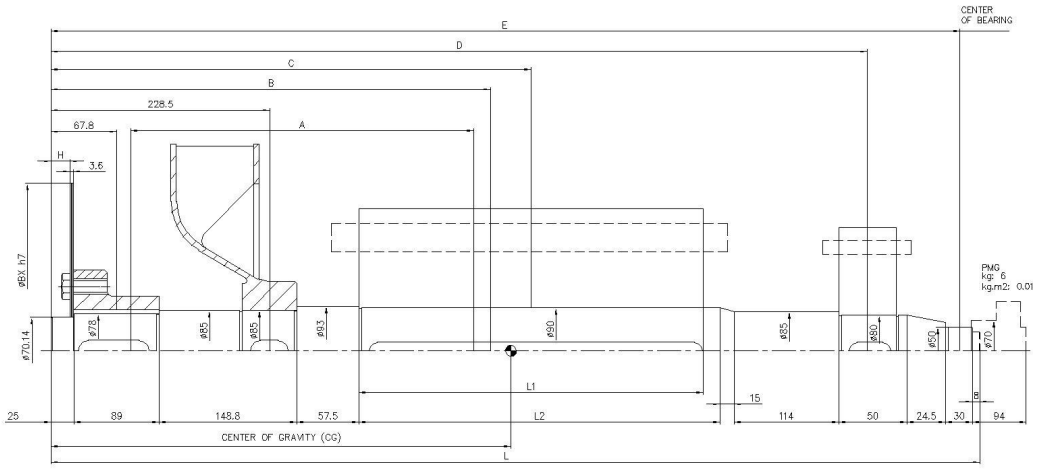

Flexplate					Hub		Fan		Shaft					Rotor center				Exciter			Total Roter			Torsional stiffness		Bearing
SAE	ΦBX	H	Kg	Kg.m2	Kg	Kg.m2	Kg	Kg.m2	B	L	L2	Kg	Kg.m2	C	L1	Kg	Kg.m2	D	Kg	Kg.m2	CG	Kg	Kg.m2	A	Nm/rad	E
14	466.6	20.4	4.6	0.13	7	0.02	9	0.15	397.6	811.8	250	35	0.03	437.3	240	103.1	1.09	722.3	10.8	0.12	428.5	167.5	1.54	316.1	1.36E+06	789.3
11.5	352.43	6.2	2.6	0.04	7	0.02	9	0.15	397.6	811.8	250	35	0.03	437.3	240	103.1	1.09	722.3	10.8	0.12	428.5	169.5	1.45	316.1	1.36E+06	789.3

Double bearing

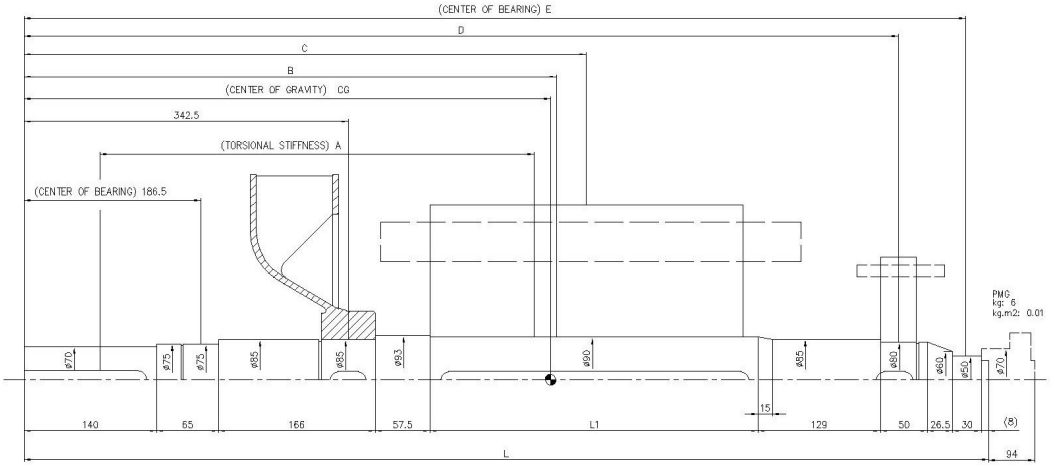

Fan		Shaft					Rotor center			Exciter			Total Roter			Torsional stiffness		Bearing
Kg	Kg.m2	B	L	L1	Kg	Kg.m2	C	Kg	Kg.m2	D	Kg	Kg.m2	CG	Kg	Kg.m2	A	Nm/rad	E
9	0.15	470	922	250	37	0.03	545.5	103	1.09	830.5	11	0.12	477	160	1.39	427	7.88E+05	897.5

Bibliography

[1] Electricity Authority. Electricity Industry Participation Code 2010, 2015. URL https://www.ea.govt.nz/code-and-compliance/the-code/. Accessed: 25.06.2015.

[2] Frank S. Barnes and Jonah G. Levine. *Large Energy Storage Systems Handbook*. CRC Press, March 2011.

[3] US Department of Energy. Grid energy storage. Dec 2013.

[4] IEC Electrical Energy Storage project team. Electrical energy storage white paper. 2011.

[5] Flow Battery. Compressed air batteries, 2015. URL http://www.flowbattery.co.uk/compressed-air-batteries. Accessed: 03.08.2015.

[6]

[7] E.ON. Huntorf power plant, 2015. URL https://www.eon.com/en/about-us/structure/asset-finder/huntorf.html. Accessed: 03.08.2015.

[8] PowerSouth Energy Cooperative. Powersouth caes, 2015. URL http://www.powersouth.com/mcintosh_power_plant/compressed_air_energy. Accessed: 03.08.2015.

[9] RWE. Adele – adiabatic compressed-air energy storage for electricity supply. RWE Brochure, 2010. URL https://www.rwe.com/web/cms/mediablob/en/391748/data/364260/1/rwe-power-ag/innovations/Brochure-ADELE.pdf. Accessed: 03.09.2015.

[10] James Varley. James varley. Modern Power Systems, 2010. URL http://www.modernpowersystems.com/features/featureintroducing-adele/. Accessed: 03.08.2015.

[11] Mark Scott. Energy for a Rainy Day, or a Windless One. The New Yotk Times, 2014. URL http://www.nytimes.com/2014/10/08/business/energy-for-a-rainy-day-or-a-windless-one.html. Accessed: 03.08.2015.

[12] Dresser-Rand. Compressed air energy storage (caes) product form, 2015. URL http://www.dresser-rand.com/wp-content/uploads/2015/01/85164-10-CAES.pdf. Accessed: 03.08.2015.

[13] Dresser-Rand. Smartcaes, 2015. URL http://www.dresser-rand.com/products-solutions/systems-solutions/compressed-air-energy-storage-solutions/. Accessed: 03.08.2015.

[14] Energy Storage Power Corporation. Compressed air energy storage, 2015. URL http://www.energystorageandpower.com/. Accessed: 03.08.2015.

[15] General Compression. Who we are, 2015. URL http://www.generalcompression.com/index.php/who. Accessed: 03.08.2015.

[16] Hydrodynamics Group. Overview - compressed air energy storage, 2015. URL http://www.hydrodynamics-group.com/geological-consulting/compressed-air-energy-storage/overview/. Accessed: 03.08.2015.

[17] Hydrostor. Underwater compressed air electrical storage, 2015. URL http://hydrostor.ca/home/. Accessed: 03.08.2015.

[18] Western Energy Hub. Magnum compressed air energy storage, 2015. URL http://westernenergyhub.com/caes.php. Accessed: 03.08.2015.

[19] Amy Westervelt. Pg&e approved for 50 million compressed air energy storage project. Inside Climate News, 2015. URL http://insideclimatenews.org/news/20100131/pge-approved-50-million-compressed-air-energy-storage-project. Accessed: 03.08.2015.

[20] SustainX. About us, 2015. URL http://www.sustainx.com/about-us-overview.htm. Accessed: 03.08.2015.

[21] Lighsail Energy. Lighsail energy technology, 2015. URL http://www.lightsail.com. Accessed: 03.08.2015.

[22] BBC Brown Boveri. Huntorg Air Storage Gas Turbine Power Plant - Energy Supply, 2014. URL https://www.eon.com/content/dam/eon-content-pool/eon/company-asset-finder/asset-profiles/shared-ekk/BBC_Huntorf_engl.pdf. Accessed: 03.08.2015.

[23] Emad Sedky. Electrical generation equipments course, Jan 2013. URL http://emadrlc.blogspot.co.nz/2013/01/chapter-2-ac-generators.html. Accessed: 15.07.2015.

[24] Stephen J Chapman. *Electric Machinery Foundamentals, 5th Edition*. McGraw-Hill, 2012.

[25] Theodore Wildi. *Electrical Machines, Drives and Power Systems*. Prentice Hall, 6th edition, Feb 2005.

[26] Prabha Kundur. *Power System Stability and Control*. McGraw-Hill Education, 1st edition, Jan 1994.

[27] M. Galal Rabie. *Fluid Power Engineering*. McGraw-Hill Book Company, Inc, 2009.

[28] F. D. Norvelle. *Electrohydraulic Control Systems*. Prentice-Hall Inc, New Jersey, USA, 2000.

[29] George E. Totten and Victor J. De Negri. *Handbook of Hydraulic Fluid Technology*. CRC Press, USA, 2012.

[30] Steve Miller Valery Tchkalov. Parameterization of directional and proportional valves in simhydraulics. *MathWorks Docuementation Centre*, 2009.

[31] ISO. *Hydraulic Fluid Power – Electrically modulated hydraulic control valves — Part 1: Test methods for four-way directional flow control valves*. ISO, Switzerland, 1998.

[32] ISO. *Hydraulic Fluid Power – Electrically modulated hydraulic control valves — Part 2: Test methods for four-way directional flow control valves*. ISO, Switzerland, 1998.

[33] Ernest E Lewis and Hansjoerg Stern. *Design of Hydraulic Control Systems*. McGraw-Hill Book Company, Inc, 1962.

[34] D. McCloy and H. R. Martin. *Control of Fluid Power*. Longman Group Limited, Great Britan, 1973.

[35] Erin Knight, Matthew Russell, Dipti Sawalka, and Spencer Yendell. Valve modeling, September 2006. URL https://controls.engin.umich.edu/wiki/index.php/ValveModeling. Accessed: 26.07.2015.

[36] B. Wayne Bequette. *Process Control: Modeling, Design, and Simulation*. Prentice Hall Professional, 2003.

[37] Parker Hannifin Corporation. Proportional throttle valves series tda technical information, 2014. URL http://www.launchrun.com/hpd/pdfs/GOLDCUP_Application%20Handbook_HY28-2668-01-GC-NA,EU.pdf. Accessed: 12.06.2014.

[38] Emerson Process Management. *Control Valve Handbook*. Fisher Controls International, USA, 2005.

[39] ValveLink Software. What's your flow control valve telling you?, 2003. URL http://www.controldesign.com/articles/2003/164/. Accessed: 05.06.2014.

[40] Michel Ruel. Stiction: The hidden menace, 2000. URL http://www.expertune.com/articles/RuelNov2000/stiction.html. Accessed: 05.06.2014.

[41] Jacques Smuts. Process control for practitioners - control valve problems, 2010. URL http://blog.opticontrols.com/archives/77. Accessed: 05.06.2014.

[42] Christian Faulhammer. Electro-proportional terms and definitions, 2010. URL www.sunhydraulics.com/sites/default/files/media_library/tech_resources/rel-Prop_terms-definitions.pdf. Accessed: 05.06.2014.

[43] W. L. Bialkowski. Dreams versus reality: A view from both sides of the gap. *Pulp and Paper Canada*, 94(11), 1993.

[44] Karl Astrom and Tore Hagglund. *Advanced PID Control*. Instrumentation, Systems and Automation Society (ISA), USA, 2006.

[45] Parker Hannifin Corporation. Porportional valves contents - catalog hy15-3502/us, 2010. URL http://www.parker.com/literature/Literature%20Files/IHD/PVsection.pdf. Accessed: 05.06.2014.

[46] ValveLink Software. Dead band plus hysteresis estimation with valvelink diagnostics, 2012. URL http://www.documentation.emersonprocess.com/groups/public/documents/bulletins/d103549x012.pdf. Accessed: 05.06.2014.

[47] Axiomatic Global Electronic Solution. Pulse width modulation, 2010. URL http://www.axiomatic.com/pulse-width-modulation.pdf. Accessed: 05.06.2014.

[48] James Beall. Improving control valve performance - report. *Chemical Engineering.*, 117(20):41 – 45, 2010.

[49] William J. Thayer. Specification standards for electrohydraulic flow control servovalves, 1962.

[50] MOOG Hydraulics. Sizing of electro-hydraulic drive systems with proportional and servo valves, 2005. URL www.moog.com/literature/ICD/Valves-Introduction.pdf. Accessed: 12.04.2015.

[51] HydraForce. Electronic control of hydraulic systems, 2011. URL http://www.hydraforce.com/electro/ElecCont_html/3-440-1_Elec_Mobile_Equip/3-440-1_Elec_Mobile_Equip.htm. Accessed: 26.07.2015.

[52] P.E. Jack L. Johnson. How to interpret valve specifications, 2005. URL http://hydraulicspneumatics.com/200/TechZone/HydraulicValves/Article/False/9480/TechZone-HydraulicValves. Accessed: 19.04.2015.

[53] Bill Fitzgerald. *Control Valves for the Chemical Process Industries*. McGraw-Hill Professional, December 1995.

[54] Equilibar. High resolution flow control valves using a back pressure regulator for precision flow control, 2015. URL http://www.equilibar.com/application/high-resolution-flow-control-valve/. Accessed: 26.07.2015.

[55] Paul Heney. Hydraulic motors, 2013. URL http://www.mobilehydraulictips.com/hydraulic-motors/. Accessed: 09.06.2014.

[56] Dension Hydraulics. Denison gold cup® application handbook piston pumps and motors, 2013. URL http://www.launchrun.com/hpd/pdfs/GOLDCUP_Application%20Handbook_HY28-2668-01-GC-NA,EU.pdf. Accessed: 12.06.2014.

[57] Werner G. Holzbock. *Hydraulic Power and Equipment*. Industrial Press, Inc, USA, 1968.

[58] Brendan Casey. Hydraulic pumps and motors: Considering efficiency, 2011. URL http://www.machinerylubrication.com/Read/28430/hydraulic-pump-motors-maintenance. Accessed: 09.06.2014.

[59] C.C. de Wit. *Friction Modeling and Compensation - The Control Handbook*. CRC Press, 1995.

[60] Trasnpower Limited. Automatic Under-Frequency Load Shedding (AUFLS) Technical Report, August 2010. URL https://www.systemoperator.co.nz/sites/default/files/bulk-upload/

documents/AUFLS_Technical_Report-aug-2010.pdf. Accessed: 26.06.2015.

[61] System Operator. System security forecast 2014 part e - frequency principal performance obligations, Dec 2014. URL https://www.systemoperator.co.nz/sites/default/files/bulk-upload/documents/Part%20E%20Frequency%20PPOs.pdf. Accessed: 15.07.2015.

[62] System Operator. Frequency barometer, Oct 2010. URL https://www.systemoperator.co.nz/documents/maps-and-diagrams. Accessed: 15.07.2015.

[63] Trasnpower Limited. AUFLS Scheme Design - Technical Summary, 07 2013. URL http://www.systemoperator.co.nz/sites/default/files/bulk-upload/documents/20130807%20AUFLS%20Scheme%20Design%20Report.pdf. Accessed: 26.06.2015.

[64] H. Bevrani, G. Ledwich, and J.J. Ford. On the use of df/dt in power system emergency control. In *Power Systems Conference and Exposition, 2009. PSCE '09. IEEE/PES*, pages 1–6, March 2009.

[65] A. Prince-Pike, D.I. Wilson, I. Ilieva, A. Li, and M. Phethean. Maintaining new zealand's electrical reserve management tool. In *IPEC, 2012 Conference on Power Energy*, pages 273–278, Dec 2012.

[66] Transpower. Glossary. URL https://www.transpower.co.nz/resources/glossary/. Accessed: 15.07.2015.

[67] Transpower. Automatic under-frequency load shedding (aufls) review, July 2015. URL https://www.systemoperator.co.nz/activites/current-projects/automatic-under-frequency-load-shedding-aufls-review. Accessed: 15.07.2015.

[68] J. Duncan Glover, Mulukutla Sarma, and Thomas Overbye. *Power System Analysis and Design*. Cengage Learning, 4th edition, 2008.

[69] Math H. Bollen. *Understanding Power Quality Problems: Voltage Sags and Interruptions*. Wiley-IEEE Press, 1999.

[70] Surya Santoso, Mark F. McGranaghan, Roger C. Dugan, and H. Wayne Beaty. *Electrical Power Systems Quality*. McGraw-Hill Education, 3rd edition, 2012.

[71] Nikunj Shah. White paper - harmonics in power systems causes, effects and control, May 2013. URL https://www.industry.usa.siemens.com/

drives/us/en/electric-drives/ac-drives/Documents/DRV-WP-drive_harmonics_in_power_systems.pdf. Accessed: 15.07.2015.

[72] D.B. Vannoy, M.F. Mcgranaghan, S.M. Halpin, W.A. Moncrief, and D.D. Sabin. Roadmap for power quality standards development. In *Petroleum and Chemical Industry Conference, 2005. Industry Applications Society 52nd Annual*, pages 267–276, Sept 2005.

[73] Ieee recommended practice and requirements for harmonic control in electric power systems. *IEEE Std 519-2014 (Revision of IEEE Std 519-1992)*, pages 1–29, June 2014.

[74] M. McGranaghan and G. Beaulieu. Update on iec 61000-3-6: Harmonic emission limits for customers connected to mv, hv, and ehv. In *Transmission and Distribution Conference and Exhibition, 2005/2006 IEEE PES*, pages 1158–1161, May 2006.

[75] N. Watson, S. Hardie, V. Gosbell, S. Elphick, and S. Perera. Power Quality Guide - Update and Amendment, Revision 3.8 . 2013.

[76] Math H. Bollen. *Understanding Power Quality Problems: Voltage Sags and Interruptions*. Wiley-IEEE Press, 1999.

[77] Pedro Rodriguez Remus Teodorescu, Marco Liserre. *Grid Converters for Photovoltaic and Wind Power Systems*. Wiley, 2011.

[78] Ahmed Al-Durra S. M. Muyeen and Hany M. Hasanien. *Modeling and Control Aspects of Wind Power Systems*. InTech, 2013.

[79] Lidong Zhang and M.H.J. Bollen. Characteristic of voltage dips (sags) in power systems. In *Harmonics and Quality of Power Proceedings, 1998. Proceedings. 8th International Conference On*, volume 1, pages 555–560 vol.1, Oct 1998.

[80] M.S. El Moursi, Weidong Xiao, and J.L. Kirtley. Fault ride through capability for grid interfacing large scale pv power plants. *Generation, Transmission Distribution, IET*, 7(9):1027–1036, Sept 2013.

[81] Hao Tian, Feng Gao, Cong Ma, Guoqing He, and Guanghui Li. A review of low voltage ride-through techniques for photovoltaic generation systems. In *Energy Conversion Congress and Exposition (ECCE), 2014 IEEE*, pages 1566–1572, Sept 2014.

[82] Hongwei Ma, Lie Xu, Yongdong Li, Zedong Zheng, and Ling Peng. Direct power control of doubly-fed-induction-generator-based wind turbines under asymmetrical

grid voltage dips. In *Energy Conversion Congress and Exposition (ECCE), 2012 IEEE*, pages 787–792, Sept 2012.

[83] Almoataz Y. Abdelaziz, Amr M. Ibrahim, Ahmed M. Asim, Ahmed H.Abdel Razek, and Y.G. Hegazy. Investigation of electrical dynamics of dfig-based wind turbines during severe symmetrical grid voltage dips. In *Engineering and Technology (ICET), 2012 International Conference on*, pages 1–6, Oct 2012.

[84] Yang Xiao-ping, Xian feng Duan, and Yan li Bai. Asymmetrical voltage dip ride-through enhancement of directly driven wind turbine with permanent magnet synchronous generator. In *Sustainable Power Generation and Supply, 2009. SUPERGEN '09. International Conference on*, pages 1–6, April 2009.

[85] V. Salas, E. Olias, M. Alonso, F. Chenlo, and A. Barrado. Dc current injection into the network from pv grid inverters. In *Photovoltaic Energy Conversion, Conference Record of the 2006 IEEE 4th World Conference on*, volume 2, pages 2371–2374, May 2006.

[86] Lars Gertmar, P. Karlsson, and O. Samuelsson. On dc injection to ac grids from distributed generation. In *Power Electronics and Applications, 2005 European Conference on*, pages 10 pp.–P.10, 2005.

[87] International standard photovoltaic (pv) systems – characteristics of the utility interface. *IEC 61727:2004*, 2004.

[88] IEEE Application Guide for IEEE Std 1547. IEEE Standard for Interconnecting Distributed Resources with Electric Power Systems. *IEEE Standard 1547.2-2008*, 16(2):1 – 217, April 2009.

[89] IEEE Recommended Practice for Utility Interface of Photovoltaic (PV) Systems. *IEEE Std 929-2000*, 2000.

[90] Jan Machowski, Janusz Bialek, and Dr Jim Bumby. *Power System Dynamics: Stability and Control,*. John Wiley & Sons, Chippenham Wiltshire, Great Britain, 2nd edition, 2008.

[91] Edward Wilson Kimbark. *Power System Stability: Synchronous Machines*. Dover Publications, Inc, 1968.

[92] Arieh L. Shenkman. *Transient Analysis of Electric Power Circuits Handbook*. Springer, 2005.

[93] M.J. Thompson. Fundamentals and advancements in generator synchronizing systems. In *Protective Relay Engineers, 2012 65th Annual Conference for*, pages 203–214, April 2012.

[94] C.J. Mozina, B. Beckwith, E.C. Fennell, A.C. Pierce, P.W. Powell, J.T. Uchiyama, and S.M. Usman. Generator synchronizing industry survey results. *Power Delivery, IEEE Transactions on*, 11(1):174–183, Jan 1996.

[95] Wellington Electricity. Technical Requirements for Connection of Distributed Generation (DG) - Rev 0, 07 2012. URL http://www.welectricity.co.nz/assets/Docs/ENG-100-Technical-Requirements-for-Connection-of-Distributed-Generation-.pdf. Accessed: 26.06.2015.

[96] ABB. *AMG Synchronous Generator Industrial Application Series for Generator type: AMG 0180-AMG 0500 (8AMG5854948)*, August 2012. Rev. E.

[97] IEEE Guide for Operation and Maintenance of Turbine Generators. *IEEE Std 67-2005 (Revision of IEEE Std 67-1990)*, pages 01–69, 2006.

[98] Katsuhiko Ogata. *Modern Control Engineering, 5th ed.* Prentice Hall, 2008.

[99] Richard C. Dorf and Robert H. Bishop. *Analysis of Synchronous Machines.* Prentice Hall, 9th edition, 2001.

[100] Girish Chowdhary, Emilio Frazzoli, Jonathan P. How, and Hugh Lui. *Handbook of Unmanned Aerial Vehicles.* Springer, 2012.

[101] Graham C. Goodwin, Jose De Dona, Osvaldo J. Rojas, and Michel Perrier). A brief overview of nonlinear control. *Automatica*, 35(1):407–427, 1999.

[102] Alberto Isidori. *Nonlinear Control Systems.* Springer, 3rd edition, 1995.

[103] Hassan K. Khalil. *Nonlinear Systems.* Prentice Hall, 3rd edition, 2002.

[104] J. K. Hedrick and A. Girard. *Control of Nonlinear Dynamic Systems: Theory and Applications*, 2010. University of California, Berkeley - ME237 lecture notes .

[105] Bela Lantos and Lorinc Marton. *Nonlinear Control of Vehicles and Robots.* Springer London, 2011.

[106] Zoran Vukic, Ljubomir KuljaCa, Dali Donlagic, and Sejid Tesnjak. *Nonlinear Control Systems.* Marcel Dekker, Inc, USA, 2003.

[107] Herbert E. Merritt. *Hydraulic Control Systems.* John Wiley & Sons, 1967.

[108] Wayne Anderson. *Controlling Electrohydraulic Systems.* CRC Press, 1988.

[109] R.R. Kadiyala. A tool box for approximate linearization of nonlinear systems. *Control Systems, IEEE*, 13(2):47 – 57, 1993.

[110] S. Boyd. Table of Laplace Transforms. Stanford University, 2015. URL https://web.stanford.edu/~boyd/ee102/laplace-table.pdf. Accessed: 28.07.2015.

[111] MathWorks. Models with time delays, 2015. URL http://au.mathworks.com/help/control/ug/models-with-time-delays.html#bsytwd0. Accessed: 26.07.2015.

[112] Declan G. Bates Matthew C. Turner. *Mathematical Methods for Robust and Nonlinear Control: EPSRC Summer School*. Springer, October 2007.

[113] Kevin Warwick. *An Introduction to Control Systems, 2nd Edition*. World Scientific Publishing, Danvers, Massachusetts, 1996.

[114] Norman S. Nise. *Control Systems Engineering*. John Wiley & Sons, 6th edition, December 2011.

[115] David Costello and Karl Zimmerman. Frequency tracking fundamentals, challenges, and solutions. *64th Annual Conference for Protective Relay Engineers*, pages 203 – 214, April 2011.

[116] Spark Y. Xue and Simon X. Yang. Accurate and fast frequency tracking for power system signals. *IEEE International Conference on Systems, Man and Cybernetics*, pages 2754 – 2759, Oct 2007.

[117] Djuric P.M. Dunlap S Begovic, M.M and A.G. Phadke. Frequency tracking in power networks in the presence of harmonics. *Power Delivery, IEEE Transactions*, 8(2):480 – 486, Aug 2002.

[118] System Operator. System operator report: Automatic under-frequency load shedding (aufls) rocof testing, July 2012. URL http://www.systemoperator.co.nz/sites/default/files/bulk-upload/documents/AUFLS-III-RoCoF-testing-summary.pdf. Accessed: 15.07.2015.

[119] Morrow D.J. Littler, T.B. Wavelets for the analysis and compression of power system disturbances. *Power Delivery, IEEE Transactions*, pages 358 – 364, April 1999.

[120] T Lin, M. Tsuji, and E. Yamada. A wavelet approach to real time estimation of power system frequency. *SICE 2001. Proceedings of the 40th SICE Annual Conference. International Session Papers*, pages 58 – 65, 2001.

[121] J Ning and W. Gao. A wavelet-based method to extract frequency feature for power system fault/event analysis. *Power and Energy Society General Meeting, 2009. PES 09. IEEE*, pages 1 – 5, 2009.

[122] V.L. Pham and K.P. Wong. Wavelet-transform-based algorithm for harmonic analysis of power system waveforms. *Generation, Transmission and Distribution, IEE Proceedings-*, 146(3):249–254, May 1999.

[123] J. K. Wu. Frequency tracking techniques of power system including higher order harmonics. *Proceedings of the Fifth IEEE International Caracas Conference on Devices, Circuits and Systems,*, pages 298 – 303, Nov 2004.

[124] A.N. Belbachir, B. Boulerial, and M.F. Belbachir. A new approach to finite wordlength coefficient fir digital filter design using the branch and bound technique. In *Signal Processing Conference, 2000 10th European*, pages 1–4, Sept 2000.

[125] P.J. Moore, R.D. Carranza, and A.T. Johns. A new numeric technique for high-speed evaluation of power system frequency. *Generation, Transmission and Distribution, IEE Proceedings-*, 141(5):529–536, Sep 1994.

[126] J.K. Wu. Numerical differentiation and digital fir filter based algorithm for power system measurement. In *Power Engineering Society General Meeting, 2005. IEEE*, pages 1367–1374 Vol. 2, June 2005.

[127] Wu Jiekang, Long Jun, and Wang Jixiang. High-accuracy, wide-range frequency estimation methods for power system signals under nonsinusoidal conditions. In *Power Engineering Society General Meeting, 2004. IEEE*, pages 956 Vol.1–, June 2004.

[128] Zhaosheng Teng Fuhai Li He Wen, Siyu Guo and Yuxiang Yang. Frequency estimation of distorted and noisy signals in power systems by fft-based approach. *Power Systems, IEEE Transactions*, 29(2):765 – 774, 2014.

[129] T. Lobos and J. Rezmer. Real-time determination of power system frequency. *Instrumentation and Measurement, IEEE Transactions on*, 46(4):877–881, Aug 1997.

[130] Jun-Zhe Yang and Chih-Wen Liu. A precise calculation of power system frequency and phasor. *Power Delivery, IEEE Transactions on*, 15(2):494–499, Apr 2000.

[131] A.A. Girgis and Fredric M. Ham. A new fft-based digital frequency relay for load shedding. *Power Apparatus and Systems, IEEE Transactions on*, PAS-101(2): 433–439, Feb 1982.

[132] H.C. Lin and C.S. Lee. Enhanced fft-based parametric algorithm for simultaneous multiple harmonics analysis. *Generation, Transmission and Distribution, IEE Proceedings-*, 148(3):209–214, May 2001.

[133] M.S Sachdev, H.C. Wood, and N.G. Johnson. Kalman filtering applied to power system measurements for relaying. *Power Engineering Review, IEEE*, 5(12):52 – 53, Dec 1985.

[134] A.A. Girgis and T.L.Daniel Hwang. Optimal estimation of voltage phasors and frequency deviation using linear and nonlinear kalman filtering: Theory and limitations. *Power Engineering Review, IEEE*, PER-4(10):46–47, Oct 1984.

[135] E. Ghahremani and I. Kamwa. Dynamic state estimation in power system by applying the extended kalman filter with unknown inputs to phasor measurements. *Power Systems, IEEE Transactions on*, 26(4):2556–2566, Nov 2011.

[136] Cheng-I Chen and Yuan-Chieh Chin. Extended real model of kalman filter for power system harmonic measurements. In *Power and Energy Engineering Conference (APPEEC), 2010 Asia-Pacific*, pages 1–5, March 2010.

[137] D. Yazdani, A. Bakhshai, and P.K. Jain. Grid synchronization techniques for converter interfaced distributed generation systems. In *Energy Conversion Congress and Exposition, 2009. ECCE 2009. IEEE*, pages 2007–2014, Sept 2009.

[138] N. Hoffmann, R. Lohde, M. Fischer, F.W. Fuchs, L. Asiminoaei, and P.B. Thogersen. A review on fundamental grid-voltage detection methods under highly distorted conditions in distributed power-generation networks. In *Energy Conversion Congress and Exposition (ECCE), 2011 IEEE*, pages 3045–3052, Sept 2011.

[139] L.R. Limongi, R. Bojoi, C. Pica, F. Profumo, and A. Tenconi. Analysis and comparison of phase locked loop techniques for grid utility applications. In *Power Conversion Conference - Nagoya, 2007. PCC '07*, pages 674–681, April 2007.

[140] A. Timbus, M. Liserre, R. Teodorescu, and F. Blaabjerg. Synchronization methods for three phase distributed power generation systems - an overview and evaluation. In *Power Electronics Specialists Conference, 2005. PESC '05. IEEE 36th*, pages 2474–2481, June 2005.

[141] He-Rong GU Xiao-Qiang GUO, Wei-Yang WU. Phase locked loop and synchronization methods for grid interfaced converters: a review. *PRZEGLAD ELEKTROTECHNICZNY*, 22:182–187, 04 2011.

[142] P. Rodriguez, J. Pou, J. Bergas, J.I. Candela, R.P. Burgos, and D. Boroyevich. Decoupled double synchronous reference frame pll for power converters control. *Power Electronics, IEEE Transactions on*, 22(2):584–592, March 2007.

[143] P. Rodriguez, L. Sainz, and J. Bergas. Synchronous double reference frame pll applied to a unified power quality conditioner. In *Harmonics and Quality of Power, 2002. 10th International Conference on*, volume 2, pages 614–619 vol.2, Oct 2002.

[144] F. Liccardo, P. Marino, C. Schiano, and N. Visciano. A new robust phase tracking system for asymmetrical and distorted three phase networks. In *Harmonics and Quality of Power, 2004. 11th International Conference on*, pages 525–530, Sept 2004.

[145] F. Liccardo, P. Marino, and G. Raimondo. Robust and fast three-phase pll tracking system. *Industrial Electronics, IEEE Transactions on*, 58(1):221–231, Jan 2011.

[146] Garth Nash. Phase-locked loop design fundamentals, 1994. URL http://www.lansdale.com/Articles/an535.pdf. Accessed: 26.06.2015.

[147] Floyd M. Gardner. *PhaseLock Techniques*. John Wiley & Sons, Inc, Hoboken, NJ, USA., 3rd edition, 2005.

[148] W.C. Duesterhoeft, Max W. Schulz, and Edith Clarke. Determination of instantaneous currents and voltages by means of alpha, beta, and zero components. *American Institute of Electrical Engineers, Transactions of the*, 70(2):1248–1255, July 1951.

[149] Petrella, R. and Revelant, A. and Stocco, P. Robust grid synchronisation in three-phase distributed power generation systems by synchronous reference frame pre-filtering. In *Universities Power Engineering Conference (UPEC), 2009 Proceedings of the 44th International*, pages 1–5, Sept 2009.

[150] Ramon Pallas-Areny and John G Webster. *Analog Signal Processing*. John Wiley & Sons, 1999.

[151] Steve Miller Valery Tchkalov. Parameterization of directional and proportional valves in simhydraulics. *MathWorks Docuementation Centre*, 2009.

[152] Aravind E Vijayan. Encoders, 2015. URL http://www.aravindev.com/optical-encoders.html. Accessed: 29.03.2015.

[153] David G. Alciatore and Michael B. Histand. *Introduction to Mechatronics and Measurement Systems*. McGraw-Hill, 1999.

[154] Phidgets Inc. Encoder primer, 2014. URL http://www.phidgets.com/docs/Encoder_Primer. Accessed: 14.03.2015.

[155] Pepperl+Fuchs. Absolute rotary encoder, 2015. URL http://www.pepperl-fuchs.com/global/en/classid_196.htm. Accessed: 29.03.2015.

[156] Hengstler GmbH. Encoder catalog. pages 344 – 345, 2004.

[157] Miles Budimir. Understanding encoders, 2013. URL http://www.motioncontroltips.com/2013/11/04/understanding-encoders/. Accessed: 10.04.2015.

[158] Encoder Products Company. Installation and wiring guide (rev g 11/11). 2009.

[159] Encoder Products Company. Trouble shooting guide for incremental encoders (ts guide, rev. a). 2013.

[160] Stefano Bifaretti Armando Bellini and Stefano Costantini. A digital speed filter for motion control drives with a low resolution position encoder. *Automatika*, 44 (1-2):67 – 74, 2003.

[161] Robert Grover Brown and Parick Y. C. Hwang. *Introduction to Random Signals and Applied Kalman Filtering with MATLAB Exerises, 4th Edition*. John Wiley & Sons, Inc, USA, 2012.

[162] Rudolf E. Kalman. *A New Approach to Linear Filtering and Prediction Problems*, volume 82. 1960.

[163] Ramsey Faragher. Understanding the basis of the kalman filter via a simple and intuitive derivation [lecture notes]. 29(5):128 – 132, 2012.

[164] Peter S. Maybeck. *Stochastic models, estimation, and control*, volume 1. Mathematics in Science and Engineering, 1979.

[165] Wang SHAOWEI and Wan SHANMING. Velocity and acceleration computations by single-dimensional Kalman filter with adaptive noise variance . *Przeglad Elektrotechniczny*, 88:283–287, 2012.

[166] MathWorks. Signal-to-noise ratio documentation, 2015a. URL http://au.mathworks.com/help/signal/ref/snr.html. Accessed: 29.03.2015.

[167] Fan Wang and M.H.J. Bollen. Frequency-response characteristics and error estimation in rms measurement. *Power Delivery, IEEE Transactions on*, 19(4): 1569–1578, Oct 2004.

[168] Fan Wang and M.H.J. Bollen. Frequency-response characteristics and error estimation in rms measurement. *Power Delivery, IEEE Transactions on*, 19(4): 1569–1578, Oct 2004.

[169] David Havelock, Sonoko Kuwano, and Michael Vorlander. *Handbook of Signal Processing in Acoustics*. Springer, 2008.

[170] Richard G. Lyonsr. *Understanding Digital Signal Processing*. Prentice Hall, 3rd edition, 2010.

[171] J. Barros and E. Perez. Limitations in the use of r.m.s. value in power quality analysis. In *Instrumentation and Measurement Technology Conference, 2006. IMTC 2006. Proceedings of the IEEE*, pages 2261–2264, April 2006.

[172] F.J. Harris. On the use of windows for harmonic analysis with the discrete fourier transform. *Proceedings of the IEEE*, 66(1):51–83, Jan 1978.

[173] Hewlett-Packard Co. The fundamentals of signal analysis - application note 243, 1994. URL http://www.hpmemoryproject.org/an/pdf/an_243.pdf. Accessed: 15.07.2015.

[174] Dr. Andrew Greensted. Fir filters by windowing, May 2010. URL http://www.labbookpages.co.uk/audio/firWindowing.html. Accessed: 15.07.2015.

[175] Hisham Odeh Alrawashdeh. An adaptive kalman filter for voltage sag detection in power systems, 2014.

[176] S.A. Hussain, F.R. Zaro, and M.A. Abido. Implementation of quadrature based rms calculation on real-time power monitoring systems. In *Power and Energy Conference at Illinois (PECI), 2013 IEEE*, pages 213–217, Feb 2013.

[177] H. Hegedus, P. Mostarac, and R. Malaric. Precision rms value measurement of non-coherent sampled signals. In *Precision Electromagnetic Measurements (CPEM), 2010 Conference on*, pages 205–206, June 2010.

[178] G.E. Mog and E.P. Ribeiro. One cycle ac rms calculations for power quality monitoring under frequency deviation. In *Harmonics and Quality of Power, 2004. 11th International Conference on*, pages 700–705, Sept 2004.

[179] Martin Novotny1 and Milos Sedlacek2. Measurement of rms values of non-coherently sampled signals. *In Proceedings of the 13th International Symposium on Measurements for Research and Industry Applications*, pages 230–235, 2004.

[180] Alstom. Kavs 100 synchronism check relay technical manual, 2010. URL http://www.alstom.com/Global/Grid/Resources/Documents/Automation/Technical%20manuals/KAVS%20100%20Manual%20GB.pdf. Accessed: 16.06.2015.

[181] Basler. Instruction manual for sync-check relay be1-25 - rev r, 09 2007. URL http://www.electricalmanuals.net/files/RELAYS/BASLER/BE1-25/9170200990R.pdf. Accessed: 16.06.2015.

[182] ABB. Spau 140 c synchro-check relay: User's manual and technical description rev b, 04 2002. URL https://library.e.abb.com/public/16ed9af8181610f9c2256bf100385d8a/FM_SPAU140C_EN_BAA.pdf?filename=FM_SPAU140C_EN_BAA.pdf. Accessed: 16.06.2015.

[183] S. Golestan, M. Monfared, F.D. Freijedo, and J.M. Guerrero. Advantages and challenges of a type-3 pll. *Power Electronics, IEEE Transactions on*, 28(11):4985–4997, Nov 2013.

[184] Jr. Costa, D.R., L.G.B. Rolim, and M. Aredes. Analysis and software implementation of a robust synchronizing circuit - pll circuit. In *Industrial Electronics, 2003. ISIE '03. 2003 IEEE International Symposium on*, volume 1, pages 292–297 vol. 1, June 2003.

[185] National Instruments. What is the difference between a line driver, open collector, and push-pull quadrature encoders and which one should i use?, 2005. URL http://digital.ni.com/public.nsf/allkb/0C5091E9099059BC86256FC1007947AA. Accessed: 12.04.2015.

[186] David .C. Drain. *Statistical Methods for Industrial Process Control*. Springer, Great Britan, 1997.

[187] Hydac USA. Sizing accumulators, 2014. URL http://www.hydacusa.com/literature/accumulators/ACU1102-1326_011_Sizing.pdf. Accessed: 12.03.2015.

[188] Ari Ingimundarson and Tore Hagglund. Robust tuning procedures of dead-time compensating controllers. *Control Engineering Practice*, 9(11):1195 – 1208, 2001.

[189] By Paul Bachman, Dr. Oscar Monteroand, and Doug Sherman. Three phase solid state relays & their application in three phase motor circuits. Crydom, Inc., 2011. URL http://www.crydom.com/en/tech/whitepapers/3p_mc_whitepaper.pdf. Accessed: 13.08.2015.

[190] OMRON Industrial Automation. G3ph product specification, 2012. URL http://www.ia.omron.com/products/family/3073/specification.html. Accessed: 13.08.2015.

[191] Phidgets Inc. Solid state relay primer, 2012. URL http://www.phidgets.com/docs/Solid_State_Relay_Primer. Accessed: 13.08.2015.

[192] Solid State Optronics. Application note 040 - solid state relay vs. electromechanical relays, 2014. URL http://www.ssousa.com/application-

notes/AppNote040_Solid-State-Relays-vs-Electromechanical-Relays.pdf. Accessed: 13.08.2015.

[193] Stephen Douglas. Electromechanical vs. solid state relays: decisions, decisions. Heilind Electronics, Inc, 2012. URL http://blog.heilind.com/2012/10/electromechanical-vs-solid-state-relays-decisions-decisions/. Accessed: 13.08.2015.

[194] Siemens. Siprotec numerical protection relays - protection systems catalog sip 2004, 2004. URL http://www.novec.ru/catalog/novosibirsk/catalog/siemens/siprotec2004_en.pdf. Accessed: 13.08.2015.

[195] ABB. Technical catalogue sace tmax xt - new low voltage moulded-case circuit-breakers up to 250a, 2015. URL https://library.e.abb.com/public/aa24223d8a99430898bc2b598f96cf94/1SDC210033D0202_GIUGNO%202015.pdf. Accessed: 13.08.2015.

[196] J.C. Das. *Power System Analysis: Short-Circuit Load Flow and Harmonics*. CRC Press, 2nd edition, 2011.

[197] US Department of Energy. Appliance and equipment standards: Distribution transformers, 2013. URL http://www1.eere.energy.gov/buildings/appliance_standards/product.aspx/productid/66. Accessed: 15.06.2015.

[198] Transpower. *Main Transmission System Planning Guideline*, rev 1.0 edition, 02 2005. URL https://www.ea.govt.nz/dmsdocument/3859. Accessed: 15.07.2015.

[199] Alstom Grid. *Network Protection & Automation*. May edition, 2011.

[200] J. Lewis Blackburn and Thomas J. Domin. *Protective Relaying: Principles and Applications*. CRC Press, 4th edition, Feb 2014.

[201] Juan A. Martinez-Velasco. *Transient Analysis of Power Systems: Solution Techniques, Tools and Applications*. John Wiley & Sons, Jan 2015.